2017

Tribological And Dynamical Study Of An Automotive Transmission System

Meng Li
Louisiana State University and Agricultural and Mechanical College

TRIBOLOGICAL AND DYNAMICAL STUDY OF AN AUTOMOTIVE TRANSMISSION SYSTEM

A Dissertation

Submitted to the Graduate Faculty of the
Louisiana State University and
Agricultural and Mechanical College
in partial fulfillment of the
requirements for the degree of
Doctor of Philosophy

in

The Department of Mechanical Engineering

by
Meng Li
B.S., China University of Petroleum, 2011
August 2017

ACKNOWLEDGEMENT

I would like to firstly thank my advisor Dr. Michael M. Khonsari, for the precious guidance he offered in both my academic research and personal growth during my Ph.D. program with his great kindness, patience, and continuous support. I would also acknowledge the energy and time from Dr. Shengming Guo, Dr. Kemin Zhou, Dr. Joonyoung Jang, and Dr. Zhiqiang Deng as members of the committee. Many thanks would be said to my colleagues in *CeRoM* laboratory for the precious experience of working together and collaborative project contributions from Volvo company group and Luleå University of Technology. Personally, I wish to express my deepest acknowledgement to the everlasting care, love, and support of my parents. Your reading is appreciated as well.

TABLE OF CONTENTS

ABSTRACT

The transmission system is critical for automotive and heavy duty equipment due to its prominent role in the powertrain system, which is often challenged with degraded torque capacity and harsh dynamic response. Simulation-guided design can provide appropriate guidelines to resolve these problems with virtual analyses. In current study, the tribological and dynamical study of an automatic transmission is performed at two levels: a wet clutch and powertrain.

In this dissertation, tribological study is performed for a wet clutch based on the thermohydrodynamic (THD) analysis that takes the following factors into account.

- The groove effect (depth, area, and pattern) is investigated for lubrication analysis;
- The elastic-plastic asperity contact model is used to predict the contact pressure;
- The heat transfer during the entire cycle of engagement from slip to lock to detachment is covered;
- The engagement time and the temperature profile are predicted for torque and thermal analysis.

With large engagement cycles, the friction lining of a wet clutch is worn off due to the material degradation at high load/temperature condition. By relating the wear behavior with the mechanism of thermal degradation and thermomechanical degradation, a physics-based wear model is proposed for the first time to analyze the wear process in a wet clutch. The predicted wear rate falls within nearly 95% confidence interval of the test results. Discrepancies of simulation are primarily due to limited availability of input data and model assumptions. Therefore, an uncertainty quantification analysis of the wear model is performed using the Monte Carlo simulations. In addition, a comprehensive parametric analysis of the clutch wear is considered with various factors, including groove design (waffle pattern shows the minimum wear), material properties and operational configurations (rotational speed plays the most influential role).

The dynamics of transmission directly affects the performance of the powertrain. The coupling effects of the key transmission components are examined. Of particular interests are the stick-slip behavior of the wet clutch and backlash of the gear train. Through simulation of the powertrain, the main source and the pattern of vibration propagation in the driveline are examined. Major vibration is observed during inappropriate clutch engagement.

CHAPTER 1 INTRODUCTION

1.1 Background and motivation

With demanding performance standards for the automotive transmission system and heavy duty equipment, researchers have resorted to simulation-guided design approach to gain insight into the machinery performance in an attempt to improve their durability and reliability.

One of the most crucial components in the transmission system is a wet clutch, which operates under lubricated conditions and provides smooth power transfer. As shown in Figure 1-1, the key elements of a wet clutch are: several core disks to both sides of which the friction material is bounded, a series of mating separator disks, and automatic transmission fluid (ATF) that lubricates the disk surfaces. For the transmission to operate smoothly, these elements must function in perfect harmony in terms of hydrodynamics, contact mechanics, and heat transfer.

The existing literature contains several tribological models proposed by different researchers to characterize the behavior of a wet clutch system. Natsumeda et al. carried out the one of the first theoretical analysis and hydrodynamic simulation of a paper-based wet clutch with consideration of permeability, compressive strain, and asperity contact [1]. Yang et al. [2] provided mathematical models with similar considerations and verified the results with experimental measurements favorably. Based on Natsumeda's work, Jang and Khonsari [3] developed a tribological model by adding the slip boundary and centrifugal terms for the hydrodynamic equation. Nevertheless, a comprehensive model to capture the entire engagement operations of the clutch system is still lacking, especially for the thermal behavior that governs all stages of the engagement cycle.

Classified by the operation and the thermal boundaries at the sliding interface, the full engagement cycle of a wet clutch translates into four distinct stages namely engagement, soaking, dwell, and stabilization periods. During the engagement stage, the engagement load is applied to reduce the film thickness, where the lubrication condition tends to shift from hydrodynamic to mixed and finally to the boundary regime. Meanwhile, the relative rotational speed gradually diminishes and a large amount of heat is generated due to the sliding motion and dynamic friction force. At the end of the engagement, the friction pair is locked up to transfer the power during the soak period and the temperature ceases to rise. When the dwell period begins, the gap between the separator disk and the friction lining is restored to the initial value by cooling of ATF flow. Investigation of important tribological performance associated with friction material degradation and frictional instability requires one to first perform a comprehensive analysis for the temperature history during the full engagement cycles [4]. Other study of thermal effects on the performance of wet clutch generally focuses on influence on torque transfer [5], the duration of the engagement time [6], and hot spot generation [7].

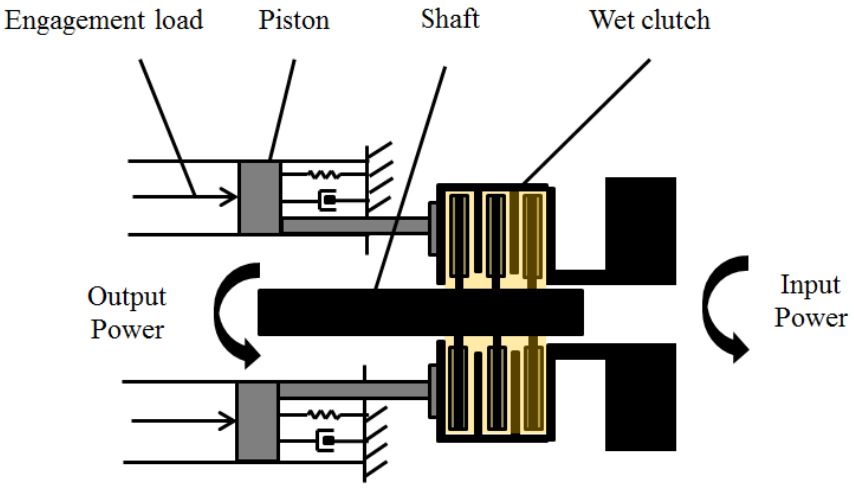

(a) A wet clutch with engagement actuation

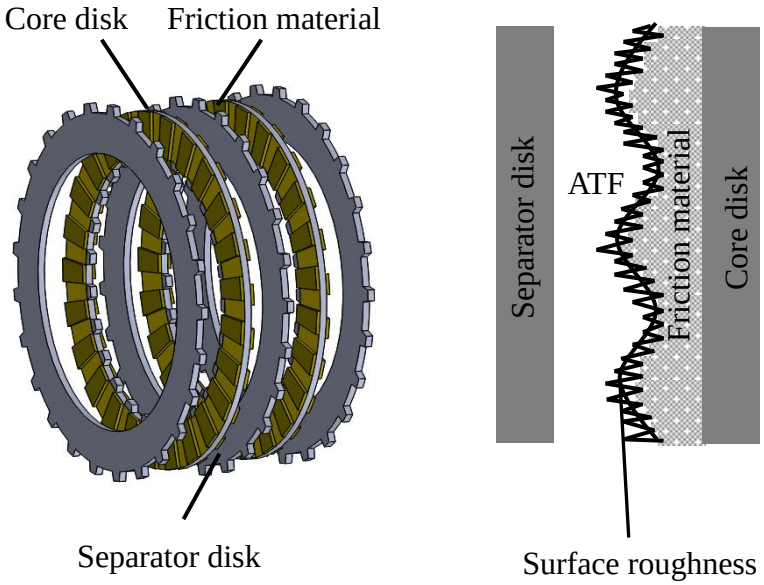

(b) A full wet clutch pack

Figure 1-1 Schematic diagram of a wet clutch system

The degradation of friction material after repeated engagement cycles directly determines the durability of a wet clutch, particularly when subjected to high-energy input. The most straightforward observation is wear, shown in Figure 1-2. Wear usually adversely affects the tribological performance of a wet clutch and can eventually result in transmission failure if the worn thickness of the friction lining is excessive. The pertinent reliability and safety considerations motivate the need for testing and prediction of wear behavior for the friction lining in a wet clutch. In a noteworthy experimental study, Lingesten et al. [8] reported an intriguing wear trend obtained using a specialized test rig equipped with several sensors capable of providing continuous measurement of the temperature, transmission torque, rotational speed

and friction lining wear rate. The test results revealed a unique two-stage wear phenomenon with distinct transition from an initially low wear rate to a much greater rate after a certain number of engagement cycles with high power input. The physical mechanisms and prediction of such a multi-stage wear behavior had remained elusive and required further investigation [9-11]. In this dissertation, we develop a model for the fiction material degradation and show that, indeed, the two-stage wear can be predicted.

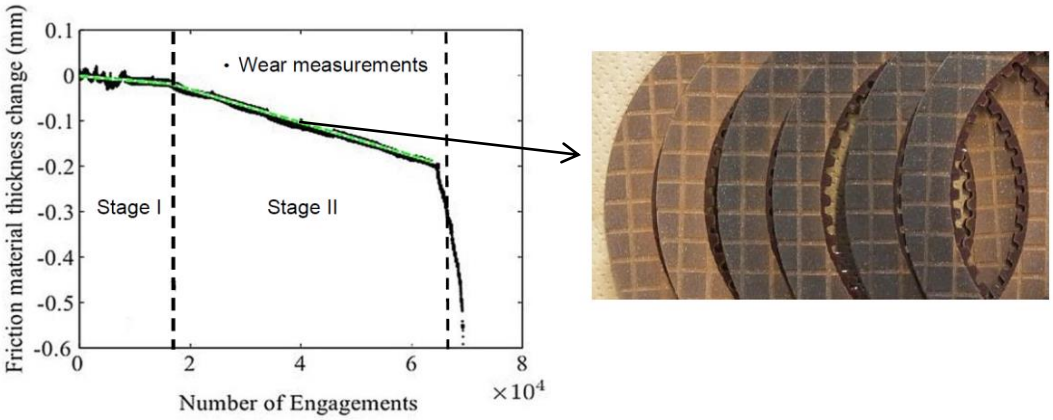

Figure 1-2 Wear and carbonization of friction material during large engagement cycles [8]

Apart from wear, generation and propagation of torsional vibration in the driveline is another possible source of mechanical fault for the powertrain system. Modeling and simulation of powertrain dynamics lay the foundation for the study of noise, vibration, and harshness (NVH) and many control applications. Essentially, a powertrain consists of the engine, the transmission, drive shafts, the differential and the final drive (or wheel). The engine converts the fuel energy into kinetic energy to perform mechanical work. The automotive engine modeling concentrates on the fuel delivery dynamics, speed/torque prediction, and inherent process, which can be referred to [12-14]. The automatic transmission produces a various range of speed and torque with different gear ratios generated by the planetary gear train and engagement/disengagement operation of the wet clutch lubricated with ATF [15-17]. The drive shaft links the transmission and the final drive. The differential appropriately slows down the rotational speed in transmission and delivers power to wheels to enable rotation at different speeds [18]. With the friction force generated at the tire/road interface, the vehicle moves with the transmitted power.

Analytical models associated with the final drive and the wheel dynamics are presented in several references [19, 20]. Although much attention has been paid to research of individual powertrain components [21-28], a comprehensive modeling framework that encompasses the components collectively is needed to investigate possible instabilities in automatic transmission system (stick-slip behavior of wet clutch and backlash of a planetary gear set), and other kind of NVH considerations. These factors are schematically illustrated in Figure 1-3.

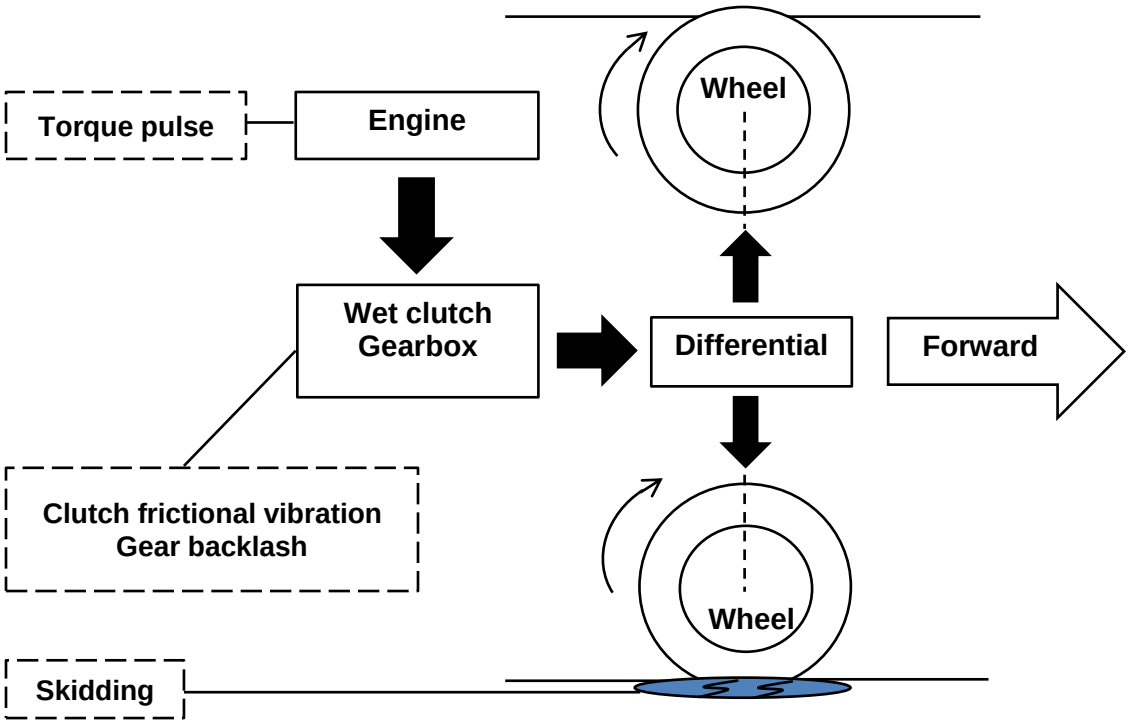

Figure 1-3 Power flow and NVH considerations in the powertrain system

1.2 Research objectives

This dissertation deals with a comprehensive study of the tribology and dynamics of transmission system for automotive applications. The study addresses two different levels: the fundamental clutch level and the holistic powertrain level described as follows.

- Wet clutch

The foremost objective of the wet clutch study is to apply a so-called thermohydrodynamic (THD) model for engagement simulation with provision for surface roughness, contact pressure, and existence of grooves in the friction material. A systematic study of the groove parameters and thermal effects involved during the full engagement cycle is performed. The use of a pertinent groove type and profiles on the friction material allows control of temperature rise and reduction of degradation and wear.

This secondary research involves the development of the wear model and prediction of wear rate with comparison with the experimental measurements. The research will, for the first time, quantify the wear and provide explanation and implication of the two-stage wear observed experimentally. The wear prediction program can serve as a unique practical tool for performance analysis, evaluation of characteristics, and product development and evaluation. Since the quality of the input data can be compromised by limited tests and availability of measured material properties, the discrepancies between the wear prediction and test results demands rigorous interpretation of uncertainties. Therefore, a sensitivity analysis of the model parameters is performed via the Monte Carlo simulation to generate quantification and validation metrics statistically.

With the development of an experimentally verified model, the extension of wear study is investigated different wear factors, including surface patterns (radial, spiral and waffle), groove design (groove depth, groove width, and spiral groove angle), engagement configuration and material consideration (friction material properties, ATF oxidation). These are important factors in optimization of performance and durability analysis of clutch. This information will be useful to investigate the coupling between degradation of friction material and ATF oxidation, which is known to give rise to undesirable performance due to friction instability. For this purpose, the degradation and aging of the components can be taken into consideration at the design stage. This is particularly crucial because of the repeated cyclic engagement and disengagement processes will result in the degradation of the ATF as well as the friction material.

- Powertrain

The objectives of the powertrain analysis are two-fold. The first one is to introduce the mechanical characteristics of the main components encompassing their individual dynamics for a comprehensive modeling. The parametric study of each component will contribute to optimal design of powertrain through simulation. The next target is to investigate of the vibration behavior and NVH factors of the entire powertrain system, which involves mode coupling and interactions between system components. By identifying the primary NVH factors, the control design will accomplish better compliance with demanded performance criteria and durability of machinery through reduction of detrimental vibrations. Application of powertrain study can also be extended to propose an efficient and robust scheme of fault diagnosis using the model-based method.

1.3 Dissertation organization

The results of current research are presented based on specific considerations in two different levels of mechanical system: the wet clutch level and the holistic powertrain level. First, the wet clutch level analysis is covered in Chapters 2 to 5. Chapter 2 discusses the performance of wet clutch with various groove designs through thermohydrodynamic simulation of engagement operations. Chapter 3 presents prediction of the friction lining wear behavior in a wet clutch. Chapter 4 presents the results of the quantification of uncertainties in the aforementioned wear prediction and probabilistic prediction results based on the Monte-Carlo simulations. Chapter 5 introduces the parametric analysis of wear factors in order to demonstrate the possible tribological considerations for extending the life time of the friction lining. The second level, modeling and the analyses of powertrain system, is presented in Chapter 6. Specifically, Chapter 6 describes the mathematical models of powertrain dynamics by comprehensive considerations of system nonlinearity and noise, vibration, and harshness (NVH) factors. Finally, Chapter 7 summarizes the aforementioned research results and proposes the future work to complete the model and analysis of transmission system. A brief summary of each chapter is as follows.

Chapter 2: Wet clutch level analysis – parametric analysis for a paper-based wet clutch with groove consideration. In this chapter, a three-dimensional thermohydrodynamic analysis of a wet clutch is performed that covers the entire cycle of engagement from slip to lock to detachment. The contact

condition of the rough surface is formulated by the statistical micro-contact model to incorporate the elastic-plastic asperity contact, which is characterized by the plastic index. Based on the parametric analysis, it is shown that the performance of a wet clutch is influenced by various groove effects. The evolution of the temperature provides insight into the thermal management of the wet clutch and is necessary step for evaluation of thermal degradation phase of wear.

Chapter 3: Wet clutch level analysis – on the wear prediction of the paper-based friction material in a wet clutch. In this chapter, a methodology for prediction of wear in the friction lining of a wet clutch subjected to repeated engagement cycles is presented. The wear mechanism is related to both the thermal degradation and the mechanical effects. The temperature history is obtained by performing a thermohydrodynamic analysis of the entire engagement process including engagement, soaking, dwelling and stabilization periods. The predictions of the model are in accordance to the experimentally observed "two-stage" wear rate phenomenon recently reported in the literature.

Chapter 4: Wet clutch level analysis – model validation and uncertainty analysis in the wear prediction of a wet clutch. In this chapter, an uncertainty quantification analysis is performed to further investigate the nature of the "two-stage" wear process of the paper-based friction lining in a wet clutch. In this approach, the results of a computerized wear prediction model are examined through sensitivity analysis and a model validation that utilizes the Monte Carlo method. Extensive computational results that take into account the uncertainty and variability in the input data are presented to gain insight into the evolution of temperature and wear during the engagement process.

Chapter 5: Wet clutch level analysis – parametric analysis on wear factors of a wet clutch. This chapter focuses on the wear characteristics to gain insight into the durability of friction lining by parametric analysis of computerized wear prediction. The influencing factors for wear are investigated by taking account of different groove designs and material properties, which facilitate industrial design of friction lining by avoiding costly wear test.

Chapter 6: Powertrain level analysis – NVH analysis of transmission in an automotive powertrain. In this chapter, a comprehensive mathematical model of the vehicle powertrain equipped with automatic transmission is developed with consideration of nonlinearities in the clutch and the planetary gear set. For the clutch, the dynamics of stick-slip is described for the transition between the slipping to locked states. The gear backlash model is used to analyze the rattle noise of the planetary gear set. Based on extensive powertrain simulations for the clutch engagement process, the magnitude of vibration propagation in the driveline are predicted to identify the primary factors of noise generation.

1.4 References

[1] S. Natsumeda, T. Miyoshi, Numerical simulation of engagement of paper based wet clutch facing, Journal of tribology, 116 (1994) 232-237.

[2] Y. Yang, R.C. Lam, Y.F. Chen, H. Yabe, Modeling of heat transfer and fluid hydrodynamics for a multidisc wet clutch, SAE Technical Paper, 1995.

[3] J. Jang, M. Khonsari, Thermal characteristics of a wet clutch, Journal of tribology, 121 (1999) 610-617.

[4] J. Jang, M. Khonsari, On the formation of hot spots in wet clutch systems, Journal of tribology, 124 (2002) 336-345.

[5]. Marklund, P, Maki, R. Larsson, R., Hoglund, E, Khonsari, M.M. and Jang, J. Y. “Thermal Influence on Torque Transfer of Wet Clutches in Limited Skip Differential Applications,” *Tribology International*, V. 40, pp. 876-884, 2007.

[6]. J. Y. Jang, M. M. Khonsari, and R. Maki: “Three-Dimensional Thermohydrodynamic Analysis of a Wet Clutch With Consideration of Grooved Friction Surfaces”, *J Tribol-T Asme*, 2011, **133**(1).

[7]. Zagrodzki, Przemyslaw, and Samuel A. Truncone. "Generation of hot spots in a wet multidisk clutch during short-term engagement." *Wear* 254.5 (2003): 474-491.

[8] N. Lingesten, P. Marklund, E. Höglund, M. Lund, J. Lundin, R. Mäki, Apparatus for continuous wear measurements during wet clutch durability tests, Wear, 288 (2012) 54-61.

[9] Y. Yang, R.C. Lam, Theoretical and experimental studies on the interface phenomena during the engagement of automatic transmission clutch, Tribology Letters, 5 (1998) 57-67

[10] M. Watson, C. Byington, D. Edwards, S. Amin, Dynamic modeling and wear-based remaining useful life prediction of high power clutch systems, Tribology Transactions, 48 (2005) 208-217

[11] L.A. Sosnovskiy, R. Sosnovskaya, K. Frolov, N. Makhutov, Tribo-fatigue: Wear-fatigue Damage and Its Prediction, Springer, 2010.

[12] L. Guzzella, C. Onder, Introduction to modeling and control of internal combustion engine systems, Springer Science & Business Media, 2009.

[13] J.J. Moskwa, Automotive engine modeling for real time control, Massachusetts Institute of Technology, 1988.

[14] R.W. Weeks, J.J. Moskwa, Automotive engine modeling for real-time control using matlab/simulink, SAE Technical Paper, 1995.

[15] E. Berger, F. Sadeghi, C. Krousgrill, Finite element modeling of engagement of rough and grooved

wet clutches, Journal of Tribology, 118 (1996) 137-146.

[16] C. Duan, R. Singh, Stick-slip behavior in torque converter clutch, SAE Transactions, Journal of Passenger Car: Mechanical Systems, 116 (2005) 2785-2795.

[17] H.N. Özgüven, D.R. Houser, Mathematical models used in gear dynamics—a review, Journal of sound and vibration, 121 (1988) 383-411.

[18] M. Fox, J. Grogg, Development of Front-Wheel-Drive ELSD for Efficient Performance and Safety, SAE Technical Paper, 2012.

[19] H. Pacejka, Tire and vehicle dynamics, Elsevier, 2005.

[20] H.B. Pacejka, E. Bakker, L. Nyborg, Tyre modelling for use in vehicle dynamics studies, SAE paper, 870421 (1987) 1-15.

[21] Isermann, Rolf. Engine Modeling and Control: Modeling and electronic management of internal combustion engines. Springer, 2014.

[22] S. Theodossiades, S. Natisivas, Non-linear dynamics of gear-pair systems with periodic stiffness and backlash, Journal of Sound and vibration, 229 (2000) 287-310.

[23] D. Centea, H. Rahnejat, M. Menday, The influence of the interface coefficient of friction upon the propensity to judder in automotive clutches, Proceedings of the Institution of Mechanical Engineers, Part D: Journal of Automobile Engineering, 213 (1999) 245-258.

[24] M. Brinkmeier, U. Nackenhorst, S. Petersen, O. Von Estorff, A finite element approach for the simulation of tire rolling noise, Journal of sound and vibration, 309 (2008) 20-39.

[25] D. Karnopp, Computer simulation of stick-slip friction in mechanical dynamic systems, Journal of dynamic systems, measurement, and control, 107 (1985) 100-103.

[26] R. Leine, D. Van Campen, A. De Kraker, L. Van Den Steen, Stick-slip vibrations induced by alternate friction models, Nonlinear dynamics, 16 (1998) 41-54.

[27] T. Sun, H. Hu, Nonlinear dynamics of a planetary gear system with multiple clearances, Mechanism and Machine Theory, 38 (2003) 1371-1390.

[28] T. Kiekbusch, D. Sappok, B. Sauer, I. Howard, Calculation of the combined torsional mesh stiffness of spur gears with two-and three-dimensional parametrical FE models, Strojniški vestnik-Journal of Mechanical Engineering, 57 (2011) 810-818.

CHAPTER 2 PARAMETRIC ANALYSIS FOR A PAPER-BASED WET CLUTCH WITH GROOVE CONSIDERATIONS [1]

2.1 Nomenclature

a = inner radius of the disk (m)

A_r = real area of contact per unit nominal area

b = outer radius of the disk (m)

d = thickness of the friction material (m)

d_c = thickness of the core disk (m)

d_s = thickness of the separator disk (m)

α = spiral groove angle (rad)

E = Young's modulus (Pa)

ν = Poisson's ratio

E' = effective Young's modulus (Pa)

E_1 = Young's modulus of steel (Pa)

E_2 = Young's modulus of friction material (Pa)

K = hardness factor

H = hardness of friction material (MPa)

y_s = distance between the mean of summit heights and that of the surface heights (m)

$\overline{\omega}$ = dimensionless interface

z^* = dimensionless asperity height

β = asperity radius (m)

σ_s = standard deviation of surface heights (m)

E_r = elastic coefficient for real area of contact (Pa)

f = friction coefficient

h = film thickness (m)

$\overline{h}$ = dimensionless film thickness

h_{gr} = groove depth (m)

h_{oi} = initial film thickness (m)

H_g = groove depth ratio

h_T = average gap (m)

[1] Reprinted by permission of Tribology International

I = mass moment of inertia $\left(\text{kg m}^2\right)$

k = thermal conductivity $\left(\text{W/m K}\right)$

L = the length of computation domain in θ direction

m = permeability $\left(\text{m}^2\right)$

n = number of grooves

N = rotational speed $\left(\text{rpm}\right)$

N_w = waviness number

P_c = contact pressure $\left(\text{Pa}\right)$

$\overline{P_c}$ = dimensionless contact pressure

P_h = hydrodynamic pressure $\left(\text{Pa}\right)$

$\overline{P_h}$ = dimensionless hydrodynamic pressure

P_o = average load per unit area $\left(\text{Pa}\right)$

q = frictional heat flux $\left(\text{W/m}^2\right)$

q_b = frictional heat flux into friction material $\left(\text{W/m}^2\right)$

q_s = frictional heat flux into separator disk $\left(\text{W/m}^2\right)$

r = coordinate in radial direction $\left(\text{m}\right)$

t = time $\left(\text{s}\right)$

T_c = torque due to contact pressure $\left(\text{N m}\right)$

T_h = torque due to hydrodynamic pressure $\left(\text{N m}\right)$

T = total torque $\left(\text{N m}\right)$

W_h = average load supported by hydrodynamic pressure per unit area $\left(\text{Pa}\right)$

W_c = average load supported by asperity contact pressure per unit area $\left(\text{Pa}\right)$

z = coordinate in axial direction $\left(\text{m}\right)$

ε = compressive strain

ξ = error tolerance

ϕ = ratio of grooved area to total area

ϕ_r, ϕ_θ = pressure flow factors in radial and circumferential directions

ϕ_s = shear flow factor

ϕ_f, ϕ_{fs} = shear stress factors

γ = asperity tip radius $\left(\text{m}\right)$

η = number of asperities per unit area $\left(\mathrm{m}^{-2}\right)$

κ = thermal diffusivity $\left(\mathrm{m}^2/\mathrm{s}\right)$

λ = aspect ratio of groove

μ = viscosity $\left(\mathrm{Pa\ s}\right)$

μ_i = initial viscosity $\left(\mathrm{Pa\ s}\right)$

θ = coordinate in circumferential direction $\left(\mathrm{rad}\right)$

ρ = density $\left(\mathrm{kg/m}^3\right)$

σ = rms roughness

ω_L = angular speed of separator disk

ω_H = angular speed of friction material

Θ = temperature $\left(^\circ\mathrm{C}\right)$

$\overline{\Theta}$ = dimensionless temperature

Θ_i = initial temperature $\left(^\circ\mathrm{C}\right)$

Θ_∞ = ambient temperature $\left(^\circ\mathrm{C}\right)$

Subscripts

i = initial value
s = separator disk
f = lubricant
b = friction material
c = core disk
∞ = ambient

2.2 Introduction

As a crucial component of the transmission system, a wet clutch plays an important role in the automotive industry. Operating under lubricated conditions, a wet clutch's function is to provide smooth power transfer. The key elements of a wet clutch are: several core disks to both sides of which the friction material is bounded, a series of mating separator disks, and automatic transmission fluid (ATF) that lubricates the surfaces. These elements must function in perfect harmony in terms of hydrodynamics, contact mechanics and heat transfer for the transmission system to run smoothly.

From the design and performance analysis viewpoint, the engagement simulation of a wet clutch has always been an important research topic in the tribology where hydrodynamic, elastohydrodynamic, mixed and boundary lubrications modes are all present during the clutch engagement process. Further research interests revolve around durability analysis of the friction material which experiences repeated engagements and disengagements during its life. The necessary step for this purpose is to perform a

systematic study of the performance parameters with provision for thermal effects involved during the full engagement cycle from slip to lock and finally detachment of the surfaces.

The most common type of the friction material is a phenolic resin with a porous and deformable structure with rough surface features that resembles a sand paper. The ATF soaked into the friction material is squeezed out by the engagement load, which partially improves the heat transfer mechanism by its cooling action. The use of a pertinent groove type and profiles on the friction material allows control of temperature rise and reduction of degradation and wear.

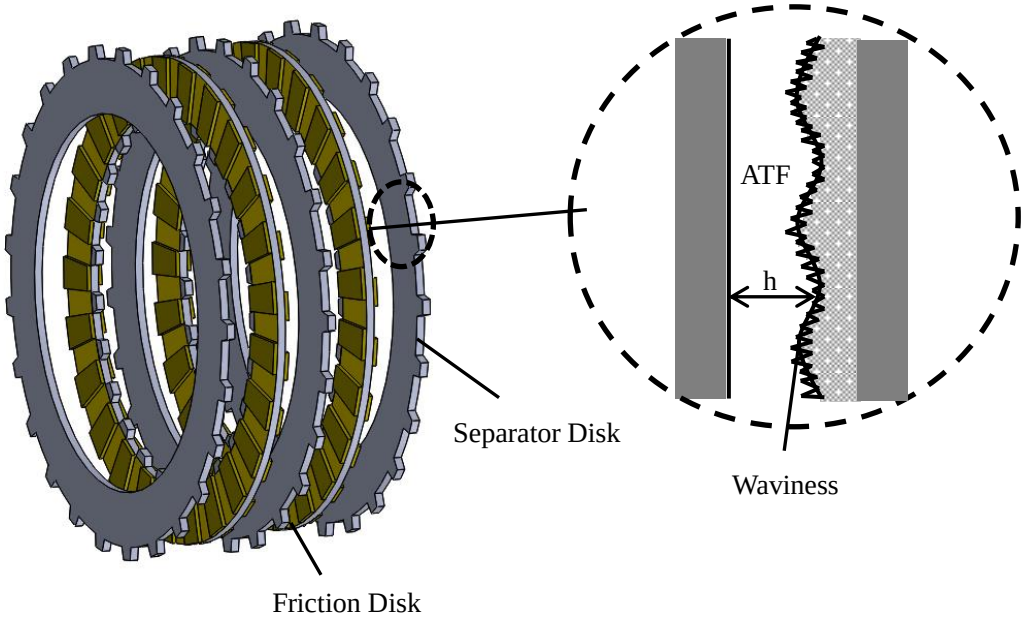

Figure 2-1 Schematic of the wet clutch model

Modeling and simulations of clutch engagement have been investigated by many researchers. Since previous publications and results are abundant, only a brief review of most pertinent research is presented here. Natsumeda et al. carried out the one of the first theoretical analysis and hydrodynamic simulation of a paper-based wet clutch with consideration of permeability, compressive strain, and asperity contact [1, 15]. Yang et al. [2] provided mathematical models with similar considerations and verified the results with experimental measurements favorably. Based on Natsumeda's work, Jang and Khonsari [3] developed a comprehensive model by adding the slip boundary and centrifugal terms for the hydrodynamic equation. They developed the three-dimensional heat transfer equations to predict the temperature field, decreasing the engagement stage. Later, the effects of groove including the radial and waffle type are discussed based on the 3-D thermohydrodynamic analysis [4]. These papers concentrated on the first stage of the engagement process, i.e. from the initial squeeze to lock-up. Furthermore, in these papers, the surface roughness was modeled using the Greenwood and Williamson asperity contact model (GW), which is restricted to elastic deformation. Recently, Kogut and Etsion [5] developed an elastic-plastic model (KE) for the contact of rough surface by the finite element analysis to incorporate the full regime of asperity contact. Since the determination of contact pressure plays a significant role in

the engagement simulation, consideration of the elasto-plastic and plastic behavior of the surfaces warrants further investigation.

The study of thermal effects on the performance of wet clutch has received much attention in the literature from several viewpoints such as the influence on torque transfer [19] and on the duration of the engagement time [20]. However, investigation of important tribological performance associated with friction material degradation and frictional instability requires one to first perform a comprehensive analysis for the temperature history during the full engagement cycles. This is the subject of the present study.

In the present paper, a parametric analysis of a wet clutch is presented using the following procedure: the groove geometry is considered by including the variation of film thickness over the planar domain; micro-contact condition of asperities for the rough surface are described by KE model; the thermal behavior of a wet clutch is predicted that spans the entire operation cycles, including engagement, soaking, dwell, and stabilization periods. Results and discussions are presented to probe into the analysis of different factors influencing the engagement performance. Also presented is a discussion on the temperature evolution during the entire engagement cycle and the role of different energy levels.

2.3 Tribological model of a wet clutch

2.3.1 Entire cycle of clutch operation

Generally, the mechanical operation states of a wet clutch can be divided into three phases: slip, locked, and detached. In terms of lubrication of the separator disk and the friction lining interface, the complete cycle translates into the engagement stage, soaking period, dwell period, and stabilization period [6].

Initially, prior to application of the engagement load, the separator disk and friction lining are separated by a gap filled with ATF. When the motor is started, the rotation speed difference between the friction pairs produces a viscous shearing torque or “drag torque”. This can leads to power dissipation and decreased transmission efficiency, which is inevitable in a wet clutch system.

At the beginning of engagement stage, the separation between the friction pair is much larger than the asperity height so that no asperity contact takes place. By applying the hydraulic pressure, the adjacency is reduced and the overall hydrodynamic pressure increases. In the meanwhile, more asperities of the friction material come into contact with the separator disk. The total load by hydrodynamic pressure of the lubricant and the contact pressure of the rough surface strikes a balance with the applied engagement load during the process. As the engagement process continues, the decrease in the relative rotational speed of the friction pair will result in a smaller hydrodynamic torque, while the torque associated with asperity contact grows larger and larger and becomes the dominant component of torque that governs the transmission power. As a result, the relative rotation speed between the friction lining and the separator disk drops and becomes nil at end of the engagement.

During the engagement stage, the squeeze effect also plays a significant role in the evolution of

hydrodynamic pressure profile. Considerable heat generation leads to a conspicuous temperature rise in the clutch system. The lubrication regime shifts from hydrodynamic to mixed and to boundary lubrication, identified by "the Stribeck curve".

After the engagement process is completed, load is continually applied to keep the friction pair "locked". The transmission power is provided by the static friction, which can be influenced by some of the ATF additives. There is no heat generation because the relative rotation between the friction pairs is nil.
At the end of soak period, the applied load is released, separating the friction lining and separator disk with an initial gap. During the dwell period, the friction lining is not immersed in the ATF and the interface is air cooled.

When the stabilization period begins, the kinetic energy is input and the gap between the friction pairs is filled with ATF again. The temperature of clutch system almost restores its initial value because of the ATF flow. Next engagement cycle is then ready to start.

2.3.2 Groove geometry

It has been demonstrated that the shape of hydrodynamic film is closely related to the load carrying capacity of lubricated mechanical components [17]. For a wet clutch, the geometry of flow domain defines the variation of film thickness and takes into account both the grooved and ungrooved sections. Moreover, the waviness of trigonometric function type and the deformation of friction material are considered [4]. In general, the film thickness can be defined as:

$$\overline{h}(r,\theta) = \overline{h_o} + \varepsilon(r,\theta)\overline{d} + \overline{h_{gr}}(r,\theta) + \overline{w}\cos N_w\theta \tag{1}$$

where h_{gr} represents the groove depth of specific geometry design, w is the waviness peak amplitude, N_w is the number of grooves, and ε is the planar compressive strain.

For a logarithmic spiral shape, the curve is formulated by [7]:

$$r = r_1 e^{\theta \tan\alpha} \tag{2}$$

where α is the angle between the circumferential direction and tangential direction of the spiral curve, r and θ are the polar coordinates, and r_1 is the base radius of the spiral curve. The geometry illustration of the spiral groove is shown in Figure 2-2 (a).

Since the groove depth is expressed by a function of location, different groove profile designs for the radial groove case can be included, which is another interesting design aspect in addition to groove pattern [18]. Current profile shapes contain arc, triangle, and rectangle. The illustration of above groove geometry consideration is shown in Figure 2-2 (b).

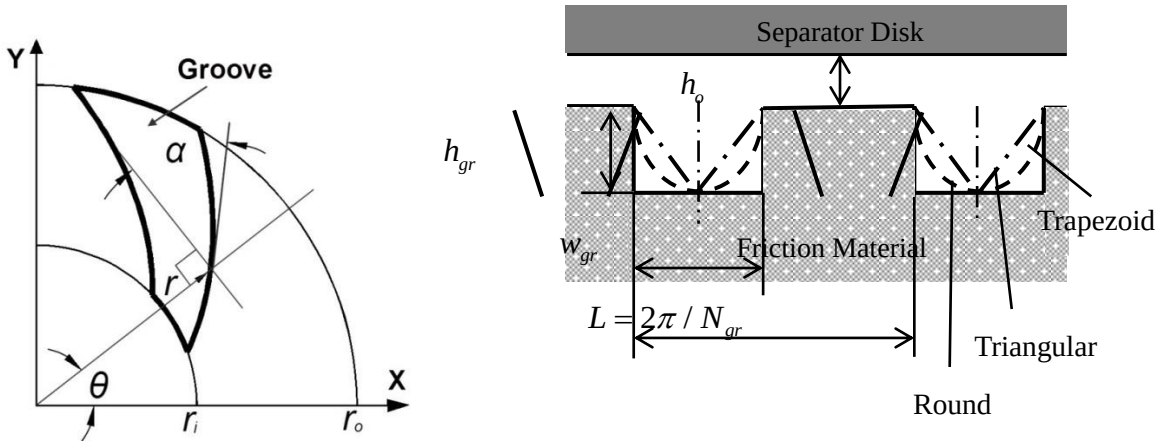

(a) (b)

Figure 2-2 Groove geometry illustration (a) spiral groove (b) radial groove profile

2.3.3 Lubrication theory

The Reynolds equation for prediction of the hydrodynamic pressure with provision for the surface roughness is used [8]. By incorporating the squeeze effect, the slip boundary at the friction lining wall, the centrifugal force and the film thickness variation over the domain, the following modified Reynolds equation is established to obtain the hydrodynamic pressure during the engagement [3]:

$$\frac{1}{\bar{r}}\frac{\partial}{\partial \bar{r}}\left[F_1\left(\frac{\partial \bar{P}_h}{\partial \bar{r}}\right)\right]+\frac{1}{\bar{r}^2}\frac{\partial}{\partial \theta}\left[F_2\left(\frac{\partial \bar{P}_h}{\partial \theta}\right)\right]=\lambda_1\frac{1}{\bar{r}}\frac{\partial}{\partial \bar{r}}\left(R_1+R_2\right)+\lambda_2 R_3 \tag{3}$$

where

$$F_1=\bar{r}\left\{\left(1+3\chi\right)\frac{\phi_r\bar{h}^3}{\bar{\mu}}+6\bar{r}\alpha\sqrt{\bar{m}}\chi\frac{\phi_r\bar{h}^2}{\bar{\mu}}+\frac{12\bar{m}\bar{d}\left(1-\varepsilon\right)}{\bar{\mu}}\right\}$$

$$F_2=\frac{\phi_\theta\bar{h}^3}{\bar{\mu}}+6\bar{r}\alpha\sqrt{\bar{m}}\chi\frac{\phi_\theta\bar{h}^2}{\bar{\mu}}+\frac{12\bar{m}\bar{d}\left(1-\varepsilon\right)}{\bar{\mu}}$$

$$R_1=\bar{r}^2\frac{\phi_r\bar{h}^3}{\bar{\mu}}\left\{\frac{3}{10}\left(1+5\chi\right)\bar{\Omega}^2+\left(1+4\chi\right)\bar{\Omega}\bar{\omega}_L+\left(1+3\chi\right)\bar{\omega}_L^2\right\}$$

$$R_2=\bar{r}^2\left\{6\bar{r}\alpha\sqrt{\bar{m}}\chi\frac{\phi_r\bar{h}^2}{\bar{\mu}}+\frac{12\bar{m}\bar{d}\left(1-\varepsilon\right)}{\bar{\mu}}\right\}$$

$$R_3=12\left[\left(\frac{d\bar{h}_T}{d\bar{t}}\right)-\bar{d}\left(\frac{\partial\varepsilon}{\partial\bar{t}}\right)\right]-6\,\bar{\Omega}\left[\left(\frac{\partial\bar{h}_T}{\partial\theta}\right)-\lambda_3\left(\frac{\partial\phi_s}{\partial\theta}\right)\right]$$

F_1 and F_2 are the flow factors. They include the squeezing flow from the porous friction lining and velocity components inside it. R_1 and R_2 represents the centrifugal force term in the adjacency and the friction lining respectively. R_3 is a time-dependent term that takes into account the variation of film thickness due to the squeeze motion and waviness. The slip boundary is incorporated by using the

coefficient χ in the above terms. The squeeze effect dominates the evolution of the hydrodynamic pressure during the engagement stage.

The dimensionless parameters in the hydrodynamic simulation are summarized as follows [3]:

$$\bar{h}=\frac{h}{h_{oi}},\ \bar{r}=\frac{r}{b},\bar{P}=\frac{P}{P_o},\ \bar{m}=\frac{m}{h_{oi}^2},\ \bar{d}=\frac{d}{h_{oi}},\ \bar{t}=\omega_i t,\ \bar{\omega}_L=\frac{\omega_L}{\omega_i},\ \bar{\Omega}=\bar{\omega}_H-\bar{\omega}_L,\ \bar{\mu}=\frac{\mu}{\mu_i},\lambda_1=\frac{\rho_f b^2\omega_i^2}{P_o},$$

$$\lambda_2=\frac{\mu_i b^2\omega_i}{P_o h_{oi}^2},\ \lambda_3=\frac{\sigma}{h_{oi}},\text{ and }\ \chi=\frac{\sqrt{\bar{m}}}{\alpha\bar{h}_T+\sqrt{\bar{m}}}$$

The velocity field can be obtained from the relevant pressure gradient and mass conservation:

$$\frac{1}{\bar{r}}\frac{\partial}{\partial\bar{r}}\left(\bar{r}\bar{u}_r\right)+\frac{1}{\bar{r}}\frac{\partial\bar{u}_\theta}{\partial\theta}+\frac{\partial\bar{u}_z}{\partial\bar{z}_f}=0 \tag{4}$$

$$\frac{1}{\bar{r}}\frac{\partial}{\partial\bar{r}}\left(\bar{r}\bar{u}_r'\right)+\frac{1}{\bar{r}}\frac{\partial\bar{u}_\theta'}{\partial\theta}+\frac{b}{d\left(1-\varepsilon\right)}\frac{\partial\bar{u}_z'}{\partial\bar{z}_b}=0 \tag{5}$$

where $\bar{u}_r$, $\bar{u}_\theta$ and $\bar{u}_z$ represents the ATF flow velocities in the gap; $\bar{u}_r'$, $\bar{u}_\theta'$ and $\bar{u}_z'$ are the flow velocities in the porous friction lining, and are related to the pressure gradient by Darcy's law. The viscosity-temperature relationship is given by American Society for Testing and Materials (ASTM):

$$\log_{10}\log_{10}\left(\frac{\mu}{\rho_f}+0.6\right)=A-B\log_{10}\left(\theta+95\right) \tag{6}$$

2.3.4 Heat transfer model

The heat transfer process can be described as follows. During the engagement stage, heat is generated due to the relative motion between the friction material and the separator disk as well as due to the asperity contact. The total amount of heat is dissipated through several mechanisms: convection by the ATF lubrication, heat conduction into the separator disk, the friction material, and the core disk. Radiation is neglected in the thermal analysis. The governing equations are:

Energy equation

The temperature of ATF in adjacency is determined by:

$$\frac{\partial\bar{\Theta}_f}{\partial\bar{t}}+\bar{u}_r\frac{\partial\bar{\Theta}_f}{\partial\bar{r}}+\frac{\bar{u}_\theta}{\bar{r}}\frac{\partial\bar{\Theta}_f}{\partial\theta}+\left[\frac{B_f\bar{u}_z}{\bar{h}_T}-\frac{\bar{z}\bar{u}_r}{\bar{h}_T}\left(\frac{\partial\bar{h}_T}{\partial\bar{r}}\right)-\frac{\bar{z}\bar{u}_\theta}{\bar{h}_T\bar{r}}\left(\frac{\partial\bar{h}_T}{\partial\theta}\right)\right]\frac{\partial\bar{\Theta}_f}{\partial\bar{z}_f}=$$
$$D_f\left[\frac{\partial^2\bar{\Theta}_f}{\partial\bar{r}^2}+\frac{1}{\bar{r}}\frac{\partial\bar{\Theta}_f}{\partial\bar{r}}+\frac{1}{\bar{r}^2}\frac{\partial^2\bar{\Theta}_f}{\partial\theta^2}+\frac{1}{\bar{h}_T^2}\left\{B_f^2+\bar{z}_f^2\left(\frac{\partial\bar{h}_T}{\partial\bar{r}}\right)^2+\frac{\bar{z}_f^2}{\bar{r}^2}\left(\frac{\partial\bar{h}_T}{\partial\theta}\right)^2\right\}\frac{\partial^2\bar{\Theta}_f}{\partial\bar{z}_f^2}+\right.$$
$$\left\{2\frac{\bar{z}}{\bar{h}_T^2}\left(\frac{\partial\bar{h}_T}{\partial\bar{r}}\right)^2-\frac{\bar{z}}{\bar{h}_T}\left(\frac{\partial^2\bar{h}_T}{\partial\bar{r}^2}\right)-\frac{\bar{z}}{\bar{r}\bar{h}_T}\left(\frac{\partial\bar{h}_T}{\partial\bar{r}}\right)+2\frac{\bar{z}}{\bar{r}^2\bar{h}_T^2}\left(\frac{\partial\bar{h}_T}{\partial\theta}\right)^2-\frac{\bar{z}}{\bar{r}^2\bar{h}_T}\left(\frac{\partial^2\bar{h}_T}{\partial\theta^2}\right)\right\}\frac{\partial\bar{\Theta}_f}{\partial\bar{z}_f}$$
$$\left.-2\frac{\bar{z}}{\bar{h}_T}\left(\frac{\partial\bar{h}_T}{\partial\bar{r}}\right)\frac{\partial^2\bar{\Theta}_f}{\partial\bar{r}\partial\bar{z}_f}-2\frac{\bar{z}}{\bar{r}^2\bar{h}_T}\left(\frac{\partial\bar{h}_T}{\partial\theta}\right)\frac{\partial^2\bar{\Theta}_f}{\partial\theta\partial\bar{z}_f}\right]+\frac{E_f\bar{\mu}}{\bar{h}_T^2}\left[\left(\frac{\partial\bar{u}_r}{\partial\bar{z}_f}\right)^2+\left(\frac{\partial\bar{u}_\theta}{\partial\bar{z}_f}\right)^2\right] \tag{7}$$

where

$$B_f=\frac{b}{h_{oi}},\quad D_f=\frac{\kappa_f}{\omega_H b^2},\quad E_f=\frac{\mu_i\omega_H b^2}{\rho_f c_f\Theta_f h_{oi}^2},\text{ and }\quad \bar{z}_f=\frac{z_f}{h_T}$$

Friction material

The temperature field for the friction lining is described by [3]:

$$\frac{\partial\bar{\Theta}_b}{\partial\bar{t}}+F_b\left(\bar{u}_r'\frac{\partial\bar{\Theta}_b}{\partial\bar{r}}+\frac{\bar{u}_\theta'}{\bar{r}}\frac{\partial\bar{\Theta}_b}{\partial\theta}+\frac{B_b\bar{u}_z'}{1-\varepsilon}\frac{\partial\bar{\Theta}_b}{\partial\bar{z}_b}\right)=$$
$$D_b\left[\frac{\partial^2\bar{\Theta}_b}{\partial\bar{r}^2}+\frac{1}{\bar{r}}\frac{\partial\bar{\Theta}_b}{\partial\bar{r}}+\frac{1}{\bar{r}^2}\frac{\partial^2\bar{\Theta}_b}{\partial\theta^2}+\left(\frac{B_b}{1-\varepsilon}\right)^2\frac{\partial^2\bar{\Theta}_b}{\partial\bar{z}_b^2}\right] \tag{8}$$

where

$$B_b=\frac{b}{d},\quad D_b=\frac{\kappa_b}{\omega_H b^2},\quad F_b=\frac{\rho_f c_f}{\rho_b c_b},\text{ and }\quad \bar{z}_b=\frac{z_b}{d\left(1-\varepsilon\right)}$$

Separator disk

The heat conduction equation for the separator disk is [3]:

$$\frac{\partial\bar{\Theta}_s}{\partial\bar{t}}+\left(\bar{\omega}_L-\bar{\omega}_H\right)\frac{\partial\bar{\Theta}_s}{\partial\theta}=D_s\left(\frac{\partial^2\bar{\Theta}_s}{\partial\bar{r}^2}+\frac{1}{\bar{r}}\frac{\partial\bar{\Theta}_s}{\partial\bar{r}}+\frac{1}{\bar{r}^2}\frac{\partial^2\bar{\Theta}_s}{\partial\theta^2}+B_s^2\frac{\partial^2\bar{\Theta}_s}{\partial\bar{z}_s^2}\right) \tag{9}$$

where

$$B_s=\frac{b}{d_s},\quad D_s=\frac{\kappa_s}{\omega_H b^2},\text{ and }\quad \bar{z}_s=\frac{z_s}{d_s}$$

Core disk

The heat conduction equation for the core disk is [3]:

$$\frac{\partial\bar{\Theta}_c}{\partial\bar{t}}=D_c\left(\frac{\partial^2\bar{\Theta}_c}{\partial\bar{r}^2}+\frac{1}{\bar{r}}\frac{\partial\bar{\Theta}_c}{\partial\bar{r}}+\frac{1}{\bar{r}^2}\frac{\partial^2\bar{\Theta}_c}{\partial\theta^2}+B_c^2\frac{\partial^2\bar{\Theta}_c}{\partial\bar{z}_c^2}\right) \tag{10}$$

where

$$B_c = \frac{b}{d_c},\quad D_c = \frac{\kappa_c}{\omega_H b^2}, \text{ and } \quad \bar{z}_c = \frac{z_c}{d_c}$$

Heat generation and heat partition during engagement

The heat generation by the relative sliding motion of the friction pair is described by

$$\bar{q} = f\bar{r}\left(\overline{\omega_H} - \overline{\omega_L}\right)\overline{P_c} \tag{11}$$

where the heat generation by the viscous shearing stress is negligible.

The heat partition process at the separator disk – friction lining interface was proposed by Xin and Tao [12]:

$$\bar{q}_b = \frac{\bar{q}}{1+s},\quad \bar{q}_s = \frac{s\bar{q}}{1+s},\quad \text{and } s = \frac{k_s}{k_b}\sqrt{\frac{\kappa_b}{\kappa_s}} \tag{12}$$

$\bar{q}$ is the total heat flux produced by the asperity contact; $\bar{q}_b$ and $\bar{q}_s$ are respectively the heat flux into the friction material and the separator disk, controlled by distribution coefficient, s.

Boundary conditions

Convective boundary condition is applied to the radial direction, the inner radius and the outer radius; period condition is applied to the circumferential direction. Heat is partitioned at the separator disk–friction interface during the engagement stage. This is changed with the air convection during the dwell period and with convection cooling due to ATF flow during the stabilization period. The symmetric boundary condition is applied at the upper and lower boundary in the z direction.

I. Engagement stage

At the interface, the heat flux into different domains is described by [3]:

$$\xi_s \frac{\partial\overline{\Theta}_s}{\partial\bar{z}_s} - \frac{\xi_f}{\bar{h}_T}\frac{\partial\overline{\Theta}_f}{\partial\bar{z}_f} = \bar{q}_s \quad \text{(ATF-separator disk interface)}$$

$$\frac{\xi_f}{\bar{h}_T}\frac{\partial\overline{\Theta}_f}{\partial\bar{z}_f} - \frac{\xi_b}{1-\varepsilon}\frac{\partial\overline{\Theta}_b}{\partial\bar{z}_b} = \bar{q}_b \text{ (ATF-friction material interface)} \tag{13}$$

where

$$\xi_b = \frac{k_b\Theta_i}{b\omega_H P_0 h_0},\quad \xi_s = \frac{k_s\Theta_i}{b\omega_H P_0 h_0}, \text{ and } \quad \xi_f = \frac{k_f\Theta_i}{b\omega_H P_0 h_0}$$

II. Soak period

At the "locked" state, the heat generation is nil so that the temperature gradient at the interface is:

$$\frac{\partial\overline{\Theta}_s}{\partial\bar{z}_s} = \frac{\xi_f}{\xi_s\bar{h}_T}\frac{\partial\overline{\Theta}_f}{\partial\bar{z}_f} \quad \text{(ATF-separator disk interface)}$$

$$\frac{\partial\overline{\Theta}_f}{\partial\bar{z}_f} = \frac{\bar{h}_T\xi_b}{\xi_f(1-\varepsilon)}\frac{\partial\overline{\Theta}_b}{\partial\bar{z}_b} \quad \text{(ATF-friction material interface)} \tag{14}$$

III. Dwell period

The convection boundary is applied at the interface since the clutch is not immersed in ATF during this period:

$$\frac{\partial \overline{\Theta}_s}{\partial \overline{z}_s} = H_s\left(\overline{\Theta}_s - \Theta_\infty\right) \quad \text{(Separator disk interface)}$$

$$\frac{\partial \overline{\Theta}_b}{\partial \overline{z}_b} = H_b\left(\overline{\Theta}_b - \Theta_\infty\right) \quad \text{(Friction material interface)} \tag{15}$$

where

$$H_s = \frac{b}{k_s} h_{conv}, \text{ and } \quad H_b = \frac{b}{k_b} h_{conv}$$

IV. Stabilization period

To prepare for the next engagement cycle, the ATF flows through the gap between the separator disk and the friction lining:

$$\frac{\partial \overline{\Theta}_s}{\partial \overline{z}_s} = \frac{\xi_f}{\xi_s}\frac{\partial \overline{\Theta}_f}{\partial \overline{z}_f} \quad \text{(ATF-separator disk interface)}$$

$$\frac{\partial \overline{\Theta}_f}{\partial \overline{z}_f} = \frac{\xi_b}{\xi_f}\frac{\partial \overline{\Theta}_b}{\partial \overline{z}_b} \quad \text{(ATF-friction material interface)} \tag{16}$$

2.3.5 Contact model

The most extensively used model was proposed by Greenwood and Williamson [13]. However, the contact characteristics of paper-based friction material are distinct in comparison with metals. Firstly, since the friction material is very soft and rough, the asperity contact condition can experience plastic deformation. To characterize this behavior, the plastic index was defined by Chang and Etsion to describe the contact conditions between the rough surfaces with [14]:

$$\psi = \frac{2E'}{\pi K H}\sqrt{\frac{\sigma_s}{\beta}} \tag{17}$$

where

$$\frac{1}{E'} = \frac{1-\upsilon_1^2}{E_1} + \frac{1-\upsilon_2^2}{E_2} \quad \text{and} \quad K = 0.454 + 0.41\upsilon$$

$\psi < 0.6$, purely elastic; $0.6 < \psi < 8$, elasto-plastic; $\psi > 8$, purely plastic.

It is shown that the plastic index depends on the surface roughness and material properties. Based on the finite element analysis, Kogut and Etsion proposed the contact model including comprehensive regimes of deformation for the asperity contact problem, which showed favorable agreement with experimental results. The KE model is used to determine the contact area [5] by evaluating the plastic index with the friction material properties as follows.

$$A(h)=n\beta\sigma A_n\left\{\int_{(h-y_s)/\sigma}^{(h-y_s)/\sigma+\omega_c^*}\left(\overline{\omega}\right)\phi^*\left(z^*\right)dz^*+0.93\pi\left(\omega_c^*\right)^{-0.136}\int_{(h-y_s)/\sigma+\omega_c^*}^{(h-y_s)/\sigma+6\omega_c^*}\left(\overline{\omega}\right)^{1.136}\phi^*\left(z^*\right)dz^*\right.$$
$$\left.+0.94\pi K\left(\omega_c^*\right)^{-0.146}\frac{H}{E'}\int_{(h-y_s)/\sigma+6\omega_c^*}^{(h-y_s)/\sigma+110\omega_c^*}\left(\overline{\omega}\right)^{1.146}\phi^*\left(z^*\right)dz^*+2\pi\int_{(h-y_s)/\sigma+110\omega_c^*}^{\infty}\left(\overline{\omega}\right)\phi^*\left(z^*\right)dz^*\right\} \tag{18}$$

where

$$y_s=\frac{0.045944}{n\beta},\quad \overline{\omega}=z^*-\frac{h-y_s}{\sigma},\quad \omega_c^*=\left(\frac{\pi KH}{2E'}\right)^2\frac{\beta}{\sigma},$$

$$\text{and}\quad \phi^*\left(z^*\right)=\frac{1}{\sqrt{2\pi}}\left(\frac{\sigma_s}{\sigma}\right)e^{-\left(\frac{\sigma_s z^*}{\sqrt{2}\sigma}\right)^2}$$

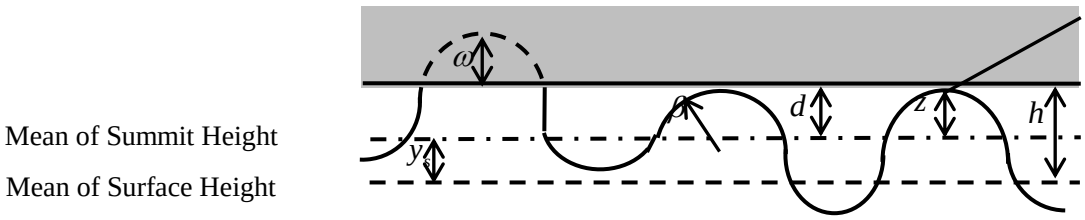

Figure 2-3 Micro-contact model of rough surface with flat surface

The parameter n represents the asperity density, β is the asperity radius and σ is the standard deviation of surface heights.

Secondly, the substrate part of the friction material is deformable during the contact process. In comparison with the rigid material, relationship between the surface contact conditions and the bulk deformation can significantly influence the determination of contact pressure. Natsumeda et al. assumed that the compressive strain should be proportional to the ratio of the real contact area to the nominal contact area [1]:

$$P_c=E\varepsilon=E_r\frac{A_r}{A_n} \tag{19}$$

where E_r is the elastic modulus for contact.

2.3.6 Engagement process

The sum of contact and hydrodynamic load must balance with the engagement load:

$$W_h+W_c=W_e \tag{20}$$

where the engagement load is configured by the response function.

By Newton's second law, the dimensionless torque composed of the contact and the hydrodynamic components is proportional to the angular acceleration of the separator disk [3]:

$$\bar{T} = \lambda_4 \int_0^{2\pi} \int_{\bar{a}}^{1} f \bar{r}^2 \overline{P_c} d\bar{r} d\theta + \int_0^{2\pi} \int_{\bar{a}}^{1} \left(\phi_f + \phi_{fs}\right) \bar{r}^3 \overline{\Omega} \frac{\overline{\mu}}{\bar{h}} d\bar{r} d\theta = I \frac{d\overline{\omega}_L}{dt} \tag{21}$$

where

$$\lambda_4 = \frac{P_o h_{oi}}{\omega_H \mu b}, \quad f = C_1 - C_2 \log\left[\frac{(a+b)}{2}\left(\omega_H - \omega_L\right)\right]$$

$$\phi_f = \begin{cases} \frac{35}{32} z \left\{ \left(1-z^2\right)^3 \left[\ln 3(z+1) + 2\right] + \frac{1}{60}\left[-55 + z\left(132 + z(345 + z\left(-160 + z\left(-405 + z\left(60 + 147z\right)\right)\right)\right)\right)\right] \right\} & 0 < H \le 3 \\ \frac{35}{32} z \left\{ \left(1-z^2\right)^3 \ln\frac{z+1}{z-1} + \frac{z}{15}\left[66 + z^2\left(30z^2 - 80\right)\right] \right\} & H > 3 \end{cases}$$

$$z = \frac{h}{3\sigma}, \quad H = \frac{h}{\sigma},$$

$$\text{and} \quad \phi_{fs} = 11.1 H^{2.31} e^{-2.38H + 0.11H^2} \quad \text{for} \quad 0.5 < H \le 7$$

2.4 Numerical scheme

The finite difference scheme is used to solve the governing equations in section 2. The iterative method of successive over-relaxation (SOR) is used to solve the modified Reynolds equation. The squeeze effect is handled by computing the strain to satisfy the following convergence criteria that is similar with the hydrodynamic pressure computation:

$$\sum_i \sum_j \left| \frac{\varphi_{i,j}^{old} - \varphi_{i,j}^{new}}{\varphi_{i,j}^{new}} \right| < \xi \tag{22}$$

where *i, j* are the node geometry index, $\varphi_{i,j}^{old}$ is the hydrodynamic pressure and strain value from the previous iteration, $\varphi_{i,j}^{new}$ is the value from current iteration, and ξ is the error tolerance ($\xi = 0.001$). The alternating direction implicit (ADI) method is applied for the heat transfer equations by handling each direction with a triadiagonal matrix solver.

To model the radial groove, the film thickness is adjusted to the appropriate depth to account for the groove geometry. The mesh density in the circumferential direction is set to twice the number of radial direction mesh (41×21).The total grid number in axial direction is uniformly 41 for the domains that include the separator disk, the friction material, ATF and the core disk. The planar mesh illustration of current numerical simulation is shown in Figure 2-4. In this figure, the red points represent the groove domain and the green points are the ungrooved domain.

The heat transfer analysis for the entire cycle involves the four phases described in section 2.4. The flow chart for engagement simulation is presented in Figure 2-5. Typical duration of the engagement stage is about 1.5 s. The duration of the soak, dwell and the stabilization periods is typically 0.8~3 s, 1.5 s, and 8 s, respectively. The time step for the thermohydrodynamic simulations is 0.001 s.

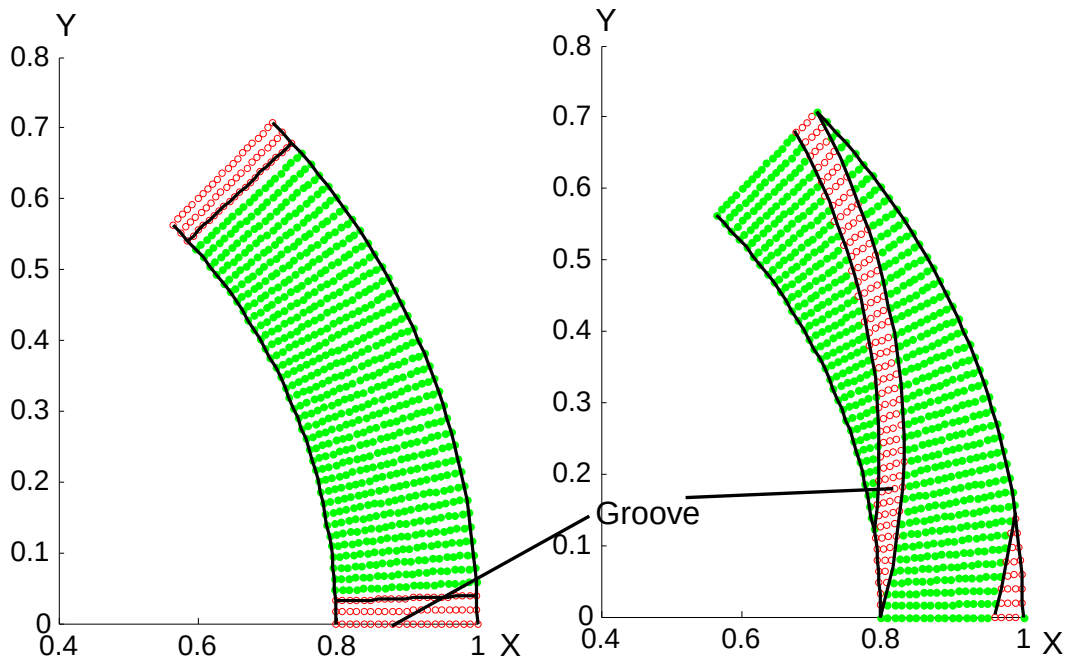

(a) (b)

Figure 2-4 Computational mesh points on the friction material (a) radial groove, (b) spiral groove

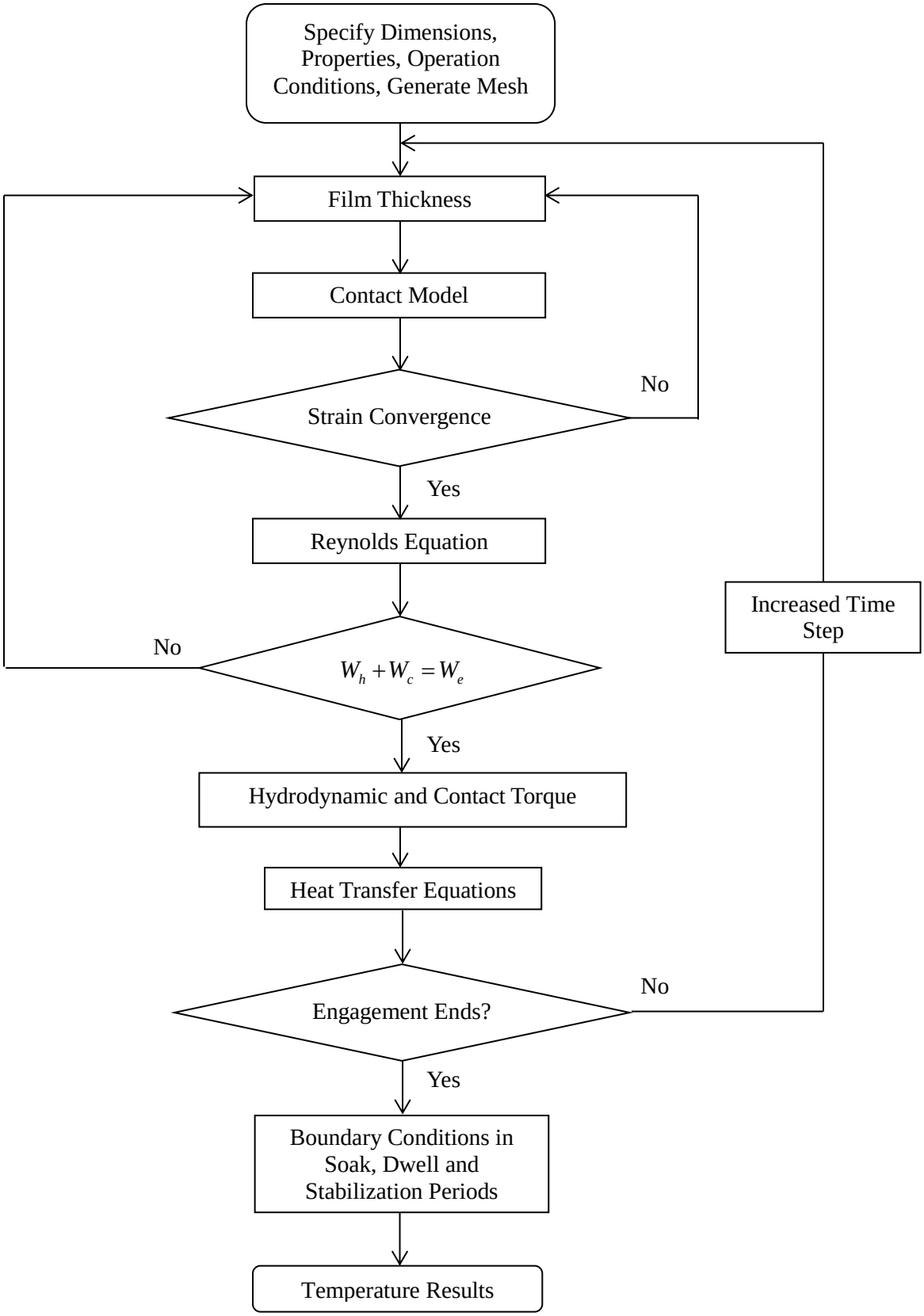

Figure 2-5 Flow chart for the clutch engagement simulation

2.5 Results and discussions

Table 2-1 presents the input data used in the simulations. These data are similar to those used by many researchers [1,3,15]. The hardness of friction material is estimated by referring to Young's modulus – shore hardness relation in ASTM D2240 and also given by Lai [16].

Table 2-1 Input data

Disk geometry		
Outer radius	58.74	mm
Inner Radius	46.83	mm
Operation configuration		
Speed	1500	rpm
Applied pressure	1.25	MPa
Moment of inertia	0.34	kgm ²
Convection coefficient	100	W/ m ²K
Ambient and initial temperature	100	℃
Friction material		
Thickness	0.5	mm
Thermal Conductivity	0.21	W/mK
Young's modulus	11.77×10^{6}	Pa
Elastic modulus for contact	10.59×10^{6}	Pa
Roughness (r.m.s)	6×10^{-6}	m
Asperity tip radius	5×10^{-4}	m
Asperity density	3×10^{7}	m^{-2}
Friction Coefficient Constants C_1, C_2	0.15, 0.011	
Hardness	1.2	MPa
Poisson's Ratio	0.4	
Waviness number	4	
Waviness	2×10^{-6}	m
Separator disk		
Thickness	3.6	mm
Thermal Conductivity	46.04	W/mK
Thermal Diffusivity	1.18×10^{-5}	m^2/s
Core disk		
Thickness	2.0	mm
Thermal Conductivity	46.04	W/mK
Thermal Diffusivity	1.18×10^{-5}	m^2/s

(Table 2-1 continued)

Automatic transmission fluid		
Initial film thickness	0.254	mm
Density	820	kg/m^3
Specific heat	2177	J/kg.K
Thermal conductivity	0.126	W/mK
Constant A, B in (6)	7.571,2.958	

2.5.1 Engagement simulation

When the load is applied, the film thickness drops very quickly to generate considerable hydrodynamic pressure. On the other hand, as the adjacency is reduced, more asperities participate in the engagement process and the asperity contact pressure increases. The total torque (summation the hydrodynamic and contact components) is increased significantly in a short period of time. The relative rotation speed between the separator and core disks decreases over time. The hydrodynamic pressure then decreases continuously because of the reduced relative rotation speed. At this period, the film thickness becomes relatively constant. This indicates stable asperity contact and torque. As a whole, the total torque does not vary much during most of the engagement time, and the relative rotation speed drops nearly linearly. During the engagement phase, the lubrication condition transverses from initially hydrodynamic to the mixed and eventually to the boundary lubrication regime. At nearly the end of engagement, the total torque experiences a sharp increase and drops to zero after the engagement is complete. At this stage, the clutch is “locked up”.

Table 2-2 shows verification of radial groove case with published results in [4] and a comparison between the GW and KE model. The number of grooves is 8, and the groove depth ratio is $H_g = 1.0$. The observation location is at the mid-plane of the inner and outer radii. Comparison of the results for the GW contact model with those published in [4] show very close predictions: nearly the same engagement time and less than 2.5 ℃ temperature difference during the engagement.

Table 2-2 Verification of present results [4]

	Jang and Khonsari [4]			GW model			KE model		
Engagement time	1.57 s			1.58 s			1.53 s		
ATF temperature	0.5 s	1.0 s	1.5 s	0.5 s	1.0 s	1.5 s	0.5 s	1.0 s	1.5 s
	174 ℃	210 ℃	220 ℃	174 ℃	212 ℃	220 ℃	175 ℃	214 ℃	220 ℃

Figure 2-6 provides contact models indicating different relationships between dimensionless contact area and dimensionless separation. For high Ψ values, the discrepancy between the GW and KE model is considerable. As Ψ increases, larger contact area is generated at the specific separation due to increased plasticity [5]. Therefore, at the end of engagement the film thickness computed using the KE model is

larger than that obtained with GW model. The computed hydrodynamic pressure using the KE model is lower, and the contact load and the contact torque are larger. So, the engagement ends faster. The predicted heat generation during the engagement phase is larger with the KE model because of more asperity contact. On the other hand, since the film thickness is larger, the predicted temperature rise does not become significantly greater than the GW model.

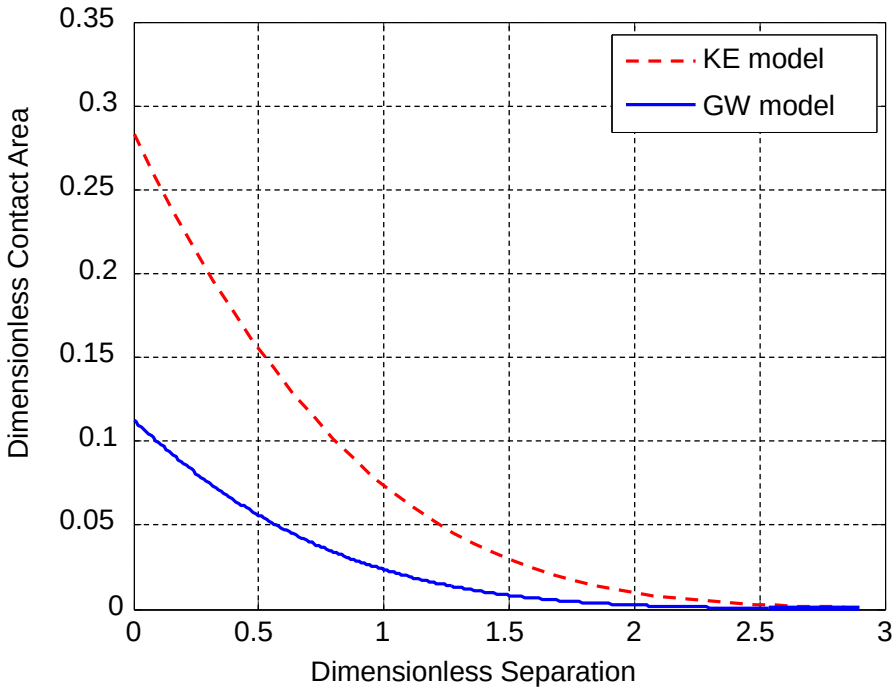

Figure 2-6 Comparison of different contact models for $\Psi = 3.7$

2.5.2 Radial groove profile effects

Figures 2-7 and 2-8 illustrate the influence of the groove profiles in the hydrodynamic pressure and the transmission torque in arc, trapezoid, and triangle cases. At the beginning of engagement (t=0.02 s) the simulation results reveal that the triangular grooves yield the highest hydrodynamic peak pressure. The pressure profile of the trapezoid and round grooves are quite close.

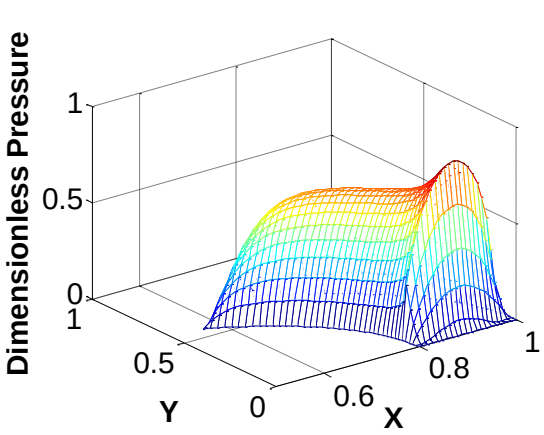

(a) Round groove profile

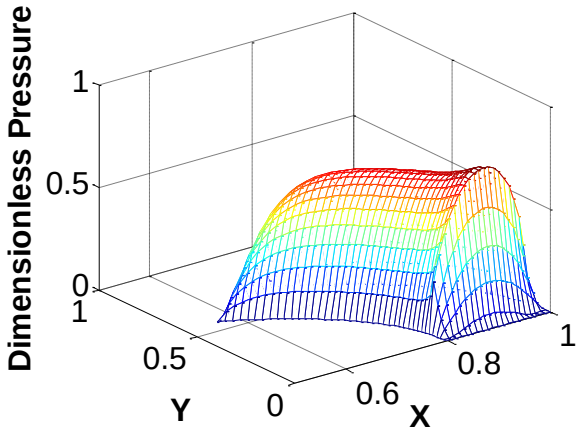

(b) Trapezoid groove profile

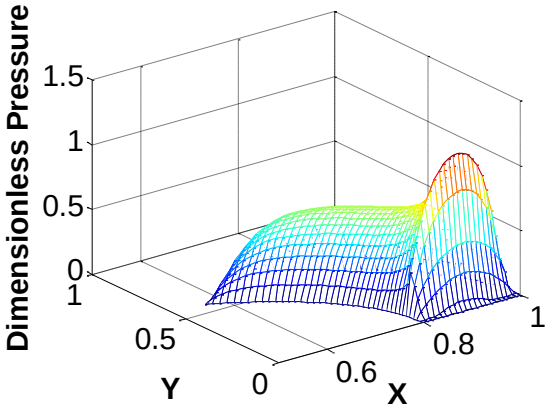

(c) Triangular groove profile

Figure 2-7 Hydrodynamic pressure profile of different groove profiles at 0.02 s ($H_g = 1.0, \phi = 0.1$)

From Figure 2-2, the cross-sectional area of triangle shape is smallest, which generates minor hydrodynamic load and resistance to squeeze motion. The film thickness drops faster, and subsequently more contact load is experienced at the beginning of engagement. Therefore, the radial groove with triangle shape is predicted to have the shortest engagement time. With a larger groove width ratio, the engagement time uniformly increases and the difference of the three cases is amplified.

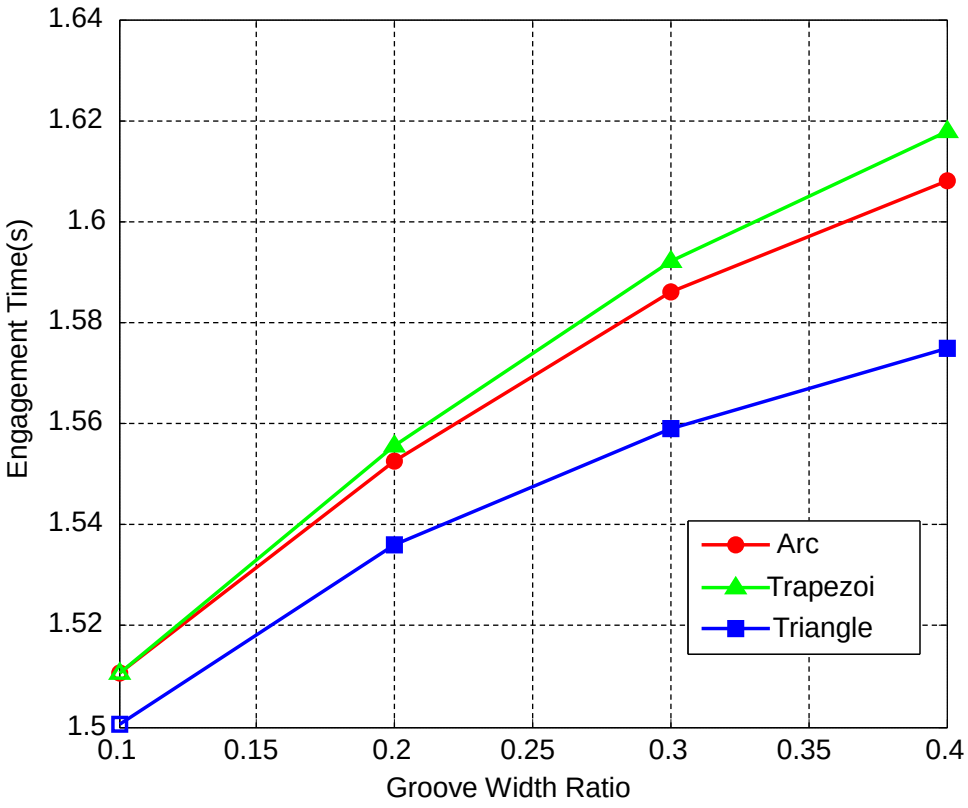

Figure 2-8 Effects of different groove profiles on the engagement time

2.5.3 Spiral groove

Spiral grooves are known to have a major influence on the hydrodynamic pressure and the temperature distribution. Thus, they find use in many mechanical components such as bearings and seals [7]. In these applications, the sliding surfaces are separated through the geometric wedge action and pumping effect. The application and parametric analysis of spiral grooves in a wet clutch are investigated as follows.

The transmission parameters, including torque, relative rotational speed between the separator disk and the friction lining, and the film thickness are output for the parametric analysis. Figure 2-9 shows a comparison between the radial groove and the spiral groove case, in which the groove depth ratio is $H_g = 1.0$ and the groove area ratio is $\phi = 0.1$.

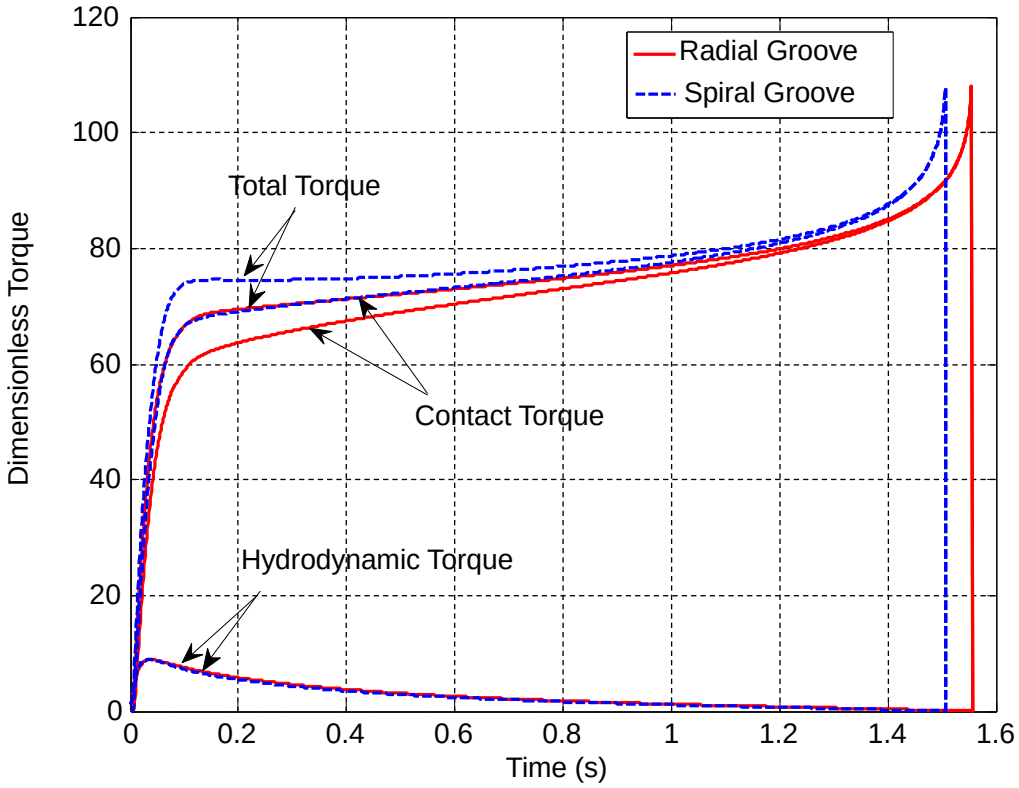

(a) Dimensionless torque

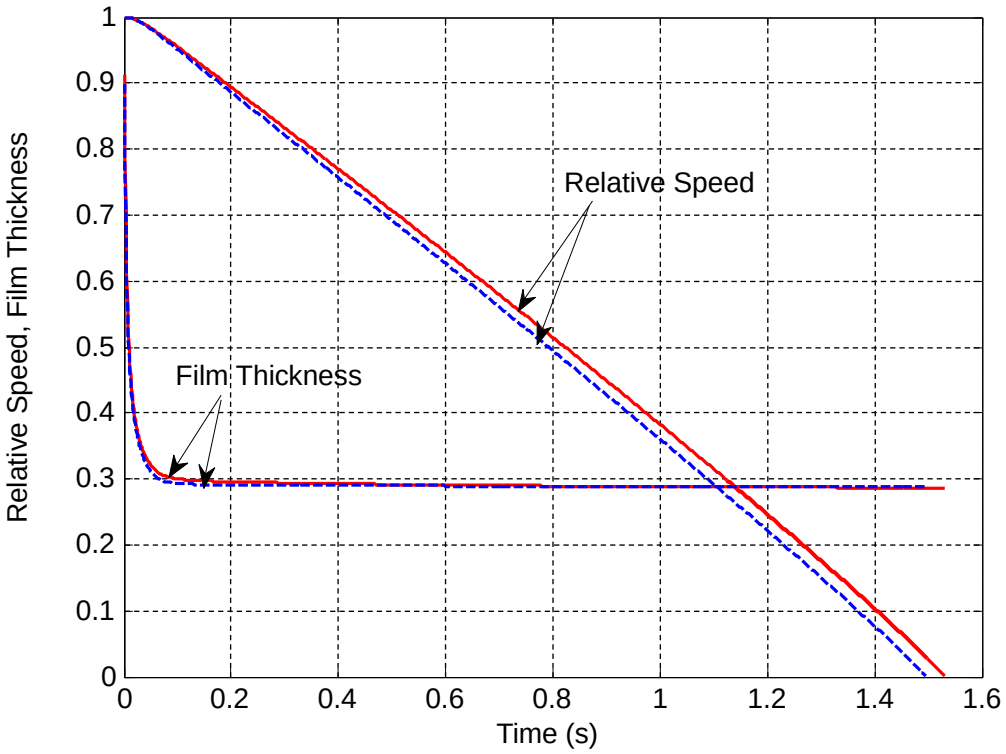

(b) Relative speed and film thicknes

Figure 2-9 Dimensionless parameters for the radial groove and spiral groove case

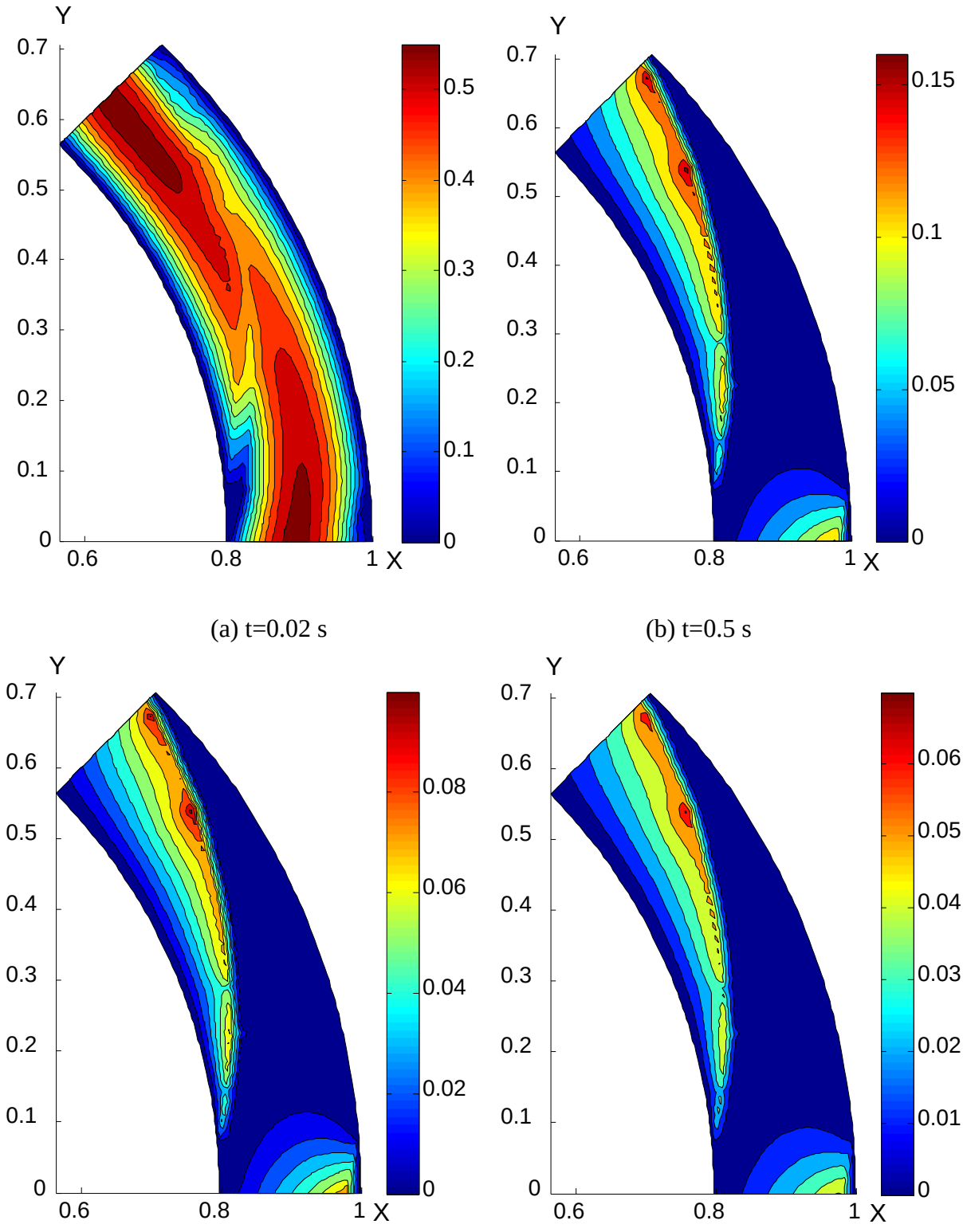

(a) t=0.02 s

(b) t=0.5 s

(c) t=1.0 s

(d) t=1.5 s

Figure 2-10 Hydrodynamic pressure distribution of the spiral groove case

Figure 2-10 shows the hydrodynamic pressure field for the spiral grooves case. From the hydrodynamic pressure profile, it is observed that the pressure peak is located at the edge of groove/ land. The decreasing rate of hydrodynamic pressure peak is relatively faster than that of the radial groove case presented by Jang et al. [4]. Within the grooved region, the pressure drops because the fluid flows into the divergent zone. In these simulations, any negative pressure is set equal to zero for simplification of the analysis.

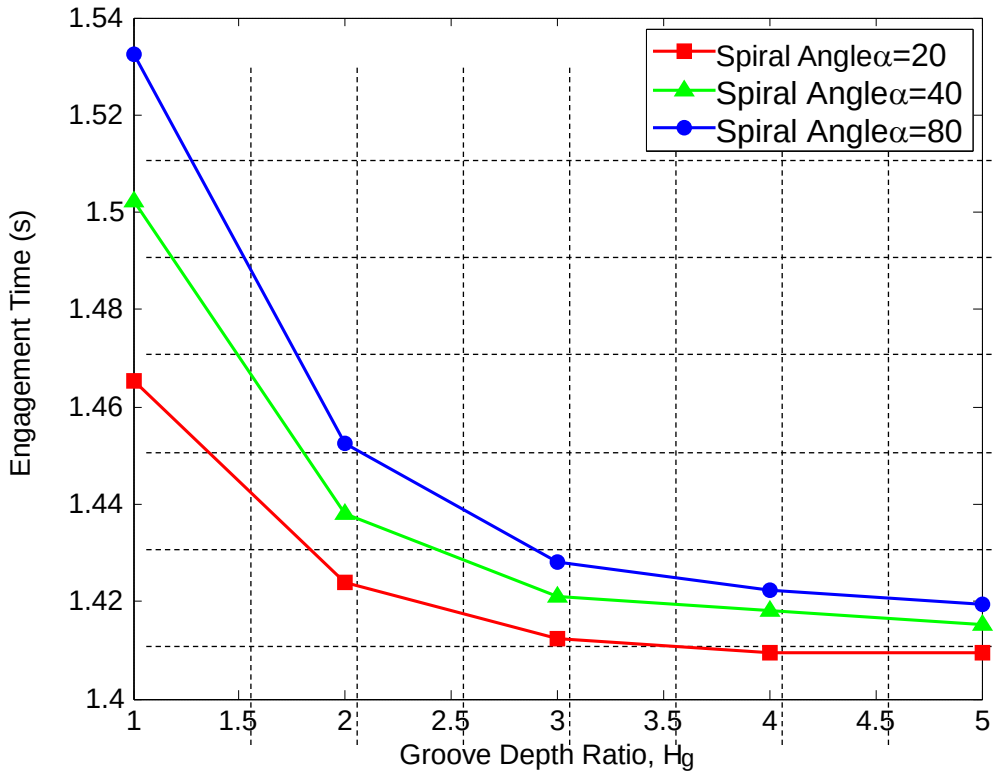

Figure 2-11 Effect of spiral groove shape on the engagement time

Figure 2-11 presents the effect of spiral groove shape on the engagement process. The geometric shape of the spiral groove is controlled by the spiral groove angle α, which determines its performance by affecting the wedge and pumping effect. By varying the spiral angle from $20°$ to $80°$ for the groove depth ratio of $H_g = 1.0$, the engagement time increases by 0.07 s. If the spiral angle is $90°$, the pumping effect is eliminated and the groove shape becomes equivalent to that of the radial groove. When the groove depth ratio increases, the engagement time uniformly decreases. It can be explained that for the deeper groove case the hydrodynamic pressure drops faster resulting in smaller film thickness with greater contact load and torque.

The pumping direction can be varied from outward pumping to inward pumping by changing the sign of α in equation (2). For the same groove depth and area ratio, the engagement time is reduced slightly (less than 0.01 s) for the inward pumping case.

2.5.4 Thermal characteristics

During the engagement process, a large amount of heat is generated at the interface between the separator disk and the friction lining. Since the film thickness of ATF is very small, the temperature curves of the separator disk–ATF interface and the ATF–friction lining interface almost coincide. After the engagement ends, no heat is generated by the friction work, so the temperature involving the ATF boundary decreases because of the ATF flow. However, the temperature difference between the friction material and the core disk still drive the heating trend in the core disk domain. When the soak period ends, the separator disk and the friction lining are detached. Convection cooling takes place at the clearance interface at the dwell period. The temperature of friction lining now begins to decrease so fast that the core disk cools down as well. It can be observed that the temperature peak at the friction lining–core disk interfaces takes place at end of the soak period. Subsequently, the ATF fills the clearance by flowing from the inner radius to the outer radius. It leads to further drop in the interface temperature. At the end of stabilization, a complete operation cycles is finished and the temperature of clutch components is restored to the original state.

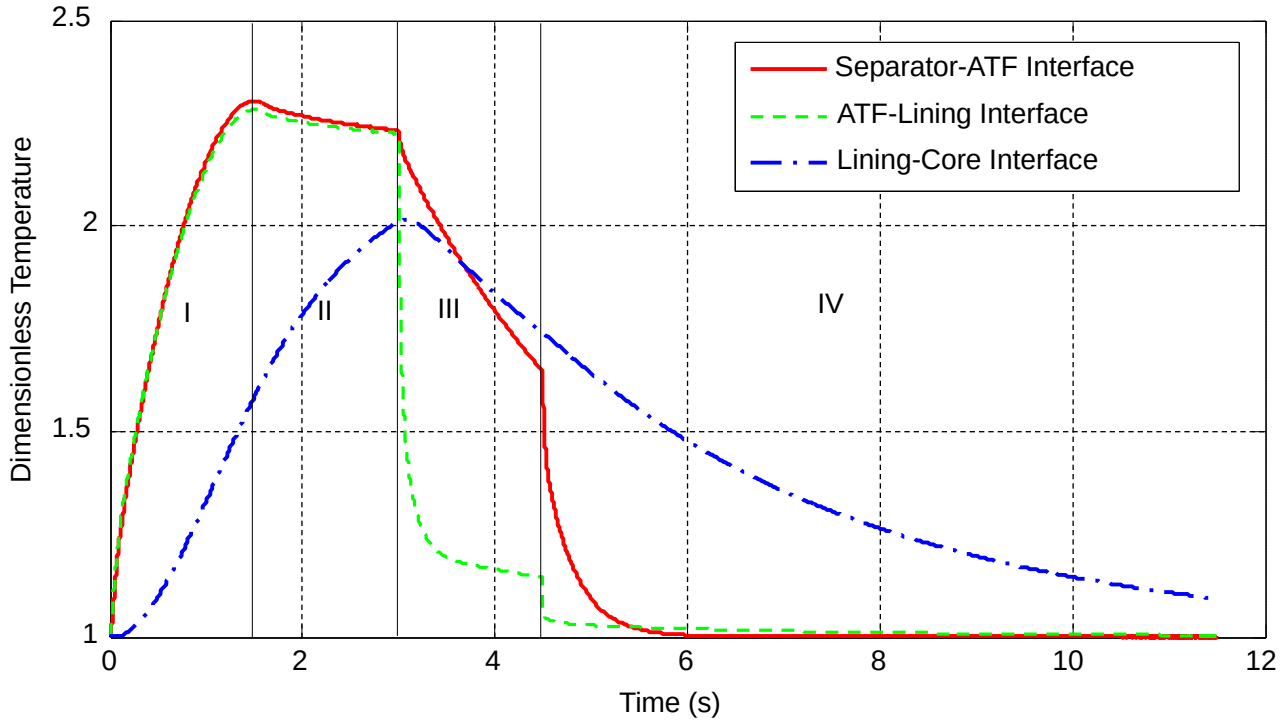

(a) 0.9 MPa, 1500rpm

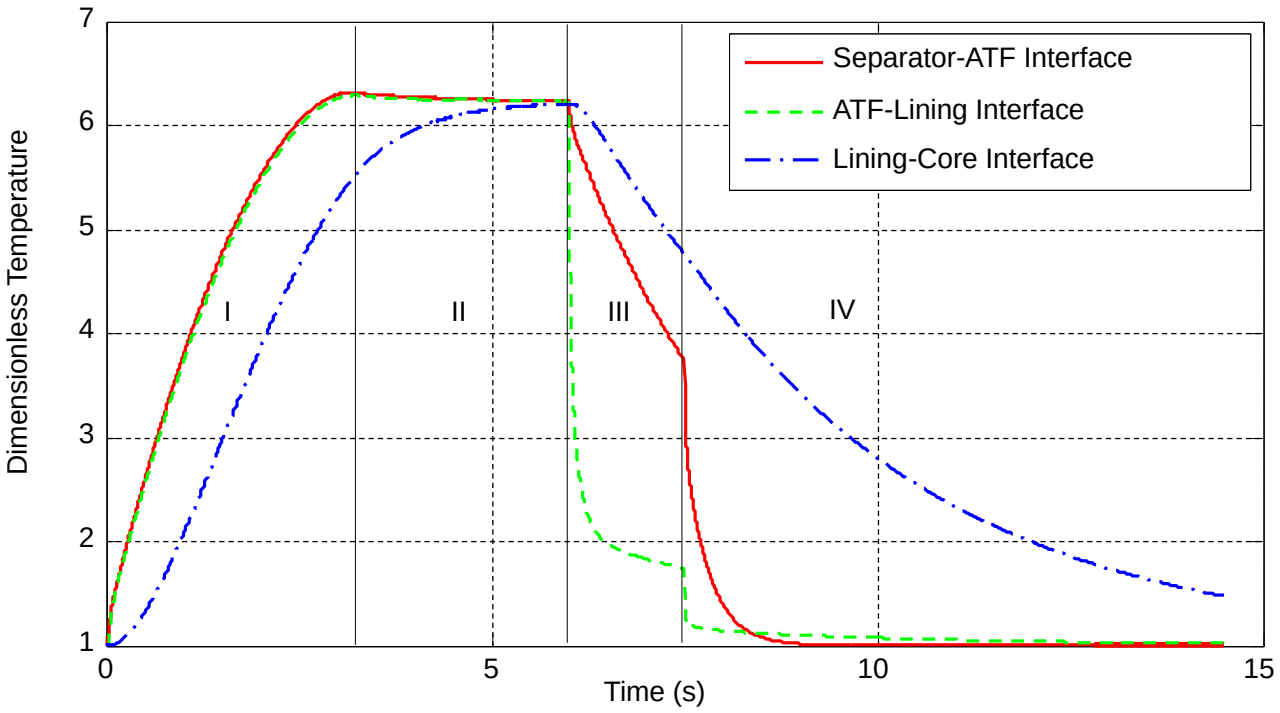

(b) 1.25 MPa, 3000rpm

Figure 2-12 Interface temperature profile with different energy input in complete periods (I – engagement stage, II – soak period, III – dwell period, IV – stabilization period, radial groove case)

The energy level is one of the most pertinent factors affecting temperature rise in a clutch system. High load indicates smaller film thickness and more asperity contact. For high rotation speed, the engagement process is longer. So is the time for temperature increase. At the high energy level (2.78 times greater than the low energy level), the predicted peak temperature is increased by almost 300%. Similarly, Yang et al. [6] reported that the peak interface temperature was about 600 ℃ at 3600 rpm. As mentioned before, the temperature profile is dependent on the choice of planar location. Figure 2-12 shows a better comparison of temperature evolution between the different groove types during the engagement stage. After the engagement ends, results in the other periods are almost the same.

Figure 2-13 shows the temperature contours at different instants for the spiral and radial grooves, where the illustration of groove/ungrooved domains are shown in Figure 2-4. The heat generation process and cooling effect of ATF is clearly demonstrated by the contour evolution process.

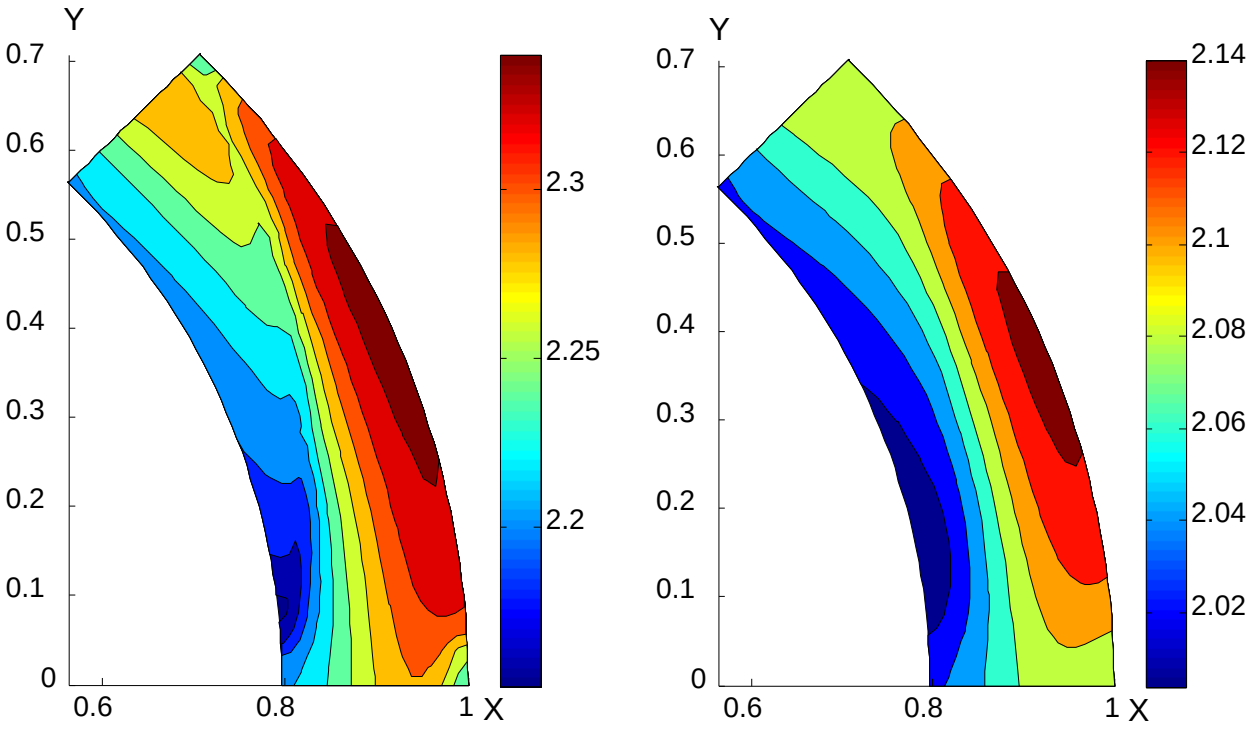

(a) Temperature at the end of engagement stage (b) Temperature at the end of dwell period

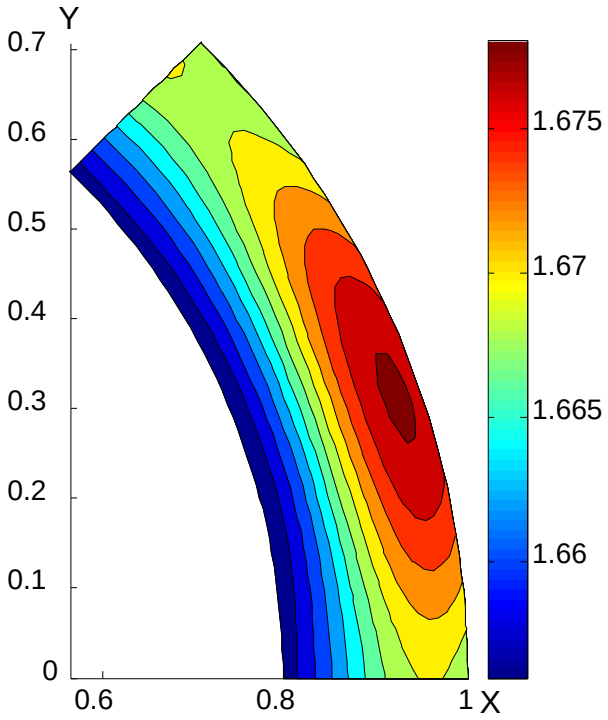

(c) Temperature at the end of soak period

Figure 2-13 Dimensionless temperature contours for the spiral groove case ($H_g = 1.0, \phi = 0.1$)

At the beginning of engagement stage, the contact pressure is very small. Although the relative rotation speed is large, the generated heat is negligible. As more and more asperities experience intimate contact and participate in carrying the load, a greater amount of heat is produced by the friction work. On the other hand, the ATF flow cools down the sliding interface in a remarkable way at first. Later on, since the flow rate and film thickness decrease, the cooling effect abates as the engagement process proceeds. The temperature rise shows obvious variation over the groove/ungrooved domains. When the engagement ends, the largest temperature rise concentrates on the outer rim and ungrooved area. Temperature at the groove domain and the inner radius boundary shows relatively smaller increase. For radial groove case, the high temperature area is located in the outer rim. For the spiral groove case, the temperature of two areas separated by the groove shows obvious difference. The maximum temperature difference between the groove and ungrooved area is roughly $18℃$ at the end of engagement.

Table 2-3 Spiral angles and the corresponding average temperature at the end of engagement

Spiral angle	20 °	30 °	40 °	50 °	60 °	70 °	80 °
Dimensionless temperature	2.2503	2.2563	2.2625	2.2669	2.2694	2.2701	2.2724

As mentioned above, the temperature distribution is affected by the spiral groove design, which directly affects the ATF flow. The induced cooling effect is investigated by computing the planar average temperature value. By varying the spiral angle from $20°$ to $80°$ for groove depth ratio $H_g = 1.0$, the average temperature at the end of engagement is increased. It is because the increased spiral angle leads to less fluid exchange between the groove and the ungrooved area and hence less convective heat transfer. For higher energy level, the temperature difference between lowest and highest spiral angle cases is more significant.

2.6 Concluding remarks

A comprehensive tribological modeling of a wet clutch is presented to study detailed parametric analysis. The groove geometry of different types (radial and spiral) is studied. Characterized by the plastic index, the contact of rough friction material is investigated by considering the full elastic-plastic regimes. Following conclusions can be drawn from solutions presented in the paper:

- Consideration of the elasto-plastic micro-contact provides a more realistic assessment of the performance of a wet clutch. Specifically, using the KE micro contact model, the final film thickness is much larger than the result obtained from GW model and the engagement time is slightly reduced.
- The parametric analysis of different groove profiles is presented for the radial groove case. Under the operating conditions simulated, the triangular profile shows the smallest engagement time.
- The spiral groove design influences the hydrodynamic load and temperature field during the engagement stage. Parametric analysis shows that the pumping effect is reduced by increasing the spiral angle and so is the hydrodynamic load and hydrodynamic torque at the beginning of the

engagement stage. Concerning the thermal characteristics, smaller spiral angle indicates more fluid exchange between the groove and the ungrooved area and generates better cooling effect.

- The heat transfer modeling and the temperature profile reflects explicit thermal behavior of the entire engagement cycle: during the engagement stage, large heat generation at the sliding interface leads to overall sharp temperature rise of the clutch system. After that, the temperature of the separator disk and the friction material is slightly reduced but the temperature of the core disk will continue to increase because of the temperature difference at the friction lining–core disk interface. The overall temperature of the clutch is intensely decreased during the dwell and stabilization periods because of the convection effect.
- The temperature contours can be applied for the durability analysis of the friction material. The higher temperature zones are more susceptible to thermal degradation. For the engagement of high energy level, the induced planar variation of degradation conditions can be remarkable.

2.7 References

[1]. S. Natsumeda and T. Miyoshi: "Numerical simulation of engagement of paper based wet clutch facing", *Journal of tribology*, 1994, **116**(2), 232-237.

[2]. Y. Yang, R. Lam, Y. F. Chen, and H. Yabe: "Modeling of heat transfer and fluid hydrodynamics for a multidisc wet clutch", *SAE transactions*, 1995, **104**(6), 1674-1688.

[3]. J. Jang and M. Khonsari: "Thermal characteristics of a wet clutch", *Journal of tribology*, 1999, **121**(3), 610-617.

[4]. J. Y. Jang, M. M. Khonsari, and R. Maki: "Three-Dimensional Thermohydrodynamic Analysis of a Wet Clutch With Consideration of Grooved Friction Surfaces", *J Tribol-T Asme*, 2011, **133**(1).

[5]. L. Kogut and I. Etsion: "A finite element based elastic-plastic model for the contact of rough surfaces", *Tribology Transactions*, 2003, **46**(3), 383-390.

[6]. Y. Yang and R. C. Lam: "Theoretical and experimental studies on the interface phenomena during the engagement of automatic transmission clutch", *Tribology Letters*, 1998, **5**(1), 57-67.

[7]. Y. Qiu and M. Khonsari: "Thermohydrodynamic Analysis of Spiral Groove Mechanical Face Seal for Liquid Applications", *Journal of tribology*, 2012, **134**(2).

[8]. N. Patir and H. Cheng: "Application of average flow model to lubrication between rough sliding surfaces", *Journal of Lubrication Technology*, 1979, **101**, 220.

[9]. R. Ausas, P. Ragot, J. Leiva, M. Jai, G. Bayada, and G. C. Buscaglia: “The impact of the cavitation model in the analysis of microtextured lubricated journal bearings”, *ASME Journal of Tribology*, 2007, **129**(4), 868.

[10]. Eric Goncalvès and Regiane Fortes Patella: “Numerical study of cavitating flows with thermodynamic effect”, *Computers & Fluids*, 2010, 99-113.

[11]. Y. Qiu and M. Khonsari: “On the prediction of cavitation in dimples using a mass-conservative algorithm”, *Journal of tribology*, 2009, **131**(4).

[12]. R. C. X. a. W. Q. Tao: “Analytical Solution for Transient Heat Conduction in Two Semi-infinite Bodies in Contact”, *Journal of Heat Transfer*, 1994, **116**(1), 5.

[13]. J. Greenwood and J. Williamson: “Contact of nominally flat surfaces”, *Proceedings of the Royal Society of London. Series A. Mathematical and Physical Sciences*, 1966, **295**(1442), 300-319.

[14]. W. Chang, I. Etsion, and D. B. BOGY: “An elastic-plastic model for the contact of rough surfaces”, *Journal of tribology*, 1987, **109**(2), 257-263.

[15]. E. Berger, F. Sadeghi, and C. Krousgrill: “Finite element modeling of engagement of rough and grooved wet clutches”, *Journal of tribology*, 1996, **118**(1), 137-146.

[16]. J. Lai: “Mechanics, Mechanisms, and Modeling of the Chemical Mechanical Polishing Process”, PhD thesis, MIT, 2001.

[17]. Fesanghary ,M. and Khonsari, M. M. “Topological and Shape Optimization of Thrust Bearings for Enhanced Load-Carrying Capacity,” *Tribology International*, V. 53, pp. 12-2, 2012.

[18]. Jang, J. Y. and Khonsari, M. M. “Wet clutch,” Encyclopedia of Tribology, Y. W. Chung and Q. J. Wang (Editors), Springer Science, New York, NY, pp. 4102-4108, 2013.

[19]. Marklund, P, Maki, R. Larsson, R., Hoglund, E, Khonsari, M.M. and Jang, J. Y. “Thermal Influence on Torque Transfer of Wet Clutches in Limited Skip Differential Applications,” *Tribology International*, V. 40, pp. 876-884, 2007.

[20]. Jang, J. Y. and Khonsari, M. M. “On the Formation of Hot Spots in Wet Clutch Systems,” ASME *Journal of Tribology*, V. 124, pp. 336-345, 2002.

CHAPTER 3 ON THE WEAR PREDICTION OF THE PAPER-BASED FRICTION MATERIAL IN A WET CLUTCH [2]

3.1 Nomenclature

a = inner radius of friction disk (m)

b = outer radius of friction disk (m)

H = thickness of the friction lining (m)

ΔH_i = wear rate (m/cycle)

k_i = thermal degradation constant (1/s)

K_i = wear coefficient (1/cycle)

l = crack length (m)

l_0 = the original length of crack (m)

q_{td} = thermal degradation rate (kg/m s)

q_{tmd} = thermomechanical degradation rate (kg/m s)

R = Boltzmann constant (J/K)

Δt = duration of an engagement cycle (s)

T = temperature (℃)

U_i = activation energy (J)

ΔW = weight loss rate (kg/cycle)

α_π^* = the formation energy for a unit of new surface (J/m)

ρ = friction material density (kg/m^3)

γ = mechanical coefficient (m^3)

σ^* = the local stress (MPa)

λ = fluctuation advance of the crack (m)

λ_π = fluctuation advance of sections of a crack front (m)

λ_m = local stress coefficient (m)

υ_0 = frequency of thermal oscillations (1/s)

$\Delta\Phi^+$ = thermodynamic potential of bond scission (J)

$\Delta\Phi^-$ = thermodynamic potential of bond recovery (J)

$\Delta\Phi_y$ = increase in the thermodynamic potential due to the presence of crack (J)

$\Delta\Phi_\pi$ = increase in the thermodynamic potential by formation of new free surfaces (J)

Subscripts

i=1, parameter in the first stage wear model

i=2, parameter in the second stage wear model

[2] Reprinted by permission of Wear

3.2 Introduction

The key component of the transmission device is a wet clutch designed to provide smooth transfer of power under lubricated conditions. The long-term, satisfactory performance of a wet clutch largely depends on the durability of the friction material. This is very susceptible to degradation after repeated engagement cycles particularly when subjected to high-energy input. Degradation results in cellulose loss and reduction in the friction lining thickness. Wear adversely affects the performance and reliability and if excessive can result in transmission failure.

The wear behavior of friction-lining in a wet clutch is distinctive in that it is made of a paper-based material composed of organic fiber, resin and other fillers. It has a porous and deformable structure with a rather rough surface. Its permeability allows the automatic transmission fluid (ATF) to soak into the friction material and allows the fluid to squeeze out and cool the surfaces upon the application of the engagement load. Friction material's distinct composition and unique features are responsible for a significantly more complex wear behavior in comparison with metallic materials [1, 2].

The literature contains reports on many experimental efforts that investigate the wear mechanism of composite material. The relevant test results are obtained by characterizing the worn surface topography [3] and by studying the tribological behavior of polymers using a pin-on-disc tribometer [4]. Myshkin et al. [5] performed a general investigation of tribology of polymers by studying how the load, sliding speed and temperature influence friction. More recently, in a noteworthy contribution, Lingesten et al. [12] reported an intriguing wear trend obtained using a specialized test rig equipped with several sensors capable of providing continuous measurement of the temperature, transmission torque, rotational speed and friction lining wear rate. The test results revealed a unique two-stage wear phenomenon with distinct transition from an initially low wear rate to a much greater rate after a certain number of engagement cycles with high power input. The physical mechanisms and prediction of such a multi-stage wear behavior remains elusive and much worth further investigation.

Friction lining wear can depend on multiple factors, including the rotational speed and loading type, contact conditions (material hardness, surface roughness, lubrication, existence of particulate contaminants, etc.), material property (composite matrix, filler, and reinforcement), and environmental factors (temperature, oxygen, and other chemical). In a notable study, Yang et al. performed thermogravimetric analysis (TGA) to quantify the change in the cellulose weight ratio in a friction material during engagement [6]. They showed that the weight and properties of the friction material are drastically affected by thermal effects. Based on this finding, they proposed a useful degradation model to characterize the material's behavior as a function of engagement cycle. This study provides an important path forward for analyzing the wear mechanism. Watson et al. [7] applied the Archard's law to predict the remaining useful life of the friction material. However, its applicability encounters difficulty in explaining the two-stage wear behavior proposed by Lingesten et al. [12].

It is noteworthy that intense thermal effects in a clutch system is related to another interesting

phenomenon known as the thermoelastic instability (TEI), which gives rise to the formation of hot spots on the separator disks. Such hot spots are typically large and visible by the naked eye. TEI is essentially a manifestation of positive feedback loop between local pressure and heat that grows if the operating speed exceeds a certain threshold [8]. The interested reader may refer to publications [9-11] for more pertinent discussions on this type of surface damage.

The objective of the present study is to propose a model for analyzing the wear characteristics of a paper-based friction material in a wet clutch subjected to both thermal and mechanical degradation. A computational procedure for wear prediction is presented to investigate the experimentally observed two-stage wear behavior reported by Lingesten et al.[12].

The structure of the paper is organized as follows: In Section 2, we briefly describe the implementation of a thermohydrodynamic analysis of the clutch engagement. This is necessary to obtain the temperature history during the full engagement cycle. Section 3 is devoted to the presentation of the proposed wear model. The necessary verifications of wear prediction with experimental results and relevant discussion are demonstrated in Section 4 followed by concluding remarks in Section 5.

3.3 Modeling clutch engagement

Figure 3-1 shows a schematic diagram of a wet clutch in the drive-train system. The engagement operation of the clutch system is controlled by a hydraulic actuator and the movement of a piston. Classified by the operation and the thermal boundaries at the sliding interface, the full engagement cycle of a wet clutch translates into four distinct stages namely engagement, soaking, dwell, and stabilization periods. Initially, the gap between the separator disk and the friction disk is filled with ATF. During the engagement stage, upon application of the hydrodynamic pressure, their proximity is rapidly reduced to a very small level and remains steady while the surface asperities come into intimate contact. With the drop in the film thickness, the lubrication condition tends to shift from hydrodynamic to mixed and finally to the boundary regime. This sequence occurs as the squeeze action when the applied pressure pushes the initially separated interface into partial contact, first at the asperity level and more fully later on. Meanwhile, the relative rotational speed gradually diminishes and a large amount of heat is generated due to the sliding motion and dynamic friction force. At the end of the engagement, the friction pair is locked up to transfer the power during the soak period and temperature ceases to rise. When the dwell period begins, the gap between the separator disk and the friction lining is restored to the initial value. In this stage, the cooling mechanism is air convection. In the final stage, the stabilization period, ATF flows in to cool the clutch, resulting in a rapid drop in temperature.

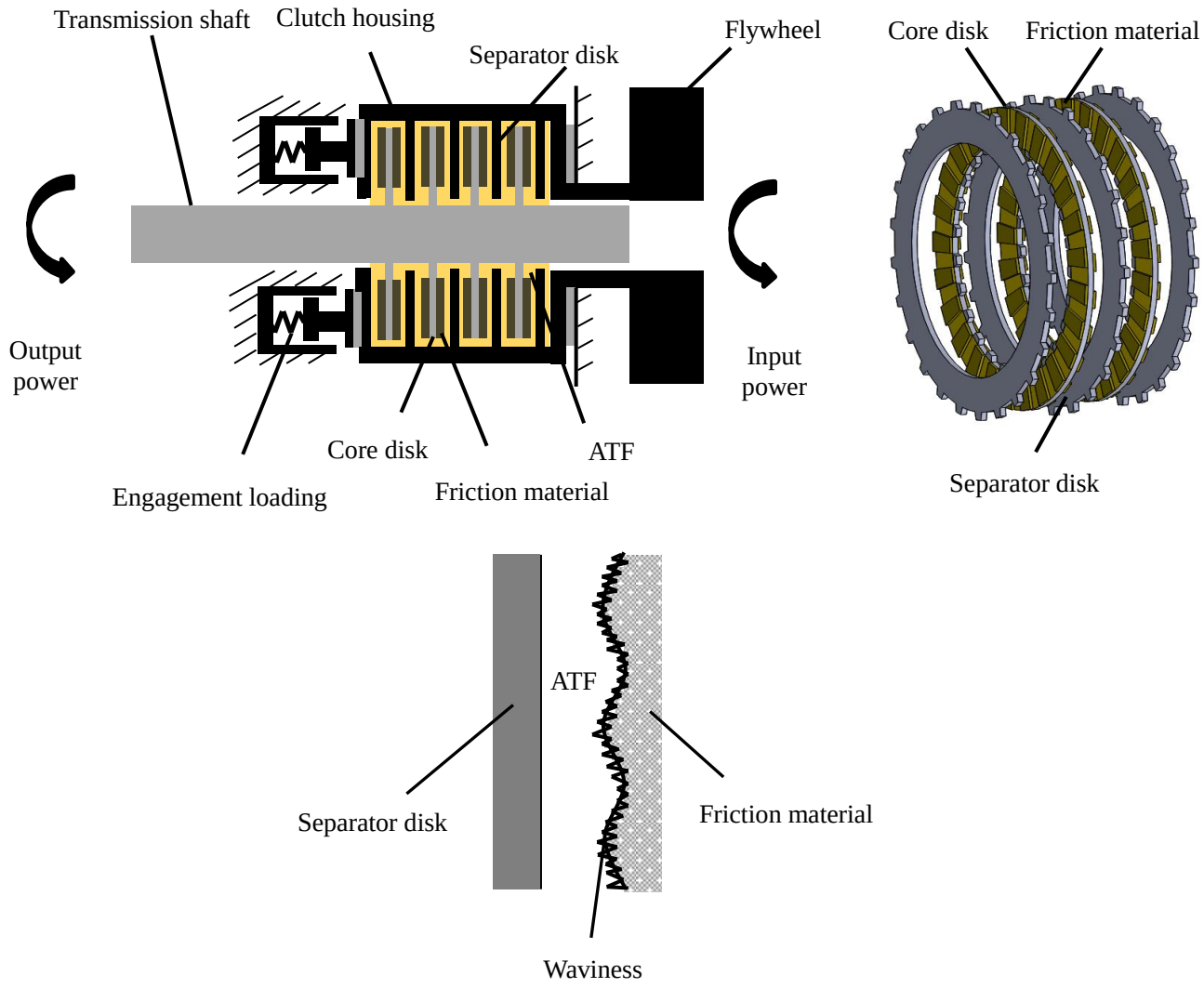

Figure 3-1 Schematic diagram of a wet clutch system

The simulation of a wet clutch engagement is a relatively mature research topic from the computational point of view. The first modeling and hydrodynamic analysis with consideration of permeability, asperity contact of rough surface and compressive strain was presented by Natsumeda and Miyoshi [13]. Berger et al. [14] used finite element method to perform the engagement simulation. Due to the significant thermal effects that occur during the engagement process, Jang and Khonsari [15, 16] proposed a more comprehensive simulation scheme that includes the combination of hydrodynamic modeling and consideration of thermal aspects, known as thermohyrdrodynamic (THD) analysis. Relevant studies that characterize the influence of temperature on torque and frictional instability have also been reported in [9, 17]. More recently, a detailed 3-D THD study of the full engagement cycle is reported in [18] that presents discussion on the friction disks with different types of groove [19].

The torque transmitted by a clutch system is composed of two parts: the viscous torque due to shearing

of the fluid and the contact torque due to the interference of asperities. The relative proportions of these two components are determined by the balance between hydrodynamic load and contact load. The hydrodynamic pressure is predicted by solving a modified Reynolds equation that incorporates surface roughness, squeeze effect of the porous and deformable friction material, as well as provision for centrifugal force. With the engagement load, the film thickness is quickly reduced at the beginning of the engagement stage and is maintained at a rather small level [18], which renders the load and the torque generated by asperity contact to become the dominating components for the total engagement load and the total torque. With the stable film thickness, the transmission torque is also quite steady during the majority of the engagement period, resulting in a quasi-linearly decreasing relative rotational speed curve.

Consideration of thermal effects requires simultaneous solution of the energy and heat conduction equations in the ATF, separator, friction lining, and core disks. The thermal boundary condition at the sliding interface varies over the different operation periods. Convective boundary condition is applied to the radial direction, the inner radius and the outer radius; periodic condition is applied to the circumferential direction. The symmetric boundary condition is applied at the upper and lower boundary. Heat is partitioned at the separator disk–friction lining interface during the engagement stage. After that, the temperature drops slightly during the soak period. In the dwell period, the interface experiences convective cooling via air. In stabilization period, convection cooling occurs via the ATF flow in the interface. The test results on the engagement behavior as well as the thermal aspects can be found in [20-22]. The computational details are available in [18]. Compared with the hydrodynamic simulation by Berger et al. [14], THD simulation predicts the thermal field in the system and its effect on the reduction of the ATF viscosity. The viscosity-temperature relationship of fluid is given by American Society for Testing and Materials (ASTM):

$$\log_{10}\log_{10}\left(10^{6}\frac{\mu}{\rho_f}+0.7\right)=A-B\log_{10}\left(\Theta+273\right) \tag{1}$$

Results of a typical THD prediction for the torque and the temperature are presented in Figure 3-2 (a) and (b), respectively. As noted, the temperature of the ATF-lining interface can experience a drastic rise (more than 250 ^{o}C) in less than 2 second during the engagement stage I. It should, therefore, be of no surprise that friction material can undergo severe thermo-mechanical degradation upon repeated engagements.

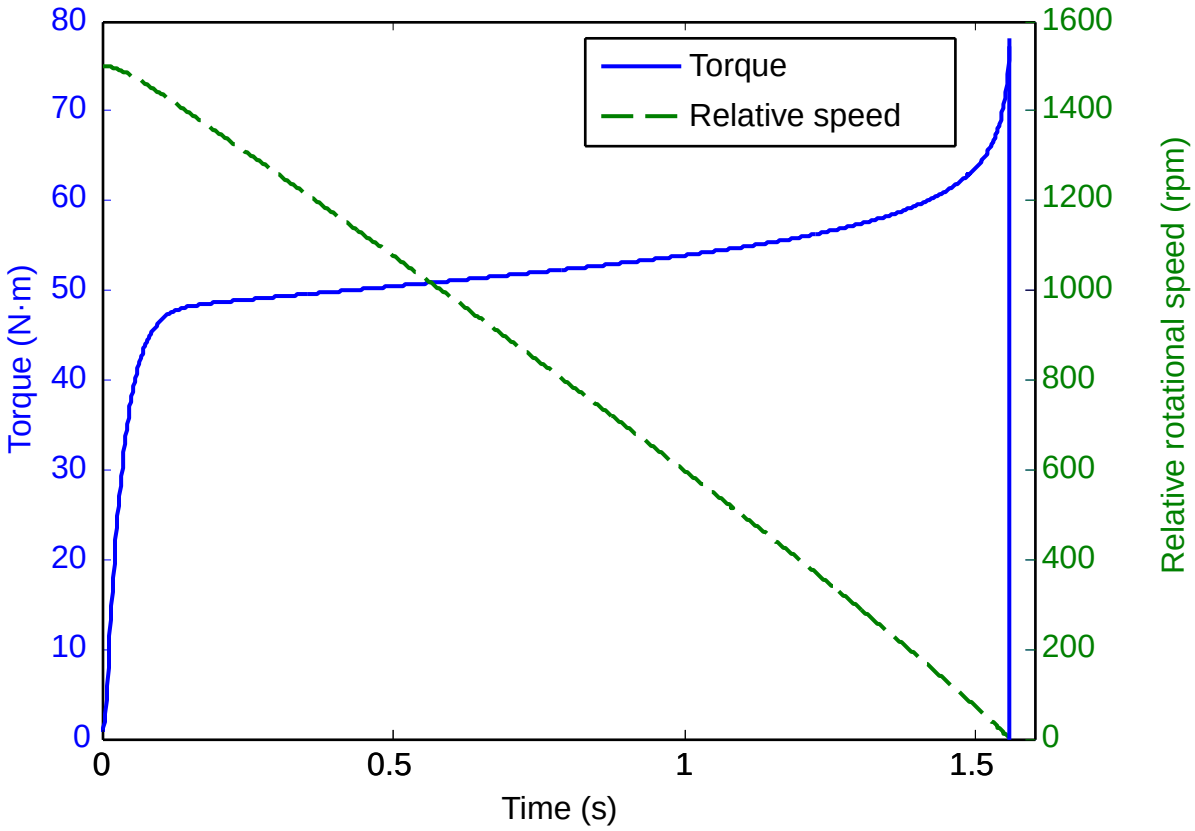

(a) A typical torque transmission during the engagement stage

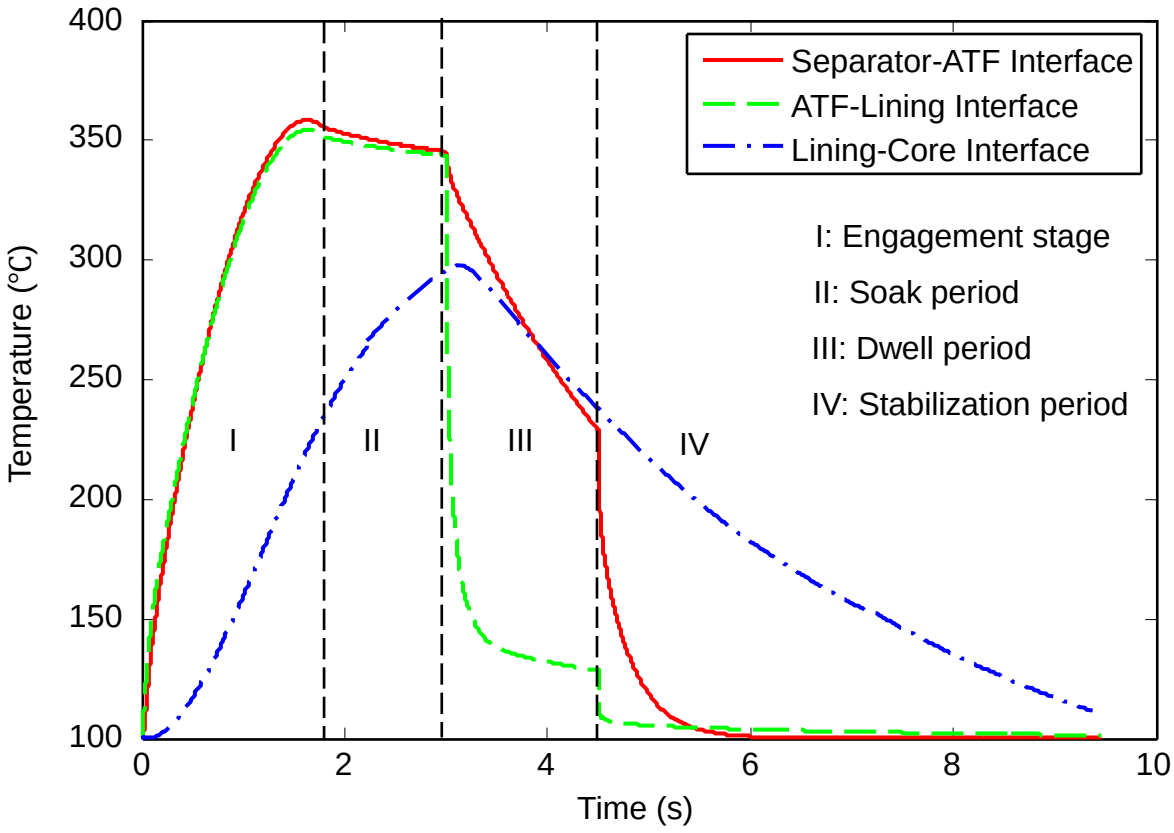

(b) Temperature evolution of engagement

Figure 3-2 Engagement results of a wet clutch (1.25 MPa, 1500 rpm)

3.4 Wear modeling

The wear behavior of the friction material is closely related to both the thermal degradation of organic fibers and the stress condition at the sliding interface. These factors contribute to removal of the friction material during the engagement cycles and lead to the observed two-stage wear phenomena. We begin this section by first describing a recently observed two-stage wear phenomena reported by Lingesten [12].

3.4.1 "Two – Stage" wear phenomena

The assessment of wear and degradation of friction material has proven to have its own complexity. Recently Lingesten et al. [12] at LTU reported the results of a series of tests with a specialized test rig design for applications in heavy-duty construction equipment. They performed continuous measurement of thickness reduction of the friction material during repeated cyclic engagements. Wear was accurately measured using a sensor (with 1μm resolution) that recorded the change in distance traveled by the piston during the engagement. Lingesten et al. reported an intriguing wear behavior as shown in Figure 3-3. This behavior— which to our knowledge had never been reported before— shows that the rate of thickness reduction of friction material changes after a certain number of repeated engagements (18000 ~19000

cycles in Figure 3-3). When the two stages of wear are finished (i.e. after ~65000 cycles), the friction lining tends to rapidly delaminate and the clutch fails shortly thereafter.

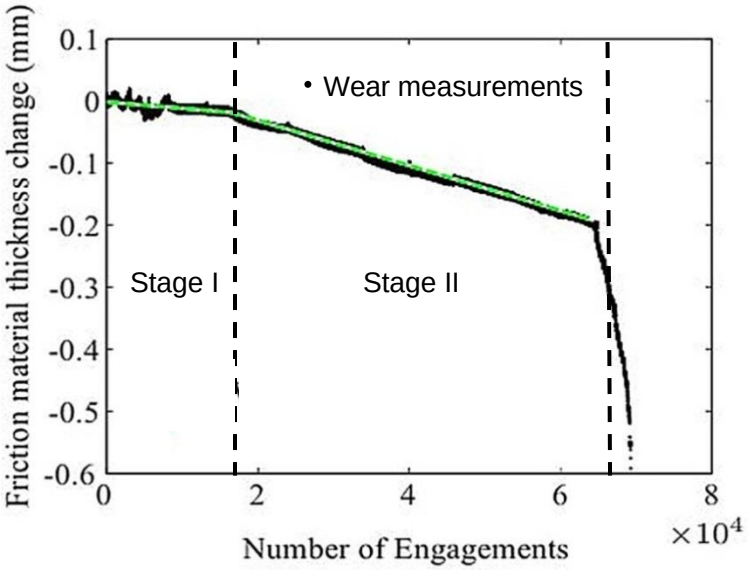

Figure 3-3 A "two-stage" wear behavior during the engagement (8.3 MW/m^2) [12]

An interesting observation is that the transition of wear rate for a specific material takes place at approximately the same depth in the friction lining thickness ($\approx 0.02\ mm$) as marked in Figure 3-4 for two additional wear test results obtained at different input power levels. Thus, the transition from Stage I to Stage II occurs when the friction lining experiences a certain material loss. Of course, with higher energy level (Figure 4b), the number of engagements to the point of wear transition is smaller.

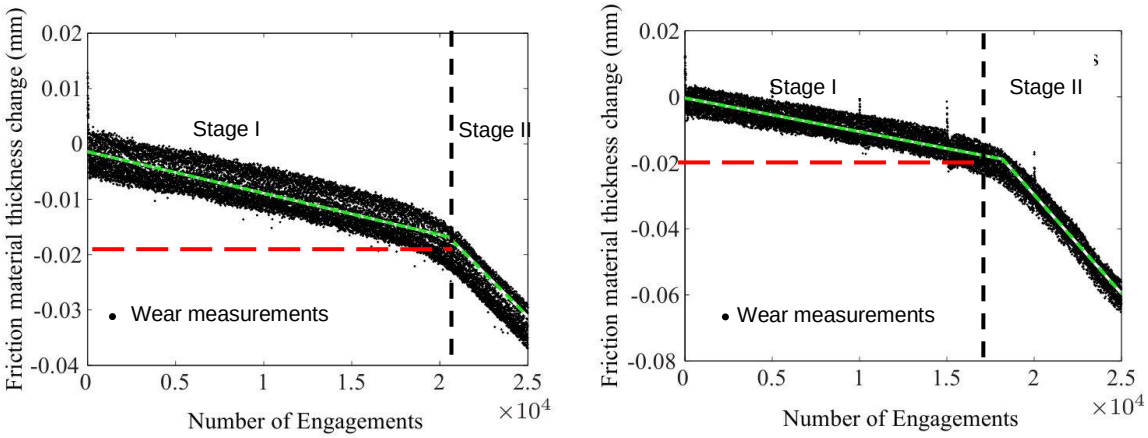

(a) Wear test of power 7.9 MW/m^2 (b) Wear test of power 9.8 MW/m^2

Figure 3-4 Wear rate transition at different energy level [12]

3.4.2 Thermal degradation mechanism

Paper-based friction material is manufactured with several compositions involving cellulose fiber, binder, polymeric fiber, and inorganic fillers, etc. According to Yang et al. [6], a thermogravimetric analysis (TGA) can be performed in order to measure the change in properties of composite materials induced by

increasing temperature. This is illustrated in Figure 3-5 which shows how a programmable furnace with a precise balance at a constant heat rate can be used to measure the mass loss of the sample over time. The response of the friction material in the TGA test can be summarized as follows: initially, the friction material has a minor weight loss of less than 5%, which corresponds to evaporation of the soaking oil. After that, a second weight loss is observed due to the carbonization of cellulose fibers until 400 ℃. When the degradation of cellulose is finished, another major weight reduction takes place because of burning of other components such as binders and other synthetic polymeric fibers. Finally, some residual material remains after the TGA test, corresponding to inorganic matter (normally filler).

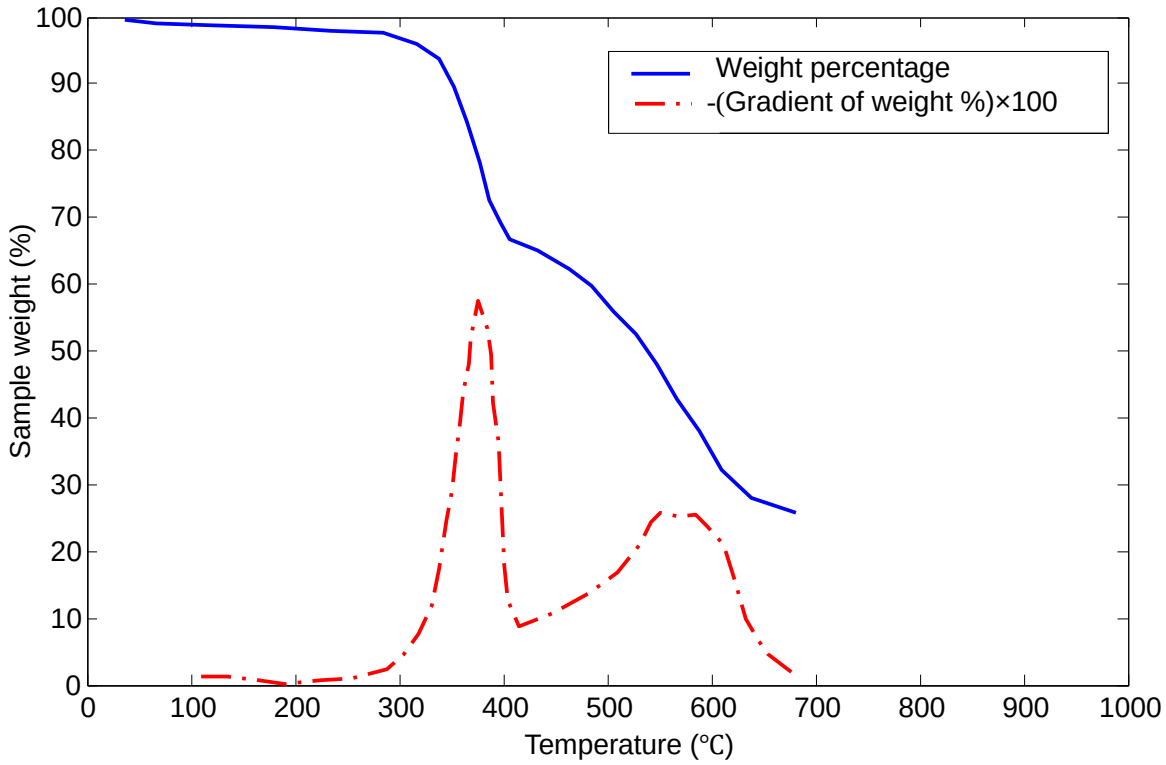

Figure 3-5 TGA result of the friction material weight loss [6]

TGA tests show that the cellulose fiber is the least heat resistant element in the composition of friction material. In general, when exposed to considerable heat, cellulose tends to degrade rapidly leading to a dramatic change in the friction material performance and mechanical properties. It should, however, be noted that the cellulose fiber can function to maintain the strength of the material and to increase the material resistance to mechanical wear. In fact, when the weight ratio of the organic fiber is significantly reduced, the material strength is impaired and more wear is generated by the intense mechanical factor. Figure 3-6 shows typical surface carbonization of the worn friction lining that can frequently be observed in the drivetrain system.

Figure 3-6 Carbonization of friction material during large engagement cycles

According to Yang et al. [6] the thermal degradation process can be regarded as a chemical reaction depending on the system temperature and activation energy according to the following relationship:

$$q_{td}\left(z,t\right) = k_1 \exp\left(-\frac{U_1}{RT\left(z,t\right)}\right) \tag{2}$$

where $q_{td}\left(z,t\right)$ is the thermal degradation rate function, k_1 is the rate constant of thermal degradation, R is the Boltzmann constant, U_1 is the activation energy of cellulose, and $T\left(z,t\right)$ is the temperature distribution.

The accumulative thermal degradation of the cellulose fiber is responsible for the reduction of the friction lining volume during the first wear stage. Once $q_{td}\left(z,t\right)$ is determined, the weight loss as a result of the thermal degradation can be evaluated using the following expression [7]:

$$\Delta W = \int_0^H \frac{dz}{H} \int_0^{\Delta t} q_{td}\left(z,t\right) dt \tag{3}$$

where ΔW is the weight reduction of cellulose per engagement cycle, H is the thickness of the friction lining, regarded as unchanged for a single operation cycle, and Δt is the duration of an entire operation cycle. A schematic of the thickness reduction of the friction lining is shown in Figure 3-7.

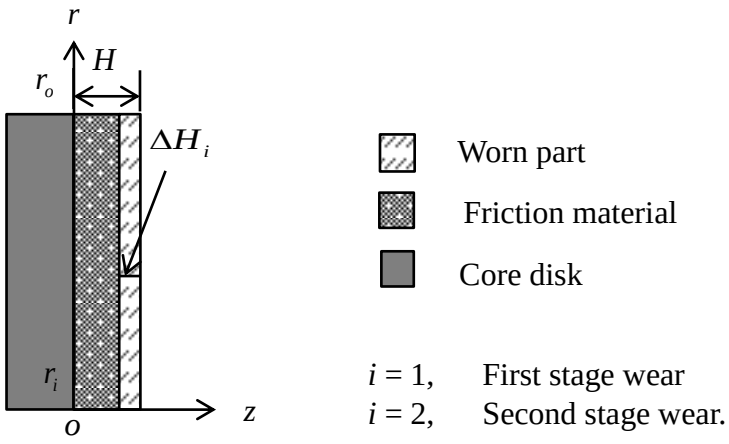

Figure 3-7 Wear of the friction lining in an engagement cycle

The corresponding change in the friction lining thickness can be computed using the following expression:

$$\Delta H_1 = \frac{\Delta W}{\rho g \pi \left(b^2 - a^2\right)} = K_1 \int_0^H dz \int_0^{\Delta t} \exp\left(-\frac{U_1}{RT\left(z,t\right)}\right) dt \tag{4}$$

where ΔH_1 is the wear rate in the first wear stage, a and b are respectively the inner radius and the outer radius, ρ is the density of the friction material, and K_1 the first stage wear coefficient.

3.4.3 Thermomechanical degradation wear

The second stage of wear is governed by thermomechanical degradation. It is defined as accumulation of the material damage due to cyclic temperature variations as well as the stress condition [23]. During the engagement, the thermal and mechanical effects undergo substantial variation due to the sliding motion and asperity contact. With the impaired material strength due to cellulose degradation, the thickness is reduced by plastic compression and material damage (micro-fracture). In comparison with the cellulose fiber, the residual components in the friction material (binder, polymeric fiber, etc) are more heat-resistant but prone to delamination when subjected to the applied stress. With cyclic loading of large engagement cycles, the dissipated energy is transmitted to the subsurface layer leading to fatigue wear. Thus, degradation in the second wear stage depends on temperature, stress conditions, and material properties.

According to Sosnovskiy et al. [24], the wear intensity of polymeric material can be described by the volumetric damage from the kinetic viewpoint. A relevant theoretical modeling approach, called "thermofluctuation theory," is proposed by E. Kartashov et al. [25] in connection with the study of the statistics of bond scission and recombination at the crack apex. The application of this theory was also extended to study wear in different types of materials including metals [23]. Thermomechanical models with relevant friction and wear discussion are also presented in [26]. The rate model applied to describe the thermomechanical degradation, q_{tmd}, is expressed as follows (see Appendix for derivation):

$$q_{tmd}\left(z,t\right)=k_2\exp\left(-\frac{U_2-\gamma\sigma}{RT\left(z,t\right)}\right) \tag{5}$$

where k_2 is the resistance coefficient of thermomechanical degradation, γ is the stress factor, and U_2 is the activation energy of heat-resistant components, including binder and polymeric fiber, etc. in the friction material.

Similar to the first stage wear model, the thickness change of the friction material during the second wear stage is calculated by the temporal and spatial integration of the degradation rate:

$$\Delta H_2=\frac{\eta_2 m_0}{\rho\pi\left(b^2-a^2\right)}\int_0^H\frac{dz}{H}\int_0^{\Delta t}q_{td}\left(z,t\right)dt=K_2\int_0^H dz\int_0^{\Delta t}\exp\left(-\frac{U_2-\gamma\sigma}{RT\left(z,t\right)}\right)dt \tag{6}$$

where ΔH_2 is the wear rate in the first wear stage, η_2 is the mass ratio of binder and polymeric fiber in the friction material, and K_2 is the second stage wear coefficient.

At the end of the second wear stage, the majority of the friction material is removed. The residual inorganic material is rapidly worn off and the clutch seizes.

3.5 Results and discussion

3.5.1 Test procedure for determining the model parameters

A viable method to evaluate the degradation model parameters (rate constant k_1 and the activation energy U_1) is to combine a slip test and the TGA data [6]. The parameters of the thermal degradation model are obtained through the relationship between degradation rate and temperature. Therefore, it is necessary to measure the weight loss of samples over time and repeat the measurement for different temperatures.

As mentioned before, a TGA test is usually used to measure the physical and chemical properties of composite materials. However, since a fixed temperature during the TGA test with constant heat rate is not available, a continuous slip test on the full-pack machinery can be performed in order to generate a pseudo-steady thermal condition for the degradation of cellulose fiber. The heat generation and dissipation needs to be balanced such that the temperature conditions at the sliding interface is approximately stable. After the slip test, the residual cellulose percentage must be measured by TGA to determine the weight reduction during the slipping. The test procedure is illustrated by Figure 3-8 and measurement results are provided in Table 3-1. These results correspond to samples of a commercially available friction material with waffle shape grooves (Figure 3-6) sent for TGA analysis to a testing center that conducted the experiments with the above procedure. By taking the logarithmic form of (1), the model parameters are obtained by linear regression analysis of the test data. Figure 3-9 shows the determination of degradation parameters where $U_1/R\approx 6100\left(K\right)$.

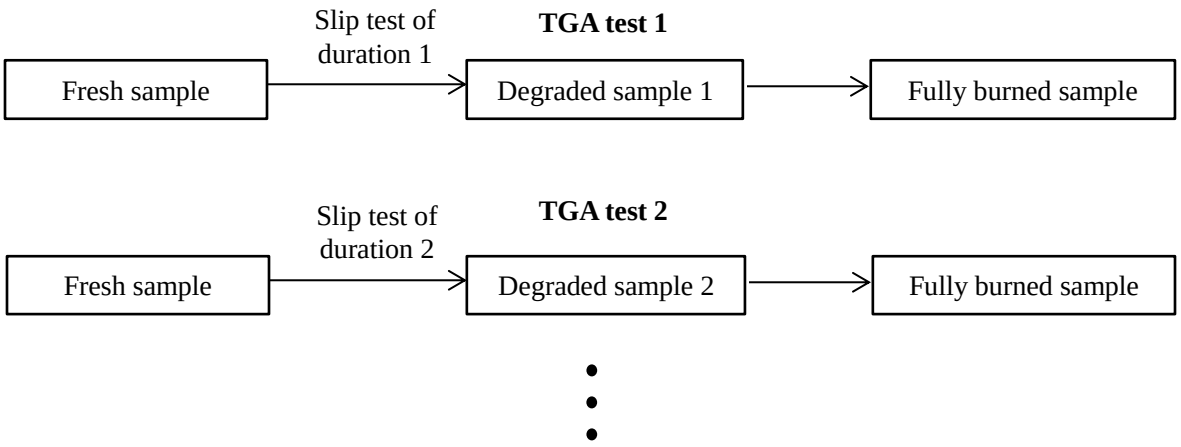

Figure 3-8 Test procedure to evaluate degradation rate at a specific temperature

Table 3-1. Measurement of cellulose degradation through TGA and slipping test

Sample number	New	1	2	3	4	5	6	7	8	9
Torque (N·m)		115			126.5			130		
temperature (℃)		230			245			260		
Slip time (sec)		1800	9000	18000	1800	9000	18000	1800	9000	18000
Cellulose weight (%)	19.6	16.6	15.4	13.7	15.5	13.6	9.1	17	12.8	6.9
Remained cellulose (%)	100	84.7	78.6	69.9	79.1	69.4	46.4	86.7	65.3	35.2

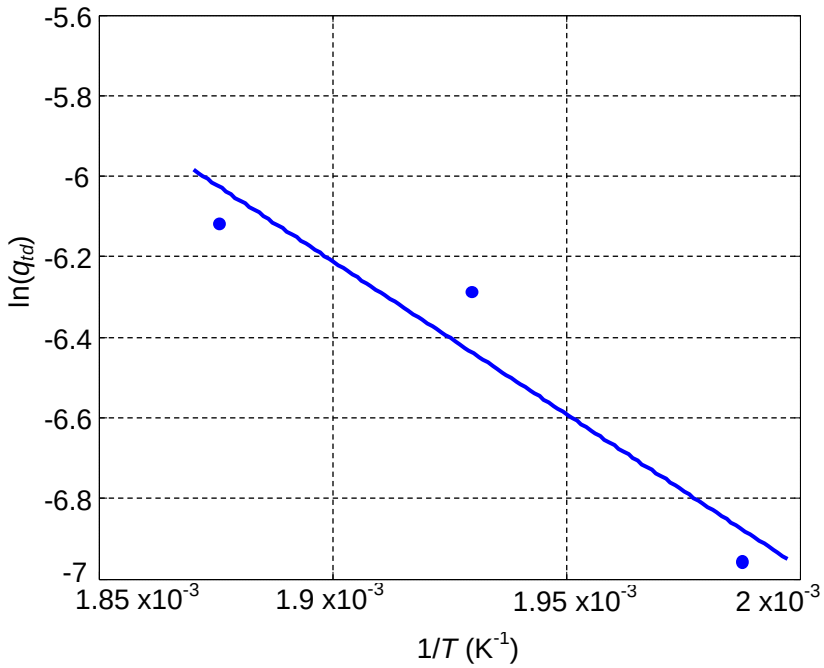

Figure 3-9 Regression of the degradation data

3.5.2 Numerical procedure

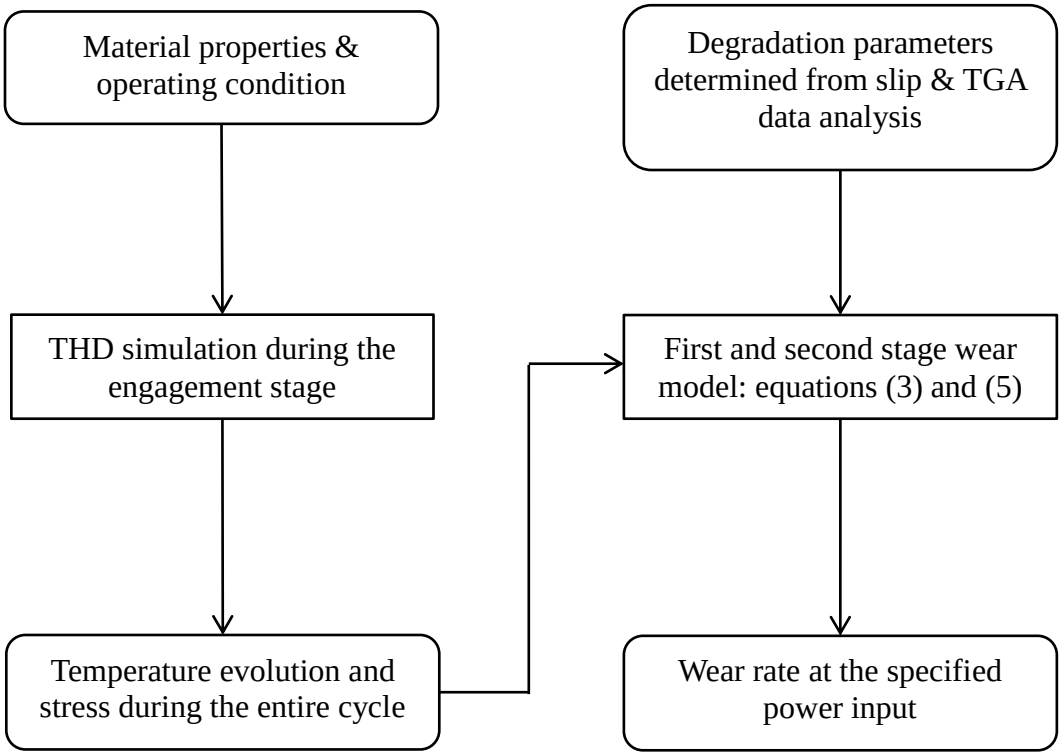

Figure 3-10 Flow chart of wear prediction

Figure 3-10 shows the procedure of wear prediction of the friction material. Since the temperature field in the clutch system is non-homogeneous, an average temperature is not appropriate to be used as input for the wear prediction. In order to obtain the temperature history of a wet clutch, we employed the THD analysis described in [18]. Briefly, the finite difference scheme is used to solve the relevant partial differential equations. The iterative method of successive over-relaxation (SOR) is used to solve the modified Reynolds equation taking squeeze action and surface roughness into account. At each time step the hydrodynamic load and the contact load must strike a balance with the engagement load before proceeding to the next time step. With the ATF flow velocity and heat generation, the temperature field is computed using the alternating direction implicit (ADI) method which provides fast numerical solution with desirable accuracy. When the engagement stage ends, the thermal boundary conditions are switched to convection boundary at the sliding interface. In this fashion the temperature history is obtained for the entire engagement cycle. Having determined the temperature results and the stress conditions, we are able to predict the wear rate with the degradation parameters determined from the regression analysis of test data. Since the wear coefficients K_1 and K_2 depend only on the material properties, they are calibrated through a benchmark case of the lowest energy level.

3.5.3 Verification of engagement simulation

The results of thermohydrodynamic simulations show that upon application of the engagement load, the torque rapidly increases at the beginning of the engagement. Consequently, the film thickness drops quickly, which generates considerable hydrodynamic pressure followed by interaction of surfaces at the asperity level. Therefore, both the hydrodynamic component and the contact component of the torque increase remarkably. However, the relative rotational speed begins to decrease and thus leads, in turn, to reduced hydrodynamic torque. In a short period of time, the film thickness reaches a small value and remains stable with contact torque becoming the major component of the total torque. During the engagement, large amounts of heat are generated at the sliding interface, resulting in a significant rise of the interfacial temperature. The temperature drops slightly in the soaking period during which the clutch is locked to provide transmission power. Afterwards, a significant cooling effect is provided by heat convection that reduces the clutch temperature rapidly.

Table 3-2 lists the input values used in the engagement simulation. Figure 3-11 shows the engagement simulation results along with the experimental measurements by Lingesten, from Lulea University of Technology in Sweden, with the same friction material. Note that the applied pressure is not perfectly fitted by the exponential response function and therefore there is some discrepancy between the computed torque and test measurements at the beginning of the engagement. However its influence on temperature history is negligible. A verification of temperature evolution is illustrated in Figure 3-11(b).

Table 3-2. Input data of engagement simulations

Energy level	Low	Medium	High
Power input (MW/m)	4.6	7.9	9.8
Speed (rpm)	2500	2800	3000
Engagement load (MPa)	1.3	3.3	4.6
Inertia (kg)	0.6764		
Initial temperature (℃)	50±1		
Inner radius (mm)	57.2		
Outer radius (mm)	73.8		
Initial friction lining thickness (mm)	0.5		
Separator disk thickness (mm)	1.75		
Core disk thickness (mm)	1.01		
Initial clearance (mm)	0.2		
Disk pack	2 friction disks and 3 separator plates		

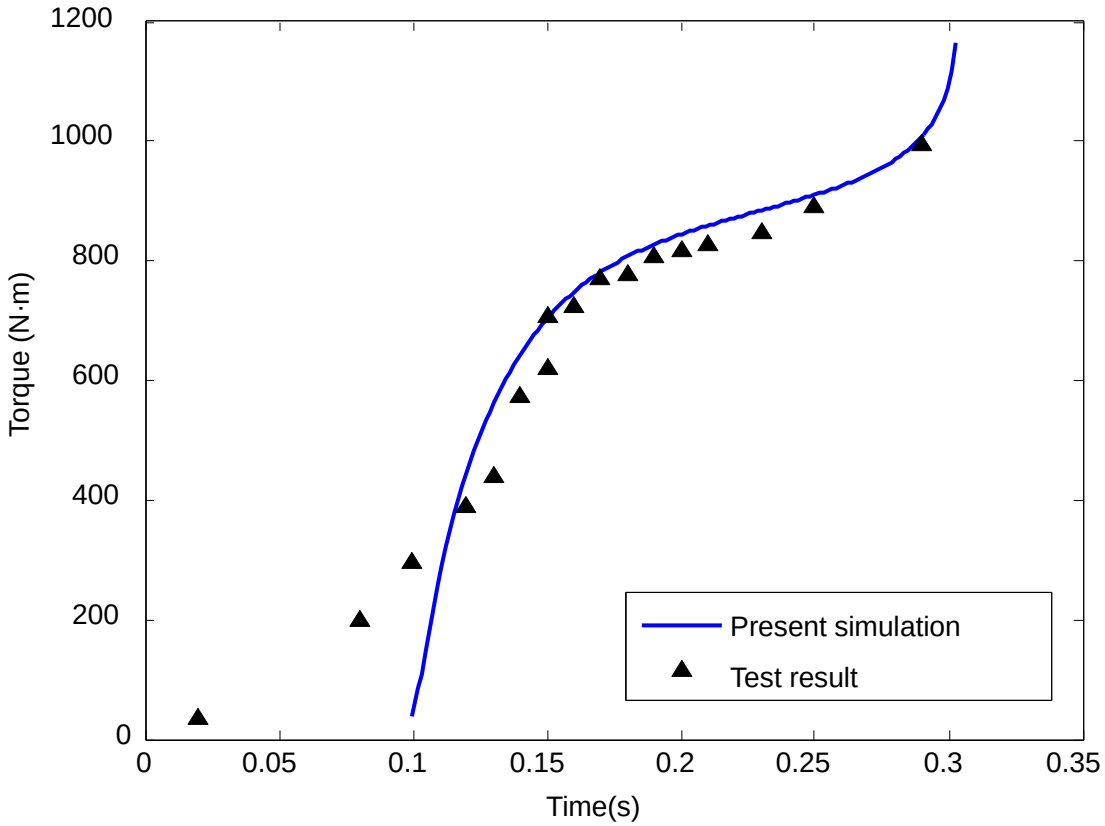

(a) Torque result

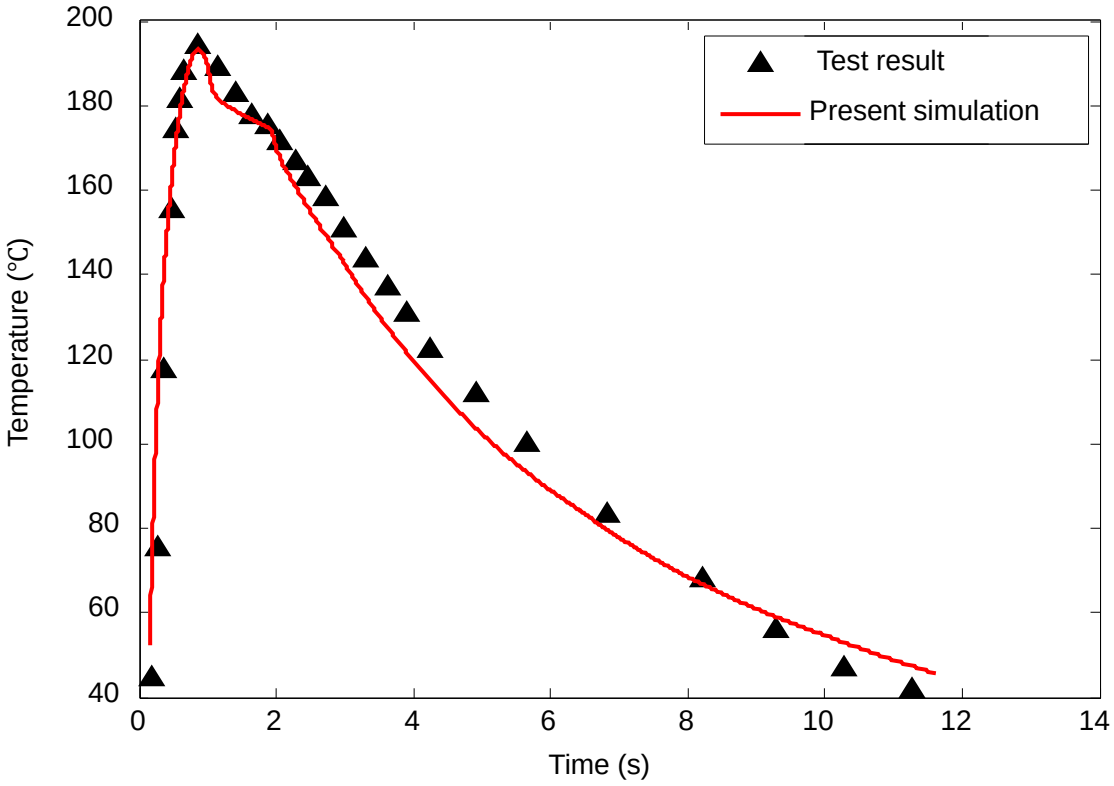

(b) Temperature evolution at the separator disk surface

Figure 3-11 Verification of the engagement simulation with experimental tests provided by Lulea University of Technology

3.5.4 Temperature evolution of different energy levels

The energy level is the most pertinent factor affecting temperature rise in the clutch system. With high engagement load, the film thickness is smaller and more asperity contact is generated. The engagement process also ends very quickly. Concerning the thermal characteristics, larger asperity contacts generate more heat in a shorter time. This is closely related to the power input. For high energy levels at approximately twice the low energy level, the peak temperature during the operation is predicted to increase by 158%, as shown in Figure 3-12.

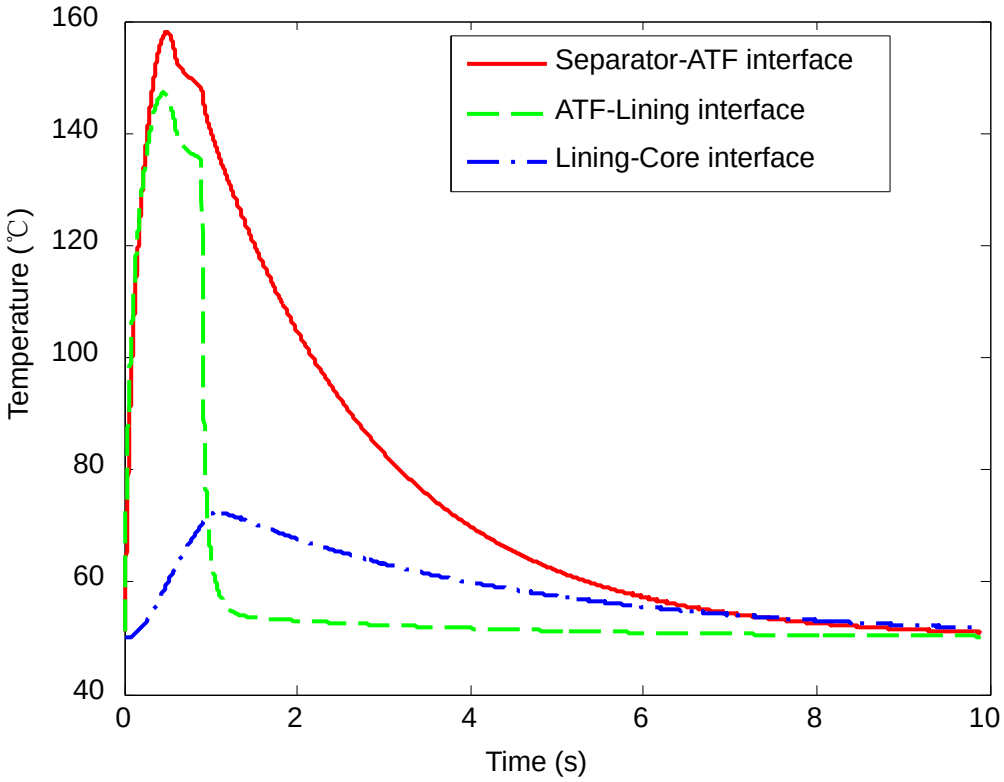

(a) Temperature profile of power input $4.8\ \mathrm{MW/m^2}$

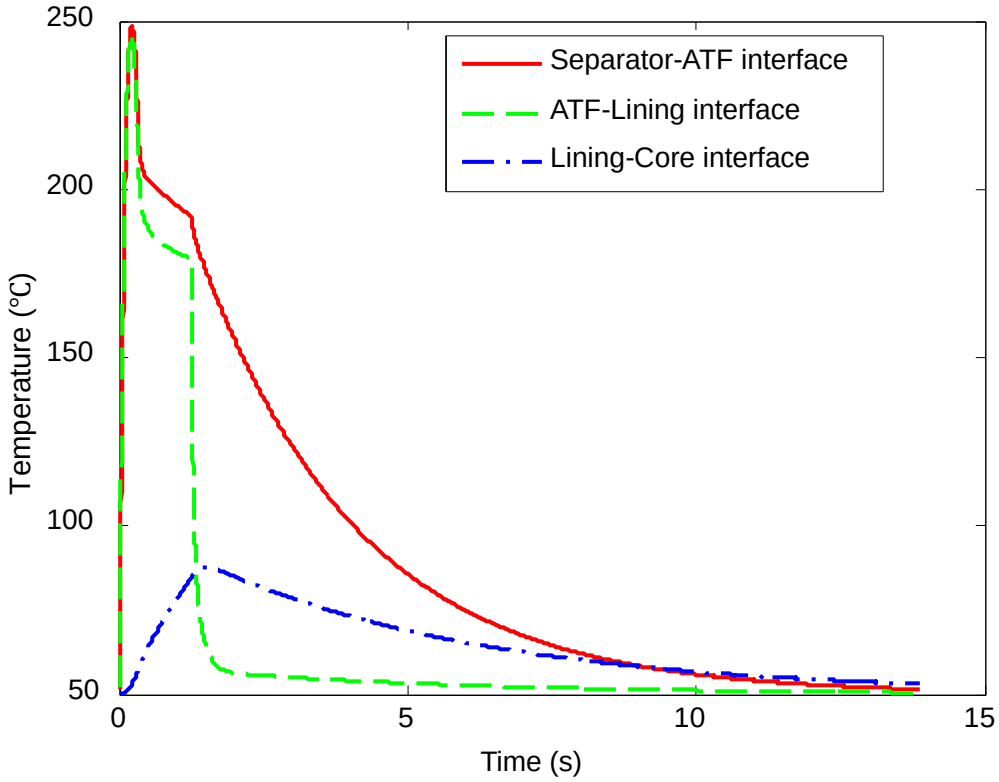

(b) Temperature profile of power input $9.8\ \mathrm{MW/m^2}$

Figure 3-12 Interface temperature profiles with different power input

3.5.5 First stage wear prediction

Figure 3-13 presents verification of the first wear prediction with the test results. In these predictions the first stage wear coefficient K_1 is determined by minimizing the average discrepancy from the test measurement, where $K_1 = 3.881\times10^{3}\ \mathrm{cycle}^{-1}$. Consistent with experimental measurements by Lingesten et al.[12] the wear rate increases with higher energy level.

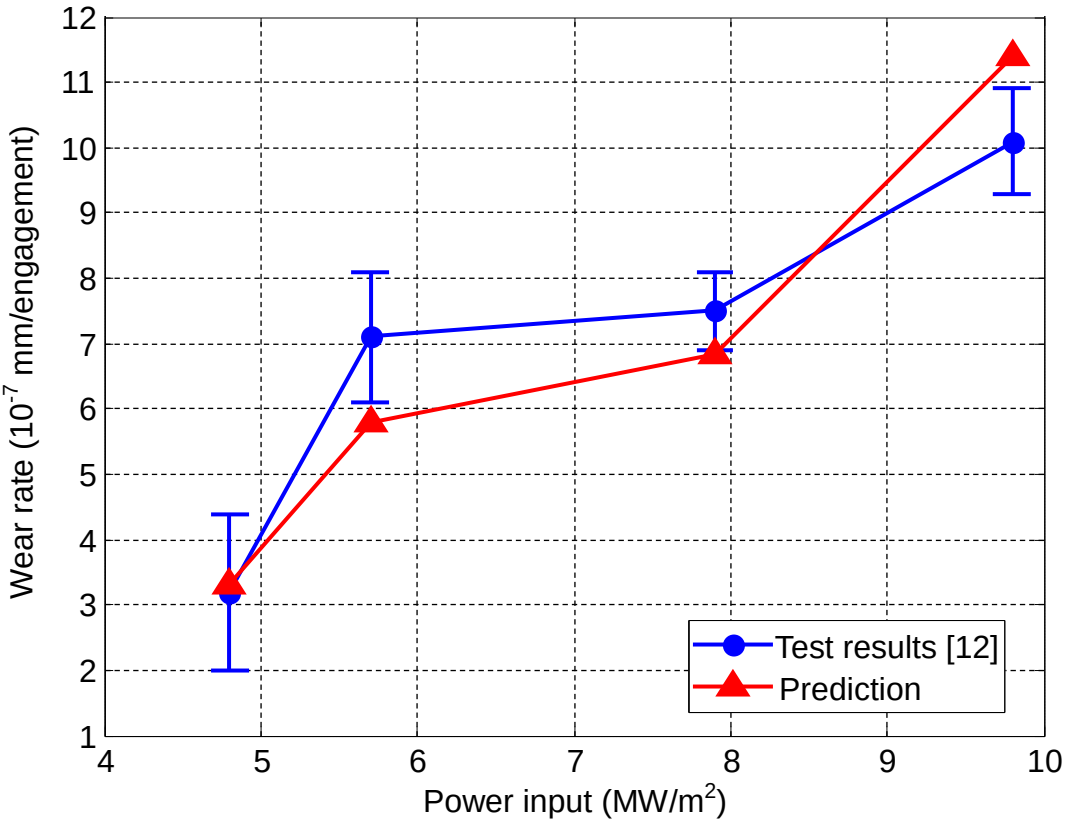

Figure 3-13 First stage wear model prediction and experimental measurements

Due to insufficient input data and possible measurement error of the test described in Section 4.1, the prediction results do not match the experimental measurement perfectly. The discrepancies are related to multiple factors described as follows:

1) Determination of degradation parameters. The parameters in the degradation model are measured through the slip test of pseudo-steady temperature environment. However, the target temperature could not be maintained constant.

2) Engagement simulation. The engagement simulation results and the temperature evolution are sensitive to a variety of input data that are not readily available and had to be estimated because of limited experimental measurements.

3.5.6 Second stage wear prediction

The prediction of the second stage wear is shown in Figure 14. The second stage wear coefficient K_2 and mechanical coefficient γ are obtained in the same fashion as the first stage wear coefficient K_1, where $K_2 = 3.366\times10^{3}$ cycle^{-1} and $\gamma = 1.154\times10^{-4}$ m^3.

The second stage wear rate is roughly 5 to 6 times greater than that of the first stage. It is also noteworthy that the wear rates for the same power input but different operation configurations (essentially, the applied load and the rotational speed) are different as a result of the different engagement time, temperature and the stress conditions.

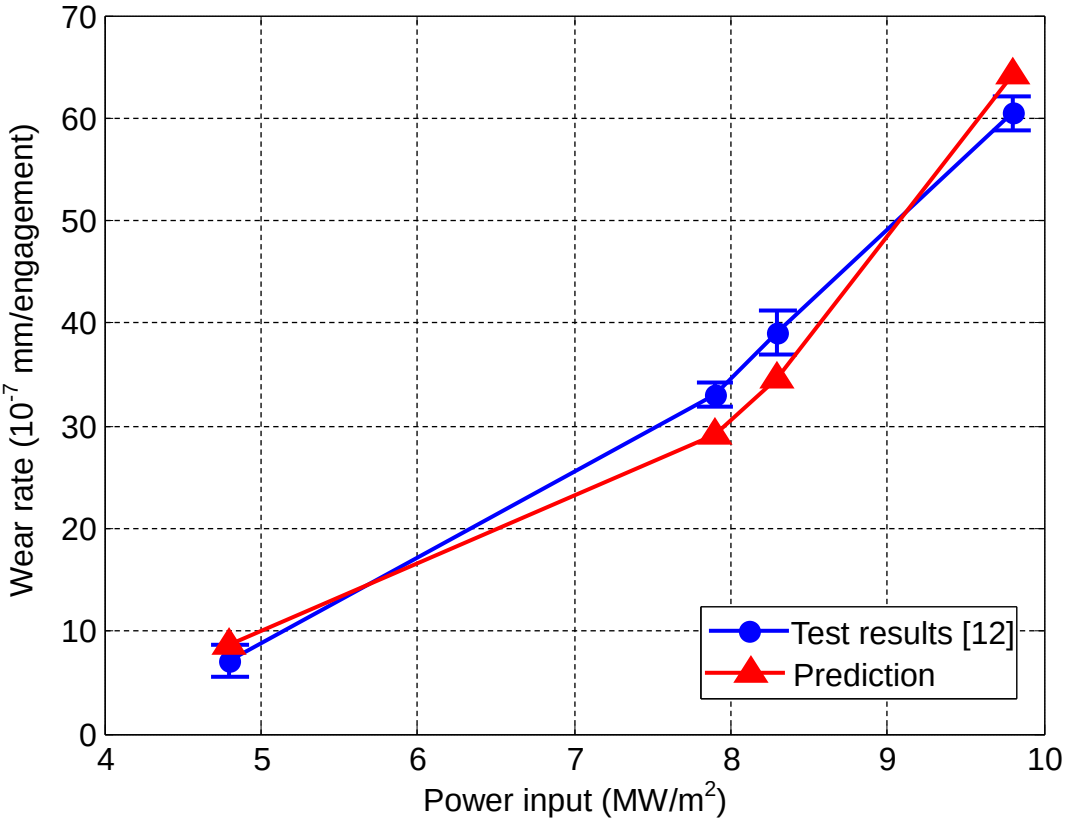

Figure 3-14 Second stage wear model prediction and experimental measurements

As shown in Figure 3-14, the discrepancies of the prediction are larger compared with the first stage results. With more parameter uncertainties involved in the wear model, the prediction is affected by the following factors:

1) The activation energy of the residual organic components, U_2 / R, is not accurately determined by the test procedure described in Section 4.1. Since these components are easily exposed to mechanical wear, the sliding test can lead to extra weight loss that is not generated by pure thermal degradation. Therefore, the method of determining the cellulose activation energy, U_1 / R, is not applicable for the residual organic components.

2) The consideration of mechanical effects is explicitly included in the rate function q_{tmd} by adding the stress term σ. However, determination of the realistic stress distribution is rather complex due to

the rotational motion and the distinctive feature of the friction material (i.e. porous deformable structure and rough surface). This requires a separate research effort of its own [27]. In order to proceed, since the engagement load is generally applied in a uniform way, a viable simplification is done by using the contact pressure to deal with the mechanical consideration, where the elasto-plastic contact model is employed [18].

3) The temperature history also influences the wear prediction in a similar way to the first stage wear. Deviations in the prediction are connected with uncertainties in the input data for the engagement simulation.

3.5.7 Transition of wear stage

As mentioned in Section 3.1, the transition of wear stage takes place within a relative fixed range of thickness reduction. The difference in wear rates of two stages is more obvious for the test of high power input. Figure 3-15 shows wear of friction material subjected to low energy input. In this case, the two-stage wear transition is much less pronounced and not easily detectable. This behavior is due to the fact that the engagement load of low power input does not generate intense stress conditions to increase the wear rate. According to the thermomechanical model, the activation energy U_2 is higher and this yields a more heat-resistant characteristic for the residual material component. Therefore, the overall thermomechanical wear rate is not much higher than the thermal degradation rate of cellulose.

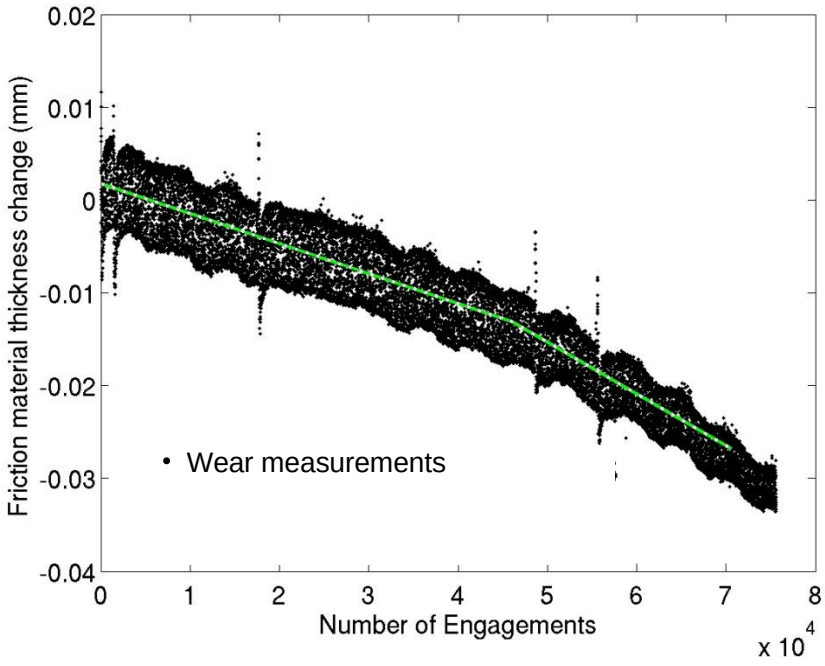

Figure 3-15 Transition of wear stage at low power input of $4.8\ \mathrm{MW/m^2}$ [12]

The engagement number where the wear transition is observed varies for different power input. Test of

long duration can usually capture the complete wear behavior. With known cellulose volume percentage and calculated wear rate, the engagement number of the transition point can be estimated. Table 3-3 shows a comparison between the test measurement and prediction of engagement number where the wear transition takes place.

Table 3-3. Wear transition prediction vs test results in [12]

Power input (MW/m^2)	4.8	5.7	7.9	8.3	9.8
Transition engagement number of test ($\times 10^5$)	4.8-5.0		1.9-2.0	1.8-1.9	1.6-1.7
Transition engagement number of prediction ($\times 10^5$)	5.6	2.6	2.4	2.4	1.8

As a classic theory of wear, Archard's law has been widely used for different materials. However, its application in the wear of friction material encounters difficulty in explaining increase of the wear rate in the second stage. While extensions of Archard's wear model to include oxidation effect exists (see for example, [7]), the multiple stage wear cannot be explained without consideration of both thermal and thermomechanical effects.

3.5.8 Further discussion on varying material properties during the wear process

Figure 3-16 shows the scanning electron microscope (SEM) images of the fresh and worn friction material [12]. Figure 3-17 compares coefficient of friction after 150 and 24,850 engagement cycles [12] during the wear test, showing only slight variation. Although the related model parameters (permeability, surface roughness, etc.) are the necessary input in the THD simulations, further numerical experiment—specifically a sensitivity analysis— demonstrates that the prediction results are not significantly influenced by the limited changes in the friction material properties during the wear process. This explains the observed stable wear rate during the two wear stages. Therefore, reasonably accurate predictions can be obtained using static input data. Pictures of scanning electron microscope (SEM) for the friction material surface are added along with explanation. It should also be noted that there is indeed certain change in roughness parameters for the friction material during the wear process. However, the overall torque and temperature results are not sensitive to these changes. So, variation of surface roughness is not a significant concern in the wear prediction.

Another relevant factor is the consideration of the absorption of ATF in the friction material. This is mainly affected by the permeability, which tends to change during the first wear stage. Nevertheless, the variation in permeability is typically not a major concern because the asperity contact is much more dominating (so the behavior of the engagement results, particularly the torque, is mainly determined by surface roughness contact), and the heat generated by the frictional work (the temperature history is mainly determined by the energy level, i.e. the operation configurations). The reduction in cellulose diminishes the mechanical strength of the friction material so that more wear is induced by mechanical factors. Therefore, compared with the degradation of cellulose that affects the wear rate, such considerations are not significant.

As more information on the nature and transient behavior of the pertinent parameters during repeated full cycle engagement become available, it would be possible to fully investigate their effect during the wear process. Currently, a path forward is to study the effect of parameter variations on simulation by performing a comprehensive sensitivity analysis of all the involved input parameters. Work is in progress toward this objective.

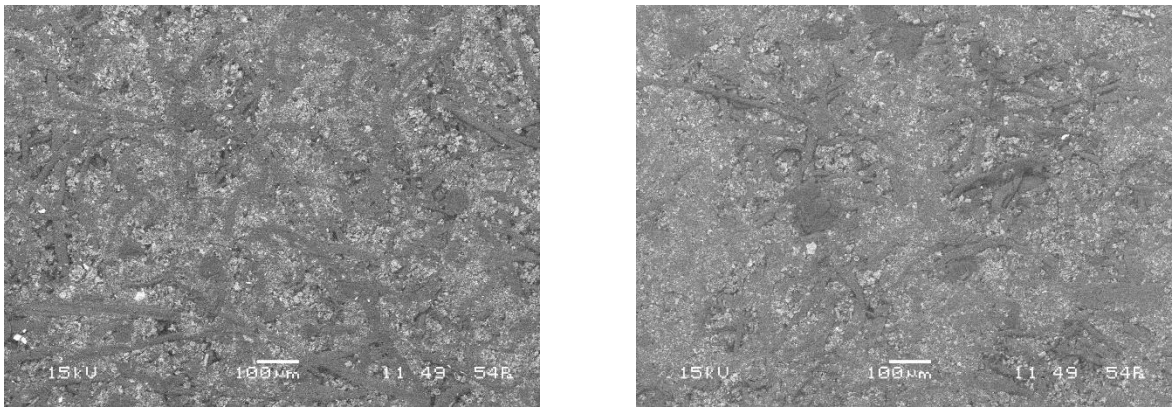

Figure 3-16 SEM of friction material change: fresh (left) and worn (right) [12]

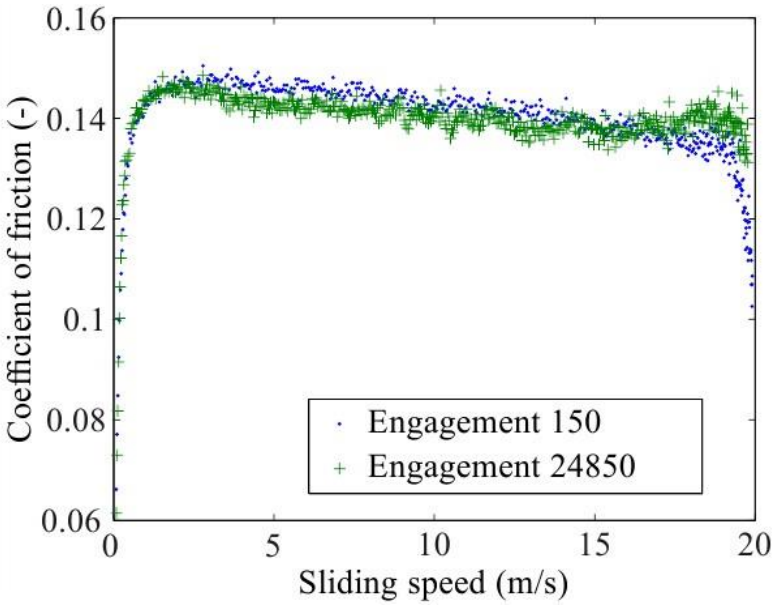

Figure 3-17 Coefficient of friction versus sliding speed undergoing different engagement cycles [12]

3.6 Concluding remarks

A theoretical model of wear is developed for the paper-based friction material of a wet clutch. Recent experimental results reveal that the wear rate during the large engagement cycles shows a “two-stage” behavior. The proposed wear theory provides a prediction that is capable of capturing this trend based on consideration of both thermal degradation and thermomechanical wear of the friction material. With significant thermal conditions during the clutch operation, the cellulose fiber in the friction lining is

firstly degraded and the material strength is impaired. Afterwards, more wear takes place due to further carbonization and intense stress conditions.

The flow chart for prediction of wear and the relevant test procedure are presented. To obtain an accurate temperature history during the entire engagement cycle, the computation incorporates comprehensive tribological modeling of the engagement process and the thermohydrodynamic simulation.

The comparison between wear test results and the prediction results shows a favorable verification in comparison with experimental results. For the wear of both stages the wear rate increases with higher power input. The transition points of wear stages at different energy levels are predicted.

Due to the complexity of engagement simulation and the degradation models, certain deviation from the test result is inevitable. Further quantification of uncertainty in the wear prediction can provide relevant deviation analysis.

3.7 Appendix – derivation of thermomechanical degradation rate

For completeness of the presentation, in this section we provide the derivation of the thermomechanical degradation rate equation based on the work presented in [17]. The rate of crack growth based on the frequency of bond scission and recovery at the tip of crack is [25]:

$$q\left(l,\sigma,T\right)=2\lambda\upsilon_0\exp\left(-\frac{\Delta\Phi^+ +\Delta\Phi^-}{2kT}\right)\sinh\left(-\frac{\Delta\Phi^+ -\Delta\Phi^-}{2kT}\right) \tag{7}$$

where λ is the fluctuation advance of the crack, υ_0 is the frequency of thermal oscillations of kinetic units participating in bond scission and recovery, $\Delta\Phi^+$ is thermodynamic potential of bond scission, and $\Delta\Phi^-$ is thermodynamic potential of bond recovery.

The thermodynamic potential $\Delta\Phi$ of a stressed polymer sample with a surface crack of length l increases during crack propagation, which is calculated by:

$$\Delta\Phi\left(l,\sigma,T\right)=\Delta\Phi_y\left(l,\sigma,T\right)+\Delta\Phi_\pi\left(l,\sigma,T\right) \tag{8}$$

where $\Delta\Phi_y$ is the increase in the thermodynamic potential of the sample due to the presence of a crack, $\Delta\Phi_\pi$ is the increase in the thermodynamic potential of sample resulting from formation of new free surfaces, $\Delta\Phi_y$ is calculated from the strain energy stored in the crack of length l:

$$\Delta\Phi_y=-\frac{\pi\sigma^2l^2}{2E} \tag{9}$$

$\Delta\Phi_\pi$ is calculated by [28]:

$$\Delta\Phi_\pi\left(l,\sigma,T\right)=2\int_{l_0}^{l}\alpha_\pi^*\left(\sigma^*\right)dl=2\alpha_\pi^*\left(l-l_0\right)-2\lambda_m\int_{l_0}^{l}\sigma^*\left(l,\sigma\right)dl \tag{10}$$

where l_0 is the original length of the crack, $\alpha_\pi^*(\sigma^*)$ is the formation energy for a unit of new surface, σ^* is the local stress, λ_m is the coefficient characterizing the effect of local stress on the magnitude of surface tension.

Therefore, we have:

$$\Delta\Phi(l,\sigma,T) = -\frac{\pi\sigma^2 l^2}{2E} + 2\alpha_\pi^*(l-l_0) - 2\lambda_m\int_{l_0}^{l}\sigma^*(l,\sigma)dl \tag{11}$$

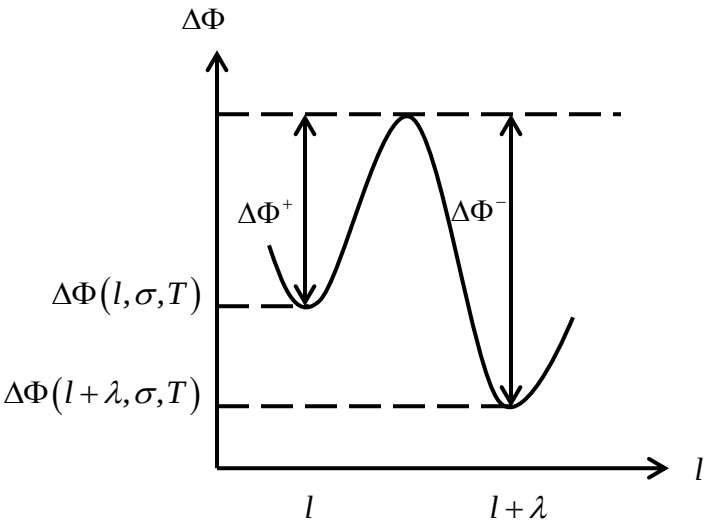

Figure 3-18 Thermodynamic potential during crack propagation [25]

For the rate of crack growth, we have:

$$\begin{aligned}\Delta\Phi^+ - \Delta\Phi^- &= \lambda_\pi\left[\Delta\Phi(l,\sigma,T) - \Delta\Phi(l+\lambda,\sigma,T)\right] \\ &\approx -\lambda\lambda_\pi\frac{\partial\Delta\Phi}{\partial l} \\ &= \lambda\lambda_\pi\left(\frac{\pi\sigma^2 l}{E} - 2\alpha_\pi^* + 2\lambda_m\sigma^*\right)\end{aligned} \tag{12}$$

where λ_π is the fluctuation advance of the crack

On the other hand, $\Delta\Phi^+$ and $\Delta\Phi^-$ can be written as [2]:

$$\Delta\Phi^+ = U - \lambda\lambda_\pi\frac{\pi\sigma^2 l}{2E} - \lambda\lambda_\pi\lambda_m\sigma^* \tag{13}$$

$$\Delta\Phi^- = U' + \lambda\lambda_\pi\frac{\pi\sigma^2 l}{2E} + \lambda\lambda_\pi\lambda_m\sigma^*$$

where U and U' are the activation energy by kinetic units during bond scission and recovery which satisfy:

$$U' - U = 2\lambda\lambda_\pi\alpha_\pi \tag{14}$$

$$\begin{aligned} q(l,\sigma,T) &= 2\lambda\upsilon_0 \exp\left(-\frac{U-\lambda\lambda_\pi\alpha_\pi}{kT}\right)\sinh\left(\frac{\lambda\lambda_\pi\lambda_m\sigma^* - \lambda\lambda_\pi\alpha_\pi}{kT} + \frac{\lambda\lambda_\pi\pi\sigma^2 l}{2EkT}\right) \\ &\approx \lambda\upsilon_0 \exp\left(-\frac{U-\lambda\lambda_\pi\lambda_m\sigma^* - \lambda\lambda_\pi\pi\sigma^2 l/2E}{kT}\right) \\ &= \lambda\upsilon_0 \exp\left(-\frac{U_0 - \gamma\sigma^*}{kT}\right) \end{aligned} \tag{15}$$

where

$$U_0 = U - \lambda\lambda_\pi\pi\sigma^2 l/2E$$

$$\gamma = \lambda\lambda_\pi\lambda_m$$

3.8 References

[1] M. Amiri, M.M. Khonsari, On the thermodynamics of friction and wear—a review, Entropy, 12 (2010) 1021-1049.

[2] A. Beheshti, M. Khonsari, An engineering approach for the prediction of wear in mixed lubricated contacts, Wear, 308 (2013) 121-131.

[3] A. Hollander, J. Lancaster, An application of topographical analysis to the wear of polymers, Wear, 25 (1973) 155-170.

[4] B.-B. Jia, T.-S. Li, X.-J. Liu, P.-H. Cong, Tribological behaviors of several polymer–polymer sliding combinations under dry friction and oil-lubricated conditions, Wear, 262 (2007) 1353-1359.

[5] N. Myshkin, M. Petrokovets, A. Kovalev, Tribology of polymers: adhesion, friction, wear, and mass-transfer, Tribology International, 38 (2006) 910-921.

[6] Y. Yang, R.C. Lam, Theoretical and experimental studies on the interface phenomena during the engagement of automatic transmission clutch, Tribology Letters, 5 (1998) 57-67.

[7] M. Watson, C. Byington, D. Edwards, S. Amin, Dynamic modeling and wear-based remaining useful life prediction of high power clutch systems, Tribology Transactions, 48 (2005) 208-217.

[8] J. Jang, M. Khonsari, A generalized thermoelastic instability analysis, Proceedings of the Royal Society of London. Series A: Mathematical, Physical and Engineering Sciences, 459 (2003) 309-329.

[9] J. Jang, M. Khonsari, On the formation of hot spots in wet clutch systems, Journal of tribology, 124 (2002) 336-345.

[10] J. Jang, M. Khonsari, Thermoelastic instability with consideration of surface roughness and hydrodynamic lubrication, Journal of tribology, 122 (2000) 725-732.

[11] J. Jang, M. Khonsari, On the growth rate of thermoelastic instability, Journal of tribology, 126 (2004) 50-55.

[12] N. Lingesten, Wear behavior of wet clutches, (2012).

[13] S. Natsumeda, T. Miyoshi, Numerical simulation of engagement of paper based wet clutch facing, Journal of tribology, 116 (1994) 232-237.

[14] E. Berger, F. Sadeghi, C. Krousgrill, Finite element modeling of engagement of rough and grooved wet clutches, Journal of Tribology, 118 (1996) 137-146.

[15] J. Jang, M. Khonsari, Thermal characteristics of a wet clutch, Journal of tribology, 121 (1999) 610-617.

[16] J. Jang, M. Khonsari, R. Maki, Three-dimensional thermohydrodynamic analysis of a wet clutch with consideration of grooved friction surfaces, Journal of tribology, 133 (2011).

[17] P. Marklund, R. Mäki, R. Larsson, E. Höglund, M.M. Khonsari, J. Jang, Thermal influence on torque transfer of wet clutches in limited slip differential applications, Tribology international, 40 (2007) 876-884.

[18] M. Li, M. Khonsari, D. McCarthy, J. Lundin, Parametric analysis for a paper-based wet clutch with groove consideration, Tribology International, (2014).

[19] J. Jang, M. Khonsari, Wet Clutch Friction Material: The Surfaced Groove Effect, Encyclopedia of Tribology, Springer, 2013, pp. 4102-4108.

[20] M. Holgerson, J. Lundberg, Engagement behaviour of a paper-based wet clutch Part 2: Influence of temperature, Proceedings of the Institution of Mechanical Engineers, Part D: Journal of Automobile Engineering, 213 (1999) 449-455.

[21] M. Holgerson, J. Lundberg, Engagement behaviour of a paper-based wet clutch Part 1: Influence of drive torque, Proceedings of the Institution of Mechanical Engineers, Part D: Journal of Automobile Engineering, 213 (1999) 341-348.

[22] P. Marklund, R. Larsson, Wet clutch under limited slip conditions-simplified testing and simulation,

Proceedings of the Institution of Mechanical Engineers, Part J: Journal of Engineering Tribology, 221 (2007) 545-551.

[23] I.G. Goryacheva, Contact mechanics in tribology, Springer, 1998.

[24] L.A. Sosnovskiy, R. Sosnovskaya, K. Frolov, N. Makhutov, Tribo-fatigue: Wear-fatigue Damage and Its Prediction, Springer, 2010.

[25] E. Kartashov, V. Shevelev, A.A. Valishin, G. Bartenev, Limiting characteristics of brittle fracture of polymers, Polymer Science USSR, 28 (1986) 899-905.

[26] A. Chichinadze, Fundamentals of Tribology, Science and Technology, Moscow, (1995) 778.

[27] J. Moraleda, J. Segurado, J. Llorca, Finite deformation of porous elastomers: a computational micromechanics approach, Philosophical Magazine, 87 (2007) 5607-5627.

[28] G. Bartenev, Y.S. Zuev, Strength and Fracture of High-Elastic Materials, Moscow-Leningrad, 342 (1964) 343.

CHAPTER 4 MODEL VALIDATION AND UNCERTAINTY ANALYSIS IN THE WEAR PREDICTION OF A WET CLUTCH [3]

4.1 Nomenclature

c = heat capacity (J/kg K)

d = disk thickness (m)

d^* = area validation metric (same unit with SRQ)

E = elastic modulus (Pa)

f = friction coefficient

h = convection coefficient (W/m^2 K)

H = thickness of the friction lining (m)

ΔH_i = wear rate (m/cycle)

I = inertia of friction disk

k = conductivity (W/m K)

K_i = wear coefficient (1/cycle)

P_0 = engagement load (MPa)

n = surface asperity density (m^{-2})

q = frictional heat flux (W/m^2)

R = Boltzmann constant (J/K)

R_i = inner radius (m)

R_o = outer radius (m)

T = temperature (K)

Δt = duration of an engagement cycle (s)

U = activation energy (J)

$\overline{\Theta}$ = dimensionless temperature

ω_L = angular speed of separator disk (rpm)

ω_H = angular speed of friction disk (rpm)

β = asperity radius (m)

ε = compressive strain of the friction lining

η = numerical precision of MC simulation

γ = asperity tip radius (m)

κ = thermal diffusivity (m^2/s)

σ = standard deviation of surface heights (m)

μ = viscosity (Pa s)

ρ = density (kg/m^3)

[3] Reprinted by permission of Wear

θ_0 = section angle

4.2 Introduction

The study of wear of the friction lining in a wet clutch has long been of interest to the tribology community because of its critical role in vehicle transmission and the overall durability of the drivetrain. Experimentally, Lingesten et al. [1] reported an intriguing two-stage wear behavior after a large number of engagement cycles that had not been observed before. Subsequently, Li et al. [2] developed a model with the relevant degradation mechanisms to explain the change in the wear rates during the cycles and to provide predictions with different power inputs. While the general trend and magnitude of the predictions yielded satisfactory results compared with experiments, some discrepancies remain that are attributed to the uncertainty in the input data. In this paper, we perform statistical interpretation of the model to gain better insight for such consideration. According to Roy and Oberkampf [3], a direct figure comparison between test and simulation is insufficient for the verification and validation framework because it gives little information on the extent of agreement that depends on the uncertainties involved in both test and simulation. In contrast, the statistical methods and relevant computation usually work better for quantification purpose.

The predicted wear rate, which is the system response quantity (SRQ) of interest, is influenced by various sources of uncertainties: model inputs, model form, and accuracy of numerical solution. Compared with deterministic simulations, the computational costs in uncertainty quantification are much greater. For quantitative characterization, these uncertainties are recognized as either “aleatory” or “epistemic”. Aleatory uncertainties emerge from the inherent randomness in the experimental measurements (precision errors) of the input data. For a sufficiently large sample, it follows a distribution that can be described by the probability density function (PDF) or cumulative distribution function (CDF). Epistemic – also called ignorance uncertainty or reducible uncertainty – is generated due to the lack of knowledge, which could possibly be eliminated by obtaining additional experimental data or performing theoretical analyses. Usually the epistemic uncertainty is irrelevant to specific PDF and is thought to be any value in the interval of equivalent probability. These sources of uncertainties can be estimated for evaluating the total variation in the simulation. For this purpose, Monte Carlo (MC) methods are widely used for stochastic computations. With the deterministic system with random input data, the repeated sampling of relevant distribution would calculate the variation in the predictions. We apply the MC method because of its simplicity, robustness and the fact that with access to high performance computing recourses, the numerical experiments necessary for prediction of wear will not become prohibitively expensive.

Composed of a series of separator disks, automatic transmission fluid (ATF) and friction material bonded to core disks, a wet clutch system is a complex device whose performance characteristics depends on multiple, coupled physical effects involved during the operational cycles. The friction material is paper-based type and is porous, rough, and deformable. Once squeezed under the applied engagement load, it experiences micro asperity contact with the separator disk at the surface asperity

level. As a result, a large amount of heat is generated at the sliding interface. The lubricant, i.e. ATF, produces hydrodynamic pressure and the cooling action by the flow of lubricant that reduces the overall temperature. The engagement behavior and the temperature profile are closely related to different material properties and operational configurations. For prediction of the friction lining wear after multiple engagement cycles, thermal degradation and thermomechanical wear must be properly taken into account. These factors depend on the temperature history and the stress conditions during the engagement cycle and, therefore, the investigation of SRQ with respect to model parameters and the uncertainty quantification can potentially contribute to more complete knowledge of the clutch model and the quality of wear prediction.

This paper presents the framework for the verification, validation, and uncertainty quantification (VV&UQ) in the application of wear prediction in a wet clutch. First, in Section 2, the procedure of computerized prediction is presented to give an overview of deterministic simulation, including comprehensive modeling, numerical error analysis and the sensitivity of SRQ to model parameters. In Section 3, the sources of uncertainty in model and test are discussed and characterized. The relevant validation metric results are presented in Section 4 through the MC simulation. The paper ends with summary and concluding remarks in Section 5.

4.3 VV&UQ framework for computerized wear prediction

While a test rig designed and operated by Lingesten et al. [1] is available to measure the wear of the friction lining, the costs involved in time and recourses motivate a reliable computational model. If successful, accurate predictions will complement physical testing and allow further consideration of different wear factors, including energy levels, groove design, and material properties.

A flow chart demonstrating the procedure of wear prediction with model validation and uncertainty quantification is shown in Figure 4-1. Based on the two-stage wear observations by Lingesten et al., the degradation mechanism of wear translates into the material's thickness reduction as a function of the energy level and the stress conditions. Thus, an engagement modeling is necessary to compute the wear rate by obtaining the thermal and mechanical conditions [2]. As shown in [4], a thermohydrodynamic (THD) analysis is needed to accurately predict the behavior of the lubricant. However, given the complexity of the model and limited inputs, a simplified heat transfer model is initially used to investigate the effectiveness of wear modeling as preliminary analysis. Next, based on the obtained information, the simulation is improved by the implementation of a comprehensive THD model. With sufficient accuracy and appropriate simplified assumptions, an optimal model is proposed to effectively achieve the prediction purpose. The last, but an important step, is validation of the model by using statistical analysis, which provides SRQ variation over the uncertainties involved in model and inputs. The above procedure is generally applicable for many other engineering simulations.

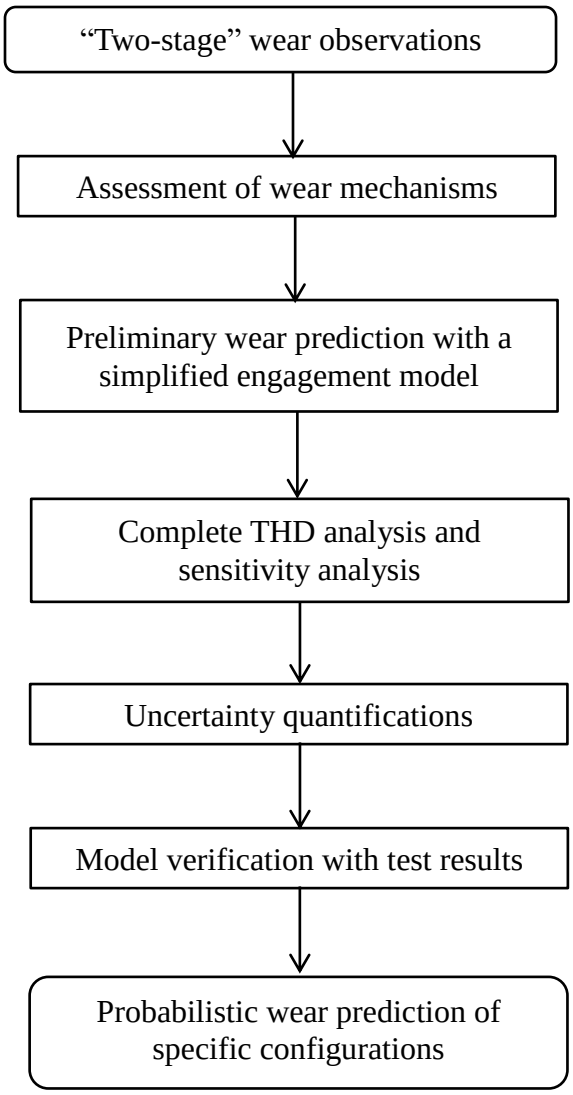

Figure 4-1 Flow chart of computerized wear prediction

4.3.1 "Two-stage" wear observations and wear mechanism

Figure 4-2 shows the observed "two-stage" wear behavior of the friction material during the engagement in a wet clutch experiments as reported by Lingesten et al. [1]. It reveals that the thickness of the friction lining is initially reduced at a low rate and later, after a certain number of engagements, is transitional to a faster – but still steady – wear rate.

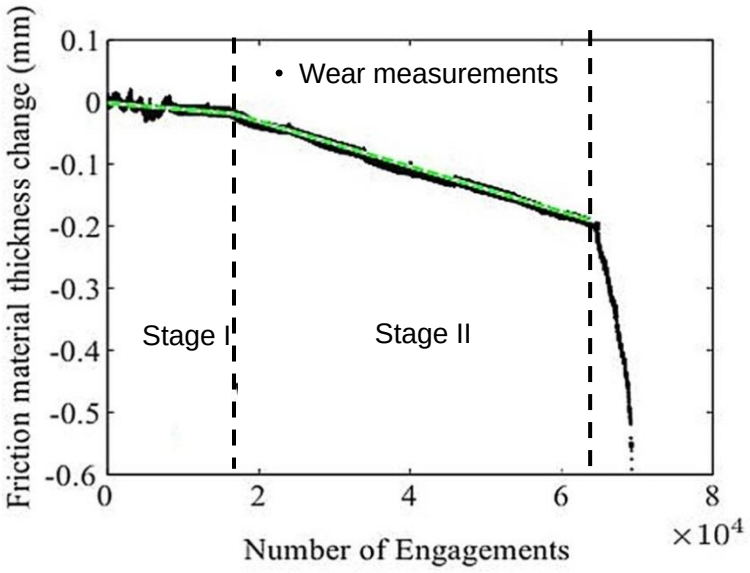

Figure 4-2 A "two-stage" wear behavior during the engagement [1]

According to Li et al. [2], the cumulative thermal degradation of the cellulose fiber is responsible for the reduction of the friction lining volume during the first wear stage. The change in thickness can be described by the following equation

$$\Delta H_1 = K_1 \int_0^H dz \int_0^{\Delta t} \exp\left(-\frac{U_1}{RT(z,t)}\right) dt \tag{1}$$

where K_1 represents the wear coefficient for the first stage, R is the Boltzmann's constant, U_1 is the activation energy of cellulose, $T(z,t)$ denotes the temperature distribution, H is the thickness of the friction lining, and Δt is duration of an engagement cycle.

With large cellulose consumption under intense thermal conditions during the engagement cycles (the temperature increment reaches more than 200 ℃ in less than 2 seconds [2, 4, 5]), a second wear stage is initiated by additional mechanical factors. Similar to the first stage wear model, the further reduction in the thickness of the friction material during the second wear stage is estimated by considering temporal and spatial integration of the degradation rate.

$$\Delta H_2 = K_2 \int_0^H dz \int_0^{\Delta t} \exp\left(-\frac{U_2 - \gamma\sigma}{RT(z,t)}\right) dt \tag{2}$$

where K_2 represents the second stage wear coefficient, γ is the material mechanical property (related to the Poisson's ratio and Young's modulus), σ is the stress field, and U_2 is the activation energy of heat-resistant components, including the binder, and the polymeric fiber, etc. in the friction material.

4.3.2 Simplified engagement modeling: a preliminary analysis

To predict wear rate, the temperature and stress conditions during the engagement cycle are needed. A brief description is given next to understand the operational and thermal behavior of a wet clutch. The full engagement cycle consists of four stages: engagement, soak, dwell, and stabilization. During the engagement stage, the contact pressure by asperities is increased to strike a balance with the applied load. Meanwhile, temperature rises rapidly through the frictional work at the sliding interface of the friction pair. At the end of the engagement and throughout the soak stage, the friction pair is locked up and the transmission power is delivered. The clutch system is then cooled down by air convection during the dwell stage and ATF flow in the stabilization stage when the clearance of the friction pair is restored to the initial value. A more detailed description of the thermal behavior during the operational cycle can be referred to [4].

Assuming that the contact pressure is approximately equal to the average engagement load P_0 and using a 1-D heat transfer model that considers conduction between the friction lining and the core disk, one can obtain an approximate temperature profile during the engagement cycle. Neglecting the viscous shearing torque that involves the film thickness calculation, we have:

$$\frac{fF_N\pi\left(R_o^3-R_i^3\right)}{3}=I\frac{d\omega}{dt} \tag{3}$$

where f is the friction coefficient, F_N is the engagement load, R_o and R_i are the outer radius and inner radius of the friction disk, I is the inertia and ω is the relative rotational speed of the friction pair. The engagement time can be estimated by solving this simple ordinary equation.

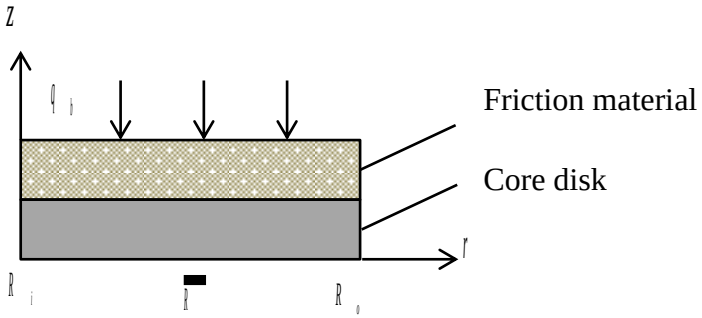

Figure 4-3 1-D heat transfer model of a wet clutch

Figure 4-3 illustrates the simplified 1-D heat transfer model to compute the temperature profile. By considering only the heat conduction in the friction lining and the core disk, the thermal model is simplified as:

$$\frac{\partial\overline{\Theta}_b}{\partial\bar{t}}+F_b\frac{B_b\overline{u}_z}{1-\varepsilon}\frac{\partial\overline{\Theta}_b}{\partial\bar{z}_b}-D_b\left(\frac{B_b}{1-\varepsilon}\right)^2\frac{\partial^2\overline{\Theta}_b}{\partial\bar{z}_b^{-2}}=0 \quad \text{(friction lining)}$$

$$\frac{\partial \bar{\Theta}_c}{\partial \bar{t}} - D_c B_c^2 \frac{\partial^2 \bar{\Theta}_c}{\partial \bar{z}_c^2} = 0 \text{ (core disk)}$$

$$\xi_b \frac{\partial \bar{\Theta}_b}{\partial \bar{z}_b} = \bar{q}_b = \frac{\bar{q}}{1+s} = \frac{f \bar{r} \bar{\Delta\omega} \bar{P}_c}{1+s} \quad \text{(sliding interface during engagement)}$$

$$\frac{\partial \bar{\Theta}_b}{\partial \bar{z}_b} = H_b \left(\bar{\Theta}_b - \Theta_\infty \right) \quad \text{(convection boundary during dwell and stabilization period)}$$

$$\frac{\partial \bar{\Theta}_b}{\partial \bar{z}_b} = \frac{k_b d_c}{k_c d} \frac{\partial \bar{\Theta}_c}{\partial \bar{z}_c} \text{ (core disk-friction lining interface)}$$

$$\frac{\partial \bar{\Theta}_c}{\partial \bar{z}_c} = 0 \quad \text{(insulation boundary of core disk)} \tag{4}$$

where $\bar{\Theta}$ denotes the dimensionless temperature, q is the heat generation at the sliding interface of the friction pair, q_b is the heat flux into the friction lining, k is conductivity, d is disk thickness, $\varepsilon = \frac{P_0}{E}$, $s = \frac{k_s}{k_b}\sqrt{\frac{\kappa_b}{\kappa_s}}$, $D_b = \frac{\kappa_b}{\omega_H R_o^2}$, $F_b = \frac{\rho_f c_f}{\rho_b c_b}$, $\bar{z}_b = \frac{z_b}{d(1-\varepsilon)}$, $D_c = \frac{\kappa_c}{\omega_H b^2}$, $H_b = \frac{R_o}{k_b} h_{conv}$, and $\bar{z}_c = \frac{z_c}{d_c}$.

Table 4-1. Input data for simplified engagement simulation

Input parameters	value
Outer radius R_o (m)	0.0738
Inner radius R_i (m)	0.0572
Inertia I (kg m^2)	0.6764
Number of friction disk	2
Friction lining thickness d_b (m)	0.0005
Core disk thickness d_c (m)	0.001
Friction lining conductivity k_b (W/mK)	0.75
Friction lining specific heat κ_b (J/kg.K)	1200
Friction lining density ρ_b (kg/m^3)	1800
Steel conductivity k_c (W/mK)	46.04
Steel heat capacity κ_c (J/kg.K)	490
Steel density ρ_c (kg/m3)	8050
Initial temperature (℃)	50
Convection coefficient during soak period (W/ m 2K)	20
Convection coefficient during dwell period (W/ m 2K)	500

(Table 4-1 continued)

Convection coefficient during stabilization period (W/ m ₭K)	500
Soak duration (s)	0.4
Dwell duration (s)	1.9
Stabilization duration (s)	7

Solving equations (4) using the finite difference method (FDM) and using the input data of Table 1, the temperature profile at the mean radius $\bar{R}$ of the friction lining is predicted as shown in Figure 4-4. Using the wear model of equation (1) and (2), the wear prediction result is presented in Figure 4-5, where the power input is determined by the engagement load and rotational speed of operational configuration.

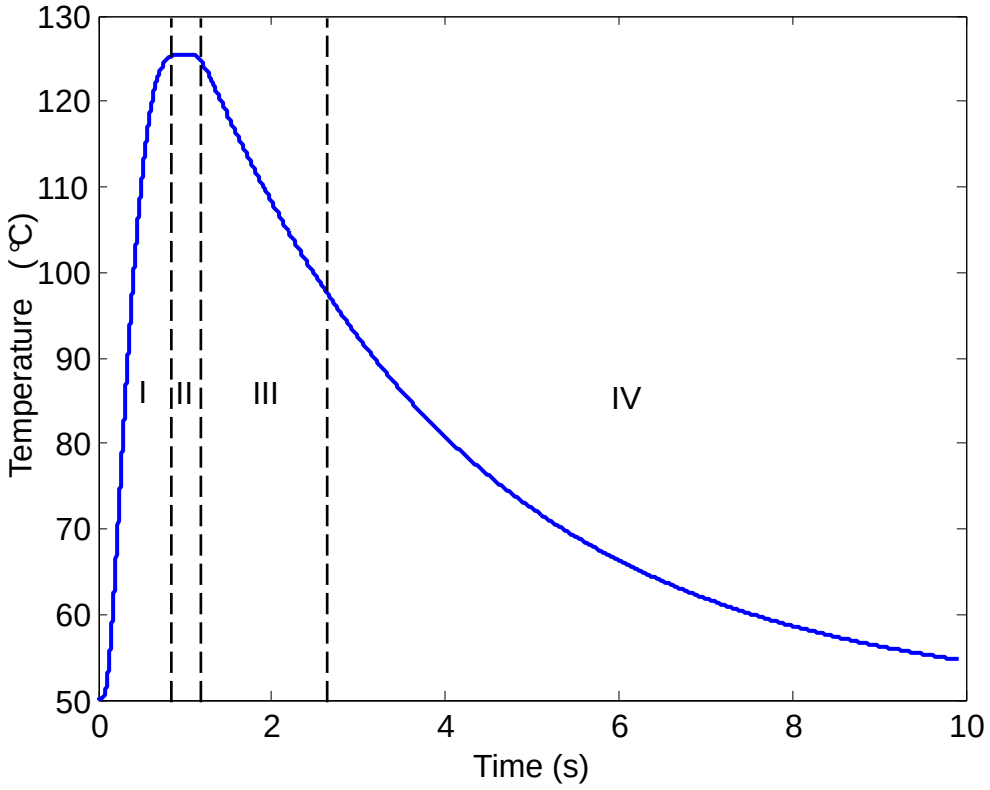

Figure 4-4 Temperature evolution by simplified engagement model (I – engagement stage, II – soak stage, III – dwell stage, IV – stabilization stage)

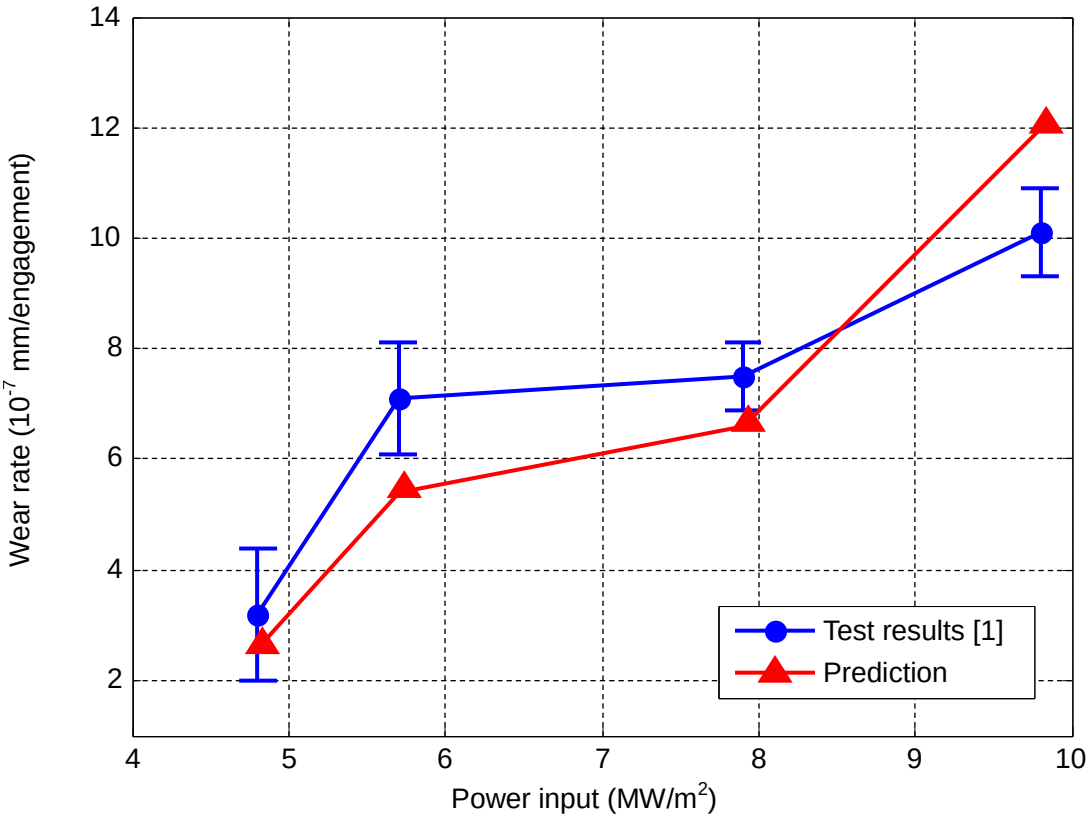

Figure 4-5 First stage wear prediction validation based on simplified engagement model

Such a preliminary model is useful for a rough estimation of wear rate by knowing fundamental information of material properties. Compared with the wear prediction in [2] involving a comprehensive THD analysis, the one-dimensional model provides a fairly reasonable characterization of the wear behavior, especially for the low and medium input energy levels. For high input power case, the temperature obtained using the simplified model is higher than the actual value because the convection at the inner and outer rim is neglected. Therefore, the predicted wear rate is greater than the measured values. It is also important to note that the 1-D heat transfer model cannot adequately predict the thermal conditions of a friction material with different groove designs, so a full THD analysis described in the next section is needed to investigate the wear behaviors.

4.3.3 THD analysis

Compared with the simplified engagement modeling presented in Section 2.1, the THD analysis provides more accurate results of thermal behavior using a three-dimensional heat transfer model including ATF, the separator disk, the core disk and the friction lining [4]. Hydrodynamic pressure of the lubricant is computed by solving the modified Reynolds equation that considers surface roughness, squeeze motion and slip boundary for the friction lining. Temperature distribution of ATF is computed by the energy equation. The heat conduction equations are used to determine the temperature of the steel

disks and the friction material. The modified Reynolds equation is solved by the successive over-relaxation (SOR) method and the 3-D heat transfer equations are solved by implementing the alternating direction implicit (ADI) method. Detailed description of the numerical scheme is given in [4] and verification of engagement results with test is shown in [2]. Figure 4-6 presents the temperature evolution at the interfaces of clutch components during the engagement cycle using the input values in Table 4-1.

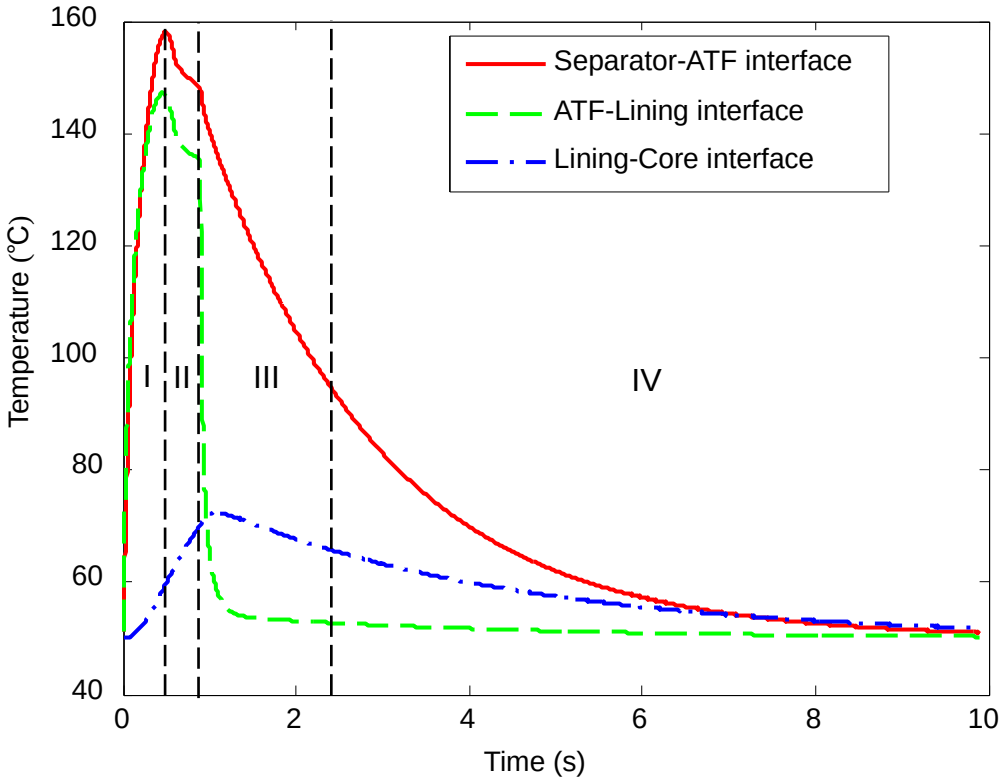

Figure 4-6 Temperature evolution of clutch components with power input of 4.8 MW/m^2 (I – engagement stage, II – soak stage, III – dwell stage, IV – stabilization stage)

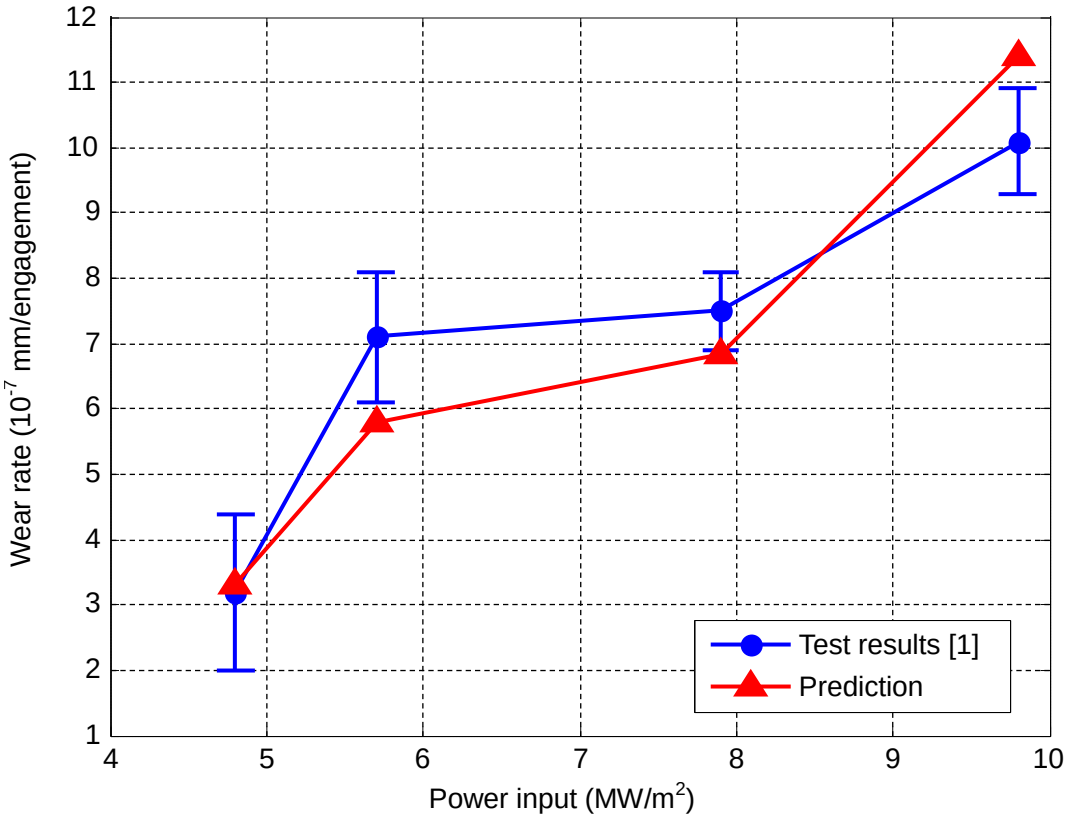

Figure 4-7 First stage wear prediction validation based on THD simulation

Figure 4-7 shows the wear prediction results with respect to different power inputs. Previously, a single location at the mean radius was calculated as the average wear rate. However, since the temperature profile at each planar node is available from the THD results, the wear rate distribution is available to obtain a more accurate average wear rate, as illustrated in Figure 4-8. Compared with wear prediction at a single point (usually chosen to be the mean radius), the distributional wear results depicts the wear behavior of the specific groove pattern. The average wear rate is also a more reasonable quantity of prediction.

$$\overline{\Delta H} = \frac{2\int_0^{\theta_0}\int_{R_i}^{R_o}\Delta H(r,\theta)\,r\,dr\,d\theta}{\theta_0\left(R_o^2 - R_i^2\right)} \tag{5}$$

where θ_0 is the section angle of wear rate computation.

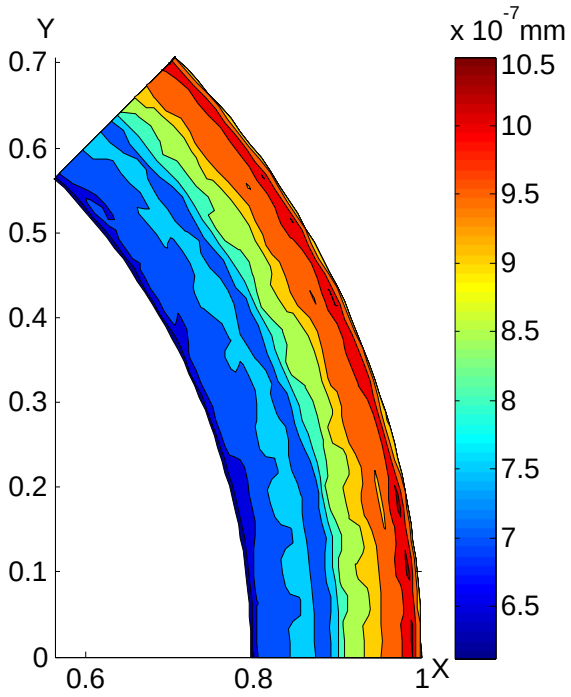

Figure 4-8 Surface wear conditions of a waffle pattern friction disk section (average wear rate = 8.79×10^{-7} mm/engagement)

4.3.4 Sensitivity analysis

Since multiple inputs are involved in the wear prediction (especially during the engagement simulation), the sensitivity, or effect coefficient of input parameters need to be analyzed to take account of different variables and to select the influential ones for further uncertainty analysis. Hence, the total number of numerical experiments is reduced without compromising the simulation accuracy very much.

Table 4-2 shows the input parameters sensitivity in the temperature computation, where the peak temperature during the engagement stage is used as the model result in response to multiple model parameters. The sensitivity of each parameter is measured through examining the percent change in the peak temperature upon perturbing each of the model parameters by 10% of their magnitude. The results are summarized in the last column of Table 4-2. Examination of the results reveals that the rotational speed is the most significant variables because it determines the heat generation rate and the duration of the engagement stage. The engagement load is less influential because a higher load increases the heat generation but reduces the engagement time. For material properties that affect the heat transfer conditions, it shows that the conductivity and diffusivity of steel disks are most influential because the heat partition at the sliding interface depends on them. In contrast, the accuracy of information for the ATF and the friction material are relatively less sensitive in the simulation results. For the model parameters of high sensitivity, the accuracy of simulation can be improved with input data close to unbiased value by repeating experiments or improve measurement accuracy.

Table 4-2. Sensitivity analysis of temperature computation

Parameter perturbation	Input parameter description	Parameter effect
$\delta\Theta/\delta\omega$	Rotational speed	0.1642
$\delta\Theta/\delta k_s$	Conductivity of steel disks	0.0845
$\delta\Theta/\delta I$	Inertia of clutch pack	0.0822
$\delta\Theta/\delta\kappa_s$	Diffusivity of steel disks	0.0788
$\delta\Theta/\delta\Theta_0$	Initial (environment) temperature	0.0159
$\delta\Theta/\delta k_b$	Conductivity of friction material	0.0087
$\delta\Theta/\delta H$	Initial thickness of friction material	0.0084
$\delta\Theta/\delta\rho_f$	Density of ATF	0.0078
$\delta\Theta/\delta c_f$	Heat capacity of ATF	0.0075
$\delta\Theta/\delta P_0$	Engagement load	0.0055
$\delta\Theta/\delta\rho_b$	Density of friction material	0.0049
$\delta\Theta/\delta c_b$	Heat capacity of friction material	0.0049
$\delta\Theta/\delta\sigma$	Surface root mean square	0.0045
$\delta\Theta/\delta\beta$	Surface asperity tip radius	0.0029
$\delta\Theta/\delta n$	Surface asperity density	0.0029
$\delta\Theta/\delta E$	Elastic modulus of friction material	0.002
$\delta\Theta/\delta h$	Convection coefficient	0.0004
$\delta\Theta/\delta k_f$	Conductivity of ATF	0.0002

4.4 Uncertainties of input in wear prediction

In general, possible sources of error can emerge from the simplified assumptions, model inputs, numerical errors, and parameter estimation used in the predictions. Since 3-D THD solutions are verified to yield results in [2, 4], we focus on uncertainty analysis of the input variables for the wear prediction, which is presented in the following sections.

4.4.1 Model input for wear prediction from measurement

In the table of sensitivity analysis, some of the input data are readily available and can be accurately specified (such as engagement load, rotational speed and inertia). These parameters are excluded from the uncertainty analysis. For model input by experimental measurements, the true value is within the confidence interval added by measurement error. The confidence interval of population mean using mean and standard deviation of sampled quantities is given by:

$$\mu \sim \left(\bar{x} - t_{\alpha/2,v} \frac{s}{\sqrt{n}}, \bar{x} + t_{\alpha/2,v} \frac{s}{\sqrt{n}} \right) \tag{6}$$

where $\bar{x}$ is the sample mean, v is the degree of freedom, $t_{\alpha/2,v}$ represents the t-distribution for $100(1-\alpha)\%$ confidence, and s is sample standard deviation. Table 4-3 collects the uncertainty information of the model input measured by Lingesten [6].

Table 4-3. Uncertainties of experimental measurement as model input

Input parameter	Sample#	Mean	Standard deviation	Measurement error	True mean with 90% confidence
Θ_0 (℃)	6	50.3	4.2	0.01	(46.8, 53.8)
k_s (W/mK)	5	63.9	2.5	3	(58.5, 69.3)
κ_s (10^{-5} m²/s)	5	1.27	0.7	0.03	(0.6, 2.0)
ρ_f (kg/m^3)	5	846	0.3	0.0001	(845.7, 846.3)
c_f (J/kg.K)	5	2200	90.8	13.2	(2074.1, 2325.9)
ρ_b (kg/m^3)	5	850	0.9	0.0001	(849.1, 850.9)
c_b (J/kg.K)	5	1750	74.1	8.75	(1649.3, 1850.7)

4.4.2 Model input for wear prediction by postprocessing of the test data

In the wear model, the activation energy of the friction material is obtained by a regression analysis of experimental data with the thermal degradation model proposed by Yang et al. [7]

$$\ln q_{td} = -\frac{U_1}{R}\frac{1}{T} + b \tag{7}$$

where q_{td} is the thermal degradation rate and b is a constant. According to the test procedure in [2], a slipping clutch machinery is used to generate the steady temperature environment for the thermal degradation of cellulose fiber. The residual cellulose percentage is then measured through thermogravimetric analysis (TGA) test to obtain the weight reduction by thermal degradation. The measurement error is possibly induced by burning a certain amount of other components during TGA, which leads to inaccurate weighting for residual cellulose after the slip test. With residual cellulose measurement error of 1.5 %, the maximum change in $\ln q_{td}$ is about 0.02. Due to the model nonlinearity and the fact that a repeat test is not performed, the uncertainty of activation energy is regarded as being epistemic type. As shown in Figure 4-9, the regression analysis for TGA data with error estimation is performed to obtain the bounded interval of activation energy, which in this case is (5927, 6273).

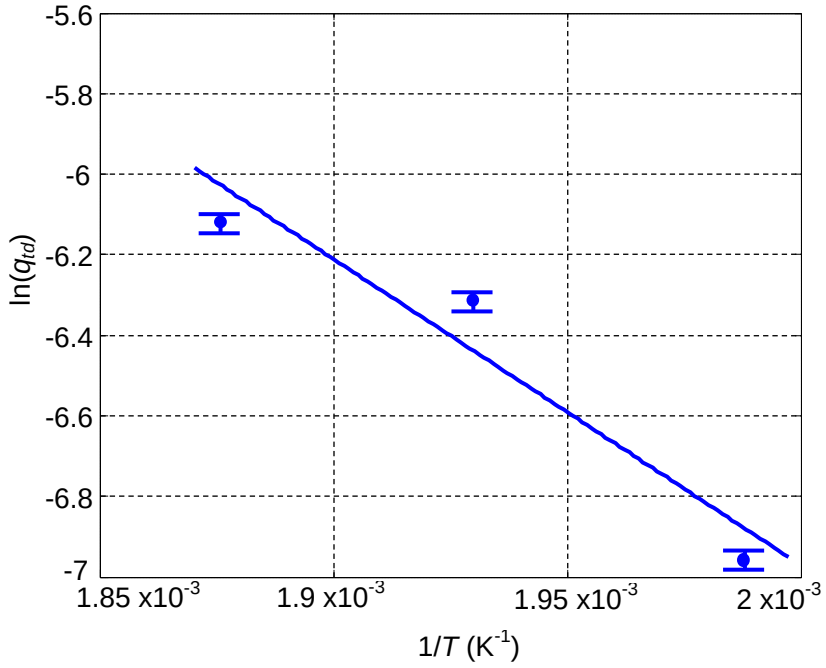

Figure 4-9 Regression of cellulose degradation data with error estimation

4.4.3 Parameter estimation in wear model

Apart from the model uncertainties discussed above, certain model input parameters are also to be determined by estimation. For current wear prediction of the friction material in a wet clutch, the wear factors K_1, K_2, and the stress factor γ are determined by least square estimation with the four test results of wear rate ΔH:

$$K_1 = \arg\min \sum_{i=1}^{4} \left| \Delta H_1^p(i) - \Delta H_1^t(i) \right|^2 \tag{8}$$

$$[K_2, \gamma] = \arg\min \sum_{i=1}^{4} \left| \Delta H_2^p(i) - \Delta H_2^t(i) \right|^2 \tag{9}$$

where the superscripts p and t represent the prediction and test results, respectively. The uncertainties in the parameter estimation are correlated with all of the mentioned model uncertainties through a highly nonlinear relationship. With the uncertainty of epistemic type, the parameters fall within the interval where the upper and lower bounds are determined by numerical experiment with the given uncertainty information of model input.

4.4.4 Approximation of stress field in thermomechanical wear

For the stress term in the second stage wear rate of equation (2), a simplified model is used because of the complexity of analyzing the stress distribution of a sliding porous deformable material with a rough surface. With a uniform engagement load applied on the friction material surface, the contact pressure is

viewed as the compressive stress and incorporated into the model as a mechanical effect. This is a simplifying assumption since treatment of the stress field requires a comprehensive thermoelastic analysis. Currently, uncertainty quantification is not performed on the stress field.

4.5 Uncertainty quantification and validation

With the uncertainty sources discussed above, the statistical measure and sampling-based approach can be used to simulate the uncertainties in SRQ. The aleatory uncertainty sampling is generated by random variables associated with the distributions for the input parameters in Section 3.1. The epistemic uncertainty sampling is taken from within a range of possible values for the parameters in Section 3.2 and 3.3. The quantified uncertainties are utilized for Monte Carlo (MC) simulation described as follows.

4.5.1 Introduction to MC simulation and validation metrics

Monte Carlo (MC) sampling is one of the simplest approaches to propagate the aleatory uncertainty. For a model with many interconnected inputs, the MC method is robust and straightforward to implement. By estimating the aforementioned uncertainties in the model, the following steps are taken for the MC simulation: generate the sampling of model inputs and randomly select each input parameter, evaluate the SRQ with the random set, and check the convergence of the simulations. Generation of input sampling and the corresponding convergence analysis of the MC simulation are described as follows.

To treat the epistemic uncertainties in the input, we use the so-called Latin hypercube sampling (LHS) technique. The practice of LHS seeks to spread the sample points evenly across all possible values by separating each input probability into a number of equally-sized division and then choosing one sample in each interval [8]. Since it shuffles the sample for each input set, the correlation between the inputs can be eliminated. An important evaluation of the MC analysis is the convergence rate. This is used to analyze the sample number to reach a given level of precision or the sampling error of a specific sample number. Published theoretical results [9] show that for a univariate sample of size N, the sampling error of MC without LHS procedure is $O\left(1/\sqrt{N}\right)$ while the sampling error of LHS is $O\left(1/N\right)$. For multivariate and highly non-linear models, discussions on LHS efficiency are more diverse [8, 10, 11]. Roy et al. [3] recommends LHS for simulation of the epistemic uncertainty because it produces satisfactory coverage of the combinations of all the epistemic uncertainties with respect to the largest range of SRQ. Such consideration reflects the characteristics of the epistemic uncertainties, i.e. the possibilities brought about by the lack of knowledge. In the current MC simulation, the sampling number of epistemic uncertainty is 10 as used by [3].

For aleatory uncertainty, we adopt the importance sampling (IS) approach, classified as a variation reduction technique. In importance sampling, a new probability density (importance density function) is chosen to give more importance to the interval closer to mean so that fewer samples are needed to reduce the sampling error [12]. By concentrating on the importance region, the original sampling input is firstly distorted and is then corrected by averaging the output from different samples using weights that are related to the bias, preserving the mean of the quantity being estimated. For the importance

sampling technique, selection of importance density function is crucial. Since the aleatory uncertainties in our model are Gaussian, the families of Gaussian distributions are tested to obtain an improved sampling accuracy than the original MC simulation. The principle of the importance sampling approach is introduced in Appendix. According to Lu and Zhang [13], The optimal estimation of mean and standard deviation is to minimize (19) by choosing an appropriate importance density function of the Gaussian distribution. For example, the sampling efficiency for a normal distribution $N(3,0.2)$ can be improved by mean translation (MT) and variance scaling (VS) using the importance density function choice $f_1(y) = N(3.2,0.3)$ to resample the data. The numerical experiment shows that variance of mean estimator $\overline{H_N}$ is $S_{h,N}^2 = 0.1465$ and efficiency ratio is $\gamma = 1.4$, which indicate that the resampling reduces variance of estimator for the model uncertainty and thus the convergence to the true value is faster.

According to the discussion in Section 3, the wear prediction model for a wet clutch includes a mixture of aleatory and epistemic uncertainties. For uncertainty quantification, the aleatory and epistemic random variables are separated to perform a nested iteration, which is to generate the epistemic uncertainties on the outer loop and then get the sampling over aleatory variables on the inner loop. Evaluation of SRQ with large sample size is enhanced by parallel computing that significantly reduces the computational cost of MC analysis. The message passing interface (MPI) program is used to implement the computation procedure. Since the realizations of sample set are independent, they are fully parallelized as individual tasks.

The final step of the simulation is validation and verification, which is indispensable for inspecting the model and computation. In many cases, the computational results are judged by the graphical comparison or by checking whether they lie within the error band of the test results. However, such evaluations of modeling can be obscure, especially when the model and test both have inherent uncertainties. Deterministic prediction results that deviate from the experimental measurement do not necessarily indicate poor applicability of the model. Improvement in agreement between prediction and test results is possibly achieved through post-processing techniques, such as parameter estimation by regression analysis [3]. For improved validation purposes, Oberkampf et al. [14] discuss the measures of agreement between computation and experiment by validation metrics. According to Roy and Oberkampf [3], the validation metric can be represented by the area between the two CDF curves of prediction and experiment:

$$d^*(F, S_n) = \int_{-\infty}^{\infty} \left| F(t) - S_n(t) \right| dt \tag{10}$$

where t is the SRQ of interest, $F(t)$ represent the CDF of prediction, and $S_n(t)$ is the CDF of experimental measurement. Such validation metric d^* of L_1 norm is of the same unit with SRQ and satisfies the conditions for a distance function on a metric space. Figure 4-10 shows a possible validation metric used for verification of MC wear prediction by test results.

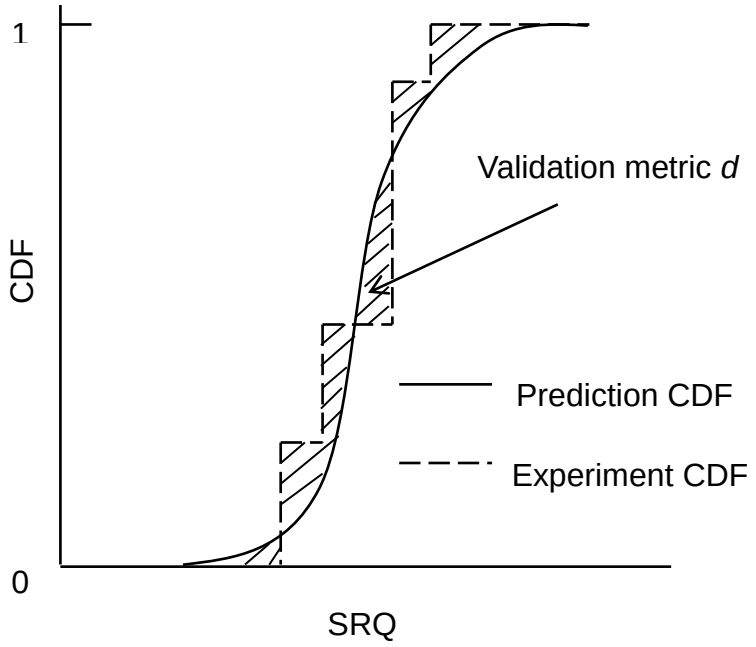

Figure 4-10 Area validation metric obtained by prediction CDF

4.5.2 Uncertainty quantification and validation results of wear prediction

Table 4-4 summarizes the uncertainty information of input data for MC simulation. These are importance density functions for aleatory uncertainties and bounded intervals for epistemic uncertainties. The total MC simulation number is 790 given by the maximum sampling number for aleatory uncertainties reaching a precision of 5% multiplied by a fixed epistemic sampling number of 10.

Table 4-4. Uncertainty information for MC simulation

Uncertainty type	Input parameters	Uncertainty information	sampling #
Aleatory	Θ_0 (℃)	$N(51.2, 4.3)$	39
	k_s (W/mK)	$N(64.1, 2.7)$	66
	κ_s (10^{-5} m²/s)	$N(1.3, 0.8)$	57
	c_f (J/kg.K)	$N(2201.0, 91.2)$	79
	c_b (J/kg.K)	$N(1750.9, 74.1)$	48
Epistemic	U_1 / R (K)	(5558, 6642)	10
	K_1 (10^3 cycle^{-1})	(3376, 4386)	10
	K_2 (10^3 cycle^{-1})	(2794, 3938)	10
	γ (10^{-4} m^3)	(1.0605, 1.2475)	10

The temperature evolution at the energy level of 9.8 MW/m^2 is output from the MC simulation, as shown in Figure 4-11. The 2 sigma interval is the confidence interval of 95.45 % of prediction results. Compared with deterministic simulation of single temperature profile, the current MC simulation provides the confidence interval of the simulation results.

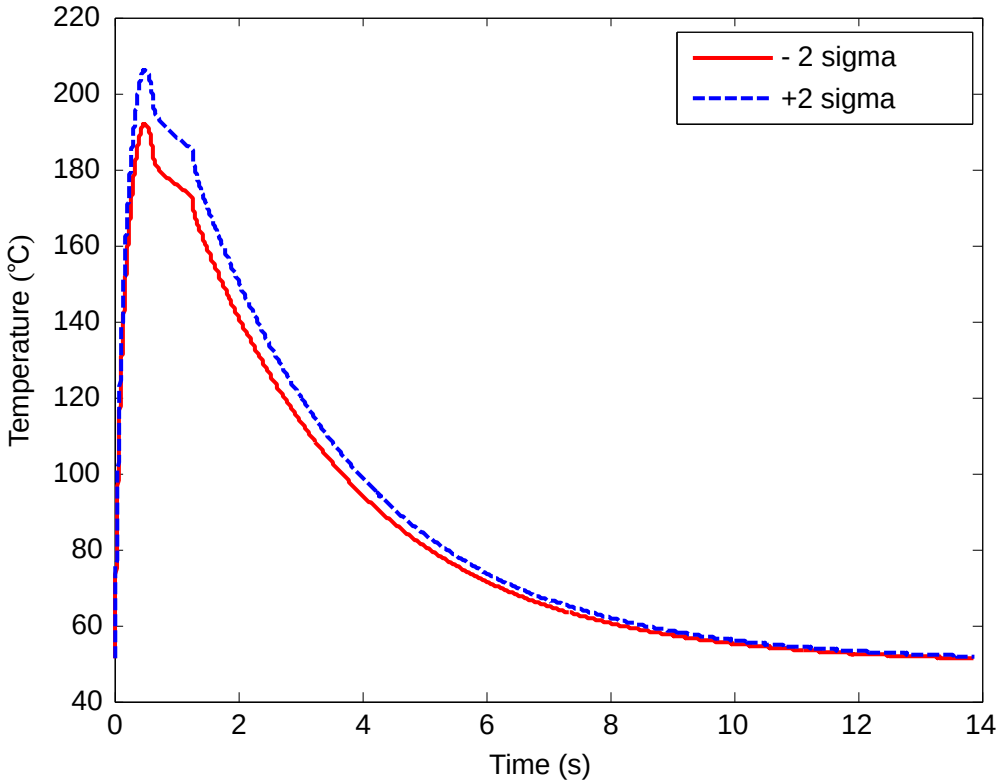

Figure 4-11 Temperature evolution of 2 sigma confidence interval

The area validation metric of wear rate in the two stages is illustrated in Figure 4-12, by including the CDF of both experimental measurement and MC simulation. The propagation of epistemic uncertainty tends to stretch the tail of the probability distribution of predicted wear rate. For example, the confidence interval span for the energy level of 4.8 MW/m^2 is 1.36×10^{-7}mm/engagement for first stage wear and 2.71×10^{-7}mm/engagement for second stage wear. For two stage wear rate at the energy level 9.8 MW/m^2, the overall prediction results are higher than the test result, which is possibly induced by bias in essential model input such as activation energy and wear factors. Using equation (9), the validation metrics in Table 4-5 are obtained. The maximum deviation of MC simulation from test of first stage wear occurs at the energy level of 9.8 MW/m^2, while the second stage wear result discrepancies are found at the energy level of 7.9 MW/m^2. The trend is consistent with the observation in [2], while the validation metrics provide a quantitative measure.

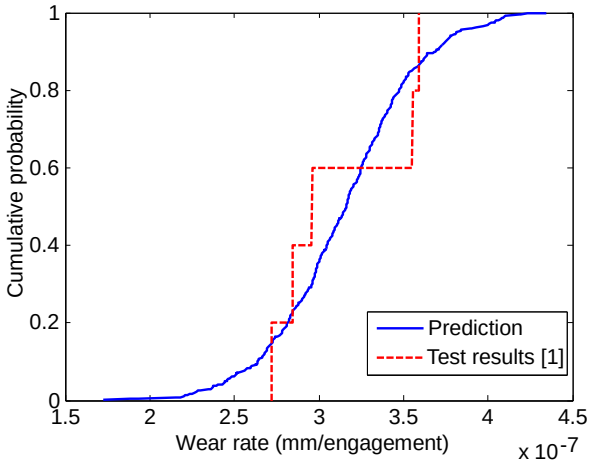

(a) First stage wear at 4.8 MW/m^2

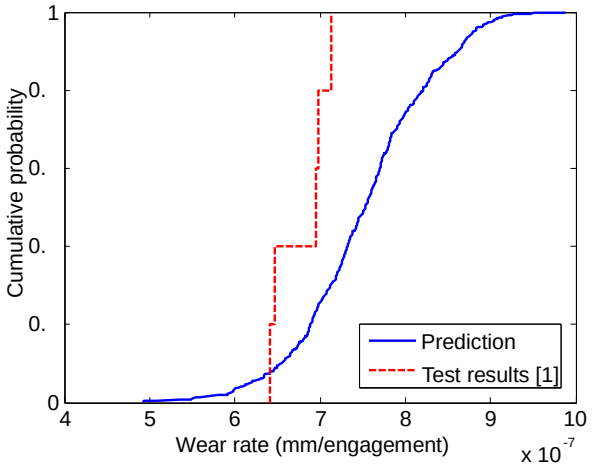

(b) Second stage wear at 4.8 MW/m^2

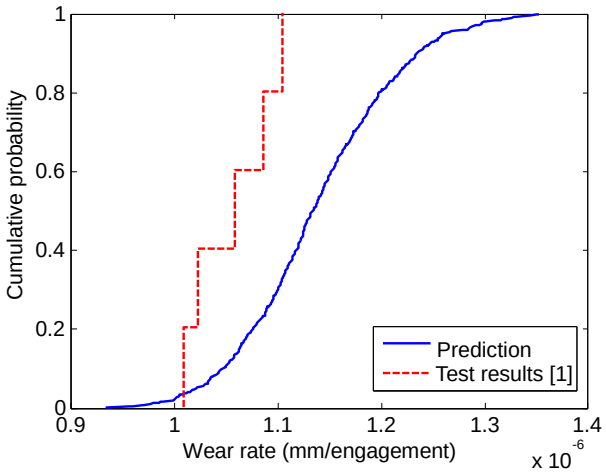

(c) First stage wear at 9.8 MW/m^2

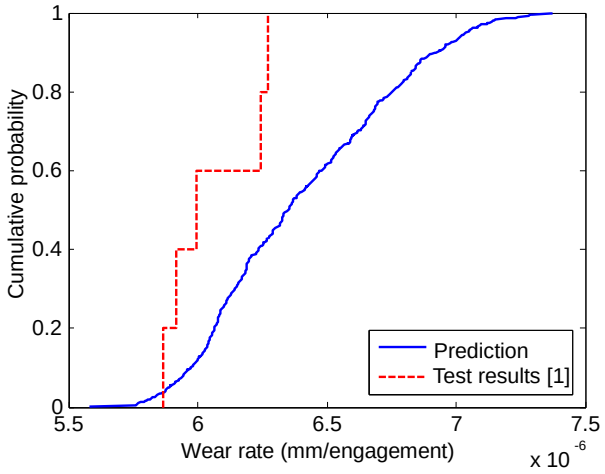

(d) Second stage wear at 9.8 MW/m^2

Figure 4-12 Validation metric with CDFs of experimental measurement and prediction

Table 4-5. Validation metrics of wear prediction at different energy levels (10^{-7} mm/engagement)

Wear stage \ Energy level (MW/m^2)	4.8	7.9	8.3	9.8
1st Stage	0.41	1.17	0.66	1.32
2nd Stage	2.29	5.35	5.13	4.71

The probabilistic prediction results using the MC simulation are presented in Table 4-6. These are the 2 sigma confidence bounds of the transition point (the engagement number of transition from the first to the second wear stage), and the wear limit (engagement number of the end of "two-stage" wear). The

lower bounds of engagement number for wear limit at each energy level could produce a conservative estimation of friction material failure that incorporates the uncertainties and error of wear prediction. These can be applied for life time prediction for the friction disk in industrial equipment. The probability that the wear limit is reached before the -2 sigma engagement number is less than 2.5%.

Table 4-6. Wear transition and wear limits of probabilistic prediction

Energy level (MW/m^2)	Transition (cycle)		Limit (cycle)	
	-2 sigma	+2 sigma	-2 sigma	+2 sigma
4.8	35935	71422	262320	419670
7.9	19529	27033	68885	76854
9.8	14294	20083	40676	44563

4.6 Concluding remarks

Previous deterministic wear predictions of the friction lining in a wet clutch are plotted together with the wear test as an initial effort of model verification. Taking into account the various sources of uncertainty in the model can contribute to improved understanding and possibly reduced prediction deviation. The uncertainties in the wear prediction are categorized as aleatory and epistemic types. The following procedures are taken as the uncertainty quantification framework: analyze the completion of model and numerical accuracy, identify and characterize the sources of uncertainty, propagate the uncertainties through the model, evaluate the uncertainties and construct the validation metrics.

By sensitivity analysis of input uncertainties, the significance of input parameters of engagement simulation is evaluated. The important experimental measurements of input are characterized statistically to quantify the input uncertainty. The most important parameters affecting simulation accuracy are rotational speed, conductivity of steel disks, inertia of clutch pack, and diffusivity of steel disks, which also indicate the significant role in design measures to consider wear of friction lining.

For validation and verification of wear prediction, the CDFs of experiment and predict are compared. Based on this, the validation metrics are calculated for a quantitative measure of discrepancy between test and simulation. From this we can conclude that wear prediction for the high power input case indicates greater deviation from test result in contrast with the low power input case. Therefore, the confidence interval of predicted wear rate is wider for the high energy level.

Following the MC simulations, probabilistic predictions of material life at different energy levels are made to estimate possible wear failure given the aforementioned prediction uncertainties. A conservative estimation of life time is the - 2 sigma engagement number, meaning the probability of wear failure occurs earlier is only 2.5%.

4.7 Appendix – mathematical principle of importance sampling

For a function of interest $g(y)$ associated with probability distribution function $f(y)$, the mean and variance are:

$$\mu_h = E\left[g(y)\right] = \int_\Omega g(y)\, f(y) dy \tag{11}$$

$$\sigma_h^2 = E\left\{\left[g(y) - \mu_h\right]^2\right\} = \int_\Omega \left[g(y) - \mu_h\right]^2 f(y) dy = \int_\Omega g^2(y)\, f(y) dy - \mu_h^2 \tag{12}$$

where Ω is the probability space. For a discrete sample $\{y_i\}$, $i = 1, 2, ..., N$, the unbiased estimator of μ_h and σ_h^2 are computed by:

$$\overline{h_N} = \frac{1}{N}\sum_{i=1}^{N} g(y_i) \tag{13}$$

$$S_{h,N}^2 = \frac{1}{N}\sum_{i=1}^{N} g^2(y_i) - \overline{h_N^2} \tag{14}$$

To realize the precision η, the minimum number of MC simulation is

$$N_{\varepsilon,MC} = \left\lceil \sigma_h^2 / \mu_h^2 \eta^2 \right\rceil \tag{15}$$

where $\lceil x \rceil$ represents rounding up of real number x.

Consider modification of $g(y)$ by $g_1(y) = g(y) w_1(y)$, where $w_1(y) = f(y) / f_1(y)$ is the weight function and $f_1(y)$ is the importance density function, we have a preserved mean value but modified variance:

$$\mu_H = E\left[g_1(Y)\right] = \int_\Omega g_1(y)\, f_1(y) dy = \int_\Omega g(y)\, f(y) dy = \mu_h \tag{16}$$

$$\sigma_H^2 = E\left\{\left[g_1(y) - \mu_H\right]^2\right\} = \int_\Omega g_1^2(y)\, f_1(y) dy - \mu_H^2 \tag{17}$$

Also, the estimators of mean and variance are:

$$\overline{H_N} = \frac{1}{N}\sum_{i=1}^{N} g_1(y_i) = \frac{1}{N}\sum_{i=1}^{N} g(y_i) w_1(y_i) \tag{18}$$

$$S_{h,N}^2 = \frac{1}{N}\sum_{i=1}^{N} g_1^2(y_i) w_1^2(y_i) - \overline{H_N^2} \tag{19}$$

To realize the same precision ε, the minimum number of MC simulation by importance sampling is:

$$N_{\varepsilon,IS} = \left\lceil \sigma_{IS}^2 / \mu_H^2 \eta^2 \right\rceil, \quad \overline{\sigma_{IS}^2} = \sigma_H^2 / N \tag{20}$$

The efficiency of MC simulation by importance sampling is measured by

$$\gamma = \overline{\sigma_{MC}^2} / \overline{\sigma_{IS}^2} \tag{21}$$

4.8 References

[1] N. Lingesten, P. Marklund, E. Höglund, M. Lund, J. Lundin, R. Mäki, Apparatus for continuous wear measurements during wet clutch durability tests, Wear, 288 (2012) 54-61.

[2] M. Li, M. Khonsari, D. McCarthy, J. Lundin, On the wear prediction of the paper-based friction materialin a wet clutch, Wear, 334 (2015) 56-66.

[3] C.J. Roy, W.L. Oberkampf, A comprehensive framework for verification, validation, and uncertainty quantification in scientific computing, Computer Methods in Applied Mechanics and Engineering, 200 (2011) 2131-2144.

[4] M. Li, M. Khonsari, D. McCarthy, J. Lundin, Parametric analysis for a paper-based wet clutch with groove consideration, Tribology International, 80 (2014) 222-233.

[5] J. Jang, M. Khonsari, Thermal characteristics of a wet clutch, Journal of tribology, 121 (1999) 610-617.

[6] N. Lingesten, Wear behavior of wet clutches, (2012).

[7] Y. Yang, R.C. Lam, Theoretical and experimental studies on the interface phenomena during the engagement of automatic transmission clutch, Tribology Letters, 5 (1998) 57-67.

[8] M. Keramat, R. Kielbasa, Latin hypercube sampling Monte Carlo estimation of average quality index for integrated circuits, Analog Design Issues in Digital VLSI Circuits and Systems, Springer, 1997, pp. 131-142.

[9] W.-L. Loh, On Latin hypercube sampling, The annals of statistics, 24 (1996) 2058-2080.

[10] C. Aistleitner, M. Hofer, R. Tichy, A central limit theorem for Latin hypercube sampling with dependence and application to exotic basket option pricing, International Journal of Theoretical and Applied Finance, 15 (2012).

[11] R.D. Manteufel, Evaluating the convergence of Latin hypercube sampling, AIAA/ASME Structures, Structural Dynamics and Materials Conference, 2000, pp. 100-106.

[12] P.W. Glynn, D.L. Iglehart, Importance sampling for stochastic simulations, Management Science, 35 (1989) 1367-1392.

[13] Z. Lu, D. Zhang, On importance sampling Monte Carlo approach to uncertainty analysis for flow and transport in porous media, Advances in Water Resources, 26 (2003) 1177-1188.

[14] W.L. Oberkampf, M.F. Barone, Measures of agreement between computation and experiment: validation metrics, Journal of Computational Physics, 217 (2006) 5-36.

CHAPTER 5 PARAMETRIC ANALYSIS OF WEAR FACTORS OF A WET CLUTCH FRICTOIN MATERIAL WITH DIFFERENT GROOVE PATTERNS

5.1 Nomenclature

A_l =land area (m^2)

H_g = groove depth ratio

k_i = thermal degradation constant (1/s)

q_{td} = thermal degradation rate (kg/m s)

q_{tmd} = thermomechanical degradation rate (kg/m s)

R = Boltzmann constant (J/K)

T = temperature $(℃)$

α = spiral groove angle (rad)

U_i = activation energy (J)

γ = mechanical coefficient (m^3)

ϕ = ratio of grooved area to total area

σ =stress distribution (MPa)

5.2 Introduction

As a crucial component of automatic transmission system, a high-power wet clutch system is usually susceptible to degradation under repeated engagement cycles, in which the wear of the friction lining is a direct consequence. The durability of friction material and degradation-related failures presents a challenging tribological problem for the industry.

A typical paper-based friction material is composed of organic fibers, resin and other fillers. The microscopic structure of the friction material is porous and deformable, which promote squeeze flow of the automatic transmission fluid (ATF) during the engagement. With applied engagement load, frictional torque is generated by asperity contact of the friction lining with the mating component of the friction pair, i.e. the metallic separator disk, to deliver the transmission power. Although the temperature of the clutch system can be cooled down by the flow of ATF, thermal effect are still quite intense. In fact a temperature rise of over 200 ^oC within 1.5 second duration of the engagement is common [1-3]. Thus, the sliding action in the presence of intense heat brings about continual removal of friction material through both mechanical and thermal degradations of organic fibers [4, 5].

To understand the nature of wear, Lingesten performed a series of wear tests for the friction lining material with waffle groove pattern [6]. For this purpose, a test rig was designed to mimic the close performance of a clutch under repeated engagements cycles for the actual operational configurations in a vehicle. Lingesten et al. [7] reported a noteworthy, two-stage wear rate phenomenon wherein the wear rate remained relatively low for certain number of operational cycles and then increased to a much

higher rate. Li et al. [5] developed a computational model to explain the wear behavior associated with both mechanical and thermal degradation mechanisms. Their study showed that the wear behavior is closely related to temperature evolution and the engagement load. In the first wear stage, the friction material volume is reduced by thermal degradation of the cellulose fiber. Subsequently, mechanical effects become dominant and promote the observed higher wear rate.

Thermohydrodynamic (THD) simulation of clutch engagement indicates that the thermal behavior is closely related to the type of the grooves engraved into the friction liner, the material's properties and the energy level [2, 8, 9]. These factors are closely related with the material degradation rate. Moreover, some remarkable work has been reported in the material manufacturing to enhance the tribological performance stability of material [10-13]. By comparing different fiber additions (steel, brass, cellulose and ceramic fibers) in the friction material, it is concluded that inclusion of copper or glass fiber maintains a stable friction coefficient and low wear amount [14, 15]. Therefore, it is desirable to investigate the multiple factors influencing the wear rate and identify the primary ones to improve the material durability through appropriate industrial design.

In this study, we report the results of an extensive set of parametric study of combination of the different factors involved, including the groove design, material properties, and operational configurations. The wear behaviors are analyzed based on the engagement results and thermal characteristics obtained by THD simulation. The effects of wear factors on the frictional material life are reflected by the two-stage wear rates. The outline of the paper is organized as follows. In Section 2, the backgrounds of engagement simulation and wear prediction are briefly introduced. Next, in Section 3 a parametric analysis of groove pattern for the friction lining is shown, where waffle groove is presented as verification with experiments and geometric configurations of radial and spiral groove are discussed for comparison purposes. The operational configurations and material considerations are presented in Section 4 and Section 5, respectively. Concluding remarks are given in the last section as a summary of the wear factors to be considered in industrial application.

5.3 Introduction to wear prediction

5.3.1 Engagement simulation of a wet clutch

The full engagement cycle is composed of engagement stage, soak period, dwell period and stabilization period. During the engagement stage, load is applied hydraulically through the motion of a piston that acts as an actuator. With continually decreasing film thickness, the lubrication condition at the sliding interface shifts from initially hydrodynamic lubrication to mixed lubrication and finally boundary lubrication. Meanwhile, large amount of heat is generated and is conducted to different components. When the relative rotation speed becomes nil, the engagement stage ends and the clutch system remains "locked" for the soak period. After the soak period, the separator disk and the friction lining are detached, and the clutch system is cooled down by convection. The initial temperature is then restored to start another engagement cycle.

There exists a close coupling between the thermal effect and hydrodynamic action due to the relationship between the viscosity of ATF and temperature. In order to obtain accurate transmission results during the engagement, a comprehensive thermohydrodynamic (THD) model is proposed by Jang et al. [9] to compute the hydrodynamic and the temperature field. The modified Reynolds equation for hydrodynamic lubrication incorporates the squeezing motion of the friction material, flow within the porous friction lining, the centrifugal force, and film thickness variation over the domain. The temperature distribution is computed by the numerical simulation of the three-dimensional energy equation for ATF and heat transfer to the bounding surfaces. For the contact load generated by the rough surface of the friction material, the elasto-plastic contact model by Etsion et al. [16] provides an appropriate description of the contact conditions. The finite difference method is applied to solve the governing partial differential equations. Specifically, the modified Reynolds equation is solved by successive over-relaxation (SOR) method to obtain a converged hydrodynamic pressure distribution at each time step. Alternative direction implicit (ADI) method is used for a fast solution of three-dimensional thermal equations. The groove configurations are also taken account of for the friction lining.

Using the input data of Table 5-1, the transmission torque and rotational speed during the engagement are predicted and the results are shown by Figure 5-1. The hydrodynamic torque is increased at the beginning of engagement stage because of rapid film thickness reduction and is then gradually diminished by decreasing the relative speed between the separator disk and the friction lining. In contrast, the torque due to the asperity contact tends to increase over time and become the major component of total torque. The interested reader is referred to [1, 2] for further discussion.

Table 5-1. Input data of engagement simulations

Input parameters	value
Engagement load P_0 (MPa)	1.25
Rotational speed ω (rpm)	1500
Outer radius R_o (m)	0.0738
Inner radius R_i (m)	0.0572
Inertia I (kg $\cdot$m^2)	0.6764
Number of friction disk	2
Friction lining thickness d_b (m)	0.0005
Core disk thickness d_c (m)	0.001
Friction lining conductivity k_b (W/mK)	0.75
Friction lining specific heat κ_b (J/kg.K)	1200
Friction lining density ρ_b (kg/m^3)	1800
Steel conductivity k_c (W/mK)	46.04
Steel heat capacity κ_c (J/kg.K)	490
Steel density ρ_c (kg/m3)	8050

(Table 5-1 continued)

Friction coefficient constants c_1,c_2	0.15, 0.011
Initial temperature (℃)	50
Convection coefficient during soak period (W/ m ²K)	20
Convection coefficient during dwell period (W/ m ²K)	500
Convection coefficient during stabilization period (W/ m ²K)	500
Soak duration (s)	0.4
Dwell duration (s)	1.9
Stabilization duration (s)	7

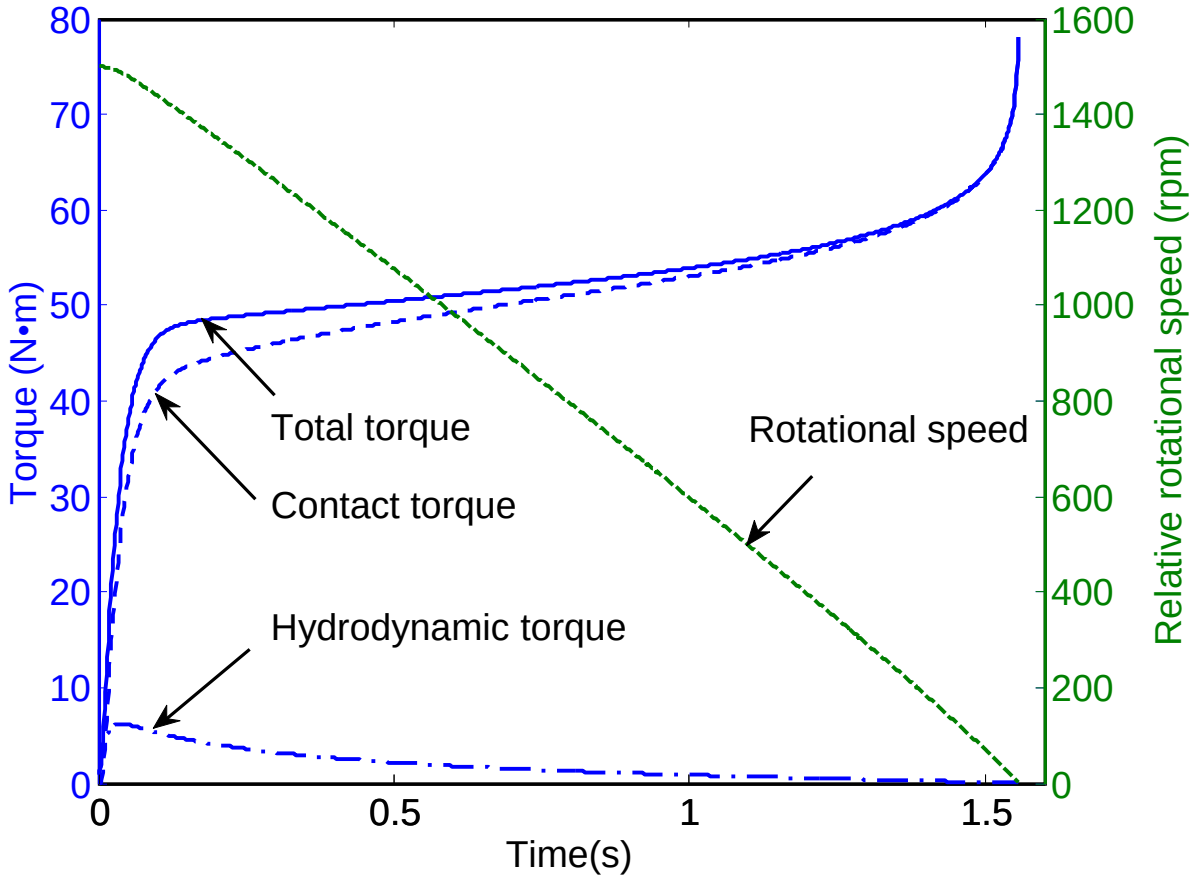

Figure 5-1 Transmission results of the wet clutch engagement

5.3.2 Wear model

Cellulose fiber is one of the common components that improve the mechanical and tribological performance of the paper-based friction material. With the addition of cellulose, the mechanical strength of the composite material and its resistance to brittle fracture are enhanced. However, its functionality can be impaired by lowering the mechanical strength leading to delamination by mechanical effects as

well as increased susceptibility to thermal degradation. In the first wear stage, cellulose thermally degrades and as a result the weight ratio of the friction material decreases leading to "shrinking" of the lining. Also involved in this initial phase of cellulose degradation is chemical reaction which directly depends on activation temperature [4]:

$$q_{td}\left(z,t\right)=k_1\exp\left(-\frac{U_1}{RT\left(z,t\right)}\right) \tag{22}$$

where k_1 is the rate constant of thermal degradation, R is the Boltzmann's constant, U_1 is the activation energy of cellulose, and $T(z,t)$ is the temperature distribution.

With an appreciable cellulose reduction under thermal conditions during the engagement cycles, the second wear stage is initiated by additional mechanical factors when brittle fracture of other organic components takes place. The theoretical modelling was initially proposed by Kartashov et al. [17]. Later, Sosnovskiy [18] elaborated its application for the analysis of wear density in polymer material. Basically, the rate model that describes the thermomechanical degradation process is expressed as follows:

$$q_{tmd}\left(z,t\right)=k_2\exp\left(-\frac{U_2-\gamma\sigma}{RT\left(z,t\right)}\right) \tag{23}$$

where σ is the stress field, k_2 is the resistance coefficient of thermomechanical degradation, estimated from wear test. γ is the material mechanical property, related to the Poisson's ratio and Young's modulus, U_2 is the activation energy of heat-resistant components, including binder, polymeric fiber, etc., in the friction material.

Detailed description of wear model along with verification of prediction results through experimental measurements is presented in [5], which includes the wear rates at different energy levels for the first stage and the second stage wear. The input data is given in Table 5-2. For further parametric study of wear factors, the temperature distribution during the entire engagement cycle is obtained through thermohydrodynamic (THD) simulation with input data of groove geometry, material properties and engagement configuration. By integrating the wear rate function over time and z-direction for each planar node with the obtained 3-D temperature evolution, the surface wear is output as the final result. The average wear rate $\overline{\Delta H}$ is computed by the mean value of planar wear rate $\Delta H\left(r,\theta\right)$:

$$\overline{\Delta H}=\frac{\int_0^{\theta_0}\int_{R_i}^{R_o}\Delta H\left(r,\theta\right)rdrd\theta}{A_l} \tag{24}$$

where A_l is the land area for the grooved friction lining.

Table 5-2. Input data of wear model

Input parameters	value
Cellulose activation energy U_1 (J)	6100
Polymer activation energy U_2 (J)	6580
Wear coefficient K_1	1450
Wear coefficient K_2	7000
Mechanical factor γ (m^3)	13000

5.4 Effect of friction lining groove on wear

Hydrodynamic lubrication plays the primary consideration in the design of the surface pattern because of its direct relationship with loading-carrying capacity by lubricant flow in the groove channels [19-21]. In a wet clutch, the generation of hydrodynamic load partially determines the engagement time, during which heat is generated (no heat is generated after the engagement stage). The convection cooling of ATF flow in the grooving patterns can also modify the temperature evolution. Since the two-stage wear of the friction material involves thermal degradations at high temperature level, the design of the groove pattern to reduce the wear rate is one of the viable measures to extend the operational life of the friction material. Apart from material degradations, Jang and Khonsari [22] show that macroscopic hot spots can be generated on the surface of the separator due to instability associated with thermoelastic phenomenon and intense local heating that renders the lubricant ineffective. The degree of surface cooling indicates the likelihood of hot spot formation on the surface of the separator disk. Therefore, heat removal capacity of the grooving pattern is crucial for durability of clutch system.

Common among the commercially used surface patterns are radial groove, spiral groove and waffle groove (Figure 5-2). The lubricant passes through the grooves from the inner rim to the out rim of the friction lining under the impetus of centrifugal force. The waffle pattern grooving generates a relatively small drag loss by less ATF flow of lubrication within two series of parallel flow channels. The motivation of waffle grooving design is a good overall distribution of lubricant that renders the surface fully wet and generates the desirable friction characteristics. However, only the grooves in the radial direction tend to actively participate in heat dissipation and a large portion of grooving remains underutilized. The radial groove provides direct flow pathways for ATF. With sufficient volumetric flow, the heat dissipation rate of radial groove case is effective. The spiral grooving design is different from other patterns because of its unique ability to produce pumping effect, which has the potential to improve the surface cooling but at the same time can increase the drag loss associated with hydrodynamic lubrication.

To investigate the influence of groove design on the surface wear of the friction lining, the wear rate distribution is computed by considering specific groove geometric configurations. Then the average

wear rate is used as the metric to evaluate the effect of wear reduction. With the computational model, the cost of testing for improved durability performance by grove design is significantly saved.

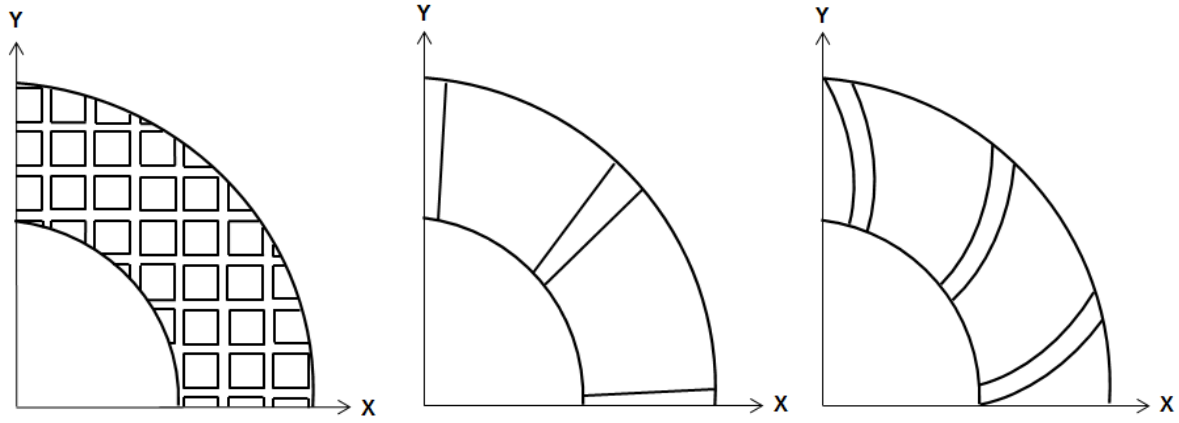

(a) (b) (c)

Figure 5-2 Surface groove pattern of the friction lining (a) waffle groove (b) spiral groove (c) radial groove

5.4.1 Waffle groove

Waffle grooving was used the validation case for the wear models and computerized wear prediction reported in [5], where the two-stage wear rates at different energy levels were presented. The land/total area ratio is 0.75. The number of parallel grooves is 18 in the horizontal and the vertical direction. By THD simulation for the medium energy level with speed of 2800 (rpm) and engagement load of 3.3 (MPa), the temperature evolution at the surface of the friction lining is obtained as shown in Figure 5-3, which illustrates the process of heat generation by frictional work and heat dissipation by flow of ATF. Initially, the temperature rises quickly at the entire land region. Later on, the high temperature domain is gradually shifted, and the temperature gradient along the circumferential direction becomes smaller. Finally, the highest temperature region develops on the outer rim because of the highest linear velocity and heat generation rate. The maximum temperature difference over the surface is about 16 (℃) at the end of engagement when the local maximum temperature reaches 236 (℃).

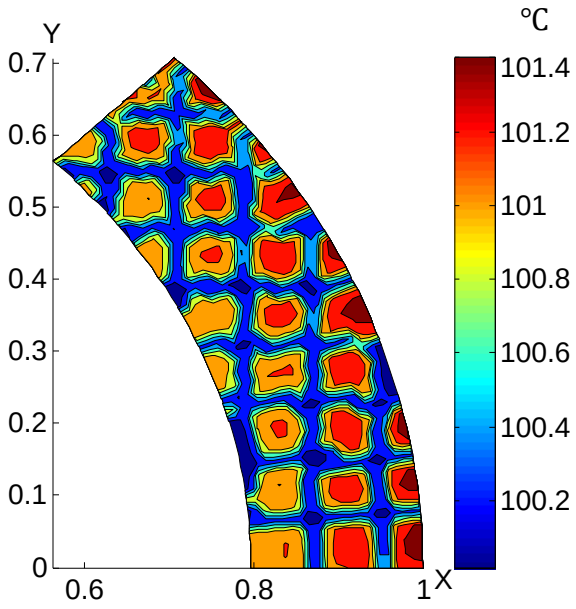

(a) t = 0.01 s

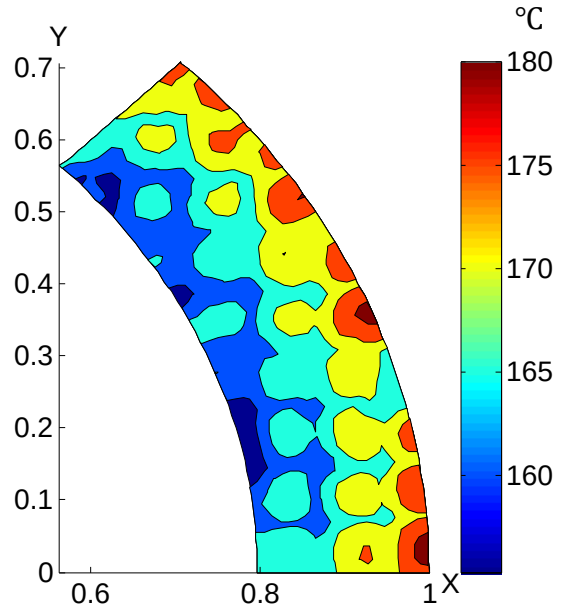

(b) t = 0.1 s

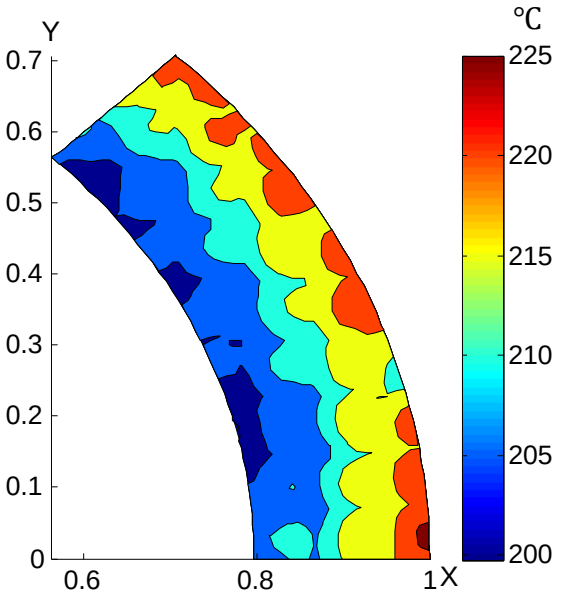

(c) t = 0.2 s

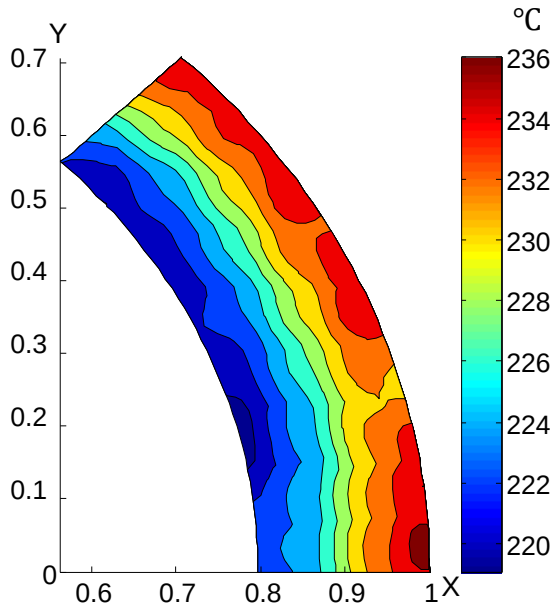

(d) t = 0.3 s

Figure 5-3 Surface temperature evolution of waffle groove pattern

Figure 5-4 shows the surface wear conditions in the first wear stage due to thermal degradation for the waffle grooving patterns. By equation (3), the average wear rate is predicted to be 5.82×10^{-7} (mm/engagement). In accordance with the temperature distribution, the thickness loss induced by thermal degradation is most appreciable on the outer rim. The maximum difference of wear rate is about 3×10^{-7} (mm/engagement). Such uneven wear distribution can be partially compensated during the entire

wear process, because as the engagement process continues larger portion of the inner rim region will contact with the separator disk and is exposed to more thermal effect that leads to more wear.

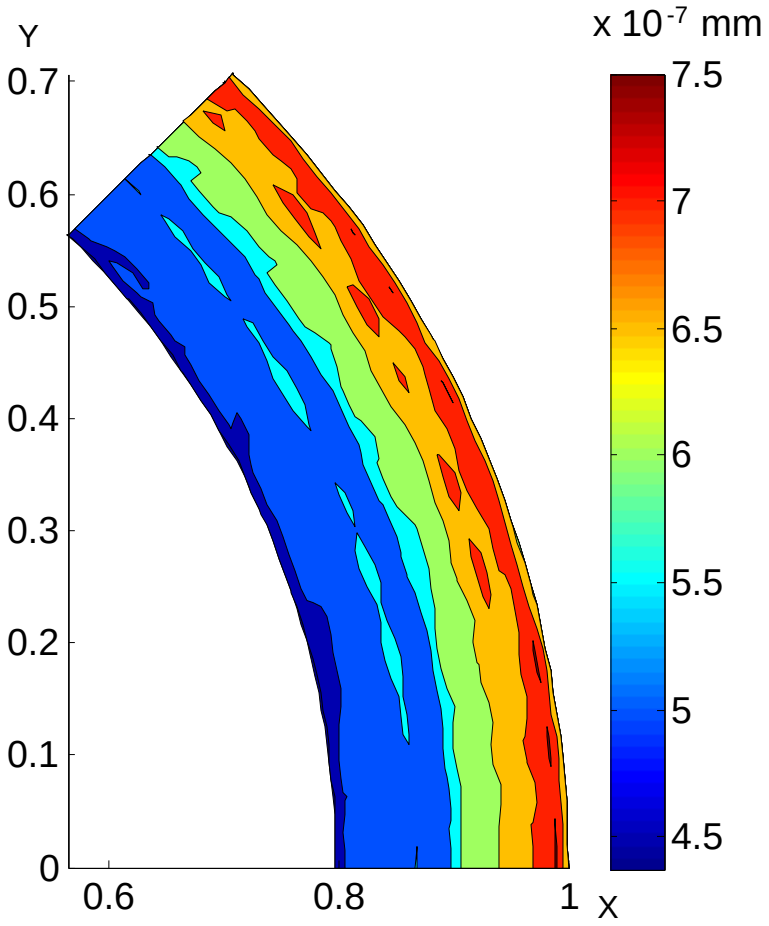

Figure 5-4 Surface wear conditions of waffle groove patterns in the first wear stage

5.4.2 Radial groove

The geometric specifications of radial groove include groove depth, groove area ratio, groove number, and groove profile. The groove depth ratio H_g is defined as the ratio of groove depth over the initial adjacency between the friction pair. The distribution of groove region is determined by both the groove area ratio ϕ and the groove number. Apart from rectangle shape, the profile of groove can be round, triangle, or trapezoid. A special case of a plain friction lining without grooves is equivalent to set $H_g = 0$. Each of possible variation on the radial groove design is considered to investigate the optimal one in terms of wear.

Simulation and discussion on temperature distribution of radial groove case are presented in [1]. The surface wear condition of radial groove ($H_g = 1.0$, and $\phi = 0.1$) is compared with the waffle groove

case by using the same operational configuration. As observed in Figure 5-5, the overall wear rate of radial groove case is smaller than the waffle case. The average wear rate is 4.73×10^{-7} (mm/engagement). The maximum difference of wear rate is about 1.8×10^{-7} (mm/engagement). Such a material durability performance is better than the waffle groove case, which indicates that the thermal capacity by radial groove is more desirable.

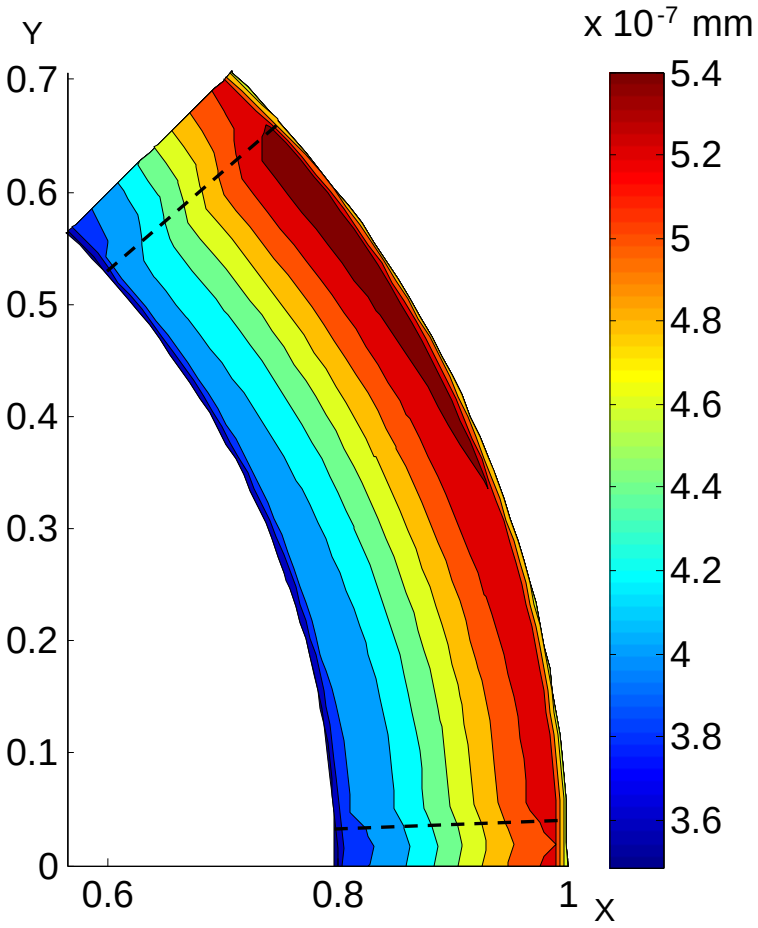

Figure 5-5 Surface wear conditions of radial groove patterns in the first wear stage ($H_g = 1.0$, and $\phi = 0.1$)

Since the temperature evolution is modified through the role of changing engagement time (or duration of heat generation) and cooling flow within grooves, the first stage wear rate is closely related with such effects for specific grooving geometries. The second stage wear is induced by thermomechanical degradation due to the asperity contact. Therefore, generation of hydrodynamic load plays a significant role in reduction of the second stage wear. The following parametric study of radial groove configurations investigates the groove factors based on THD analysis.

- Groove depth for radial groove case

The effect of groove depth on the averaged surface wear in the two wear stage is illustrated in Figure 5-6. With deeper grooves, the wear rate at the first stage is increased by a moderate degree and is then slight decreased. The maximum wear rate occurs when the groove depth ratio is approximately equal to 2. The second stage wear rate shows a similar trend with the first stage wear. Figure 5-6 (a) and (b) imply that if the groove depth is zero, namely a plain friction lining without groove, wear rates are minimum in both wear stages.

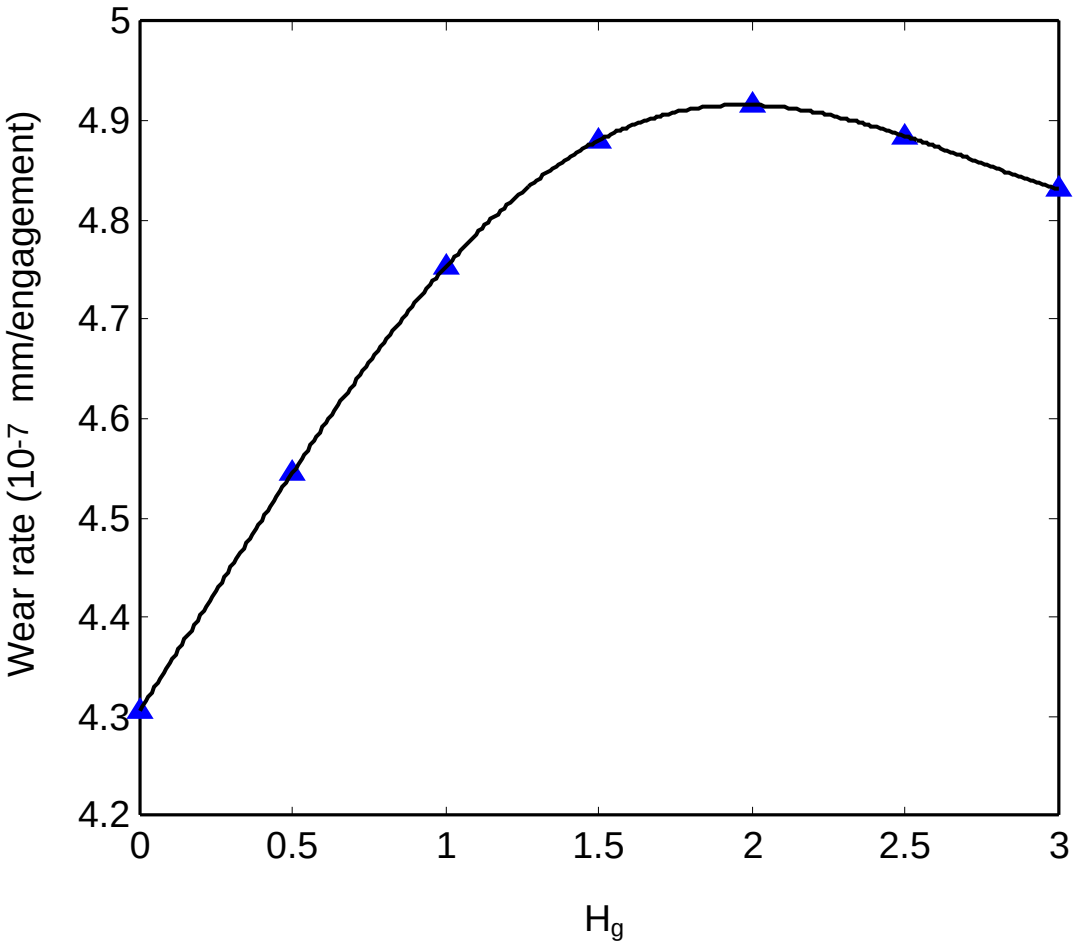

(a) First stage wear

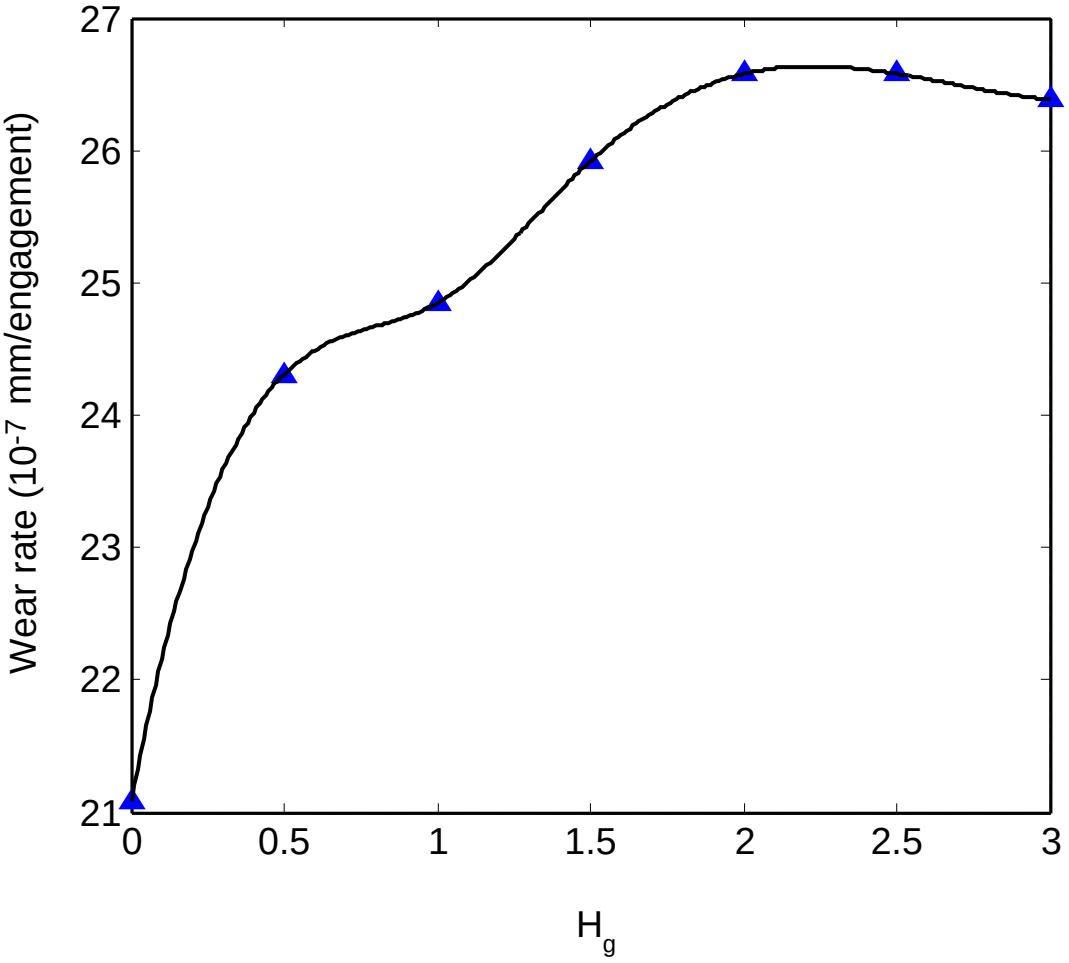

(b) Second stage wear

Figure 5-6 Effect of groove depth on average surface wear of the two stages ($\phi = 0.1$)

To analyze the effect of groove depth, we refer to the results of engagement time in Figure 5-7 and contact load in Figure 5-8. Figure 5-7 shows that the engagement time is increased until the groove depth ratio reaches 1 and is then gradually reduced. For shallow grooves ($H_g < 1.0$), a high hydrodynamic pressure is generated within the grooved region at the beginning of the engagement stage. By striking a balance with the applied engagement load, the contact pressure and induced asperity contact torque is smaller for higher groove depth ratio, leading to a longer engagement time. For deep grooves ($H_g > 1.0$), the engagement time begins to decrease with larger groove depth due to a smaller resistance for the squeeze motion (instead of forming large hydrodynamic load, the ATF tends to flow through the groove channel). When the friction lining comes into full contact with the separator disk, the contact load is larger as compared with the shallow groove case. We define the dimensionless contact load as the ratio of the contact load by asperity divided the applied engagement load. As shown in Figure 5-8, the dimensionless contact load follows an inverse trend with the engagement time. The case of

$H_g = 0.5$, and 1.5 are very close so only the result of $H_g = 0.5$ is shown. For the close case of $H_g = 2,\ 2.5$, and 3, we show the contact load for $H_g = 2$. The overall contact load for the case of $H_g = 1.0$ is smallest. Since the existence of groove definitely increases the load-carrying capacity, a plain friction lining without groove case produces the largest contact load.

Overall, the first stage wear induced by thermal degradation depends on two factors: engagement time as duration of heat generation and the heat flux rate by asperity contact. As the groove depth is increased, the longer engagement time indicates more cumulated thermal degradation. Although the engagement time decreases for $H_g > 1.0$, the overall contact load is higher, which also contributes to the increased wear rate. For $H_g \geq 2.0$, the contact load is only slightly increased and deeper grooves reduce the wear rate with a smaller engagement time. Therefore, with a minimal engagement time, a plain friction lining without groove case shows smallest wear rate in both wear stages. The case of $H_g = 1.0$ implies the minimum contact load, and hence the mechanical effect for the second stage wear is smaller. Therefore, Figure 5-6 (b) shows a gentle slump for the wear rate when $H_g = 1.0$, compared with the trend of the first stage wear in Figure 5-6 (a).

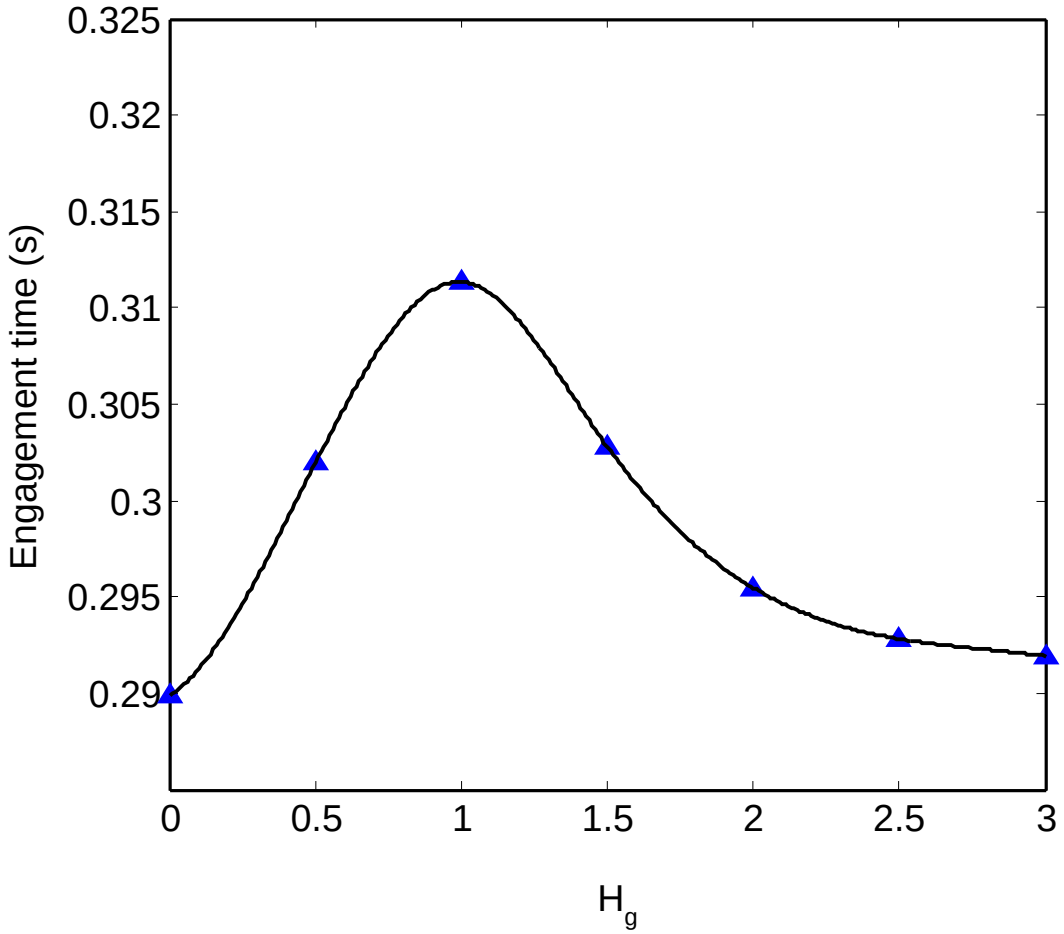

Figure 5-7 Effect of groove depth on engagement time ($\phi = 0.1$)

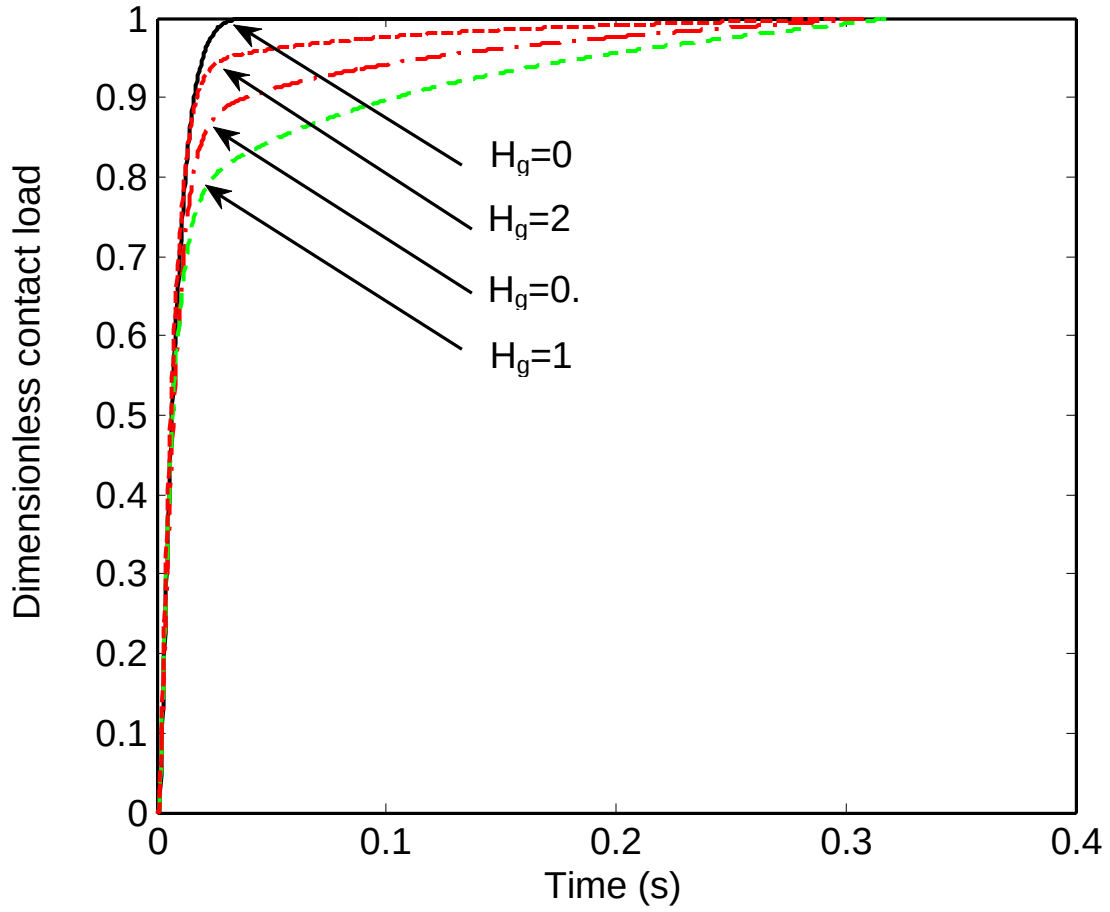

Figure 5-8 Effect of groove depth on contact load ($\phi = 0.1$)

- Groove area ratio for radial groove case

Figure 5-9 illustrates the role of groove area ratio on the surface wear of the friction lining with a groove depth ratio of $H_g = 1.0$. It shows an increasing trend of the wear rates for larger groove area ratios. Figure 5-10 shows the effect of groove area ratio on the engagement time. Since large hydrodynamic load is generated for a high groove area ratio, the engagement time is increased. There are two reasons for the correlation between the high groove width and the increased wear rates: more thermal degradation is cumulated in groove patterns with larger groove area ratio due to longer engagement time; the asperity contact and heat generation will concentrate on a smaller land area and intensifies the thermal and mechanical degradation of wear. However, since wider grooves can promote stronger convectional cooling by ATF (especially for $\phi = 0.2$), the wear rates in the first stage, are not uniformly increased with higher groove area ratios, which are observed in Figure 5-9 (a). In contrast, the contact pressure at the land area is higher for wider groove and hence the second stage wear that incorporates mechanical effect is promoted with increased groove area ratio, as illustrated in Figure 5-9 (b).

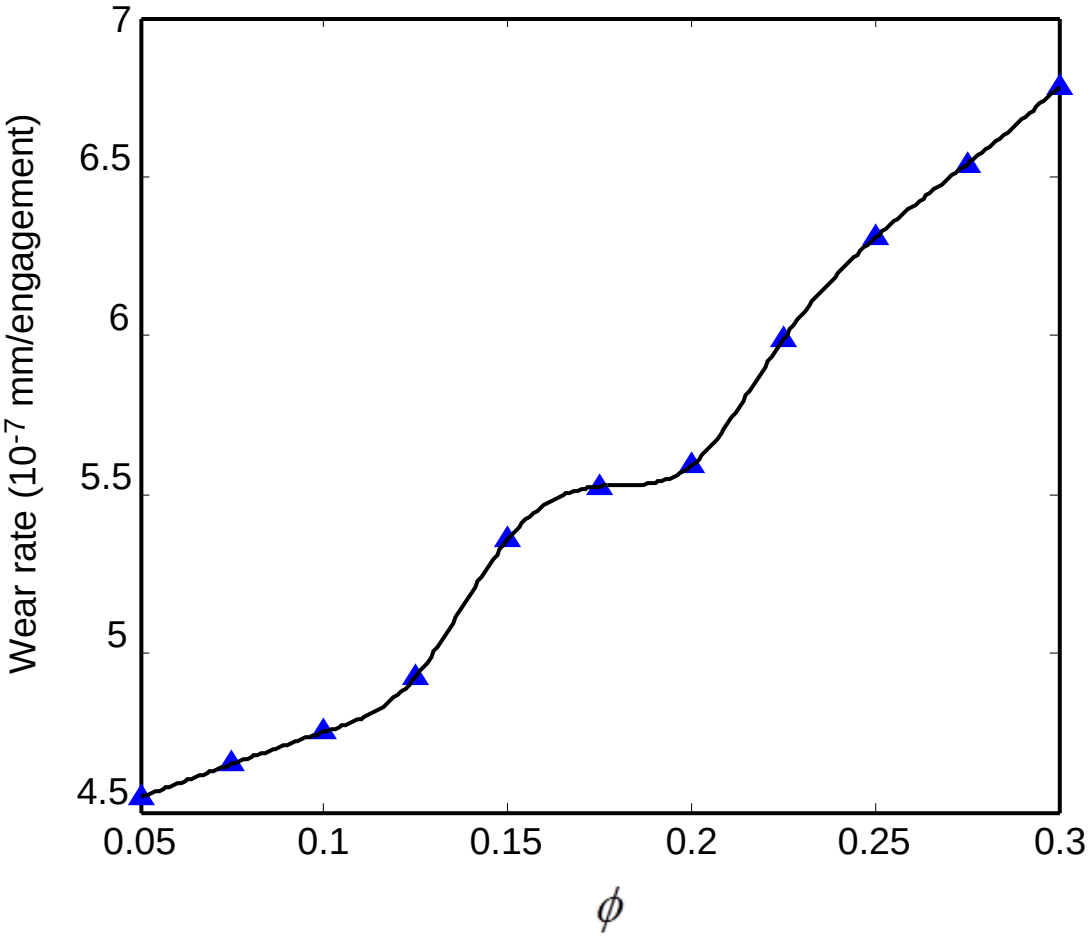

(a) First stage wear

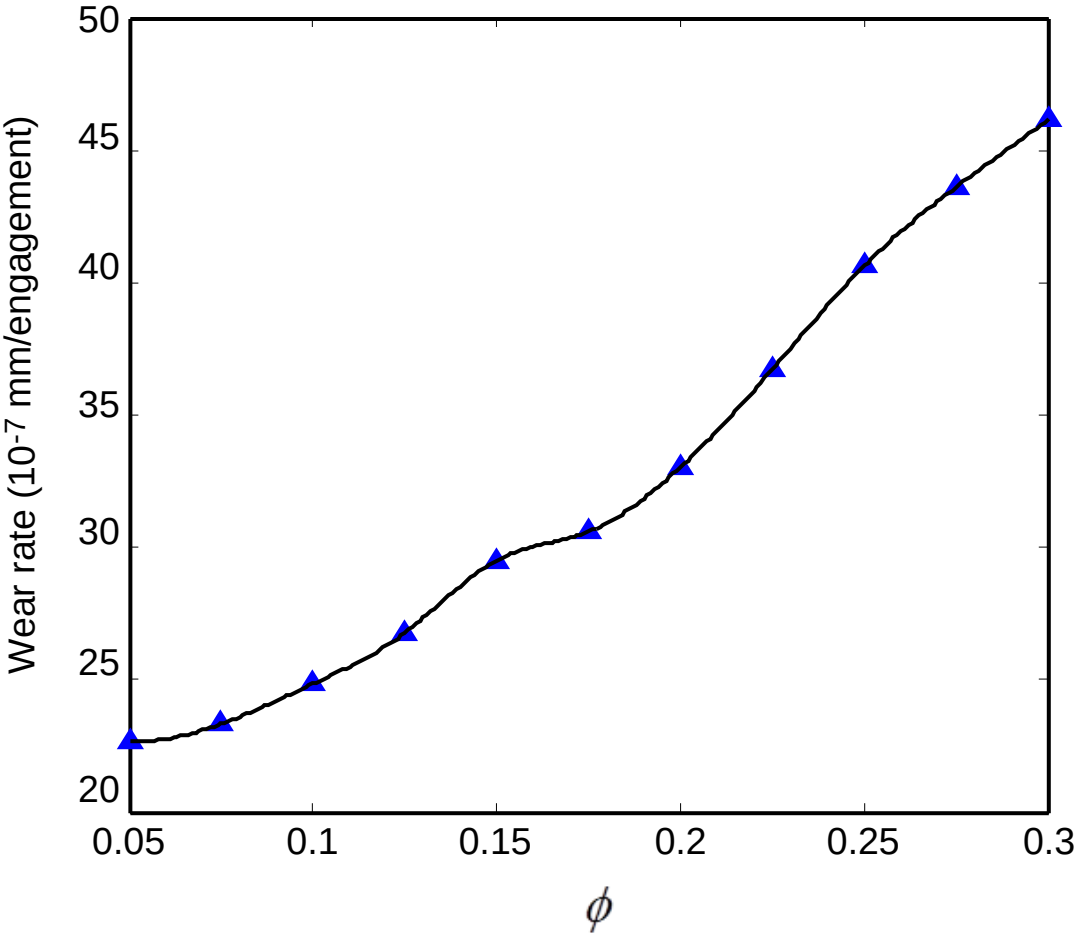

(b) Second stage wear

Figure 5-9 Effect of groove area ratio on average surface wear of the two stages ($H_g = 1.0$)

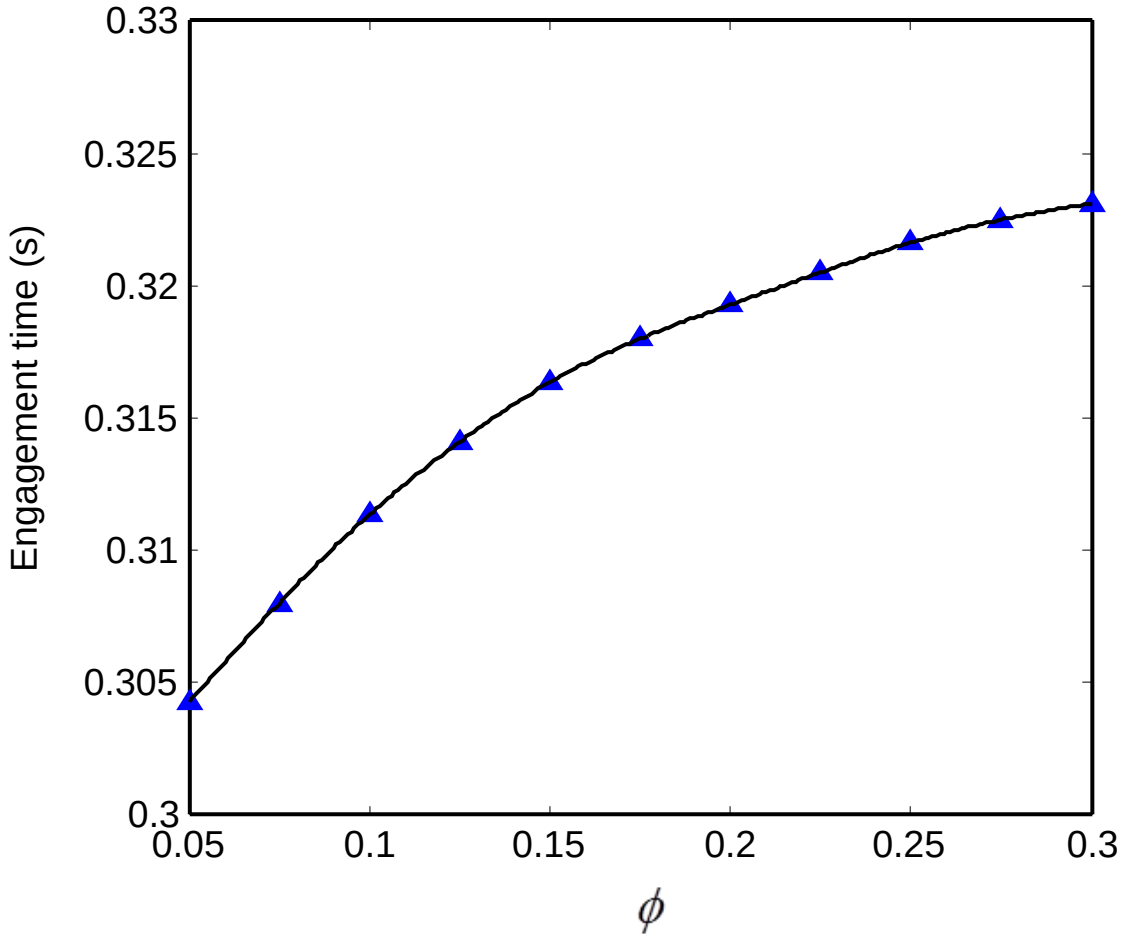

Figure 5-10 Effect of groove area ratio on engagement time ($H_g = 1.0$)

- Effect of groove number in radial groove

We now consider the wear behavior of various groove numbers for a fixed total groove area, as shown in Figure 5-11. For friction lining of 8 grooves at medium input energy level, the first and second stage wear rates are 4.73×10^{-7} (mm/engagement) and 2.49×10^{-6} (mm/engagement). When 16 grooves are implemented, the first and second stage wear rates are 4.91×10^{-7} (mm/engagement) and 2.51×10^{-6} (mm/engagement). Generally, more grooves leads to larger hydrodynamic load which prolongs the engagement time and produces more thermal degradation, which explains larger first stage wear rate for the 16 grooves case. On the other hand, the induced contact load is also smaller, which indicates less thermomechanical degradation in the second wear stage. Therefore the second stage wear rate of the two cases tends to be close.

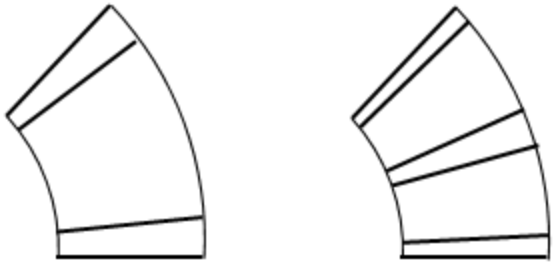

(a) 8 grooves (b) 16 grooves

Figure 5-11 Different groove number with same groove area ratio ($\phi = 0.2$)

- Internal groove profile for radial groove case

The influence of internal groove profile (round, trapezoid, and triangle) on the engagement was studied in [2]. For medium energy level with $H_g = 1.0$ and $\phi = 0.1$, the maximal engagement time of trapezoid groove section is 0.312 (s) and the minimal engagement time of round groove section is 0.311 (s). The difference of the corresponding first stage wear rate is 4.2722×10^{-9} (mm/engagement), which shows small effect of groove profile because the limited influence on generation of hydrodynamic load.

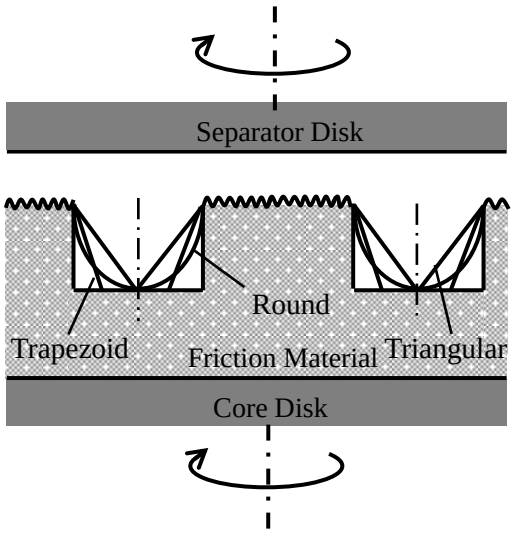

Figure 5-12 Different groove profile

5.4.3 Spiral groove

The geometric shape of the spiral groove is formulated as follows [23]:

$$r = r_1 e^{\theta \tan \alpha} \tag{25}$$

where α is the angle between the circumferential direction and tangential direction of the spiral curve, r and θ are the polar coordinates, and r_1 is the base radius of the spiral curve. Figure 5-14 shows the surface wear of the first stage for spiral groove with $\alpha = 20°$. The thermal characteristics of a wet clutch

with spiral groove pattern was presented in [2]. Compared with waffle and radial grooving pattern, the spiral groove case is predicted to have smaller wear rates with better thermal capacity. The influence of spiral angle on the two-stage wear rate is illustrated by Figure 5-15. With increased spiral angle, the wear rates in both stages are increased.

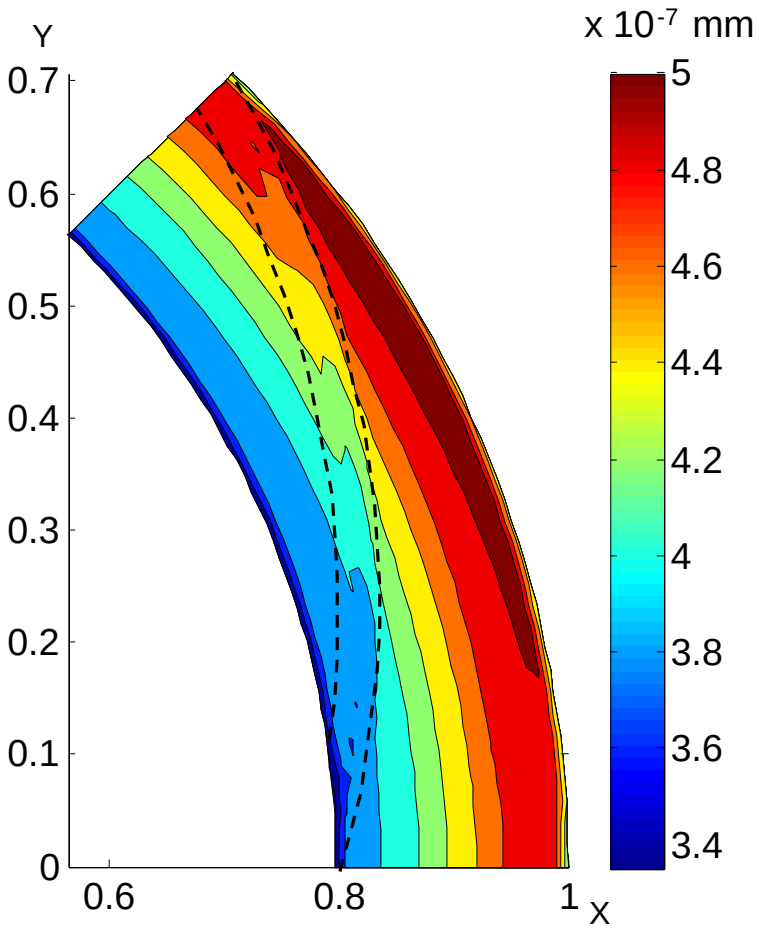

Figure 5-13 Surface wear conditions of spiral groove patterns in the first wear stage ($H_g = 1.0,\ \phi = 0.05$)

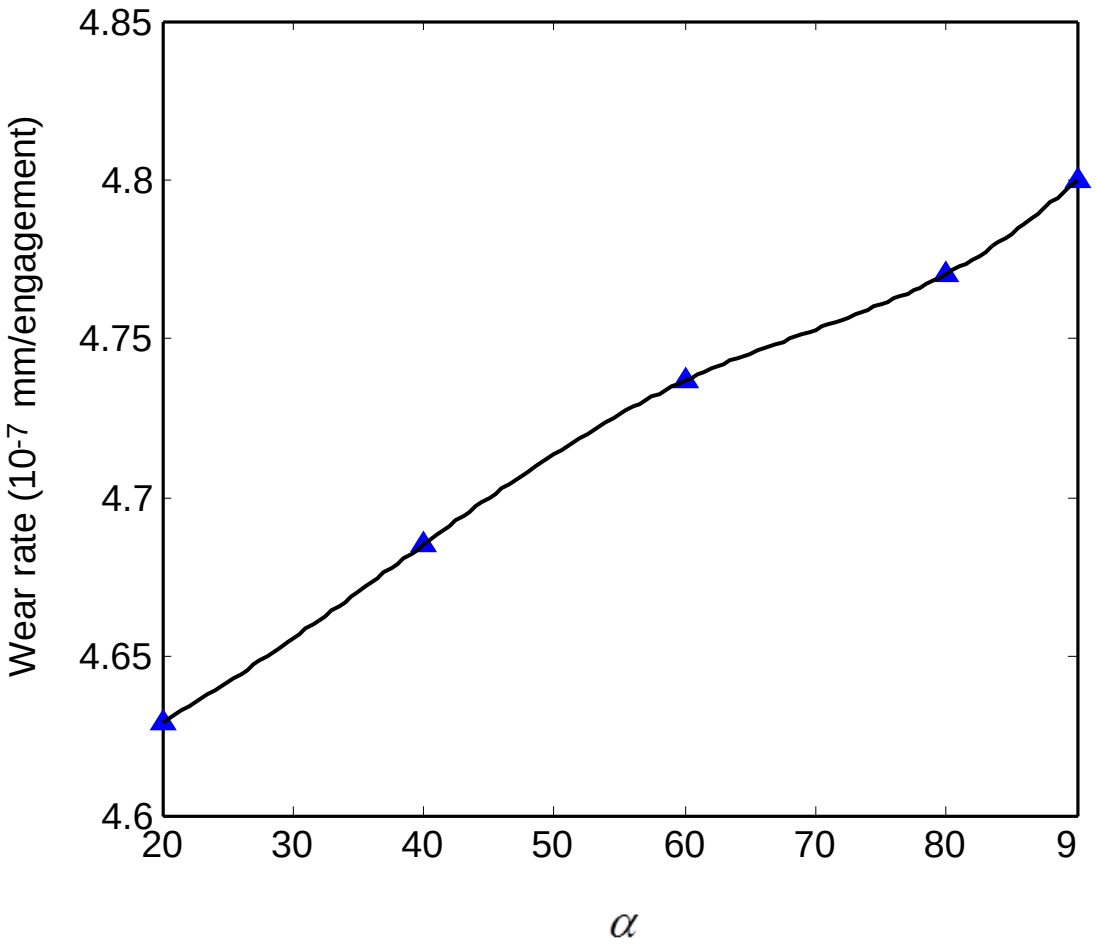

(a) First stage wear

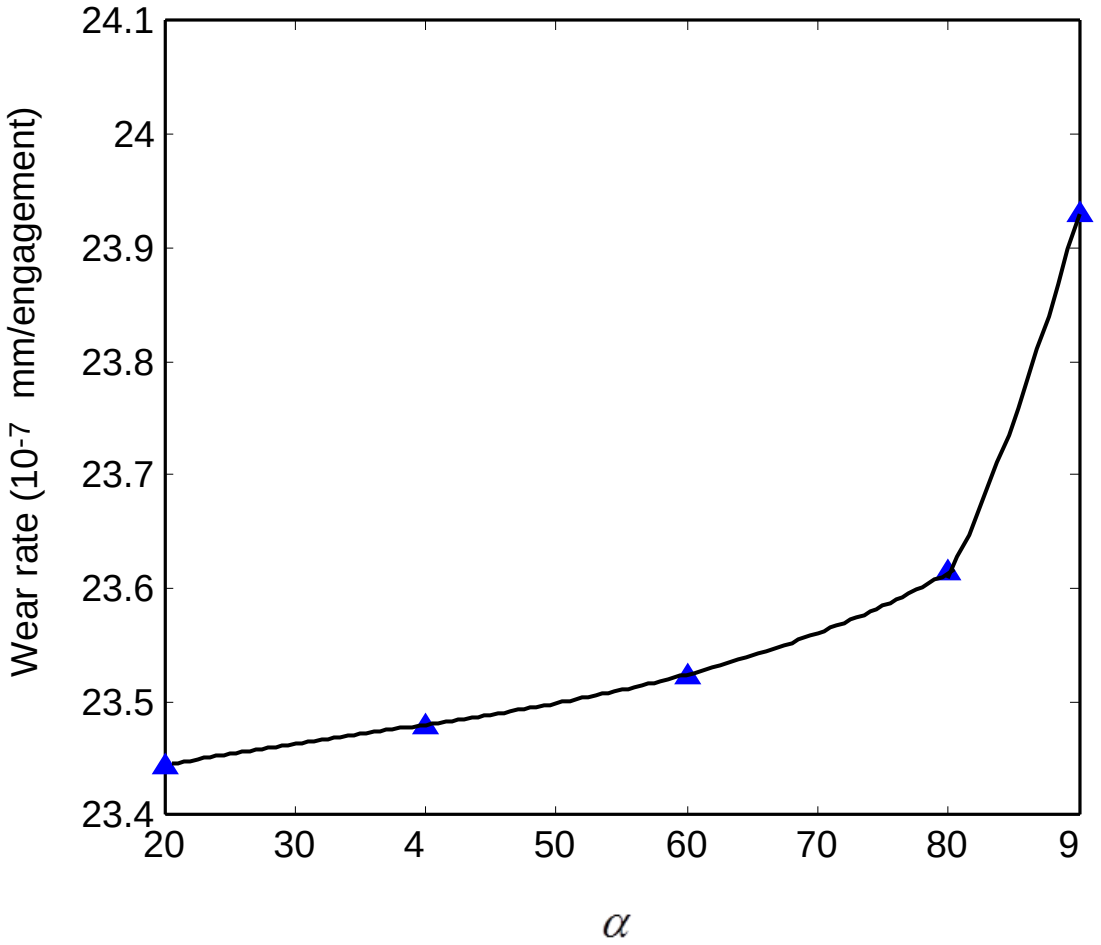

(b) Second stage wear

Figure 5-14 Effect of spiral groove angle on average surface wear ($H_g = 1.0,\ \phi = 0.05$)

With the wedge action and the pumping capability in spiral grooves, the sliding interfaces generate greater hydrodynamic pressure and the surfaces are cooled down by flowing of ATF. The groove shape is mainly controlled by the spiral angle α. It determines the wedge and pumping effect. A parametric result on the spiral angle effect is shown in Figure 5-15. By increasing the spiral angle from 20 ° to 80 °, the engagement time increases by about 0.56 (s). If the spiral angle is 90 °, the pumping effect is eliminated and the groove shape becomes equivalent to that of the radial groove. For a lower spiral angle, the hydrodynamic pressure at the beginning of the engagement stage drops faster, which leads to higher contact load and a larger total torque. Therefore, for the same groove depth ratio and groove area ratio, the engagement time of the spiral grooving pattern is generally smaller than the radial grooving one.

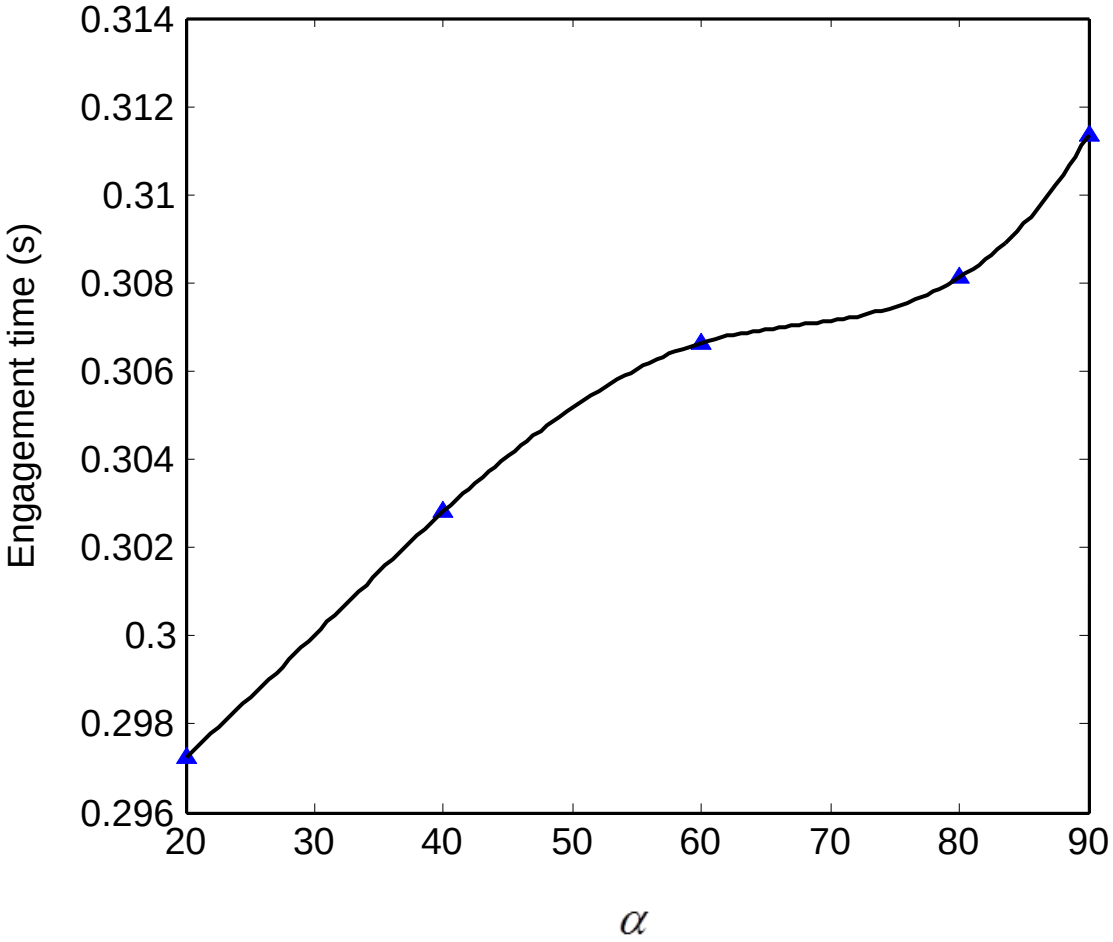

Figure 5-15 Effect of spiral groove angle on engagement time ($H_g = 1.0$, $\phi = 0.05$)

5.4.4 Summary on groove effect

From comparison among the various groove pattern and geometric specifications, it can be concluded that the hydrodynamic effect by groove is significant for the two-stage wear rates due to its relationship with engagement time and the induced contact load. From the parametric study, the smallest first stage wear rate occurs for the no groove case and the spiral groove case produces the minimum second stage wear rate. Table 5-3 shows the total material life of the friction lining as the engagement number at the end of the second wear stage, which is volume of organic fiber divided by the two-stage wear rate. Overall, a plain friction lining without groove provides most desirable durability in term of wear.

Table 5-3 Groove effect on material life

Groove pattern	First stage wear rate (10^{-7} mm/engagement)	Second stage wear rate (10^{-7} mm/engagement)	Material life (10^4 cycle)
Waffle	5.82	36.95	8.31
Radial ($H_g = 1.0,\ \phi = 0.05$)	4.80	23.93	11.69
Spiral ($\alpha = 20°$)	4.63	23.44	12.00
Plain (no groove)	4.31	23.79	12.21

5.5 Wear under different operational configurations

Compared with other influential factors of friction lining wear, the engagement energy level is the most dominating one. According to the THD simulation, the peak temperature of a high energy level is 300% higher than that of a low energy level, where the energy input ratio of high and low energy level is 2.78. Comparison of wear rate for different power input is reported in [5].

Although the target energy of a clutch system configuration is determined by the load and the speed, the engagement results and the thermal characteristics can be different for the same energy input because of the two important settings. Therefore, for a specific power input, the wear rate can be different for various load – speed combinations. A comparison is made for relatively low energy level, which is shown in Table 5-4.

Table 5-4 First stage wear rate of specific energy level but different load – speed settings

Applied pressure (MPa)	Speed (rpm)	Engagement time (s)	Wear rate (10^{-7} mm/engagement)
1.25	1500	1.59	66.61
1.875	1000	0.7005	8.06
1.55	1500	1.29	50.37

From the above table, the wear rate of the low speed – high load case is much smaller than the high speed – low load one. For specific energy level, the heat generation rate is the same for different load – speed settings. However, with high target speed but low engagement load, the engagement time is much longer, which results in considerable degradation accumulation. For same speed but moderately higher applied pressure, the decreased engagement time generates lower wear rate, while the energy input is higher. Therefore, it is desirable to set engagement load to be appropriately large for the high target speed cases in order to a faster engagement completion and less wear.

5.6 Material considerations in a wet clutch system

5.6.1 Permeability and friction lining thickness

Due to its permeable nature, the friction lining soaks portion of ATF, which can be squeezed out under applied engagement load. The squeeze motion generates extra hydrodynamic load and lubricate the sliding interface to provide smooth transmission power. According to the Darcy's law, the flow in the porous medium is directly determined by the permeability, which can be adversely affected by several factors. One of the cases is that manufacturing of the grooves on the friction facing might make the groove wall less permeable. Another possibility takes place for the friction material that undergoes large engagement cycles. Both cases can reduce the squeeze motion, affecting transmission performance and thermal characteristics.

The torque response with different permeability of the friction material is presented in Figure 5-16, which is the engagement simulation for radial groove case ($H_g = 1.0$ and $\phi = 0.1$). For the higher permeability case, the hydrodynamic pressure at the beginning of the engagement stage is larger. Soon, the film thickness is reduced to a smaller level, which leads to more asperity contact and larger contact torque. Therefore, the duration of the engagement becomes shorter than the low permeability case. With respect to the wear rate results, it is shown that wear rate for the high permeability case is smaller as well. For the friction lining with permeability of 1.0×10^{-12} (m^2), or, 1.01 (darcy), the first stage wear rate is 6.55×10^{-6} (mm/engagement); with permeability being 1.0×10^{-13} (m^2), or, 0.10 (darcy), the first stage wear rate is 6.97×10^{-6} (mm/engagement). Such result mainly results from shorter engagement time that produces thermal degradation of smaller magnitude during the engagement cycle.

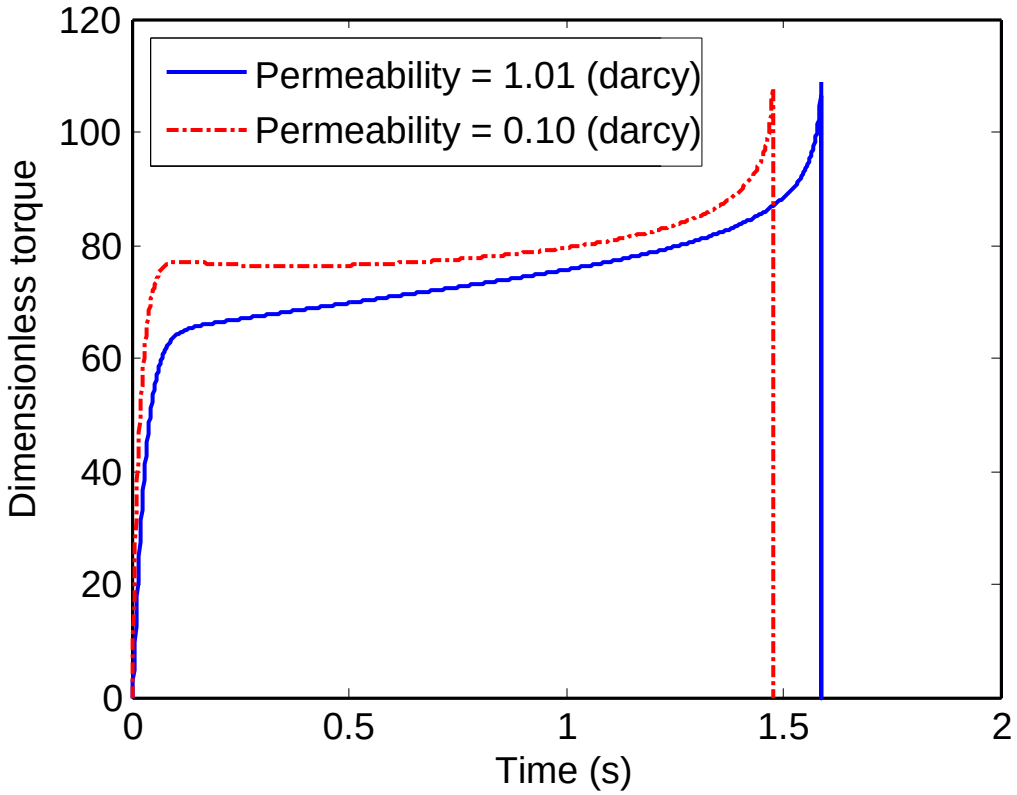

Figure 5-16 Torque curve of different permeability (1.25 MPa and 1500 rpm)

The thickness of friction lining can influence both the squeeze flow and the heat conduction in the clutch system, where the heat partition is determinant in the temperature evolution during the engagement cycles. Reduced thickness of the friction lining indicates that more heat is conducted to the interior and more thermal degradation is induced. The computed wear rates for different friction lining thickness are summarized as follows: for the initial thickness of H_0 = 5.652 (mm), first stage wear rate is 6.97×10^{-6} (mm/engagement); for the half thickness of H_0 = 2.826 (mm), first stage wear rate is increased to 7.40×10^{-6} (mm/engagement).

5.6.2 Fiber additions

According to Ho et al. [14], the tribological and mechanical performance of the friction material can be influenced by different fiber additions, which include steel, brass, cellulose and ceramic fibers. For paper-based friction material, such wear of mechanical consideration only takes place in the second wear stage. To investigate the wear resistance of improved mechanical strength, a decreased the mechanical coefficient γ is assumed for previous prediction case. For waffle grooving pattern at medium energy level, the second stage wear rate is decreased by 5.27% by reducing γ by 10%. Such effect is more phenomenal for higher power input.

5.7 Concluding remarks

A comprehensive analysis of wear factors is performed for the friction of a wet clutch. The relevant factors include groove design, engagement power, material properties of ATF and the friction lining. Based on the wear modeling and the engagement simulation, the parametric study shows the corresponding wear behavior of the involved factors and the relevant discussion is presented.

For surface pattern, three kinds of grooves are investigated including waffle, radial and spiral. The groove effect is analyzed based on the accumulation of thermal degradation during engagement and generation of contact load involving mechanical factor in the second wear stage. Under the same operational configurations, the waffle groove case shows the largest wear rate for both wear stages. More parametric study is presented for radial groove case by considering groove depth ratio, groove area ratio, groove number and groove profile. With low engagement time, plain friction lining and the spiral groove case shows the smaller wear rate than other grooving patterns. Summarizing the effect of surface pattern on total material life, the existence of groove tends to promote greater wear rates by prolonging the engagement time.

Although the power input of the clutch system is usually regarded as the challenge for the thermal capacity of clutch system, the wear rate is most closely related to engagement time, which varies respect to the configuration of engagement operation for the same energy level. For high speed, higher load results can reduce the wear rate by reducing the engagement time, though the energy level is increased.
The material properties play a significant role in the wear behavior by affecting the transmission results and the heat transfer during the engagement. Higher permeability and higher thickness of the friction lining indicates a lower wear rate. Improved mechanical strength of the friction material also moderately enhances the wear resistance.

5.8 References

[1] J. Jang, M. Khonsari, R. Maki, Three-dimensional thermohydrodynamic analysis of a wet clutch with consideration of grooved friction surfaces, Journal of Tribology, 133 (2011) 011703.

[2] M. Li, M. Khonsari, D. McCarthy, J. Lundin, Parametric analysis for a paper-based wet clutch with groove consideration, Tribology International, 80 (2014) 222-233.

[3] M. Holgerson, J. Lundberg, Engagement behaviour of a paper-based wet clutch Part 2: Influence of temperature, Proceedings of the Institution of Mechanical Engineers, Part D: Journal of Automobile Engineering, 213 (1999) 449-455.

[4] Y. Yang, R.C. Lam, Theoretical and experimental studies on the interface phenomena during the engagement of automatic transmission clutch, Tribology Letters, 5 (1998) 57-67.

[5] M. Li, M. Khonsari, D. McCarthy, J. Lundin, On the wear prediction of the paper-based friction materialin a wet clutch, Wear, 334 (2015) 56-66.

[6] N. Lingesten, Wear behavior of wet clutches, (2012).

[7] N. Lingesten, P. Marklund, E. Höglund, M. Lund, J. Lundin, R. Mäki, Apparatus for continuous wear measurements during wet clutch durability tests, Wear, 288 (2012) 54-61.

[8] R. Tatara, P. Payvar, Multiple engagement wet clutch heat transfer model, Numerical Heat Transfer: Part A: Applications, 42 (2002) 215-231.

[9] J. Jang, M. Khonsari, Thermal characteristics of a wet clutch, Journal of tribology, 121 (1999) 610-617.

[10] B. Satapathy, J. Bijwe, Performance of friction materials based on variation in nature of organic fibres: Part I. Fade and recovery behaviour, Wear, 257 (2004) 573-584.

[11] W. Scott, P. Suntiwattana, Effect of oil additives on the performance of a wet friction clutch material, Wear, 181 (1995) 850-855.

[12] P.S. Winckler, Clutch with pyrolytic carbon friction material, Google Patents, 1987.

[13] J. Fei, H.-J. Li, Y.-W. Fu, L.-H. Qi, Y.-L. Zhang, Effect of phenolic resin content on performance of carbon fiber reinforced paper-based friction material, Wear, 269 (2010) 534-540.

[14] S. Ho, J.C. Lin, C.-P. Ju, Effect of fiber addition on mechanical and tribological properties of a copper/phenolic-based friction material, Wear, 258 (2005) 861-869.

[15] P. Gopal, L.R. Dharani, F.D. Blum, Fade and wear characteristics of a glass-fiber-reinforced phenolic friction material, Wear, 174 (1994) 119-127.

[16] L. Kogut, I. Etsion, A finite element based elastic-plastic model for the contact of rough surfaces, Tribology transactions, 46 (2003) 383-390.

[17] E. Kartashov, V. Shevelev, A.A. Valishin, G. Bartenev, Limiting characteristics of brittle fracture of polymers, Polymer Science USSR, 28 (1986) 899-905.

[18] L.A. Sosnovskiy, R. Sosnovskaya, K. Frolov, N. Makhutov, Tribo-fatigue: Wear-fatigue Damage and Its Prediction, Springer, 2010.

[19] M. Fesanghary, M. Khonsari, Topological and shape optimization of thrust bearings for enhanced load-carrying capacity, Tribology International, 53 (2012) 12-21.

[20] M.M. Razzaque, T. Kato, Effects of groove orientation on hydrodynamic behavior of wet clutch coolant films, Journal of tribology, 121 (1999) 56-61.

[21] E. Berger, F. Sadeghi, C. Krousgrill, Finite element modeling of engagement of rough and grooved wet clutches, Journal of Tribology, 118 (1996) 137-146.

[22] J. Jang, M. Khonsari, On the formation of hot spots in wet clutch systems, Journal of tribology, 124 (2002) 336-345.

[23] Y. Qiu, M. Khonsari, Thermohydrodynamic analysis of spiral groove mechanical face seal for liquid applications, Journal of Tribology, 134 (2012) 021703.

CHAPTER 6 DYNAMICS ANALYSIS OF TORSIONAL VIBRATION INDUCED BY CLUTCH AND GEAR SET IN AUTOMATIC TRANSMISSION

6.1 Introduction

The powertrain in a motor vehicle is a multi-component system that generates power and delivers it to the vehicle to provide motion. Essentially, it consists of the engine, transmission, drive shafts, differential and the final drive (i.e., the wheels). The transmission is responsible for producing a range of speeds and torques through a combination of the planetary gear train (to generate different gear ratios) and the wet clutch (to control the shift action with engagement/disengagement operations). The differential appropriately slows down the rotational speed of transmission and delivers power to wheels via the drive shaft, enabling rotation at different speeds. Thus, by converting fuel energy into kinetic energy that overcomes the friction force generated at the tire/road interface, the vehicle moves with the transmitted power.

Modeling and simulation of powertrain dynamics lay the foundation for optimal design in the automotive industry. The study of the factors affecting noise, vibration, and harshness (NVH) in a powertrain system is closely related to propagation of torsional vibration in the driveline, which adversely affects the vehicle's performance and reliability. These factors are interconnected. Nevertheless, most of the published papers on powertrain dynamics have treated individual components of the powertrain system separately, without taking into account the holistic aspect of the system. For example, references [1-4] on automotive engine modeling concentrate on the fuel delivery dynamics, speed/torque prediction, and torque harmonics. References [5, 6] focus their attention on the nonlinear engine diagnostics with the particular attention to the engine's state in an attempt to minimize the energy dissipation and smooth shifting of the gears in the transmission system.

Studies of the transmission system include modeling and simulation of both the gearbox and the clutch. According to the review by Özgüven and Houser [7], analytical and modeling approaches on gear dynamics research can be classified in the following categories: models that are based on simple dynamic factors, models that deal with tooth compliance, models for gear dynamics, and models for geared rotor dynamics with consideration of torsional vibration. Nonlinear dynamics studies of gear systems show that the transient stiffness and backlash lead to the loss of contact and promote gear rattling response, a phenomenon that can be observed in the frequency domain and the time domain [8, 9].

A thorough analysis of a wet clutch in the automatic transmission system requires a comprehensive tribological modeling of the hydrodynamic squeeze action and contact pressure due to the interaction of the surface asperities [10] with consideration of thermal effects. This type of a model is often classified as thermohydrodynamic (THD) analysis, which investigates the transmission results and temperature profile under different groove design. An undesirable phenomenon associated with the torsional vibration in the wet clutch system is a form of instability known as shudder, or judder [11]. According to [12], the mechanism of transmission instability can be explained by the frictional characteristics of a wet clutch, which is closely influenced by the aging of ATF or stick-slip behavior.

References [13-15] devote their studies to the final drive. They present mathematical models of the wheel dynamics and study the interaction of road and tires under different operating conditions. The rolling noise of tires has also been investigated using the finite element approach [16-18].

This paper aims to investigate NVH factors in an automotive powertrain system through a comprehensive modeling framework that encompasses the major components. A detailed description of the nonlinearities of the transmission system is presented together with the tire model to consider the skidding effects at the slippery road conditions. In Section 2, modeling of the powertrain dynamics is described by delving into its various components in order to characterize the nonlinear behaviors of the system. In Section 3, the essential components are represented by torsional elements to be assembled into a 12-DOFs system. Simulation results are obtained by solving the dynamic equations to perform the NVH analysis. Concluding remarks on current powertrain study are summarized in the last section.

6.2 Model of driveline nonlinearities

Traditional models of powertrain dynamics are constructed by assembling the linear dynamics of torsional elements [19] or through using the bond graph representation to describe the corresponding differential equations in the driveline [20]. Nonlinearities are often neglected for simplification of the analysis. However, they are known to be significant especially for characterizing the behavior of transmission as described in the following sections. In this paper, we first describe the clutch engagement process with consideration of stick-slip, followed by a model of the planetary gear with backlash, and consider the tire-road interaction with a dynamic friction model. We then present results for the entire powertrain dynamics by incorporating the transmission nonlinearities.

6.2.1 Engagement and stick-slip behavior of a wet clutch

The major components of an automatic transmission include a torque converter, planetary gear sets, clutch and hydraulic system (including oil pump, valves, and control units). When the rotational speed difference between the input and output is significant, the torque is multiplied to serve as a reduction gear. The engagement operation of a wet clutch is controlled hydraulically via a piston.

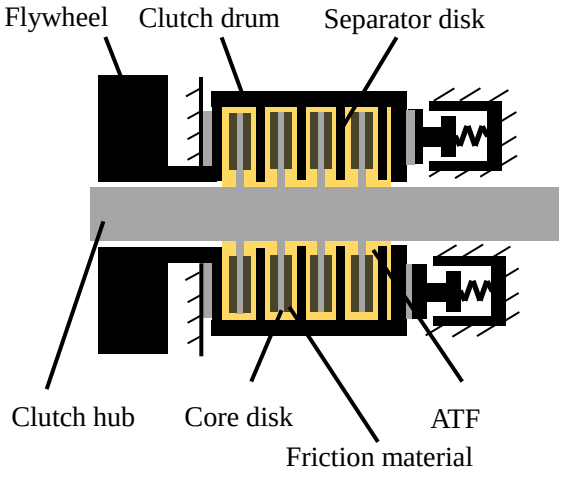

Figure 6-1 Schematic of a wet clutch

As shown in Figure 6-1, a wet clutch is composed of a series of core disks with the friction material attached on both sides, several metallic separator disks, and the ATF that lubricates the sliding surfaces. The hydraulic system controls its engagement operation by the movement of a piston. The entire engagement cycle of a wet clutch is separated into four stages: engagement, soaking, dwell, and

stabilization periods. The last three periods belong to the "disengaged state". During the engagement stage, an axial load is applied that forces the disks to come together and hydrodynamically squeezes the ATF. The lubrication condition shifts from initially hydrodynamic regime —where the surfaces are completely separated by ATF— to mixed lubrication regime —where the contact occurs at the surface asperity level—and eventually to the boundary lubrication regime, where the surfaces are in intimate contact. These regimes are typically described by what is universally known as the "Stribeck curve" [10]. During the engagement, the total transmission torque is composed of viscous shear torque and asperity contact torque:

$$T_{ac} = f_d \int_0^{2\pi} \int_{r_i}^{r_o} r^2 P_c dr d\theta \tag{1}$$

$$T_{hd} = \left(\dot{\theta}_{CD} - \dot{\theta}_{CH}\right) \int_0^{2\pi} \int_{r_i}^{r_o} \left(\phi_f + \phi_{fs}\right) \frac{\mu r^3}{h} dr d\theta \tag{2}$$

where

$$f_d = C_1 - C_2 \log\left[\frac{\left(r_i + r_o\right)}{2}\left(\dot{\theta}_{CD} - \dot{\theta}_{CH}\right)\right]$$

T_{ac} represents the asperity contact torque, T_{hd} is the hydrodynamic torque, r_o and r_i are respectively the outer radius and the inner radius of the friction disk, P_c is the contact pressure determined by the elasto-plastic asperity contact model, $\dot{\theta}_{CD}$ and $\dot{\theta}_{CH}$ are the rotational speed of clutch drum and clutch hub, ϕ_f and ϕ_{fs} are the shear stress factors, μ is the viscosity of the ATF that is temperature-dependent, and h is the film thickness of lubrication, f_d is the dynamic coefficient of friction, C_1 and C_2 are two parameters, often determined experimentally, to characterize the dynamic coefficient of friction.

Due to the intense thermal effect by the heat generation of frictional work at the sliding interface of the friction pair (usually more than 200 ℃ within 1s), the viscosity of the ATF drastically changes. To take the variation of viscosity with temperature into account, the following nonlinear relationship recommended by the American Society for Testing and Materials (ASTM) is used:

$$\log_{10} \log_{10}\left(10^6 \frac{\mu}{\rho_f} + 0.7\right) = A - B \log_{10}\left(\Theta + 273\right) \tag{3}$$

The detailed numerical simulation that investigates the thermal characteristics of a wet clutch with groove consideration is available in recent publications [10, 21].

The dynamic instability in a wet clutches, the so-called shudder (or judder), gives rise to an undesirable performance in terms of vibration and noise with a frequency range of 5-20 Hz [11]. It stems from the nonlinear frictional behavior when the transition between static and kinematic friction occurs. The phenomenon is closely related to the frictional characteristics of the clutch system and the configurations of powertrain components (driveline inertia, damping, and mode coupling, etc.). Shudder usually emerges from the negative slope of the friction-velocity curve and causes instability due to negative damping in pure slipping motion.

Different approaches have been reported to study the stick-slip behavior such as smoothing method [22] and switch model [23]. The smoothing method takes friction smoothing procedures with an arctan-type function for μ-v curve and the switch model computes the friction forces under different motion state. Analysis and simulation of clutch shudder taking account of a stick-slip factor are presented by Crowther et al. [24]. As shown in Figure 6-2, the switched frictional torque between sticking and slipping can be expressed as follows [25]:

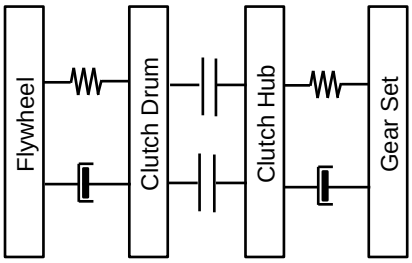

Figure 6-2 A 4 DOF system of clutch stick-slip behavior

$$T_C = \begin{cases} T_{hd} & \text{(locked)} \\ N_f \operatorname{sgn}\left(\dot{\theta}_{CD} - \dot{\theta}_{CH}\right)\left(T_{ac} + T_{hd}\right) & \text{if } \left|\dot{\theta}_{CD} - \dot{\theta}_{CH}\right| \geq \varepsilon \text{ (slip)} \\ N_f \operatorname{sgn}\left(T_{INT}\right)\left(T_{ac} + T_{hd}\right) & \text{if } \left|\dot{\theta}_{CD} - \dot{\theta}_{CH}\right| < \varepsilon \text{ and } T_{LT} < \left|T_{INT}\right| \text{ (stick-slip)} \\ T_{INT} & \text{if } \left|\dot{\theta}_{CD} - \dot{\theta}_{CH}\right| < \varepsilon \text{ and } T_{LT} \geq \left|T_{INT}\right| \text{ (stick)} \end{cases} \quad (4)$$

where

$$T_{INT} = T_{INT\_left} + T_{INT\_right}$$

$$T_{LT} = \frac{2\pi f_s P_0}{3}\left(r_o^3 - r_i^3\right)$$

$$T_{INT\_left} = -I_{CD}\ddot{\theta}_{CD} + C_{FCD}\left(\dot{\theta}_F - \dot{\theta}_{CD}\right) + K_{FCD}\left(\theta_F - \theta_{CD}\right) - C_{CDCH}\left(\dot{\theta}_{CD} - \dot{\theta}_{CH}\right)$$

$$T_{INT\_right} = I_{CH}\ddot{\theta}_{CH} - C_{CDCH}\left(\dot{\theta}_{CD} - \dot{\theta}_{CH}\right) - C_{CHG}\left(\dot{\theta}_{CH} - \dot{\theta}_G\right) + K_{CHG}\left(\theta_{CH} - \theta_G\right)$$

N_f is the number of friction pair, T_{INT} is the clutch torque at the instant of zero relative speed, T_{INT_left} and T_{INT_right} are calculated via the dynamic equations of clutch drum and clutch hub, T_{LT} is the "lock-up" torque, f_s is the static coefficient of friction, P_0 is the engagement pressure, ε denotes the tolerance of velocity calculation in simulations, θ is the angular displacement, $I, C,$ and K are the component's inertia, damping and stiffness, respectively. Equation (4) shows that the clutch torques T_{INT} and T_{LT} depend on the static and kinetic friction. Thus, the occurrence of stick-slip in a wet clutch depends on frictional characteristics, applied engagement load, and the operating conditions of the driveline (torque and speed).

6.2.2 Backlash of a planetary gear set

The gear system in transmission must deliver rotational motion with high mechanical reliability and efficiency. As shown in Figure 6-3, a conventional planetary gear set in the automatic transmission has three main components: a sun gear, several planetary gears supported by the carrier, and a ring gear. By

locking up one of the three components and switching the others to either input or output, various gear ratios can be achieved in a flexible manner to provide high power density for transmission. For a high gear ratio to slow down the transmission speed, the sun gear serves as the power input and rotates with a set of planetary gears supported by planet carrier while the ring gear is locked. For a low gear ratio to increase the transmission speed — the so-called outdrive — the power goes directly to the planet carrier and the planetary gears rotate against the ring gear, i.e. the output side of the gear transmission. Thus, the transmission performance largely depends on the characteristic of various types of gears.

One of the nonlinear behaviors of the gear system is the backlash, which is induced by the clearance between the mating gear teeth. Although a clearance is needed for the lubricant to form a protective film and to partially compensate for manufacturing errors, it can cause a loss in the gear teeth contact and generate transient mesh stiffness and vibration. These types of backlash-induced issues are considered to be the most common type of fault in the gear system. Investigations of the backlash of a planetary gear system are available in [26-28]. Sun et al. [26] developed a lateral-torsional model that takes into account multiple backlashes and error excitation. They computed the dynamic tooth load of a gear set as a nonlinear function of equivalent displacements or gear mesh deformation. The nonlinear dynamics of the planetary gear set is described as follows.

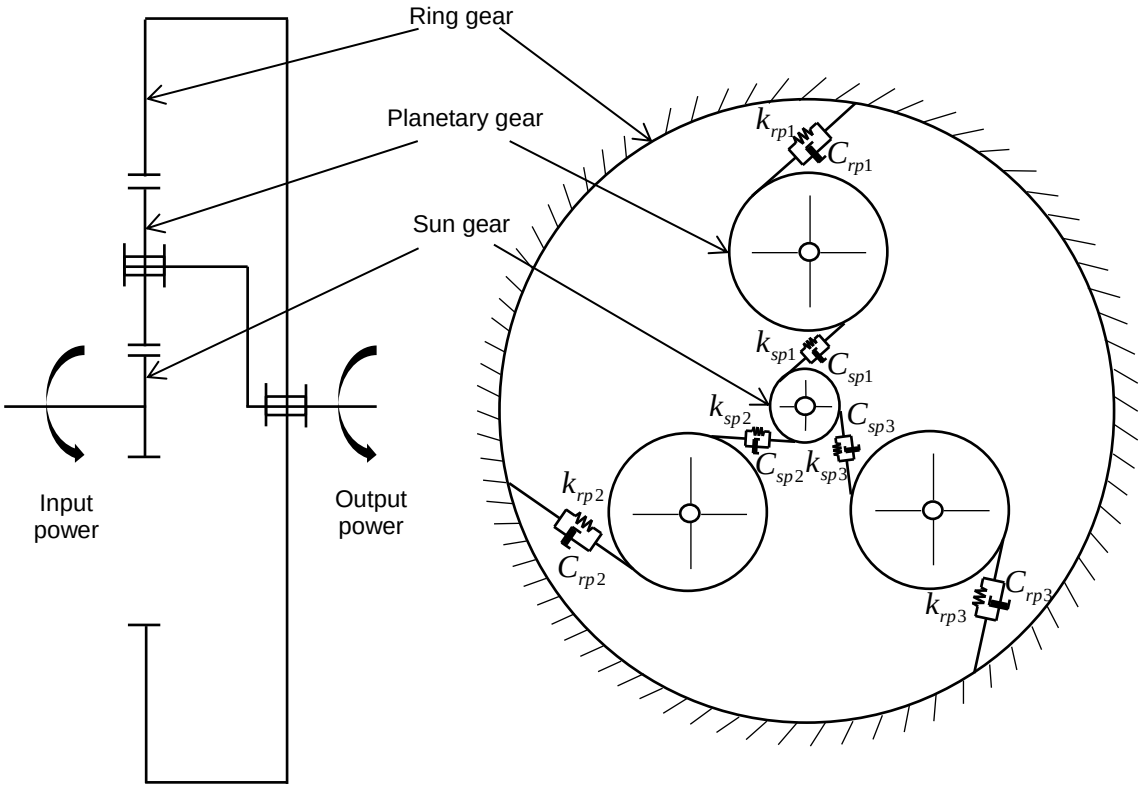

Figure 6-3 Schematic of a planetary gear set and backlash

As shown in Figure 6-4, the gear mesh is given by a nonlinear displacement function $f(\delta - e)$, which is an anti-symmetric function of gear mesh deformation of the mating gears δ and static transmission error e:

$$f\left(\delta-e\right)=\begin{cases}\delta-e-b & \delta>b\\ 0 & -b\le\delta\le b\\ \delta-e+b & \delta<-b\end{cases} \tag{5}$$

where b represents the backlash.

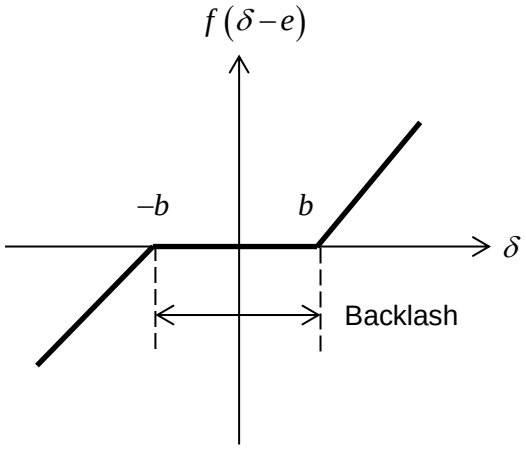

Figure 6-4 Nonlinear function of teeth deflection

Referring to Figure 6-3, the dynamic tooth load between the gear pairs W_{spi} and W_{rpi} are:

$$W_{spi}=k_{spi}\,f\left(\delta_{spi}-e_{spi}\right);\qquad W_{rpi}=k_{rpi}\,f\left(\delta_{rpi}-e_{rpi}\right) \tag{6}$$

where the subscripts 's', 'pi', 'r' represent the sun gear, i^{th} planetary gear component (i = 1, 2, 3), and ring gear, respectively. The parameters k_{spi} and k_{rpi} denote the transient mesh stiffness. They can be calculated using the finite element method (FEM) [29] or directly measured [30]. The damping forces between the gear pairs D_{spi} and D_{rpi} are:

$$D_{spi}=c_{spi}\left(\dot{\delta}_{spi}-\dot{e}_{spi}\right);\quad D_{rpi}=c_{rpi}\left(\dot{\delta}_{rpi}-\dot{e}_{rpi}\right) \tag{7}$$

where c_{spi} and c_{rpi} are the corresponding viscous damping.

The gear mesh displacement is calculated by incorporating the equivalent transverse displacement of gear components (sun gear, ring gear, planetary gear, and planetary carrier) in the line of action and the plane motion of sun gear along with the planetary carrier. Consider the high gear ratio transmission when the ring gear is locked, the gear mesh displacements between the i^{th} sun gear/planetary gear pair δ_{spi} and the displacements between i^{th} ring gear/planetary gear pair δ_{rpi} are given by [26]:

$$\delta_{spi}=r_s\theta_s+r_p\theta_{pi}-r_c\theta_c-\xi_s\sin\left(\phi_i-\alpha\right)+\eta_s\cos\left(\phi_i-\alpha\right),\ \ \delta_{rpi}=r_r\theta_r-r_p\theta_{pi}-r_c\theta_c \tag{8}$$

where the subscripts 'c' represent the planetary carrier, ξ_s and η_s denote the horizontal and vertical displacements of the sun gear – shaft compliance, α is the pressure angle of the gear pair, and $\phi_i=0,\ \pi/3,\ 2\pi/3$ indicates the theoretical position angle of the i^{th} planetary gear mounted on the

planetary carrier.

6.2.3 Wheel model

A friction model for the longitudinal interaction of the road and the tire is illustrated in Figure 6-5. The friction dynamics is velocity-dependent and is closely related to the rolling conditions. Since the nonlinear tire-road interaction determines the dynamics of the final drive in the driveline, a transient wheel torque model that can capture such frictional characteristics is necessary for characterizing the dynamics of the powertrain, rather than a static model.

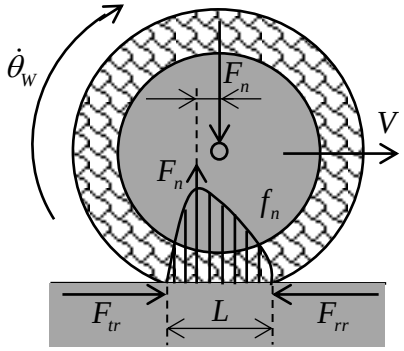

Figure 6-5 Schematic of one-wheel friction model

The static model, such as Pacejka's model, applies for the steady-state velocity condition. By modulating the linear and angular velocities separately, the friction/slip curve are measured to validate the analytical results with empirical corrections [31]. However, such an idealization does not always hold true for the transient phases of vehicle motion with continuous acceleration/braking. The dynamic friction model, in contrast, is capable of characterizing the transient tire/road forces and kinetic conditions of the wheel. Generally, in such a model the contact is formulated to be either distributed (assuming a line contact patch at the tire/road interface and formulating the partial differential equation of friction state) or lumped contact (assuming a point contact between tire and road and solving the ordinary differential equation of friction state). As a close approximation of the distributed friction model, the lumped LuGre model in [32] is widely used to predict the friction force during transient vehicle motion, where the frictional traction force F_{tr} is described as follows:

$$F_{tr}(t) = \left(\sigma_0 z + \sigma_1 \dot{z} + \sigma_2 v_r\right) F_n \tag{9}$$

with

$$\dot{z} = v_r - \frac{\sigma_0 |v_r|}{g(v_r)} z, \quad v_r = r_W \dot{\theta}_W - V, \quad g(v_r) = \mu_c + (\mu_s - \mu_c) e^{-|v_r / v_s|^{\tau}}$$

where v_r is the relative velocity, σ_0 is the rubber longitudinal lumped stiffness, σ_1 is the rubber longitudinal lumped damping, σ_2 is the viscous relative damping, F_n is the normal force, r_W is the wheel radius, V is the vehicle motion velocity, g is the characteristic function, μ_c is the Coulomb friction coefficient, μ_s is the static friction coefficient, v_s is the Stribeck relative velocity that defines the dependence of friction on velocity, τ is the constant capturing the friction/slip characteristic. By fitting the model to experimental data, Canudas-de-Wit et al. [32] show that the lumped model of Equation (9) yields a close approximation of the fully distributed LuGre model that accurately determines the friction force of tire during transient vehicle motion.

For simplification purposes in the modeling of the vehicle dynamics, we consider merely the rectilinear motion V and neglect the yaw rotation by steering and maneuvering. At the final drive, the wheel torque, T_W, in the powertrain is determined by the traction force, the rolling resistance, the air drag force and the braking torque described by the following relationships.

$$T_W = r_W \left(F_{tr} - F_{rr} - F_{air} \right) - T_b \tag{10}$$

where

$$F_{rr} = \frac{b_W k_\phi}{n+1} \left[\frac{3F_n}{b_W \left(3-n\right) k_\phi \sqrt{2r_W}} \right]^{\frac{2n+2}{2n+1}}, \quad F_{air} = \frac{1}{2} \rho_{air} A_V C_d V^2$$

T_b is braking torque, F_{rr} is rolling resistance force for pneumatic tire behaving like a rigid wheel [33], F_{air} is air drag force, b_W is the width of the tire, k_ϕ is the so-called pressure-sinkage parameter, n is the resistance constant depending on the terrain, ρ_{air} is air density, A_V is vehicle area, C_d is drag coefficient.

Figure 6-6 illustrates the dynamics model of the powertrain system by assembling the essential components that are represented by the torsional elements, including an engine, a flywheel, transmission, a drive shaft, a differential, and one wheel. These constitute a 12-DOFs system that represents the transmission as a single combination of a wet clutch and a planetary gear set. The mechanical structure of a planetary gear system consists of the ring gear, sun gear, planetary carrier and three planetary gears. The power delivery for transmission cases including the high- and low-gear ratios is shown. The following assumptions are also made to reduce the complexity of modeling.

1) A torque converter is merely taken as a constant-value damper between the flywheel and the clutch. It, thus, neglects the nonlinear dynamics of the underlying physical structure such as modulated gyrators and transformers;

2) Connections of many propeller shafts and universal joints are not modeled;

3) Nonlinear damping of the tire is not considered;

4) By neglecting the steering and maneuvering for vehicle dynamics, only the longitudinal motion of the vehicle is described.

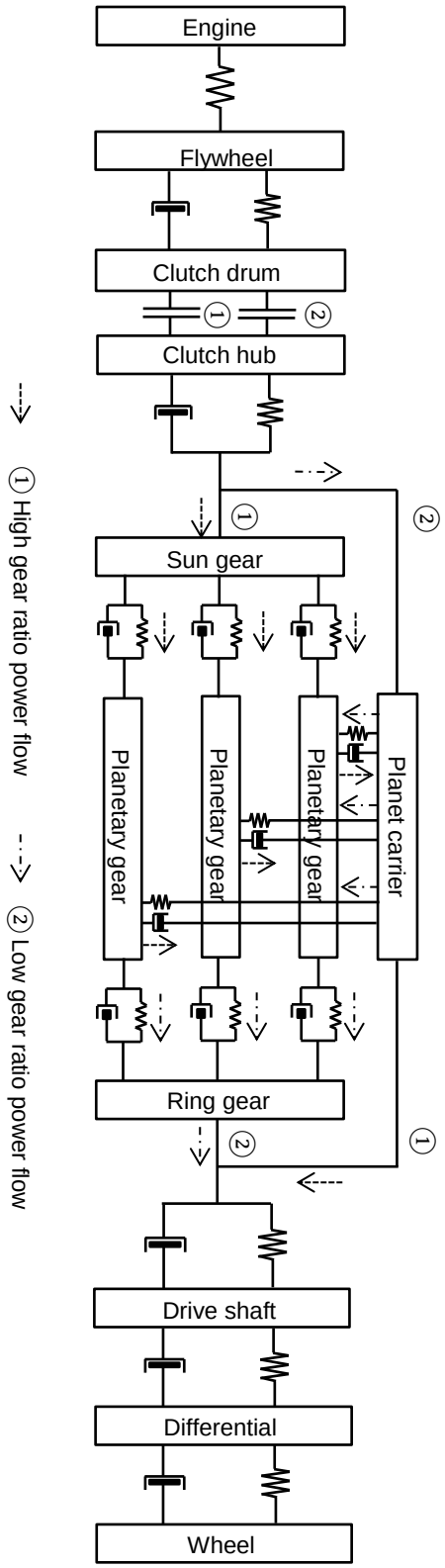

Figure 6-6 Torsional element model for the powertrain system with automatic transmission

The governing equations of torsional motion of powertrain components are given by equations (11)-(30).

Dynamics of a planetary gear train involving backlash is considered for both the high- and low- gear ratios. The vehicle motion relating the wheel rolling traction and resistance is determined by equation (30). Subscripts of inertia and angular motion parameters represent the powertrain components; subscripts of stiffness and damping coefficients denote the relevant connection between the torsional elements.

Engine

$$I_E\ddot{\theta}_E + K_{EF}\left(\theta_E - \theta_F\right) = T_E \tag{11}$$

Flywheel

$$I_F\ddot{\theta}_F + C_{FCD}\left(\dot{\theta}_F - \dot{\theta}_{CD}\right) - K_{EF}\left(\theta_E - \theta_F\right) + K_{FCD}\left(\theta_F - \theta_{CD}\right) = 0 \tag{12}$$

Wet clutch

$$I_{CD}\ddot{\theta}_{CD} - C_{FCD}\left(\dot{\theta}_F - \dot{\theta}_{CD}\right) + C_{CDCH}\left(\dot{\theta}_{CD} - \dot{\theta}_{CH}\right) - K_{FCD}\left(\theta_F - \theta_{CD}\right) = -T_C \tag{13}$$

$$I_{CH}\ddot{\theta}_{CH} - C_{CDCH}\left(\dot{\theta}_{CD} - \dot{\theta}_{CH}\right) - C_{CHS}\left(\dot{\theta}_{CH} - \dot{\theta}_S\right) + K_{CHS}\left(\theta_{CH} - \theta_S\right) = T_C \quad \text{(high gear ratio)} \tag{14}$$

$$I_{CH}\ddot{\theta}_{CH} - C_{CDCH}\left(\dot{\theta}_{CD} - \dot{\theta}_{CH}\right) - C_{CHP}\left(\dot{\theta}_{CH} - \dot{\theta}_P\right) + K_{CHP}\left(\theta_{CH} - \theta_P\right) = T_C \quad \text{(low gear ratio)} \tag{15}$$

Planetary gear set

(i) High gear ratio

$$I_S\ddot{\theta}_S - C_{CHS}\left(\dot{\theta}_{CH} - \dot{\theta}_S\right) + \sum_{i=1}^{3} c_{spi}\left(\dot{\delta}_{spi} - \dot{e}_{spi}\right) - K_{CHS}\left(\theta_{CH} - \theta_S\right) + \sum_{i=1}^{3} k_{spi} f\left(\delta_{spi} - e_{spi}\right) = 0 \tag{16}$$

$$m_S\ddot{\xi}_S + c_S\dot{\xi}_S - \sum_{i=1}^{3} c_{spi}\left(\dot{\delta}_{spi} - \dot{e}_{spi}\right)\sin\left(\phi_i - \alpha\right) + k_S\xi_S - \sum_{i=1}^{3} k_{spi} f\left(\delta_{spi} - e_{spi}\right)\sin\left(\phi_i - \alpha\right) = 0 \tag{17}$$

$$m_S\ddot{\eta}_S + c_S\dot{\eta}_S + \sum_{i=1}^{3} c_{spi}\left(\dot{\delta}_{spi} - \dot{e}_{spi}\right)\cos\left(\phi_i - \alpha\right) + k_S\eta_S + \sum_{i=1}^{3} k_{spi} f\left(\delta_{spi} - e_{spi}\right)\cos\left(\phi_i - \alpha\right) = 0 \tag{18}$$

$$I_{pi}\ddot{\theta}_{pi} - c_{spi}\left(\dot{\delta}_{spi} - \dot{e}_{spi}\right) + c_{rpi}\left(\dot{\delta}_{rpi} - \dot{e}_{rpi}\right) - k_{spi} f\left(\delta_{spi} - e_{spi}\right) + k_{rpi} f\left(\delta_{rpi} - e_{rpi}\right) = 0 \quad \left(i = 1, 2, 3\right) \tag{19}$$

$$\begin{aligned} &I_P\ddot{\theta}_P + C_{PDS}\left(\dot{\theta}_P - \dot{\theta}_{DS}\right) - \sum_{i=1}^{3} c_{spi}\left(\dot{\delta}_{spi} - \dot{e}_{spi}\right) - \sum_{i=1}^{3} c_{rpi}\left(\dot{\delta}_{rpi} - \dot{e}_{rpi}\right) \\ &+ K_{PDS}\left(\theta_P - \theta_{DS}\right) - \sum_{i=1}^{3} k_{spi} f\left(\delta_{spi} - e_{spi}\right) - \sum_{i=1}^{3} k_{rpi} f\left(\delta_{rpi} - e_{rpi}\right) = 0 \end{aligned} \tag{20}$$

(ii) Low gear ratio

$$I_P\ddot{\theta}_P - C_{CHP}\left(\dot{\theta}_{CH} - \dot{\theta}_P\right) - \sum_{i=1}^{3} c_{spi}\left(\dot{\delta}_{spi} - \dot{e}_{spi}\right) - \sum_{i=1}^{3} c_{rpi}\left(\dot{\delta}_{rpi} - \dot{e}_{rpi}\right)$$
$$-K_{CHP}\left(\theta_{CH} - \theta_P\right) - \sum_{i=1}^{3} k_{spi} f\left(\delta_{spi} - e_{spi}\right) - \sum_{i=1}^{3} k_{rpi} f\left(\delta_{rpi} - e_{rpi}\right) = 0 \quad (21)$$

$$I_{pi}\ddot{\theta}_{pi} - c_{spi}\left(\dot{\delta}_{spi} - \dot{e}_{spi}\right) + c_{rpi}\left(\dot{\delta}_{rpi} - \dot{e}_{rpi}\right) - k_{spi} f\left(\delta_{spi} - e_{spi}\right) + k_{rpi} f\left(\delta_{rpi} - e_{rpi}\right) = 0 \quad (i = 1,2,3) \quad (22)$$

$$m_R\ddot{\xi}_R + c_R\dot{\xi}_R - \sum_{i=1}^{3} c_{rpi}\left(\dot{\delta}_{rpi} - \dot{e}_{rpi}\right)\sin\left(\phi_i - \alpha\right) + k_R\xi_R - \sum_{i=1}^{3} k_{rpi} f\left(\delta_{rpi} - e_{rpi}\right)\sin\left(\phi_i - \alpha\right) = 0 \quad (23)$$

$$m_R\ddot{\eta}_R + c_R\dot{\eta}_R - \sum_{i=1}^{3} c_{rpi}\left(\dot{\delta}_{rpi} - \dot{e}_{rpi}\right)\cos\left(\phi_i - \alpha\right) + k_R\eta_R - \sum_{i=1}^{3} k_{rpi} f\left(\delta_{rpi} - e_{rpi}\right)\cos\left(\phi_i - \alpha\right) = 0 \quad (24)$$

$$I_R\ddot{\theta}_R + C_{RDS}\left(\dot{\theta}_R - \dot{\theta}_{DS}\right) + \sum_{i=1}^{3} c_{rpi}\left(\dot{\delta}_{rpi} - \dot{e}_{rpi}\right) + K_{RDS}\left(\theta_R - \theta_{DS}\right) + \sum_{i=1}^{3} k_{rpi} f\left(\delta_{rpi} - e_{rpi}\right) = 0 \quad (25)$$

Drive shaft

$$I_{DS}\ddot{\theta}_{DS} - C_{PDS}\left(\dot{\theta}_P - \dot{\theta}_{DS}\right) + C_{DSD}\left(\dot{\theta}_{DS} - \dot{\theta}_D\right) - K_{PDS}\left(\theta_P - \theta_{DS}\right) + K_{DSD}\left(\theta_{DS} - \theta_D\right) = 0 \quad \text{(high gear ratio)} \quad (26)$$

$$I_{DS}\ddot{\theta}_{DS} - C_{RDS}\left(\dot{\theta}_R - \dot{\theta}_{DS}\right) + C_{DSD}\left(\dot{\theta}_{DS} - \dot{\theta}_D\right) - K_{RDS}\left(\theta_R - \theta_{DS}\right) + K_{DSD}\left(\theta_{DS} - \theta_D\right) = 0 \quad \text{(low gear ratio)} \quad (27)$$

Differential

$$I_D\ddot{\theta}_D - C_{DSD}\left(\dot{\theta}_{DS} - \dot{\theta}_D\right) + C_{DW}\left(\dot{\theta}_D - \dot{\theta}_W\right) - K_{DSD}\left(\theta_{DS} - \theta_D\right) + K_{DW}\left(\theta_D - \theta_W\right) = 0 \quad (28)$$

Wheel

$$I_W\ddot{\theta}_W - C_{DW}\left(\dot{\theta}_D - \dot{\theta}_W\right) - K_{DW}\left(\theta_D - \theta_W\right) = T_W \quad (29)$$

Vehicle

$$M_V\dot{V} = F_{tr} - F_{rr} - F_{air} \quad (30)$$

6.3 Simulation of powertrain dynamics with NVH factors

Dynamic equations (11)-(30) are solved using an ordinary differential equation (the ode45 solver) which utilizes the Runge-Kutta method in the Matlab® environment, with a maximum time step of 10^{-7} s. The system torques determined at each time step are the engine torque, clutch torque, and the wheel torque. The engine torque is represented by a harmonic signal with a mean torque value of 425.6 N m. In the current simulations, only the stick-slip behavior under the isothermal assumption is taken into account due to the high computational cost associated with full thermohydrodynamic (THD) analysis [34]. The wheel torque is computed using equation (10). The data of element inertia, stiffness and damping are provided in Table 6-1, where the parameters of a planetary gear set are adopted from [26] and the input values for other powertrain components use the lumped inertia-stiffness information of a powertrain model provided in [25].

Table 6-1. Model input of powertrain dynamics

Parameter	Inertia (kg·m^2)	Parameter	Stiffness (N·m/rad)	Parameter	Stiffness (N·m)
I_E	0.4	K_{EF}	95000	k_S	4.2×10^8
I_F	0.2	K_{FCD}	106000	k_R	4.0×10^8
I_{CD}	0.1	K_{CHS}	4.58×10^8	k_{spi}	2.4×10^8
I_{CH}	0.02	K_{PDS}	4.95×10^8	k_{rpi}	2.9×10^8
I_S	2.0×10^{-3}	K_{DSD}	165000	Parameter	Damping (N·m·s)
I_{pi}	1.4×10^{-3}	K_{DW}	165000	c_{spi}	0.02
I_P	0.6	Parameter	Damping (N·m·s/rad)	c_{rpi}	0.02
I_R	4.0×10^{-3}	C_{FCD}	0.02		
I_{DS}	0.1	C_{CDCH}	0.02		
I_D	0.16	C_{CHS}	0.02		
I_W	0.2	C_{PDS}	0.02		
Parameter	Mass (kg)	C_{CHP}	0.02		
m_S	0.417	C_{RDS}	0.02		
m_R	0.254	C_{DSD}	0.25		
M_V	1200	C_{DW}	1		

6.3.1 Verification of dynamic models of powertrain components

For verification purposes, crucial results obtained by the dynamic models of powertrain component described above are compared with the published papers, including the stick-slip of a wet clutch, backlash of a planetary gear set, and the lumped LuGre model of a tire.

With the same input parameters by Crowther et al. [24], the stick-slip behavior for a four degree of freedom powertrain system (as shown in Figure 2) is simulated. Figure 6-7 (a) presents the kinetics and torque results of the clutch system with a positive-slope friction coefficient (stable case) and Figure 6-7 (b) shows the results for a negative sloped friction coefficient (unstable case). As verified with ref. [24], the torque results show that the torsional oscillation in stable case (with a gradient of the friction coefficient $m_s = 0.0001$) is damped and the engagement ends at 0.36 s. When the friction slope is negative ($m_s = -0.0001$), the torsional oscillation is excited and the engagement process takes much longer to complete. The same model is applied to the full powertrain model to determine the stick-slip state of a wet clutch during the engagement.

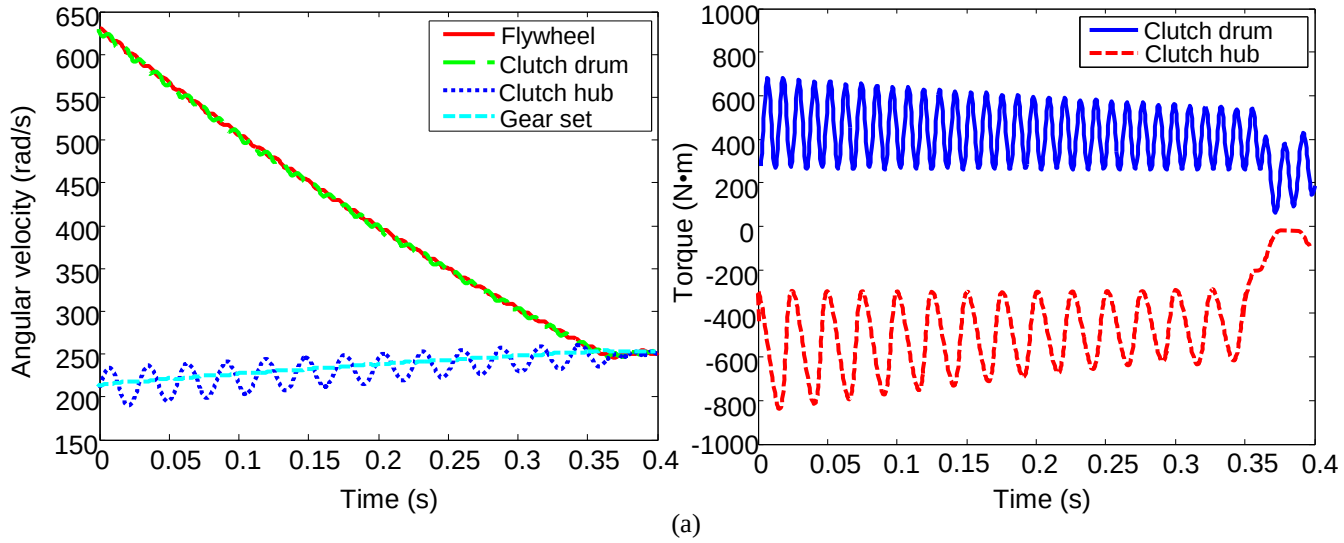

(a)

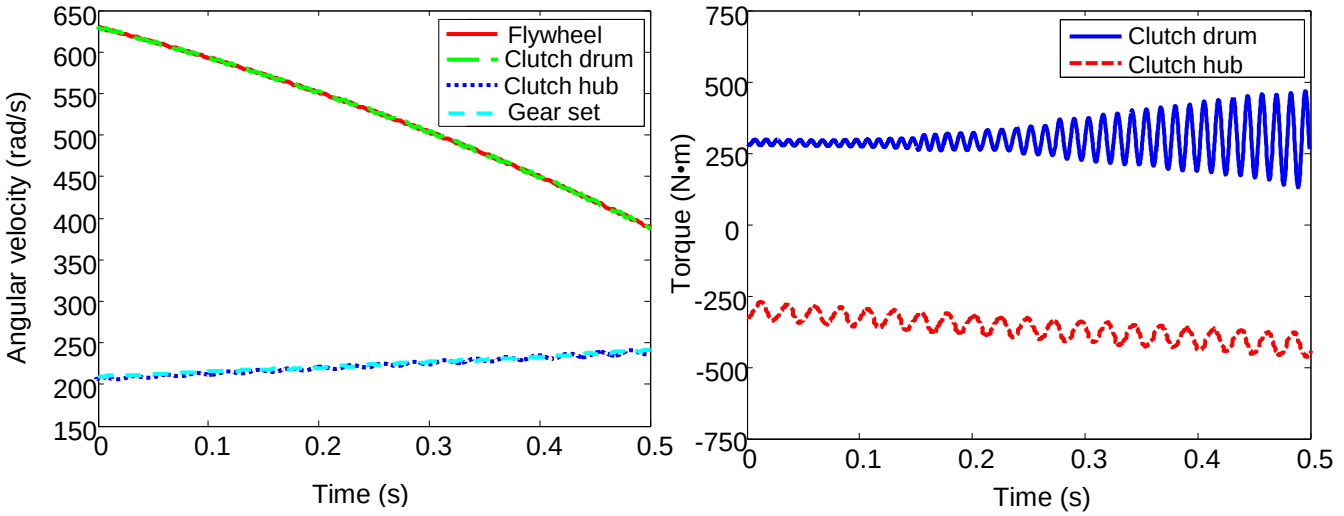

(b)

Figure 6-7 Stick-slip of a 4-DOF powertrain system verified with [24] (a) stable case with m_s=0.0001 and (b) unstable case with m_s=-0.0001

For the tire model, the traction coefficient is the key parameter that controls the dynamics of the tire. This is verified through the LuGre model results in ref. [32]. Let us define the longitudinal slip rate $s = V / r_W \dot{\theta}_W - 1$ for the braking case. Then, by using the equation (9) and the input data in [32], the traction coefficient $\mu = F_{tr} / F_n$ is obtained in Figure 6-8. When the difference between the rolling velocity $r_W \dot{\theta}_W$ and the vehicle velocity V is small, i.e., the slip rate is small, the traction coefficient is transient with dynamic motion state. With an increased slip rate, the traction coefficient reaches a stable value with a steady sliding at the interface between the tire and the road. The different conditions of the tire/road adhesion can be simulated by a multiplier χ in the modified characteristic function $\tilde{g}(v_r) = \chi g(v_r)$, where $\chi = 1$ indicates the dry road condition. $\chi = 0.8$ and $\chi = 0.2$ represent slightly and very slippery road condition, respectively. In this paper, the dry road condition is assumed in the

simulations presented in Section 3.2-3.3.

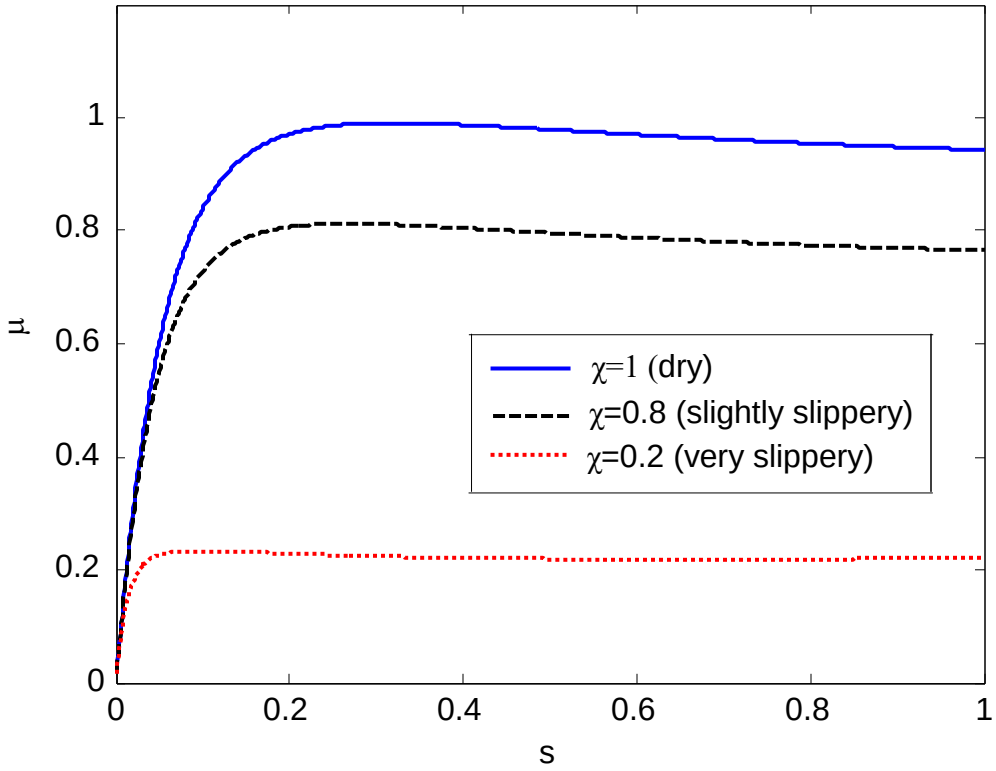

Figure 6-8 Traction coefficient at different road conditions that is verified with [32]

Figure 6-9 shows the vibration response of the gear components including a sun gear, three planetary gears, and a planetary carrier with constant torque applied to the clutch hub and the drive shaft as the input of the high-speed part and output of the low-speed part. The transient results of the planetary gear set model are simulated to obtain the relative displacement of the gear pair. To convert the results from the time domain into the frequency domain, the fast Fourier transform (FFT) is performed. A major peak amplitude of 3.2 at the frequency around 1.76 Hz is observed, which is in agreement with the resonant frequency with a peak amplitude of 2.5 at the frequency around 1.55 Hz that is reported in ref. [26]. The discrepancies mainly stem from input difference in the powertrain components (the whole powertrain system vs the planetary gear set itself in [26]) and the assumed harmonic excitation in the vibrational analysis using harmonic balance method (HBM) by Sun et al. [26].

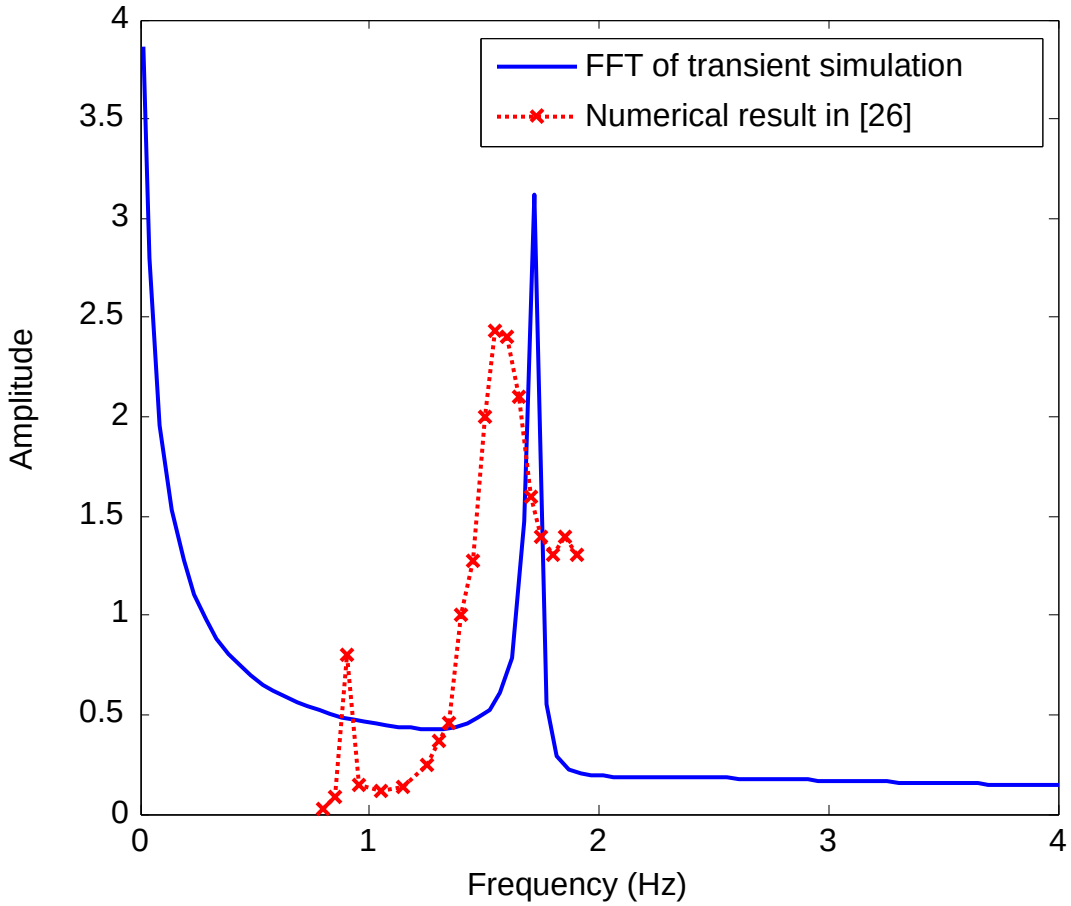

Figure 6-9 Frequency response of relative displacement between sun gear and planetary gear

The subsystem validation of the clutch, gear set, and tire provides model fidelity of powertrain system that assembles the components through relevant connection between the torsional elements.

6.3.2 Transient simulation of powertrain dynamics

Nonlinearities in powertrain dynamics are mainly characterized by the dynamic behavior of automatic transmission, i.e. the stick-slip behavior in the wet clutch and the backlash in planetary gearbox. For the wheel, we consider the tire traction assuming a dry road condition ($\theta = 1.0$). Figure 6-10 presents transmission results of a wet clutch and the planetary gear set. As the vehicle begins to move, the engine, the flywheel and the clutch drum are accelerated simultaneously to a high rotational speed by the engine torque (the slippage at the torque converter is neglected in the model). The relative speed between the clutch drum and the clutch hub is increased as well. Meanwhile, the control unit of the automatic transmission will register the acceleration signal and the engagement load is then applied through the hydraulic system, and the shift is realized by reaching a specific gear ratio in the transmission. During the engagement process, the clutch torque is rapidly increased by the frictional torque due to the asperity

contact at the sliding interface of the separator disk and the friction disk. Therefore, the relative speed between the clutch drum and the clutch hub decreases and becomes nil at the end of the engagement. The clutch is then “locked up” and delivers the transmission power in the driveline. For the engagement load of 6,000 N, the engagement process is completed in only1.06 s. The vibration response of the speed difference between the clutch drum and the clutch hub is shown on the bottom of Figure 6-10 (a). The low vibrational amplitude at low frequency range indicates a smooth engagement. The transmission speed is translated to a smaller speed with a high gear ratio (about 0.2) in the planetary gear train. The horizontal and vertical displacement of the sun gear with regard to the planetary carrier is around 100 μm. With the nonlinearity of backlash caused by losing contact between the mating gears, the speed of the sun gear, planetary gear and the planetary carrier varies approximately in a linear fashion.

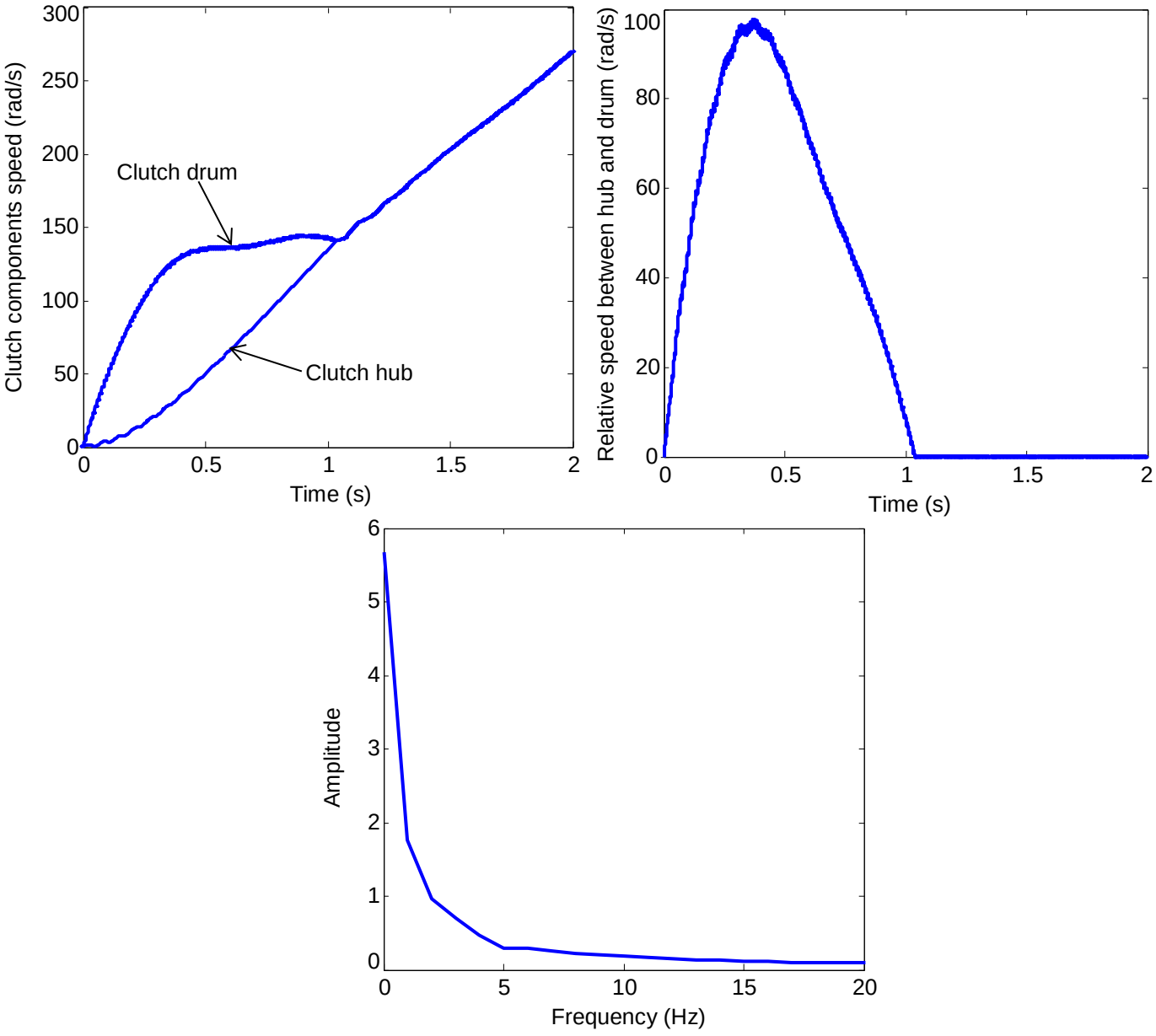
Clutch components speed (rad/s)
Clutch drum
Clutch hub
Time (s)
Relative speed between hub and drum (rad/s)
Time (s)
Amplitude
Frequency (Hz)

(a) Wet clutch

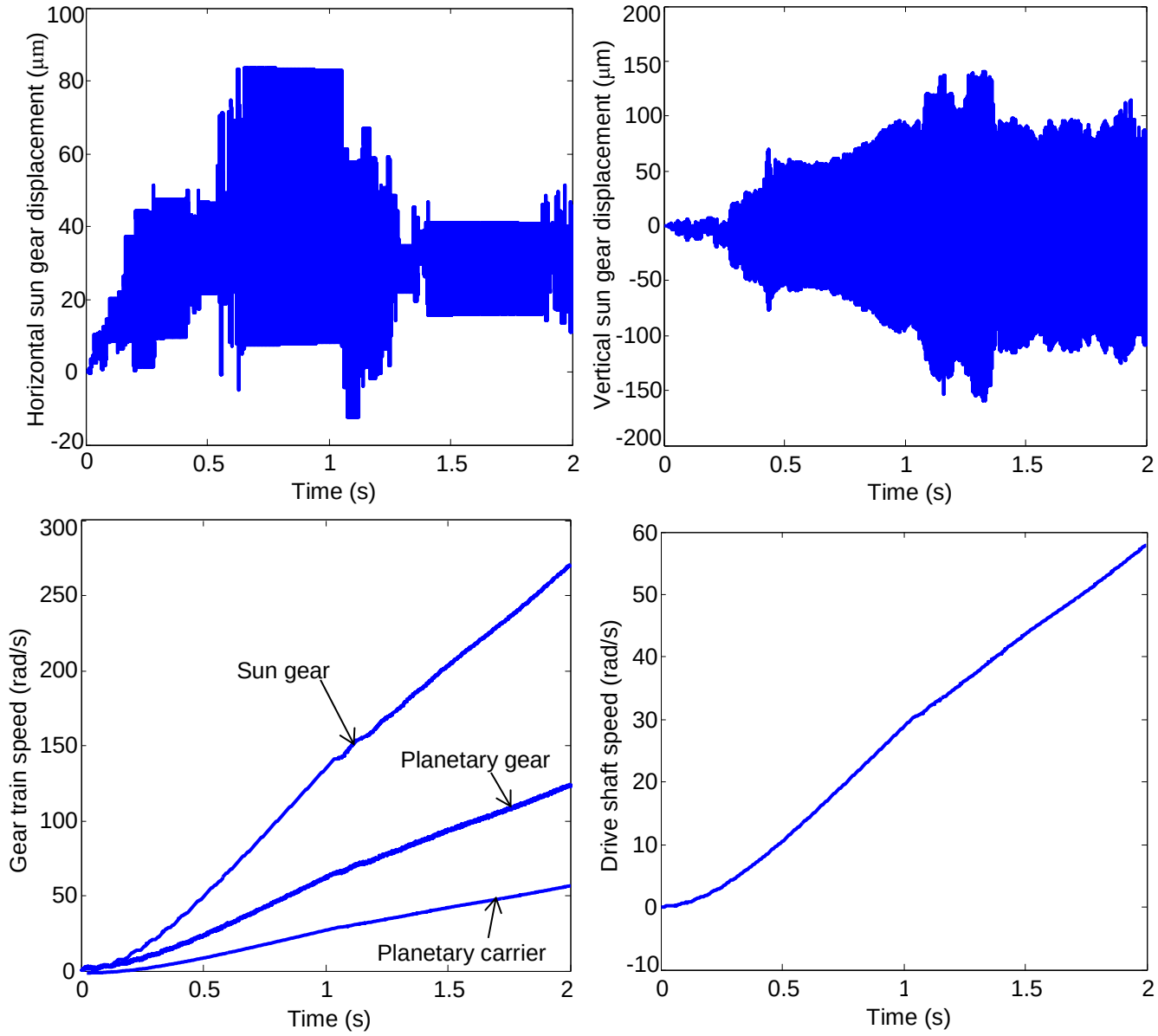

(b) Planetary gear set

Figure 6-10 Transient simulation of planetary gear set with nonlinearity considerations

Figure 6-11 shows the result of a parametric study of the backlash effect on the vibration response when the mesh clearance is reduced from 50 μm to 10 μm. The transverse displacement of the sun gear is significantly decreased to less than 100 μm (especially for the vertical displacement), yielding a smaller rattling noise within the planetary gearbox. In addition, the vibration magnitude of planetary gear is reduced and the peak is slightly modified. The low-speed part, drive shaft, remains almost unchanged, which indicates a rather limited vibration propagation from the planetary gear set. With a reduced mesh clearance, the gear train speeds increase in an approximately linear fashion with time. When the teeth of the gear pair do not lose contact, nonlinearity of teeth deflection shown in Figure 6-4 will cease to exist.

Compared with the vibration response shown in Figure 6-9 (mesh clearance = 50 μm), the vibration peak is almost nil with smaller backlash.

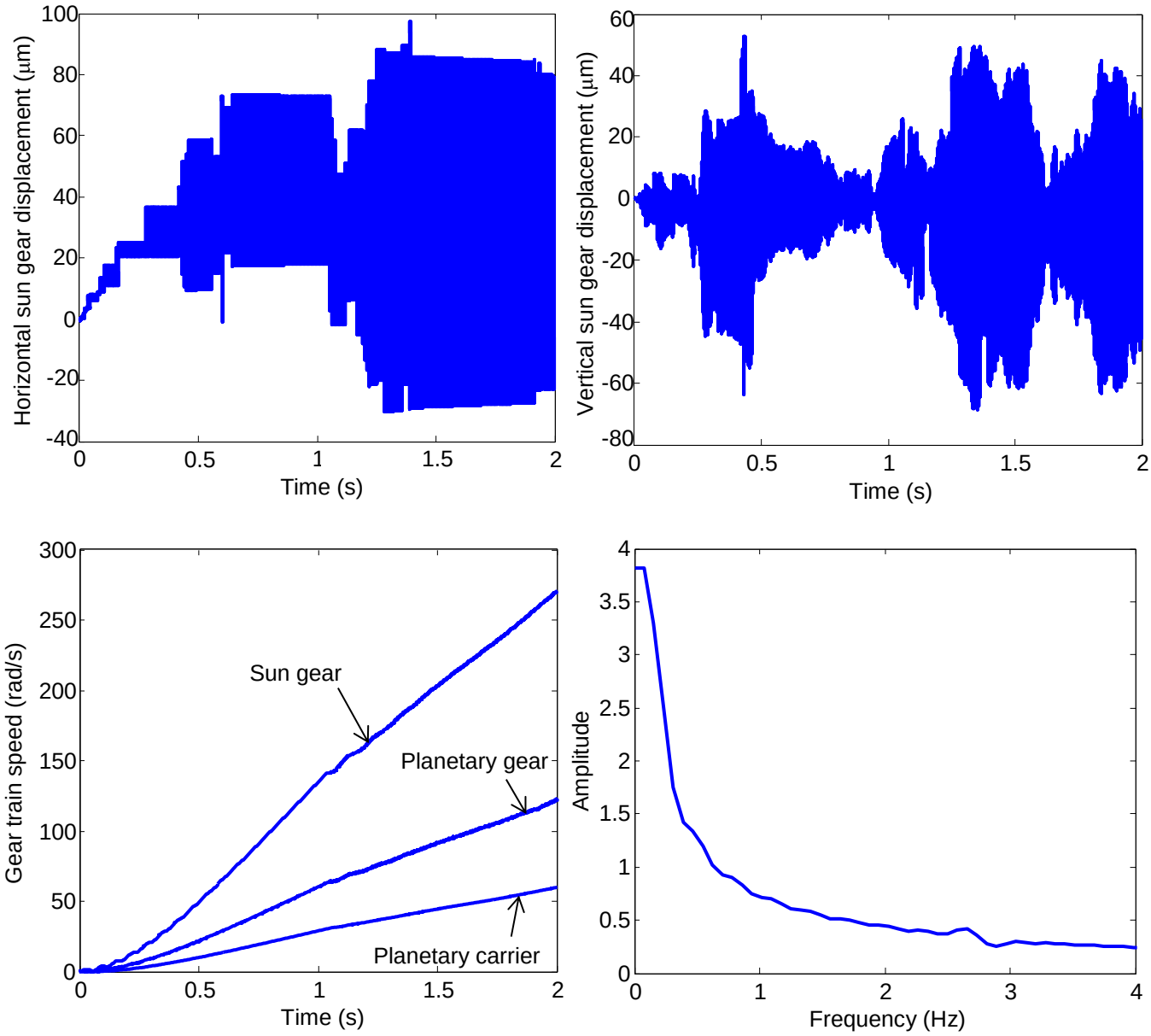

Figure 6-11 Transient simulation of planetary gear set with reduced mesh clearance (10 μm)

6.3.3 Vibration induced by clutch engagement

Since the clutch engagement behavior is closely related to the dynamics characteristics of the entire driveline, the mode of engagement loading determines the essential response of vibration in transmission. This section discusses the possible scenarios that are involved with driveline NVH by clutch engagement, including engagement load magnitude, engagement load fluctuation, and shudder.

- Engagement load magnitude

Compared with the previous simulation for normal load case of 6,000 N used in [24], a high load of 12,000 N and a low load of 4,000 N are considered to analyze the effect of engagement load magnitude on powertrain NVH. For the high load (12,000 N) case in Figure 12, the engagement stage is completed in 0.28 s, much faster than the normal load case of 1.06 s. Consequently, the oscillation in the clutch speed during the short engagement process is larger. It is generated by the trend of rotational speed (associated with an increase followed by a decrease) at the beginning of engagement stage, since the speed difference is firstly increased by a high engine torque and then reduced by the increasing clutch torque. The vibration is of low frequency and high amplitude, and is directly observable by the passenger in the vehicle. The difference between the engine torque and the generated clutch torque serves as excitation in the clutch system that causes intense oscillation, especially at the beginning of the engagement. According to the vibration response, a wider range of vibration at low frequency (0-8.6 Hz) is observed in comparison to the normal engagement loading case.

Figure 6-13 presents the results of the low engagement load 4,000 N. It shows the dynamic behavior of driveline when the engagement load is not high enough to fully eliminate the speed difference between the clutch drum and the clutch hub. Near the end of the engagement (at 1.2 s), the clutch torque continues to be lower than the target value of 445 N•m. As a result, the interface between the friction pair of a wet clutch experiences slip. Such vibrations not only lead to cyclic loading to the rotational components but also generate intense heat that induces much more degradation of friction material of clutch pack [35]. Therefore, such a load case is detrimental to both the material durability and performance. For the vibrational response, both the magnitude and the width of low frequency range are increased due to the oscillating clutch slip.

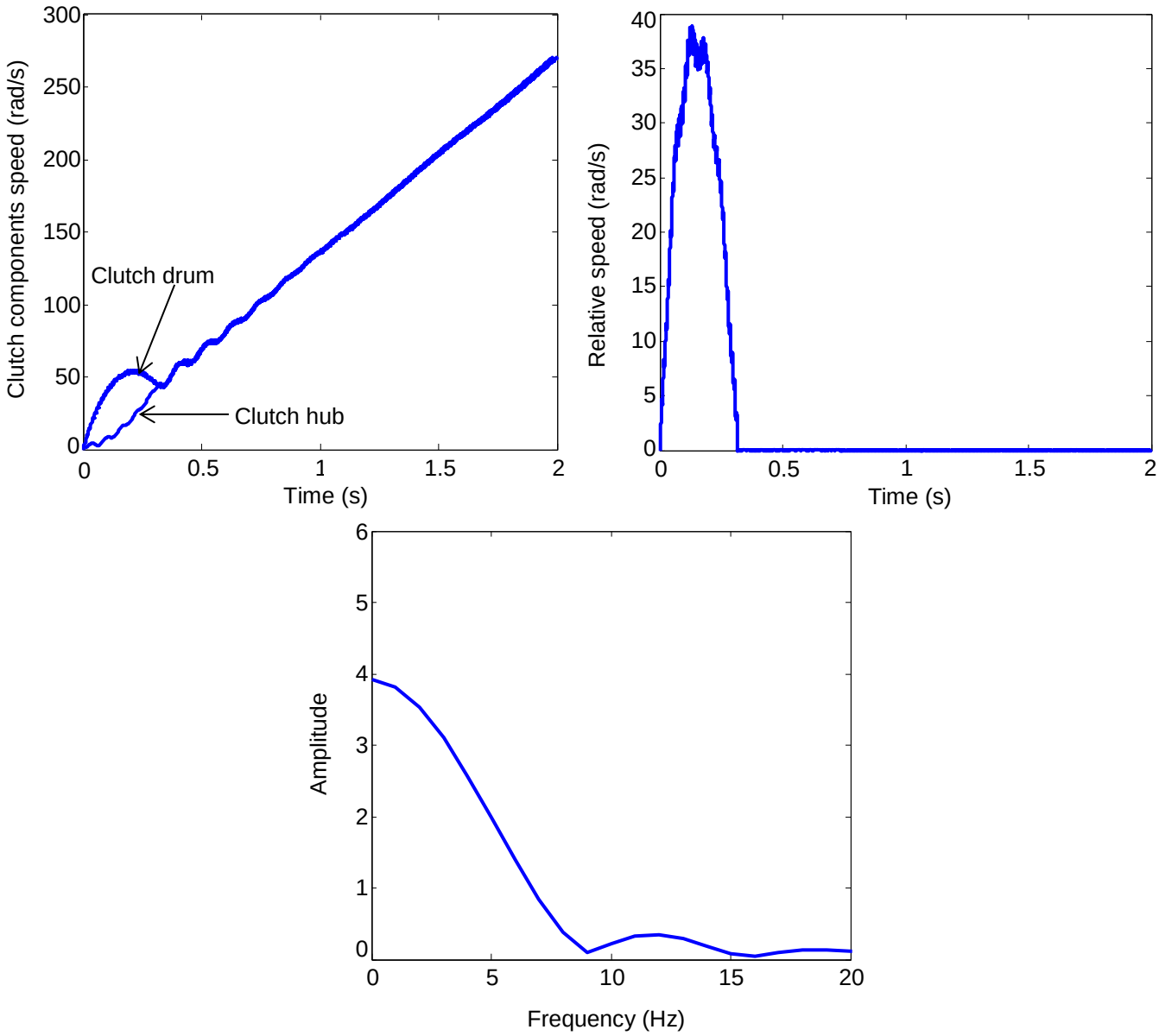

Figure 6-12 Transient simulation of a wet clutch at high engagement load (12000N)

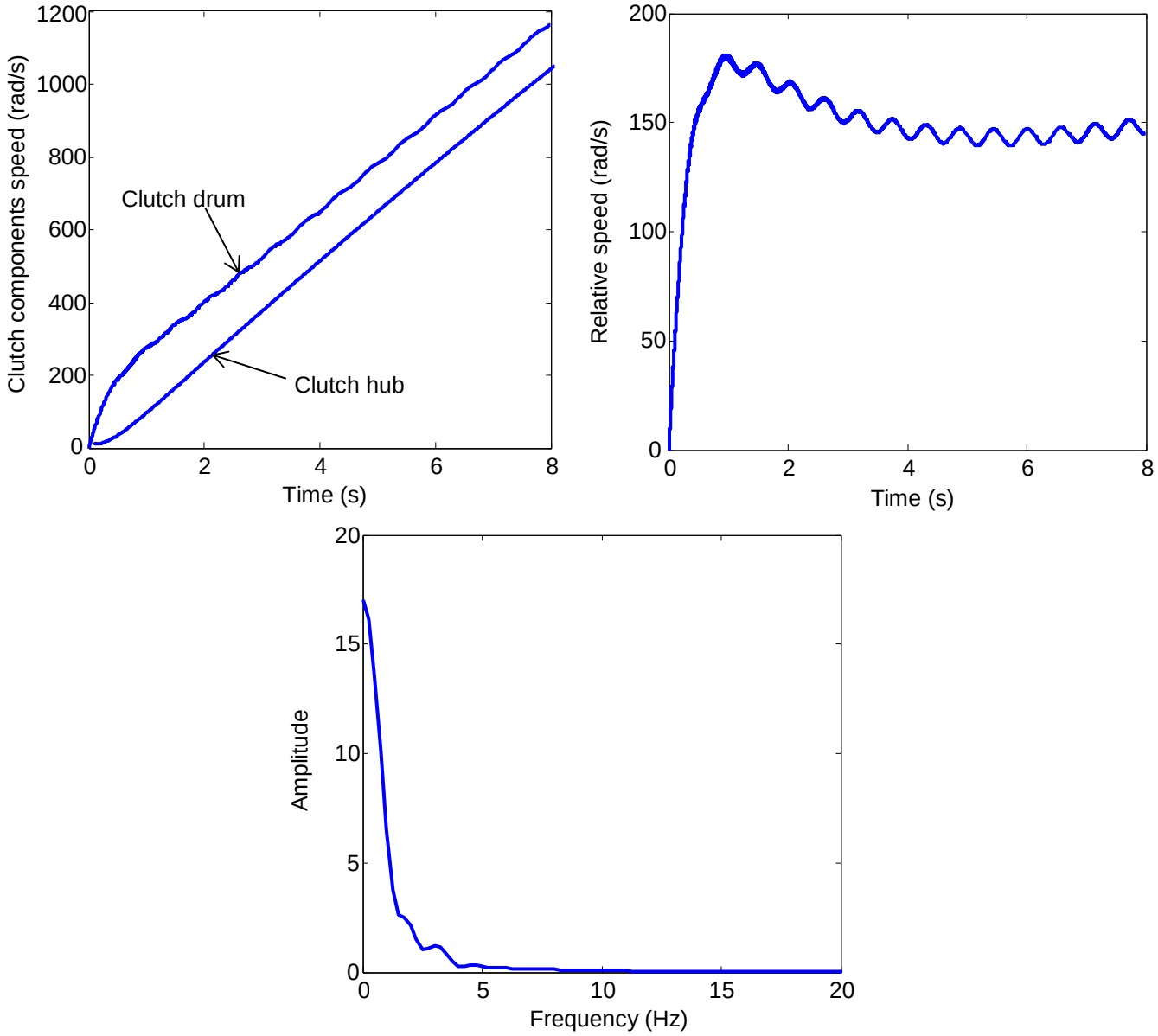

Figure 6-13 Transient simulation of a wet clutch at low engagement load (4000 N)

- Engagement load oscillation

The effect of fluctuation in engagement loading arising from the fault of hydraulic system can be simulated using equation (31) where the magnitude and rate of loading during engagement is determined by the base load P_0 and the response time t_0, respectively. In order to simulate the oscillation of the engagement pressure P_{eng}, a pseudo-random zero-mean Gaussian noise is used to produce the signal of faulty engagement load, with a signal-to-noise ratio (SNR) of 18, as shown in Figure 6-14. σ is the noise deviation, determined by SNR, signal norm and sample size. Such a signal is used as an input of the powertrain simulation to investigate the effect of engagement load fluctuation.

$$P_{eng} = P_0\left(1-e^{-t/t_0}\right) \tag{31}$$

$$\text{SNR} = 10\log_{10}\frac{\left\|P_{eng}\right\|_F^2}{MN\sigma^2} \tag{32}$$

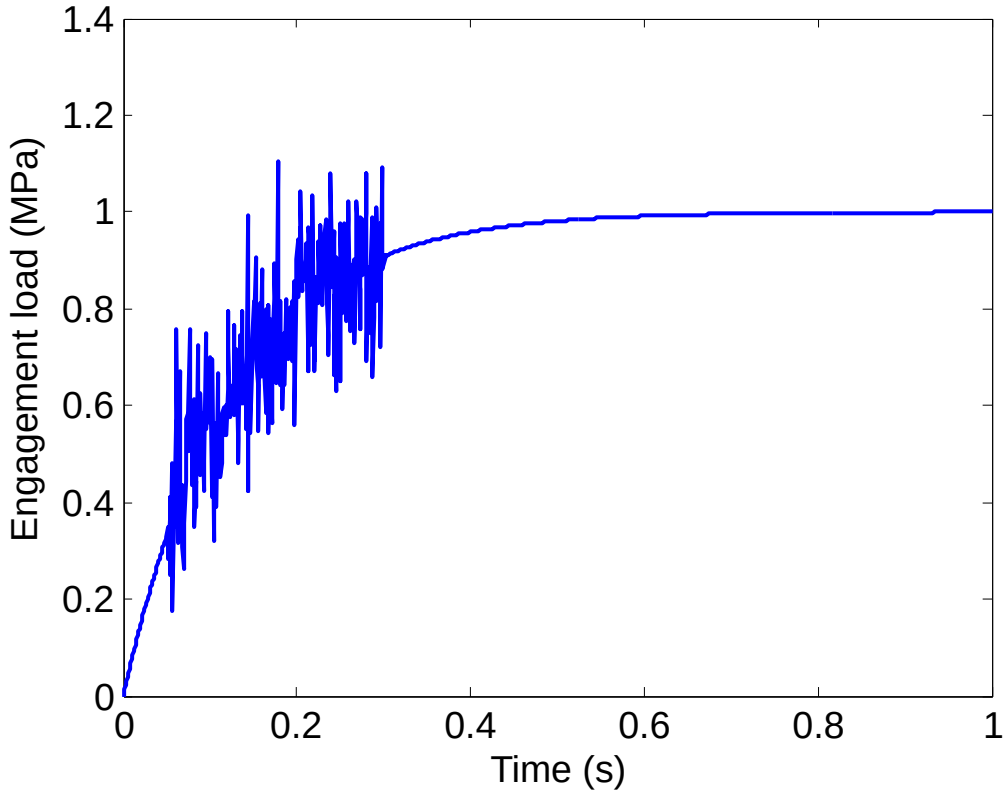

Figure 6-14 Faulty engagement loading profile with oscillation (SNR = 18)

As shown in Figure 6-15, the engagement load fluctuation can generate vibration that is quite similar to high load case. The frequency of noise in the loading signal is dispersed in an interval of low magnitude (0~25 Hz). With such a low-frequency torsional oscillation, a pronounced response is observed in the clutch hub and a large propagation of vibration is generated in the driveline, as shown in the vibrational response of the relative speed in a wet clutch. Overall, the engagement process is completed faster than the normal loading case because the oscillated torque generates a higher average acceleration of clutch hub.

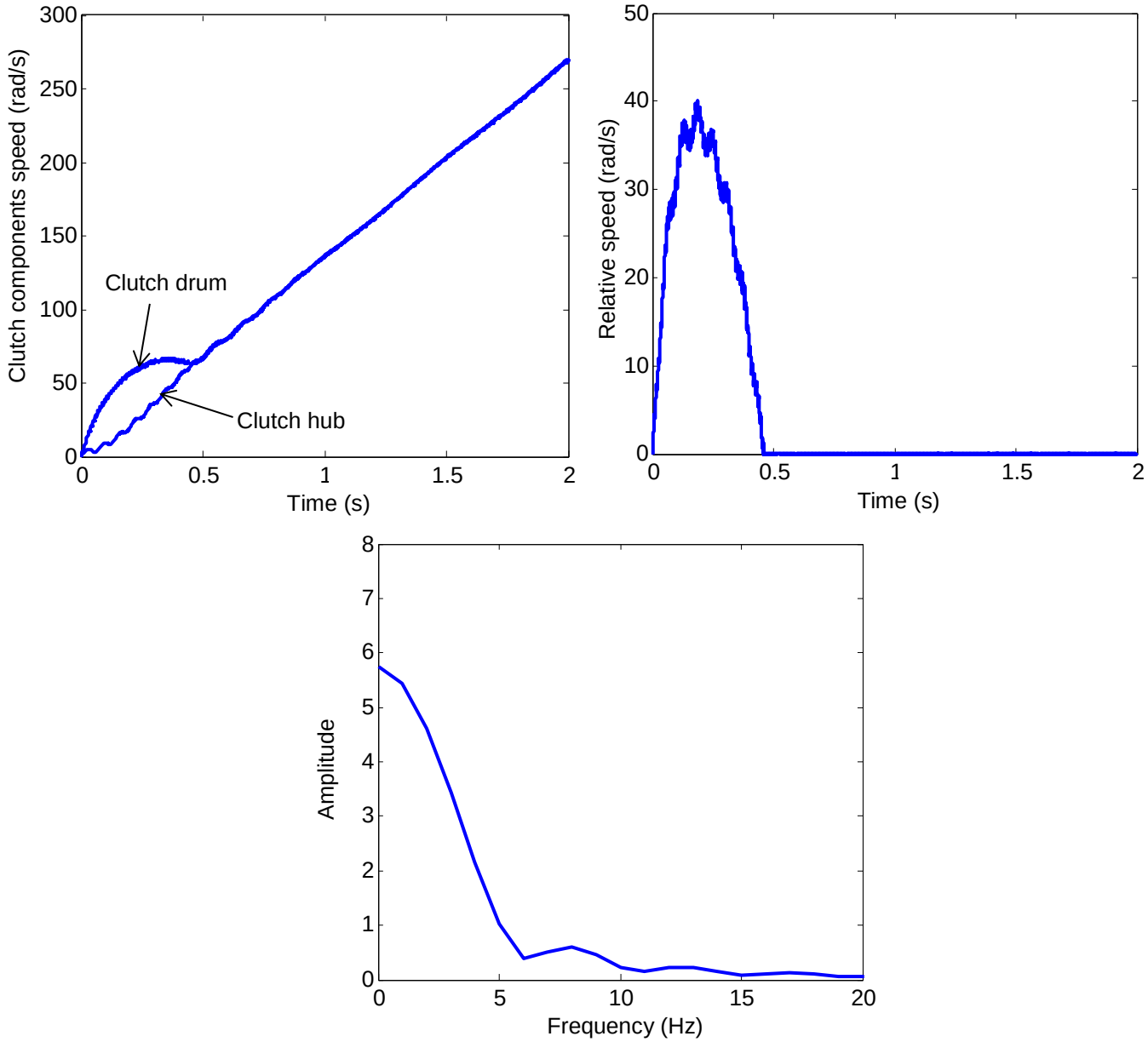

Figure 6-15 Vibration generation and propagation in the driveline by engagement load oscillation

- Shudder by ATF oxidation

During the large engagement cycles of transmission, ATF degrades by oxidation in the intense thermal environment of a wet clutch. It usually leads to a negative slope of friction versus velocity (μ-V) curve. The induced vibration, called shudder (or judder), indicates the deteriorated transmission stability by such frictional characteristics. Measurements by Willermet et al. [36] provide dynamic friction test with degraded ATF as the friction data to characterize the friction degradation along with a paper-based friction material (Borg-Warner 1777C). Figure 6-16 show the μ-V curves for the ATF approved to the MERCON^{TM} specification of the fresh condition and from a shuddering durability test vehicle [36].

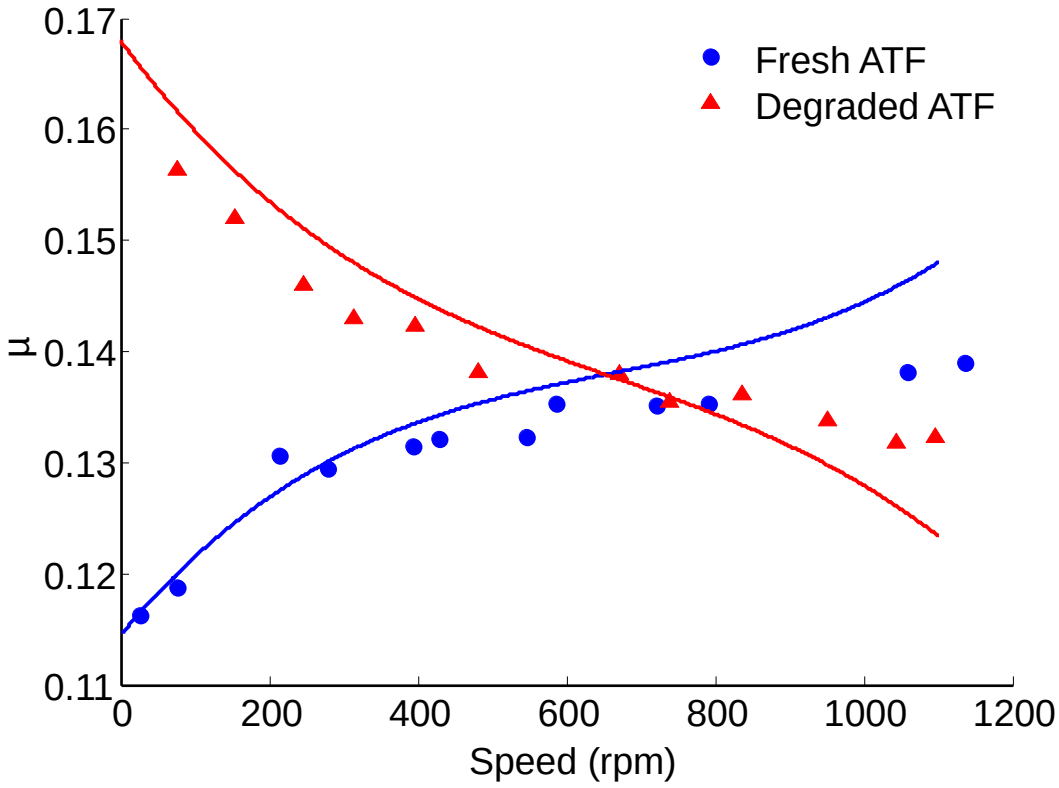

Figure 6-16 Friction coefficients of different ATF type [36]

Figure 6-17 presents transmission results of powertrain system with degraded ATF, including the transmission torque and rotational speed of the clutch components. Because of the low friction coefficient at high speed level for degraded ATF, the transmission torque is smaller at the beginning of engagement stage than that for fresh ATF case. The relative speed curve shows an accelerated rate of a slump, which leads to oscillation in the speed curve of the clutch drum. This is also reflected in the diagram of vibration response. The entire engagement process also takes longer time to complete than the case with fresh ATF.

For the traditional open-loop control module such as proportional integral derivative (PID), the control input of engagement load applied by the hydraulic system as the actuator cannot achieve the clutch torque of control objective with the modified friction characteristics by ATF degradation. Therefore, the actual shifting may take longer time than the results of control design, which causes a worse shifting performance and more degradation of the clutch system in the long run. To achieve smooth power transmission by a wet clutch, replacement of degraded ATF with the fresh one is necessary. A great deal of studies on the ATF formulation is also available to enhance the tribological performance of ATF durability, anti-shudder properties, heat transfer, etc., by combining the specific friction material selection (organic fibers, synthetic fibers, carbon fibers, or sintered bronze). [37-41] and the groove designs [42]. Appropriate friction characteristics will contribute to improved transmission smoothness, especially when the control design of the clutch actuation system is integrated and the addition of drivetrain damping is limited.

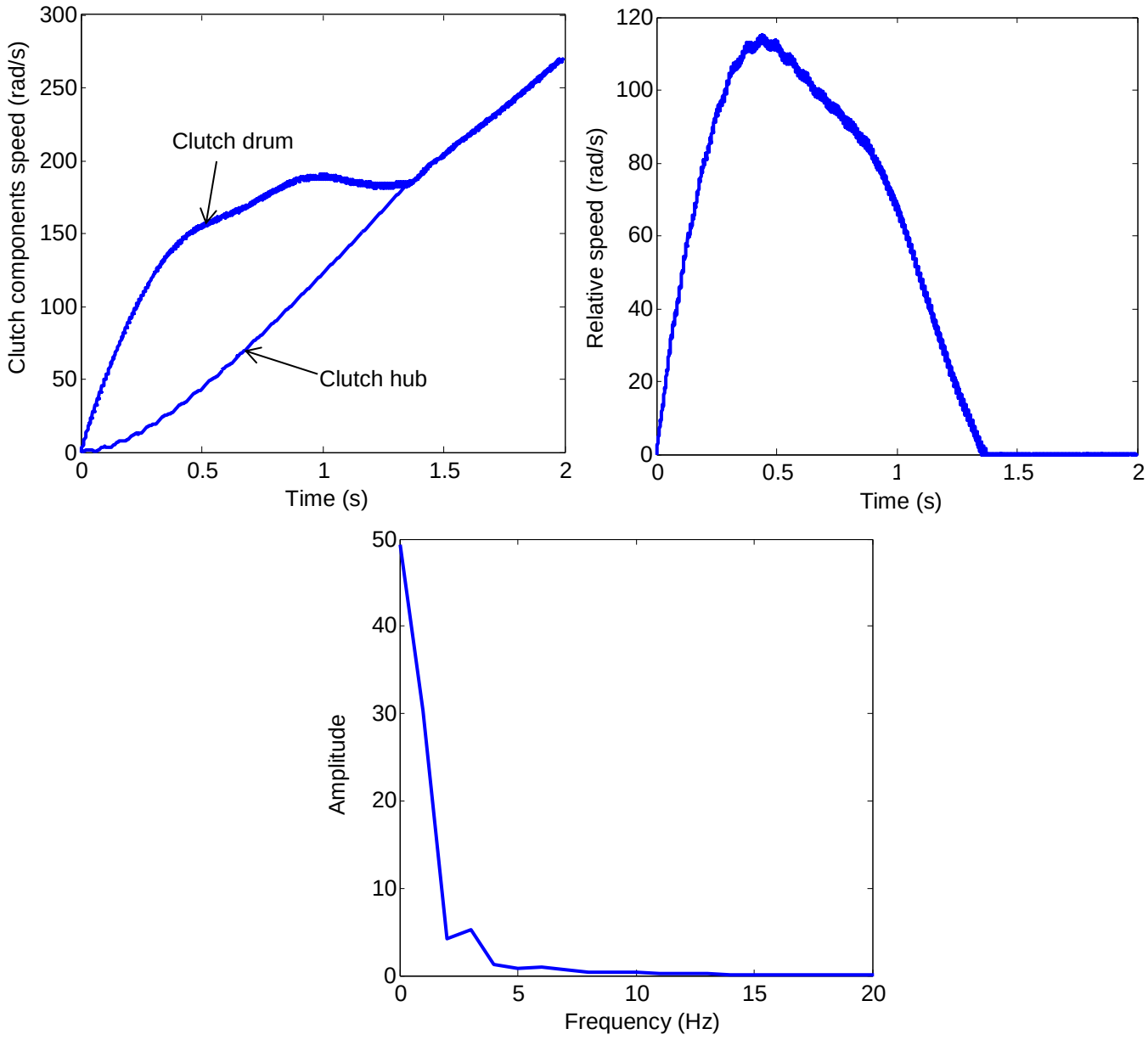

Figure 6-17 Transient simulation of a wet clutch with ATF degradation

The powertrain dynamics is analyzed for various engagement pattern of the clutch, including rapid engagement of high load, continuous clutch slippage by low load, engagement load fluctuation, and shudder-inductive friction response of clutch with negative slope μ-V curve. The comparison shows highest vibration magnitude of low frequency range for clutch shudder and clutch slippage with low load, where both cases involve stick-slip behavior.

6.4 Concluding remarks

A comprehensive vibrational analysis is presented by modeling powertrain dynamics and numerical simulation to investigate the NVH factors of the automotive powertrain system. Compared with previous

powertrain studies, this research tackles transmission nonlinearities in detail and provides appropriate simplification to balance the simulation complexity. Discussions on the dynamical behavior of the powertrain system and NVH solutions can be briefly summarized as follows.

The vibrational influence of nonlinearities within the powertrain system is studied by modeling the nonlinear behaviors of the automatic transmission. It is shown that the major torsional vibration can be mainly produced by loading of the clutch during the engagement, including engagement loading magnitude, engagement loading fluctuation, and shudder by ATF oxidation. A high engagement load shortens the engagement time and leads to an oscillatory transmission speed in both the clutch hub and clutch drum. When the magnitude of engagement load is not sufficient to fulfill the shifting operation, a continuous slippage occurs in the friction pair, which generates significant interfacial heat and thermally degrades the friction material in the clutch system. A problematic engagement loading process with observable noise is also an important source of vibration that propagates in the driveline. Therefore, design and optimal control of engagement load are crucial to guarantee a smooth shifting for the transmission system. With ATF oxidation, the friction characteristics tend to deteriorate. In particular, when the slope of the μ-V curve becomes negative, the system tends to vibrate dues to negative damping. Compared with these factors, the backlash of the planetary gear, while important, incurs limited vibration propagation within the driveline.

6.5 References

[1] J.J. Moskwa, Automotive engine modeling for real time control, Massachusetts Institute of Technology, 1988.

[2] R.W. Weeks, J.J. Moskwa, Automotive engine modeling for real-time control using matlab/simulink, SAE Technical Paper, 1995.

[3] L. Guzzella, C. Onder, Introduction to modeling and control of internal combustion engine systems, Springer Science & Business Media, 2009.

[4] R. Isermann, Engine modeling and control, Springer, 2014.

[5] Y. Shiao, J.J. Moskwa, Cylinder pressure and combustion heat release estimation for SI engine diagnostics using nonlinear sliding observers, Control Systems Technology, IEEE Transactions on, 3 (1995) 70-78.

[6] Y.-W. Kim, G. Rizzoni, V. Utkin, Automotive engine diagnosis and control via nonlinear estimation, Control Systems, IEEE, 18 (1998) 84-99.

[7] H.N. Özgüven, D.R. Houser, Mathematical models used in gear dynamics—a review, Journal of sound and vibration, 121 (1988) 383-411.

[8] T. Fakhfakh, L. Walha, J. Louati, M. Haddar, Effect of manufacturing and assembly defects on two-stage gear systems vibration, The International Journal of Advanced Manufacturing Technology, 29 (2006) 1008-1018.

[9] S. THEODOSSIADES, S. NATSIAVAS, Non-linear dynamics of gear-pair systems with periodic stiffness and backlash, Journal of Sound and vibration, 229 (2000) 287-310.

[10] M. Li, M. Khonsari, D. McCarthy, J. Lundin, Parametric analysis for a paper-based wet clutch with groove consideration, Tribology International, 80 (2014) 222-233.

[11] C. Duan, R. Singh, Stick-slip behavior of torque converter clutch, SAE Technical Paper, 2005.

[12] D. Centea, H. Rahnejat, M. Menday, The influence of the interface coefficient of friction upon the propensity to judder in automotive clutches, Proceedings of the Institution of Mechanical Engineers, Part D: Journal of Automobile Engineering, 213 (1999) 245-258.

[13] H. Pacejka, Tire and vehicle dynamics, Elsevier, 2005.

[14] E. Bakker, L. Nyborg, H.B. Pacejka, Tyre modelling for use in vehicle dynamics studies, SAE Technical Paper, 1987.

[15] R.N. Jazar, Vehicle Dynamics, Theory and Applications. Riverdale, NY: Springer Science+ Business Media, (2008).

[16] M. Brinkmeier, U. Nackenhorst, S. Petersen, O. Von Estorff, A finite element approach for the simulation of tire rolling noise, Journal of sound and vibration, 309 (2008) 20-39.

[17] A. Kamoulakos, B. Kao, Transient dynamics of a tire rolling over small obstacles-a finite element approach with PAM-SHOCK, Tire Science and Technology, 26 (1998) 84-108.

[18] M. Shiraishi, H. Yoshinaga, A. Miyori, E. Takahashi, Simulation of dynamically rolling tire, Tire Science and Technology, 28 (2000) 264-276.

[19] N. Zhang, D. Liu, J. Jeyakumaran, L. Villanueva, Modelling of dynamic characteristics of an automatic transmission during shift changes, Proceedings of the Institution of Mechanical Engineers, Part I: Journal of Systems and Control Engineering, 216 (2002) 331-341.

[20] J. Deur, J. Petrić, J. Asgari, D. Hrovat, Recent advances in control-oriented modeling of automotive power train dynamics, Mechatronics, IEEE/ASME Transactions on, 11 (2006) 513-523.

[21] J. Jang, M. Khonsari, Thermal characteristics of a wet clutch, Journal of tribology, 121 (1999) 610-617.

[22] D. Karnopp, Computer simulation of stick-slip friction in mechanical dynamic systems, Journal of dynamic systems, measurement, and control, 107 (1985) 100-103.

[23] R. Leine, D. Van Campen, A. De Kraker, L. Van Den Steen, Stick-slip vibrations induced by alternate friction models, Nonlinear dynamics, 16 (1998) 41-54.

[24] A. Crowther, N. Zhang, D. Liu, J. Jeyakumaran, Analysis and simulation of clutch engagement judder and stick-slip in automotive powertrain systems, Proceedings of the Institution of Mechanical Engineers, Part D: Journal of Automobile Engineering, 218 (2004) 1427-1446.

[25] P.D. Walker, N. Zhang, Numerical investigations into shift transients of dual clutch transmission equipped powertrains with multiple nonlinearities, Journal of Vibration and Control, (2013) 1077546313499179.

[26] T. Sun, H. Hu, Nonlinear dynamics of a planetary gear system with multiple clearances, Mechanism and Machine Theory, 38 (2003) 1371-1390.

[27] J. Lin, R. Parker, Planetary gear parametric instability caused by mesh stiffness variation, Journal of Sound and vibration, 249 (2002) 129-145.

[28] A. Bodas, A. Kahraman, Influence of carrier and gear manufacturing errors on the static load sharing behavior of planetary gear sets, JSME International Journal, Series C: Mechanical Systems Machine Elements & Manufacturing, 47 (2004) 908-915.

[29] T. Kiekbusch, D. Sappok, B. Sauer, I. Howard, Calculation of the combined torsional mesh stiffness of spur gears with two-and three-dimensional parametrical FE models, Strojniški vestnik-Journal of Mechanical Engineering, 57 (2011) 810-818.

[30] A. Kahraman, R. Singh, Interactions between time-varying mesh stiffness and clearance non-linearities in a geared system, Journal of Sound and Vibration, 146 (1991) 135-156.

[31] H.B. Pacejka, R.S. Sharp, Shear force development by pneumatic tyres in steady state conditions: a review of modelling aspects, Vehicle system dynamics, 20 (1991) 121-175.

[32] C. Canudas-de-Wit, P. Tsiotras, E. Velenis, M. Basset, G. Gissinger, Dynamic friction models for road/tire longitudinal interaction, Vehicle System Dynamics, 39 (2003) 189-226.

[33] J.Y. Wong, Theory of ground vehicles, John Wiley & Sons, 2001.

[34] E. Berger, F. Sadeghi, C. Krousgrill, Finite element modeling of engagement of rough and grooved wet clutches, Journal of Tribology, 118 (1996) 137-146.

[35] M. Li, M. Khonsari, D. McCarthy, J. Lundin, on the wear prediction of the paper-based friction material in a wet clutch, Wear, (2015).

[36] P. Willermet, G. Gupta, D. Honkanen, J. Sprys, D. Mcwatt, ATF bulk oxidative degradation and its effects on LVFA friction and the performance of a modulated torque converter clutch, SAE Technical Paper, 1998.

[37] T. Kugimiya, N. Yoshimura, T. Kuribayashi, J.i. Mitsui, F. Ueda, Y. Ando, T. Nakada, H. Ohira, Next generation high performance ATF for slip-controlled automatic transmission, SAE Technical Paper, 1997.

[38] J.J. Rodgers, M.L. Haviland, Friction of transmission clutch materials as affected by fluids, additives, and oxidation, SAE Technical Paper, 1960.

[39] T.S. Derevjanik, Detergent and friction modifier effects on metal/metal and clutch material/metal frictional performance, SAE Technical Paper, 2001.

[40] R. Oldfield, R. Watts, Impact of lubricant formulation on the friction properties of carbon fiber clutch plates, Lubrication Science, 18 (2006) 37-48.

[41] T. Newingham, Automatic Transmission Fluid-Component Effects on Friction, SAE Technical Paper, 1963.

[42] J. Jang, M. Khonsari, Wet clutch friction material: the surfaced groove effect, Encyclopedia of tribology, Springer, 2013, pp. 4102-4108.

CHAPTER 7 SUMMARY AND FUTURE WORKS

7.1 Summary

In the dissertation, the transmission system is studied at two different levels: the component level of a wet clutch and the system level of the powertrain. For simulation-based design with the objective to enhance the durability and the performance of shifting, the following topics are covered.

7.1.1 Tribological study of a wet clutch

The thermohydrodynamic analysis of a wet clutch is investigated by comprehensive considerations of lubrication, rough surface contact and heat transfer. The temperature field during the full engagement cycle (engagement, soak, dwell, and stabilization) is presented that takes into account the heat generation and convectional cooling. Groove effects of the friction lining design are taken into account by parametric study of the groove pattern, section profile, width, and the depth. The engagement results (temperature and clutch dynamics) provide guidelines for future design of clutch and durability analysis.
A wear model of a wet clutch is proposed for the first time for realistic prediction of the thickness reduction of the friction lining during large engagement cycles. Based on the experimental observation of the "two-stage" wear, the wear is shown to be closely related to thermal and mechanical degradations that are caused by repeated engagement with intense temperature rise. The temperature history is computed with thermohydrodynamic analysis, which is verified with test results. Comaprison of the predicted wear rate is shown to be satisfactory and in accordance with the experimental results published recently.

The wear model is further investigated with an uncertainty quantification analysis that considers the uncertainty and variability in the input data, which causes deviation of wear prediction in a probabilistic sense. The Monte Carlo simulation is performed to compute the cumulative distribution function (CDF) of the predicted wear rate, where the uncertainties are quantitatively characterized by be classified as “aleatory” or “epistemic”. Compared with deterministic simulations, the uncertainty quantification framework provides a rigorous analysis of wear simulation. The efficiency of Monte Carlo simulation is improved by the sensitivity study of wear input, which identifies the most influential variables to reduce the total numerical experiments.

The wear factors on the frictional material life are fully investigated to enhance the durability performance of the friction lining. Previous thermohydrodynamic (THD) simulation of a wet clutch indicates the groove effects on the thermal behaviors of the friction lining during the engagement cycle. Further analysis of the groove factors (groove pattern, width, and depth) is presented to aid the engineer in selecting the optimal groove design that would extend the material life in the maximum extent.

7.1.2 Transmission dynamics

A comprehensive procedure and details of the mathematical models for analyzing the dynamics of automotive powertrain are described that takes into account the nonlinearities in the key transmission

components, i.e. the wet clutch and the planetary gear set. Noise, vibration, and harshness (NVH) factors of engagement loading and backlash in transmission are studied based on extensive powertrain simulations. With the parametric study of transmission NVH, the main source and the pattern of vibration propagation are identified.

7.2 Recommendations for future research

Future work to further enhance the simulation-guided design of transmission system can concentrate on the following aspects.

- Model development of the hydraulic system

Engagement loading profile is crucial for a smooth shift at different driving conditions. Therefore, the model of hydraulic actuator contributes to the CAE design of transmission system and selection of hydraulic components. The comprehensive model of hydraulic system usually includes shift valve, pressure relief valve, oil pump, oil circuit etc. Such consideration will enhance the simulation-guided design of the power train.

- Clutch thermal management

The temperature rise during the engagement is intense, and leads to severe degradation of the friction material and transmission fluid. For durability consideration, sufficient lubricant supply for the clutch cooling is important, especially at high rotational speed. To achieve the cooling objective, an appropriate control strategy should be developed along with the lubrication model of the flow circuit. Moreover, the simulation accuracy of the heat dissipation in the clutch pack can be improved by the calculation of the heat transfer coefficient with computational fluid dynamics (CFD) simulation.

- Transmission NVH analysis

The NVH analysis of transmission tackles the vibration propagation in the driveline to minimize noise and enhance component durability. The previous model of transmission dynamics can be improved by considering the dynamic interactions between the engine (crankshaft, piston, valvetrain, timing drive, and accessory drive systems) and the transmission. Based on the vibration signal evaluated through powertrain virtual analysis, clutch control at transient engine velocity/torque trajectory during gear shift can be achieved to eliminate powertrain NVH appropriately. Moreover, the causes and mechanisms leading to excessive impact noise can be identified at the early design stage, where the transmission rattle could be removed through optimal selection of gear design and clutch damper performance.

- Fault diagnosis application

The dynamic model of powertrain system can be applied to estimate the system state, which lays the foundation for fault diagnosis of the transmission by using the model-based method. In future development of detection program, model uncertainties should be tackled appropriately to prevent false alarm. The occurrence of system fault would be reported by signal residual correlated with the estimation error as deviation when the threshold of alarm is exceeded.

APPENDIX LETTERS OF PERMISSION TO USE PUBLISHED MATERIAL

ELSEVIER LICENSE
TERMS AND CONDITIONS

Jun 30, 2017

This Agreement between Louisiana State University -- Meng Li ("You") and Elsevier ("Elsevier") consists of your license details and the terms and conditions provided by Elsevier and Copyright Clearance Center.

License Number	4138940642092
License date	Jun 30, 2017
Licensed Content Publisher	Elsevier
Licensed Content Publication	Tribology International
Licensed Content Title	Parametric analysis for a paper-based wet clutch with groove consideration
Licensed Content Author	M. Li,M.M. Khonsari,D.M.C. McCarthy,Joakim Lundin
Licensed Content Date	Dec 1, 2014
Licensed Content Volume	80
Licensed Content Issue	n/a
Licensed Content Pages	12
Start Page	222
End Page	233
Type of Use	reuse in a thesis/dissertation
Intended publisher of new work	other
Portion	full article
Format	electronic
Are you the author of this Elsevier article?	Yes

Will you be translating?	No
Order reference number	
Title of your thesis/dissertation	Tribological and Dynamical Study of an Automotive Transmission System
Expected completion date	Jul 2017
Estimated size (number of pages)	160
Elsevier VAT number	GB 494 6272 12
Requestor Location	Louisiana State University 3304 Patrick F Taylor hall BATON ROUGE, LA 70803 United States Attn: Louisiana State University
Publisher Tax ID	98-0397604
Total	0.00 USD

ELSEVIER LICENSE
TERMS AND CONDITIONS

Jun 30, 2017

This Agreement between Louisiana State University -- Meng Li ("You") and Elsevier ("Elsevier") consists of your license details and the terms and conditions provided by Elsevier and Copyright Clearance Center.

License Number	4138940551383
License date	Jun 30, 2017
Licensed Content Publisher	Elsevier
Licensed Content Publication	Wear
Licensed Content Title	On the wear prediction of the paper-based friction materialin a wet clutch

Licensed Content Author	M. Li,M.M. Khonsari,D.M.C. McCarthy,J. Lundin
Licensed Content Date	Jul 15, 2015
Licensed Content Volume	334
Licensed Content Issue	n/a
Licensed Content Pages	11
Start Page	56
End Page	66
Type of Use	reuse in a thesis/dissertation
Intended publisher of new work	other
Portion	full article
Format	electronic
Are you the author of this Elsevier article?	Yes
Will you be translating?	No
Order reference number	
Title of your thesis/dissertation	Tribological and Dynamical Study of an Automotive Transmission System
Expected completion date	Jul 2017
Estimated size (number of pages)	160
Elsevier VAT number	GB 494 6272 12
Requestor Location	Louisiana State University 3304 Patrick F Taylor hall BATON ROUGE, LA 70803 United States Attn: Louisiana State University
Publisher Tax ID	98-0397604
Total	0.00 USD

ELSEVIER LICENSE
TERMS AND CONDITIONS

Jun 30, 2017

This Agreement between Louisiana State University -- Meng Li ("You") and Elsevier ("Elsevier") consists of your license details and the terms and conditions provided by Elsevier and Copyright Clearance Center.

License Number	4138940725019
License date	Jun 30, 2017
Licensed Content Publisher	Elsevier
Licensed Content Publication	Wear
Licensed Content Title	Model validation and uncertainty analysis in the wear prediction of a wet clutch
Licensed Content Author	M. Li,M.M. Khonsari,N. Lingesten,P. Marklund,D.M.C. McCarthy,J. Lundin
Licensed Content Date	Oct 15, 2016
Licensed Content Volume	364
Licensed Content Issue	n/a
Licensed Content Pages	10
Start Page	112
End Page	121
Type of Use	reuse in a thesis/dissertation
Intended publisher of new work	other
Portion	full article
Format	electronic
Are you the author of this Elsevier article?	Yes
Will you be translating?	No

Order reference number	
Title of your thesis/dissertation	Tribological and Dynamical Study of an Automotive Transmission System
Expected completion date	Jul 2017
Estimated size (number of pages)	160
Elsevier VAT number	GB 494 6272 12
Requestor Location	Louisiana State University 3304 Patrick F Taylor hall BATON ROUGE, LA 70803 United States Attn: Louisiana State University
Publisher Tax ID	98-0397604
Total	0.00 USD

VITA

Meng Li was born in Taian, China. He received Bachelor of Engineering from China University of Petroleum in 2011. In August 2011, he started to pursue his doctoral study in the Department of Mechanical and Industrial Engineering of Louisiana State University. Since then, he has been a doctoral student under the guidance of Dr. Michael M. Khonsari, Dow Chemical Endowed Chair and Professor in the Department of Mechanical Engineering of Louisiana State University. Meng Li is a candidate to receive his Doctor of Philosophy degree at the 2017 Summer Commencement.